CORA Cork Open Research Archive
Cartlann Taighde Oscailte Chorcaí

Title	Integrated spot size converters for InP based photonic systems
Authors	Wieczorek, Andreas
Publication date	2013
Original Citation	Wieczorek A. 2013. Integrated spot size converters for InP based photonic systems. PhD Thesis, University College Cork.
Type of publication	Doctoral thesis
Rights	© 2013, Andreas Wieczorek. - http://creativecommons.org/licenses/by-nc-nd/3.0/
Download date	2026-11-03 21:22:14
Item downloaded from	https://hdl.handle.net/10468/1172



UCC
University College Cork, Ireland
Coláiste na hOllscoile Corcaigh

Integrated Spot Size Converters for InP based Photonic Systems

by

Andreas Wieczorek

THESIS SUBMITTED TO
THE NATIONAL UNIVERSITY OF IRELAND, CORK
FOR THE DEGREE OF

Doctor of Philosophy

TYNDALL NATIONAL INSTITUTE, DEPARTMENT OF PHYSICS
NATIONAL UNIVERSITY OF IRELAND, CORK
IRELAND



October 2012

RESEARCH SUPERVISOR: Brian Corbett and Dr. Frank H. Peters
HEAD OF DEPARTMENT: Prof. John McInerney

I declare that this thesis contains my own work and has not been submitted for another degree, either at University College Cork or elsewhere.

Andreas Wieczorek

Acknowledgements

I would like to start to acknowledge all those who have contributed to this thesis by thanking my supervisor Brian Corbett for all his help, advice and encouragement. I would also like to thank my second supervisor Frank Peters for managing the Photonic Integration from Atoms to Systems (PIFAS) project and fruitful discussions.

This work would not have been possible without the financial support from Science Foundation Ireland, SFI. SFI founded the PIFAS project.

The measurements would not have been possible without the help of Brendon Roycraft, who also gave me good advices during the whole thesis period.

Especially, James O'Callaghan, KoHsin Lee, Vladimir Djara, John Justice, Dan O'Conell and Carmel Murphy helped me and gave me good advises during the device processing. I would like to thank Kevin Thomas for growing the chips.

Many colleagues and friends from the Tyndall National Institute provided a helping hand in solving small and not-so-small problems, or just made work more enjoyable: Mehmet Copuroglu, Brad Snyder, Vimal Jeyaseelan, Pio Jessudos, Santhos Kulkarni, Brian McGarthy, Aidan Daly, Valeria Dimastrodonato, Shane McDermot, Jeffrey Godsell, Tom Sadler, Carmel Kellegher, Padraig Curran, Clair Barrett, Rathnait Long, Pierre Lovera, Nicolas Sassiat, Rosemary O'Keeffe, Yang Hua, Han Wei, Jan Peter Engelstädter Robert Sheehan, David Goulding, Nicolas Holubowitch, Chris Daunt, Pawel Sajewicz.

My thanks go to my friends and family, especially my parents Elisabeth and Ulrich Wieczorek, my sister Barbara Wieczorek and her family for all their support and encouragement. Especially, without support of my father it would not have been possible to finish my work. Unfortunately he cannot experience the last stages of my work anymore.

Abstract

The ever increasing demand for broadband communications requires sophisticated devices. Photonic integrated circuits (PICs) are an approach that fulfills those requirements. PICs enable the integration of different optical modules on a single chip. Low loss fiber coupling and simplified packaging are key issues in keeping the price of PICs at a low level. Integrated spot size converters (SSC) offer an opportunity to accomplish this.

Design, fabrication and characterization of SSCs based on an asymmetric twin waveguide (ATG) at a wavelength of 1.55 μm are the main elements of this dissertation. An improved fabrication tolerance by tapering the mode beating section is found for resonant coupling. It is theoretically and experimentally shown that a passive ATG facilitates a polarization filter mechanism. A reproducible InP process guideline is developed that achieves vertical waveguides with smooth sidewalls and a minimum taper width of 1 μm.

Birefringence and resonant coupling are used in an ATG to enable a polarization filtering and splitting mechanism. For the first time such a filter is experimentally shown. At a wavelength of 1610 nm a power extinction ratio of (1.6$\pm$0.2) dB was measured for the TE- polarization in a single approximately 372 μm long TM-pass polarizer. A TE-pass polarizer with a similar length was demonstrated with a TM/TE-power extinction ratio of (0.7$\pm$0.2) dB at 1610 nm.

The refractive indices of two different InGaAsP compositions, required for a SSC, are measured by the reflection spectroscopy technique. A SSC layout for dielectric-free fabricated compact photodetectors is adjusted to those index values.

The development and the results of the final fabrication procedure for the ATG concept are outlined. Critical aspects, such as photoresist properties, exposure con-

tact, dry etch recipe and etch mask quality, are explained. The etch rate, sidewall roughness and selectivity of a $Cl_2/CH_4/H_2$ based inductively coupled plasma (ICP) etch are investigated by a design of experiment approach. The passivation effect of CH_4 is illustrated for the first time. Conditions are determined for etching smooth and vertical sidewalls up to a depth of 5 μm. A waveguide loss of (2.6±0.4) dBcm^{-1} for the TE-polarization and (1.9±0.3) dBcm^{-1} for the TM-polarization was calculated at 1550 nm.

Contents

List of Tables **5**

List of Figures **6**

Acronyms **18**

1 Introduction **20**

1.1 Data Communication and Photonic Integrated Circuits 20

1.2 Importance of Integrated Spot Size Converters 22

2 Brief Overview of Optical Waveguide Theory and Simulation Methods **25**

2.1 Optical Waveguide Theory 25

2.1.1 Slab Waveguide 26

2.1.2 Coupled Mode Theory 31

2.2 Simulation Methods for Optical Waveguides 35

3 Spot size converter concepts **39**

3.1 The grating coupler 39

3.1.1 Applications of Grating Couplers in Silicon on Insulator Systems 40

3.1.2 Applications of Grating Couplers for InP Systems 41

3.2 Taper Assisted Spot Size Converters 43

3.2.1 Lateral Tapers 44

3.2.2 Vertical Tapers 46

3.2.3 Combined Tapers 47

3.3 Asymmetric Twin Waveguides 50

3.4 Antiresonant Reflecting Optical Waveguides 54
3.5 Polymer and Silicon Oxynitride Waveguides 58
3.6 Conclusion 61

4 Optical Coupling between Waveguides 63
4.1 Coupling between Two Vertically Separated Waveguides 63
4.1.1 Resonance and Cut-off Points 66
4.1.2 Adiabatic Coupling 71
4.1.3 Resonant Coupling 74
4.2 Improving the Fabrication Tolerance for Resonant Couplers in an Asymmetric Twin Waveguide 76
4.2.1 Analysis of the Loss Factors for Adiabatic and Resonant Couplers 76
4.2.2 Tapering the Mode Beating Section 83
4.3 Conclusion 85

5 Polarization Filter and Splitter 87
5.1 Data Communication and Photonic Integrated Circuits 87
5.2 Asymmetric Twin Waveguide and Resonant Coupling 89
5.3 TE/TM-Pass Polarizer 90
5.4 Polarization Splitter 97
5.5 Conclusion 104

6 Characterization of the Polarization Filters 105
6.1 Layout and Fabrication Steps of the Polarizations Filters 105
6.2 Measurement Setup and Method 109
6.3 Measurements of the Polarizer Spectra 111
6.4 Conclusion 118

7 Spot Size Converters for a PIN-Photodiode 119
7.1 PIN-photodiode with a 5 μm Spot Size Input Waveguide 119
7.1.1 Photodiode and Spot Size Converter Layout 121
7.1.2 Optical Field Behaviour 123

7.2 PIN-photodiode with a 8 μm Spot Size Input Waveguide 127
7.2.1 Photodiode and Spot Size Converter Layout 127
7.2.2 Fabrication Tolerance 129
7.3 Conclusion 134

8 Determining the Refractive Index of $In_{1-x}Ga_xAs_yP_{1-y}$ Layers 135
8.1 Refractive Index of $In_{1-x}Ga_xAs_yP_{1-y}$ relative to the Composition . . 135
8.2 Measurements of $In_{1-x}Ga_xAs_yP_{1-y}$ Refractive Indices 138
8.2.1 Measurement Method 138
8.2.2 MOVPE Growth A0983 139
8.2.3 MOVPE Growth A1034 144
8.3 Conclusion 148

9 Device Fabrication 150
9.1 Simplified Alignment Process with a SiO_2/Si_3N_4 Etch Mask 151
9.1.1 Process Outline 152
9.1.2 Problems during the Si_3N_4 Patterning Step 154
9.1.3 Problems during the Inductively Coupled Plasma (ICP) Etch Step 160
9.2 Simplified Alignment Process with a SiO_2 and Titanium Mask 163
9.2.1 Process Outline 163
9.2.2 SiO_2 Etch Mask 165
9.3 Inductively Coupled Plasma Deep Etching using $Cl_2/CH_4/H_2$ 169
9.3.1 Experimental Conditions 170
9.3.2 Etch Analysis 171
9.3.3 Optimized conditions 176
9.4 Optimized Process Steps 185
9.5 Conclusion 189

10 Conclusion 191
10.1 Summary of Results 191
10.2 Main Conclusion 193

10.3 Outlook 194

A Publications **196**

B Numerical Methods **198**

B.1 Maxwell's Equations 198

B.2 Finite Element Method 199

B.2.1 Variational Method 199

B.2.2 Galerkin Method 200

C MOVPE Growth A0887 **202**

D Photodiode-Spot Size Converter MOVPE Growth **203**

E Process Guideline **205**

E.0.3 SiOSiNx Process 205

E.0.4 TiSiO process 207

E.0.5 Spot Size Converter and Photodiode 209

Bibliography **213**

List of Tables

3.1 Best coupling result of each taper design. 49

5.1 Polarizer properties at a wavelength of 1.55 μm 88
5.2 Polarization splitter properties at a wavelength of 1.55 μm 88
5.3 Configuration of the 372 μm long TM-pass polarizer. 91
5.4 Configuration of the 242 μm long TE-pass polarizer. 94
5.5 Configuration of the 605 μm long first sector in the polarization splitter. 99
5.6 Simulation results of the polarizers and the polarization splitter. . . . 104

6.1 Losses in the lower waveguide. 115
6.2 Waveguide losses in Filter1. 116
6.3 Waveguide losses in Filter2. 117
6.4 Power extinction ratio for a single stage of Filter1 and Filter2. 118

7.1 Configuration of the spot size converter and the photodiode 121
7.2 Configuration of the spot size converter and the photodiode 129

9.1 Process equipment used at Tyndall National Institute 151
9.2 Photoresist properties [1, 2] 156
9.3 Established ICP etch chemistries 160
9.4 Gas flows investigated 170
9.5 Temperature relative to etch time. 180

List of Figures

1.1 Predicted monthly data traffic increase from 2011 till 2016 (EB = exabyte) [3]. 21

1.2 Photograph of a monolithic InP PIC comprising four O-band distributed feedback lasers and an arrayed waveguide grating with 24.5 nm channel spacing. The chip size is 1.1 x 2.4 mm [4] 22

1.3 Photograph of an integrated Mach-Zehnder-Interferometer (MZI) module coupled to lensed fibers [5]. 23

1.4 Intensity of the TE-polarization. (a) 10.4 μm diameter circular spot size of a single mode fiber. (b) 2.4 (horizontal) and 1.0 μm(vertical) spot size of a 1.55 μm laser 24

2.1 Schematic of a slab waveguide 26

2.2 $u - w$ relationship in a symmetric slab waveguide. 28

2.3 Dispersion curves for the TE modes in the slab waveguide. 30

2.4 Directionally coupled optical waveguides. 31

2.5 Optical power in a codirectional coupler with (a) F = 1.0 and $\delta = 0$ and (b) F = 0.2 and $\delta = 2\kappa$. 34

2.6 Semiconductor ridge waveguide, represented by a number of slices and layers their in. 37

3.1 Grating coupler for coupling between a SOI photonic wire and an optical fiber [6]. 41

3.2 (a) Sketch of grating coupler. (b) Cross-section of fabricated structure with AR-coating [7]. 43

3.3 Lateral taper designs: (a) Laterally down-tapered buried waveguide (b) Laterally up-tapered waveguide (c) Dual lateral overlapping buried waveguide taper (d) Dual lateral overlapping ridge waveguide taper (e) Nested waveguide taper transition (f) Single lateral taper transition (g) Multisection taper transition [8]. 44

3.4 Vertical taper designs: (a) Vertical down-tapered buried waveguide. (b) Vertical down-tapered ridge waveguide. (c) Vertical overlapping ridge waveguide. (d) Vertical overlapping taper transition from a buried waveguide to a fiber-matched waveguide. (e) Vertical overlapping waveguide taper transition from a ridge waveguide to a fiber-matched waveguide [8]. 46

3.5 Combined vertical and lateral taper designs: (a) Combined lateral and vertical ridge waveguide taper. (b) 2-D overlapping waveguide taper transition from a buried waveguide to a fiber-matched waveguide. (c) Overlapping waveguide taper transition with two sections from a ridge waveguide to a fiber matched waveguide [8]. 48

3.6 Model for the ITG laser [9]. 51

3.7 Schematic diagram of the twin waveguide structure with passive waveguide. Inset: Refractive index and calculated mode profiles in the TG structure with InGaAs loss layer [10]. 52

3.8 (a) Three-dimensional schematic view of the integrated ATG SOA/p-i-n chip. (b) Index profile of the SOA/p-i-n epitaxial structure. . The tapered section of the passive guide joins these two parts together [11]. 53

3.9 Waveguide scheme using antiresonant reflection. 54

3.10 Scheme of the optically pumped/optical grating InGaAsP/InP ARROW with active and passive region [12]. 57

3.11 Schematic drawing and SEM images of a laser and an integrated ARROW [13]. 57

3.12 Basic structure under consideration illustrating the transfer of power from the fiber to the polymer and then to the GaAs waveguide [14]. . 59

4.1 Schematic cross-section of the ATG with the diluted lower waveguide 64

4.2 E_x profile at an upper cladding width of 2.5 μm, (a) for the even TE-mode, (b) for the odd TE-mode. 65

4.3 TE mode intensity profile, (a) ridge width 2.5 μm, lower waveguide width 6 μm: optical field width ($1/e^2$) horizontal: 2.2 μm, width vertical ($1/e^2$): 1.2 μm,
(b): lower waveguide width 6 μm: optical field width ($1/e^2$) horizontal: 4.6 μm, width vertical ($1/e^2$): 4.3 μm, ... 66

4.4 E_x profile at an upper InP cladding width of 1.6 μm, (a) for the even TE-mode, (b) for the odd TE-mode. 67

4.5 Propagation constants (n(upper wg) = 3.40) and its difference for the (a) TE-polarization (b) TM-polarization. 68

4.6 Propagation constants (n(upper wg) = 3.50) and its difference for the (a) TE-polarization (b) TM-polarization. 69

4.7 Intensity profile of the TE-polarization (a) at a upper cladding width of 1.0 μm, (b) only the lower waveguide is present, the upper cladding is removed. 70

4.8 Intensity profile of the TE-polarization (a) at a upper cladding width of 1.0 μm, (b) only the lower waveguide is present, the upper cladding is removed. 71

4.9 Schematic diagram of the resonantly coupled-mode expander [15]. . . 75

4.10 Layout of the (a) adiabatic coupler and (b) the resonant coupler . . . 77

4.11 Side view of the adiabatic coupler, contour plot of the field intensity distribution. The vertical lines correspond to section boundaries. . . . 78

4.12 Power distribution between even and odd mode for the adiabatic coupler. The power is in the even mode initially 79

4.13 Side view of the resonant coupler, contour plot of the field intensity distribution. The vertical lines correspond to section boundaries. . . . 79

4.14 Power distribution between even and odd mode for the resonant coupler. The power is in the even mode initially 80

4.15 Mode power in the output mode regarding to a upper waveguide width variation 81

4.16 Power distribution between even and odd mode for the 200 nm wider resonant coupler 82

4.17 Side view of the 200 nm wider resonant coupler, contour plot of the field intensity distribution. The vertical lines correspond to section boundaries. 82

4.18 Mode power in the output mode regarding to a lower waveguide refractive index variation 83

4.19 Comparison of the mode power of the output mode of a straight resonant coupler to one with $\Delta W_d = 200$ nm 84

4.20 Mode power of the output mode for different ΔW_ds. The ideal case and a ± 100 nm variation are displayed 84

4.21 Mode power of the output mode for $\Delta W_d = 200$ and 500 nm 85

4.22 Mode power of the output mode regarding to a lower waveguide refractive index variation for a straight and a $\Delta W_d = 500$ nm mode beating section 85

5.1 Schematic of the TM-pass polarizer 90

5.2 Power distribution along the TM-pass polarizer. The vertical lines correspond to the section boundaries of Tab. 5.3, additional there is a 10 μm long in- and output section. (a) Input: fundamental TM-mode, (b) Input: fundamental TE-mode. 92

5.3 Side view of the intensity distribution of the TM-field, the input is on the left side in the lower waveguide. The vertical lines correspond to section boundaries. 93

5.4 Side view of the intensity distribution of the TE-field, the input is on the left side in the lower waveguide. The vertical lines correspond to section boundaries. 93

5.5 Power distribution along the TE-pass polarizer. The vertical lines correspond to section boundaries. (a) Input: fundamental TE-mode, (b) Input: fundamental TM-mode. 95

5.6 Side view of the intensity distribution of the TM-field, the input is on the left side in the lower waveguide. The vertical lines correspond to section boundaries. 96

5.7 Side view of the intensity distribution of the TM-field, the input is on the left side in the lower waveguide. The vertical lines correspond to section boundaries. 96

5.8 Power extinction ratio for the TM- and TE-pass polarizer. 97

5.9 Sketch of the polarization splitter 98

5.10 Power distribution among the modes for the polarization splitter (a) Input is the fundamental TE-mode, (b) Input is the fundamental TM-mode 100

5.11 Intensity distribution of the TE-polarization at a z-position of 690 μm in the splitter section (a) fundamental mode, (b) first order mode 101

5.12 Plan view of the intensity distribution for the TE-polarization 102

5.13 Plan view of the intensity distribution for the TM-polarization 102

5.14 Relative power extinction ratio versus wavelength for the polarization splitter 103

6.1 SEM cross-section images (a) of the single mode input waveguide, (b) of the ATG with an upper InP cladding width of 2.5 μm. 106

6.2 Side view of the intensity distribution of the TE-field, the input is on the left side in the lower waveguide. The vertical lines correspond to section boundaries. 108

6.3 Side view of the intensity distribution of the TM-field, the input is on the left side in the lower waveguide. The vertical lines correspond to section boundaries. In both cases the taper start width is 700 nm. The total taper width is reduced by 300 nm compared to the ideal case in Chapter 5. 108

6.4 Side view of the intensity distribution of the TE-field, the input is on the left side in the lower waveguide. The vertical lines correspond to section boundaries. 109

6.5 Side view of the intensity distribution of the TM-field, the input is on the left side in the lower waveguide. The vertical lines correspond to section boundaries. In both cases the taper start width is 900 nm. The total taper width is reduced by 100 nm compared to the ideal case in Chapter 5. 109

6.6 Schematic of the measurement setup. 110

6.7 SEM cross-section images (a) of Filter1, (b) of the taper end of the polarizer, (c) of the center of Filter1. 112

6.8 Fabry-Pèrot spectrum (1550 nm) of the lower 5400 μm long waveguide and the polarization state of the TLS beam (a) for the TE-polarization, (b) and the TM-polarization, (c) Comparison of both polarizations. 113

6.9 Fabry-Pèrot spectrum (1610 nm) of the lower waveguide and the polarization state of the TLS beam (a) for the TE-polarization, (b) and the TM-polarization, (c) Comparison of both polarizations. 114

6.10 Fabry-Pèrot spectrum (1550 nm) of Filter1 (cavity length: 5400 μm) and the polarization state of the TLS beam (a) for the TE-polarization, (b) and the TM-polarization, (c) comparison of both polarizations. . . 115

6.11 Fabry-Pèrot spectrum (1550 nm) of Filter1 (cavity length: 5400 μm) and the polarization state of the TLS beam (a) for the TE-polarization, (b) and the TM-polarization, (c) comparison of both polarizations. . . 116

6.12 Cross-section SEM images of Filter2 (a) of the taper end of the polarizer, (b) of the center of Filter2. 117

6.13 Fabry-Pèrot spectrum of Filter2 (cavity length: 5400 μm) for both polarizations and the polarization state of the TLS beam (a) at a wavelength of 1550 nm, (b) and a wavelength of 1610 nm. 117

7.1 Schematic drawing of dielectric-free ridge waveguide PD using isolated pedestal contact configuration [16]. 120

7.2 (a) Three-dimensional schematic view of the photodiode and the waveguides. (b) Schematic cross-section side-view of the layer structure. 122

7.3 Excited mode intensity distribution at the intersection SSC-PD (a) lowest order mode with an overlap between the CWG and absorber, (b) next higher order mode with an overlap between the CWG and absorber, (c) higher order mode with hardly any overlap between the CWG and absorber,(d) Cross section view of the layers of the SSC and PD. 124

7.4 Intensity distribution of the TE-polarization in the PD-SSC structure, (a) plan view, (b) side view. 125

7.5 Absorption efficiency relative to a misalignment of the PD (a) taper end width equals PD width, (b) taper end 400 nm wider than PD, (c) comparison of both cases for the TM-polarization 126

7.6 (a) Schematic cross-section view of the layer structure. (b) Three-dimensional schematic view of the photodiode and the waveguides. . . 128

7.7 Intensity distribution of the TE-polarization in the PD-SSC structure, (a) plan view, (b) side view. 130

7.8 Absorption efficiency relative to a misalignment (a) of the input to the transition waveguide, (b) of the transition to the coupling waveguide, (c) of the coupling waveguide to the photodiode. 131

7.9 Absorption efficiency relative to a width variation (a) of the input waveguide, (b) of the transition waveguide, (c) of the coupling waveguide. 132

7.10 Absorption efficiency relative to a refractive index variation of (a) InGaAsP ($\lambda_g = 1020$ nm), (b) InGaAsP ($\lambda_g = 1140$ nm), (c) InGaAsP ($\lambda_g = 1175$ nm). 133

7.11 Absorption efficiency relative to a difference in the n-contact etch depth 134

8.1 Refractive index of InGaAsP lattice matched to InP (a) versus wavelength in the transparent region (b) versus bandgap wavelength for a fixed wavelength of 1550 nm 137

8.2 SEM images of run A0983: (a) InGaAsP epi layer on InP substrate at the center of the wafer (b) InGaAsP epi layer on InP substrate at the edge of the wafer 140

8.3 Refractive indices of the InP substrate calculated from the reflection measurements 141

8.4 A0983: (a) Reflection measurements at different positions (b) Calculated refractive indices and Sellmeier-fit 143

8.5 SEM images run of A1034: (a) InGaAsP epi layer on InP substrate at the center of the wafer (b) InGaAsP epi layer on InP substrate at the edge of the wafer 145

8.6 A1034: (a) Reflection measurements at different positions (b) Calculated refractive indices and Sellmeier-fit 146

8.7 Rocking curve of chip A1034 147

8.8 Photoluminescent measurement of chip A1034. 148

9.1 Consecutive process steps used, (a) after the first lithography step, (b) after the SiN_x mask is patterned, (c) after the SiO_2 layer is patterned, (d) after the first 4μm deep III-V material ICP etch, (e) after the overlaying SiO_2 mask is removed by wet chemical etching, (f) the final ATG structure with the SiN_x mask removed. 153

9.2 Image of the first level lithography mask. A clear field mask is shown to define different shaped upper waveguides. This mask was used to obtain a resist pattern shown in Fig. 9.1(a). 155

9.3 Microscope image of UVIII after an exposure of 9 s, (a) several ridges, (b) ridge end. 156

9.4 InP/InGaAsP chip, (a) microscope image after the first UV26 processing step (b) SEM image of a taper end of a poorly processed chip 157

9.5 Image of the 100 mm diameter two level polarization filter and two level delta mask. Four different mask elements are on a single mask. . 157

9.6 Images of the MA 6 mask aligner, (a) quarter wafer chuck without a sample and with the indicated sample position (b) quarter wafer chuck with a sample and two cover chips 158

9.7 Microscope images of a properly processed InP test chip. The exposure time of UV26 was 11.5 s. (a) ridge width measurement, (b) taper section length measurement. 159

9.8 PECVD deposited SiN_x on an InP chip. 159

9.9 Cross-section SEM images of an InP-chip after a 10 min CH_4/H_2 etch. (a) cross-section of the ridge, (b) top view. 161

9.10 SEM images of a resonant coupler 200 nm wider than ideal after a 7 min 45 s and 2 min 45 s Cl_2/N_2 etch. (a) top view of the taper to the mode beating section, (b) top view of the end taper. 161

9.11 Cross-section SEM images after a 7 min 45 s and 2 min 45 s Cl_2/N_2 etch. (a) of a parabolically tapered down ridge, (b) front facet 162

9.12 Cross-section SEM images of a constant ATG after a 7 min 45 s and 2 min 45 s Cl_2/N_2 etch. (a) sidewall of the upper and lower waveguide , (b) sidewall of the upper waveguide. 163

9.13 Consecutive process steps scheme of the chip, (a) after the first lithography step, (b) after the Ti lift-off, (c) after the SiO_2 layers are patterned, (d) after the first III-V material ICP etch, (e) after the overlaying SiO_2 mask is removed by an ICP etch, (f) the final ATG structure with SiO_2/Ti mask removed. 164

9.14 Cross-section SEM images of SiO_2 on InP. (a) before the InP etch, (b) after the InP etch. 166

9.15 Cross-section SEM images of UV26 exposed and developed for 9.5 s and 25 s respectively. (a) height measurement, (b) width measurement. 167

9.16 Cross-section SEM images of UV26 exposed and developed for 5.5 s and 25 s respectively. (a) height measurement, (b) width measurement. 167

9.17 Cross-section SEM images of AZ5214 exposed and developed for 7.5 s and 25 s respectively. (a) height measurement, (b) sidewall. 168
9.18 Cross-section SEM images of AZ5214 after an SiO_2 etch. (a) front facet, (b) sidewall. 168
9.19 Cross-section sidewall SEM images, (a) $Cl_2/CH_4/H_2 = 10/15/20$ sccm sidewall roughness value 3, (b) $Cl_2/CH_4/H_2 = 4/7/20$ sccm sidewall roughness value 5, (c) $Cl_2/CH_4/H_2 = 4/15/10$ sccm sidewall roughness value 7 171
9.20 Cross-section SEM images of the front facet and sidewall of the 195 s etch of $Cl_2/CH_4/H_2 = 10/7/10$ sccm. 172
9.21 Cross-section SEM images of the front facet and sidewall of the 195 s etch of $Cl_2/CH_4/H_2 = 10/15/10$ sccm. 173
9.22 Main effects plot for the etch rate of InP/InGaAsP, (a) main effect of Cl_2, (b) main effect of CH_4, (c) main effect of H_2. 174
9.23 Interaction plot for the etch rate of of InP/InGaAsP, (a) interaction between Cl_2 and CH_4, (b) interaction between Cl_2 and H_2, (c) interaction between H_2 and CH_4. 174
9.24 Sum of squares percentages and the 80 % limit for the etch rate of InP/InGaAsP. 175
9.25 Main effects plot for the selectivity, InP/InGaAsP to SiO_2, (a) main effect of Cl_2, (b) main effect of CH_4, (c) main effect of H_2. 176
9.26 Interaction plot for the selectivity, InP/InGaAsP to SiO_2, (a) interaction between Cl_2 and CH_4, (b) interaction between Cl_2 and H_2, (c) interaction between H_2 and CH_4. 177
9.27 Sum of squares percentage and the 80 % limit for the selectivity, InP/InGaAsP to SiO_2. 177
9.28 Main effects plots for the sidewall roughness of InP/InGaAsP, (a) main effect of Cl_2, (b) main effect of CH_4, (c) main effect of H_2. . . . 178
9.29 Interaction plot for the sidewall roughness of InP/InGaAsP, (a) interaction between Cl_2 and CH_4, (b) interaction between Cl_2 and H_2, (c) interaction between H_2 and CH_4. 179

9.30 Sum of squares percentage and the 80 % limit for the sidewall roughness of InP/InGaAsP. 179

9.31 Time dependent etch rate (InP/InGaAsP) of $Cl_2/CH_4/H_2 = 10/18/12$ sccm. 180

9.32 Cross-section sidewall SEM images, (a) 120 s Cl_2/H_2 = 10/12 sccm, (b) 120 s $Cl_2/H_2/Ar$ = 10/12/18 sccm, (c) 120 s $Cl_2/CH_4/H_2$ = 10/18/12 sccm. The 'scratch' like line is most probably caused by an inferior SiO_2 mask. 181

9.33 SiO_2 etch rate and selectivity (InP/InGaAsP to SiO_2) of $Cl_2/CH_4/H_2$ = 10/18/12 sccm. 182

9.34 Cross-section SEM images of the front facet and sidewall of the 180 s etch ($Cl_2/CH_4/H_2$ = 10/18/12 sccm, InP/InGaAsP). 182

9.35 Cross-section SEM images of the sidewalls, etch ($Cl_2/CH_4/H_2 = 10/18/12$ sccm, InP/InGaAsP), (a) run 2, 180 s, (b) run 1, 210 s. The 'scratch' like lines in (a) and (b) are most probably caused by an inferior SiO_2 mask. 183

9.36 Cross-section SEM images of the front facet and sidewall of the 190 s etch ($Cl_2/CH_4/H_2$ = 10/18/12 sccm , InP substrate). 184

9.37 Microscope images after the Ti-lift-off step. (a) Section of a single TM-pass polarizers, (b) Taper end of a TM-pass polarizer with a designed width of 1.0 μm 186

9.38 Microscope images after the AZ5214 lithography step. (a) Section of a single TM-pass polarizers, (b) Taper end of a TM-pass polarizer with a designed width of 1.0 μm 186

9.39 Microscope images after the ICP removal of the second SiO_2 mask. (a) Section with two TM-pass polarizers, (b) unmodified ATG along the whole section. 187

9.40 SEM cross-section images after the process run. (a) Middle section of a 300 nm narrower TM-pass polarizer, (b) Taper end of a TM-pass polarizer with an designed width of 0.7 μm. 187

9.41 SEM cross-section images after the process run. (a) Front facet of the input waveguide, (b) sidewall of a 300 nm narrower TM-pass polarizer. 188
9.42 Microscope images of patterned UV 26 on an InP-test chip before the 200 nm thick Ti-evaporation. (a) multiple PDs with SSC, (b) SSC waveguide aligned to a 4 μm wide PD. 189
9.43 Microscope images of an InP-test chip after the 200 nm thick Ti-lift-off. (a) PDs with SSC, (b) SSC upper waveguide end 189

B.1 Analysis region. 200

Acronyms

ARROW Antiresonant reflecting optical waveguide

ATG Asymmetric twin waveguide

DBR Distributed Bragg-reflector

DFB Distributed feedback

DQPSK Differential quaternary phase shift keying

FEM Finite element method

FD-BPM Finite difference beam propagation method

FMM Film mode matching

GCSEL Grating coupled surface emitting laser

ICP Inductively coupled plasma

ITG Integrated twin guide

LPCVD Low-pressure chemical vapor deposition

MMI Multi mode interference

MOVPE Metalorganic vapour phase epitaxy

MQW Multi quantum well

MZI Mach-Zehnder-Interferometer

PD Photodiode

PECVD Plasma-enhanced chemical vapor deposition

PER Power extinction ratio

PIC Photonic integrated circuit

RIE Reactive ion etching

SEM Scanning electron microscope

SMF Single mode fiber

SMG Shadow mask growth

SOA Semiconductor optical amplifier

SOI Silicon on insulator

SSC Spot size converter

TE Transvers electric

TLS Tunable laser source

TM Transvers magnetic

WDM Wavelength division multiplexer

Chapter 1

Introduction

The subject of this thesis is the design and implementation of spot size converters for an InP based optical system. Spot size converters (SSCs) act as a passive component that facilitates the matching of the mode size and shape of different elements in a photonic integrated circuit (PIC) and improves the direct in- and out-coupling of the circuit with a fiber. This chapter gives a brief overview of the increasing demand for photonic integrated circuits for optical data communication and lays out the importance of spot size converters. Finally, the different aspects of this thesis are outlined.

1.1 Data Communication and Photonic Integrated Circuits

Nowadays data communication is omnipresent in everyday life. Around the world more and more people and companies are connected to the internet and are using it to exchange information. Online services such as search engines (e.g.: Google, Bing, Yahoo), shopping sites (e.g.: Amazon), live streams of news channels (e.g.: RTE, CNN), video platforms (e.g.: Youtube) , social networking sites (e.g.: Facebook), voice over IP (e.g.: Skype), cloud computing and filesharing are used frequently around the world. More and more devices such as smartphones, tablets, laptops and personal computers enable direct access to the internet. The increasing wealth

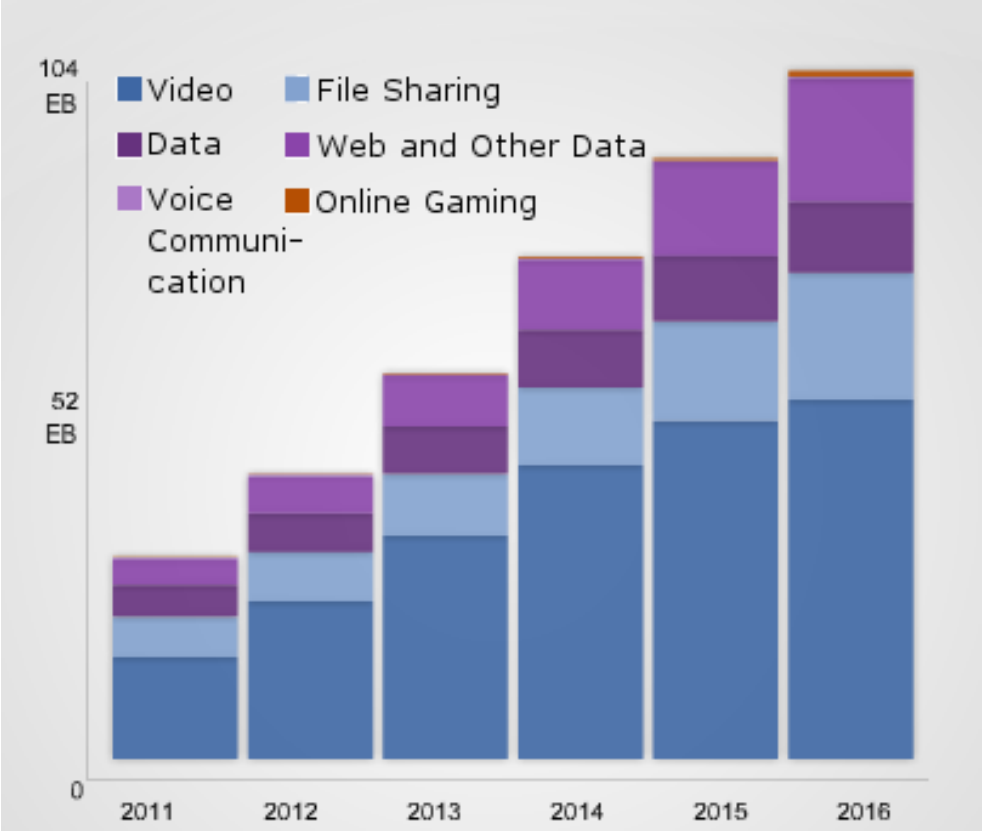


Figure 1.1: *Predicted monthly data traffic increase from 2011 till 2016 (EB = exabyte) [3].*

in highly populated countries such as China or India makes it possible for a larger number of people to get connected to the internet. These factors result in an ever increasing demand for network traffic.

Cisco Systems has predicted an increase of the world wide data traffic by a factor of three by 2016 [3]. In 2016 total IP traffic will reach 109.5 exabytes per month (Fig. 1.1. Digital modulation schemes such as differential quaternary phase shift keying (DQPSK) are required to enable higher data transfer rates with the available infrastructure. Nevertheless, several optical and electro-optical components for the signal generation/detection and modulation (e.g. laser, photodiode, arrayed waveguide grating, Mach-Zehnder-interferometer) need to be combined for implementation of DQPSK. The combination of each individual component makes the fabrication of systems complicated and expensive.

Photonic integrated circuits (PICs) offer a solution to this problem. Multiple

photonic functions can be integrated on a single semiconductor chip. PICs simplify the system design and reduce the required space and necessary power. Fig. 1.2 shows an example of a PIC. Four distributed feedback (DFB) lasers operating at

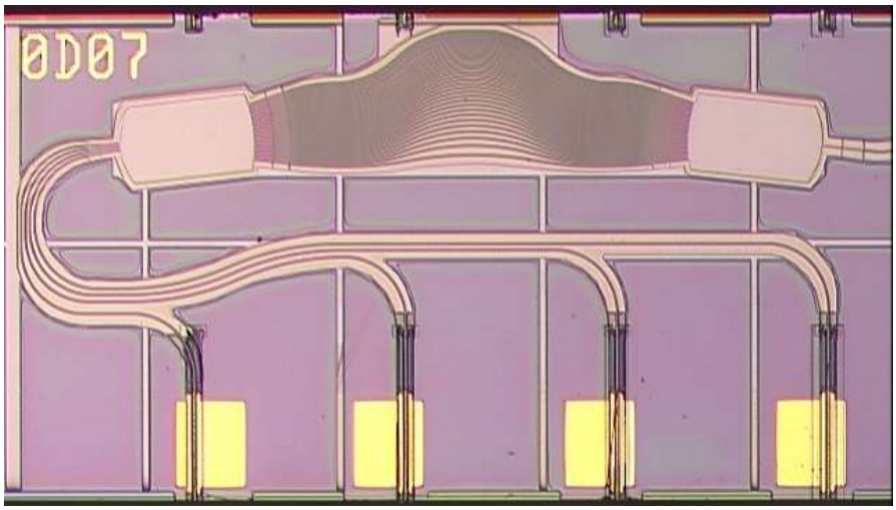


Figure 1.2: *Photograph of a monolithic InP PIC comprising four O-band distributed feedback lasers and an arrayed waveguide grating with 24.5 nm channel spacing. The chip size is 1.1 x 2.4 mm [4]*

1.3 μm are integrated with waveguide multi mode interference structures and an arrayed waveguide grating (AWG). The optical signal are combined into a single output on the right. The device has an area of only 2.64 mm^2.

1.2 Importance of Integrated Spot Size Converters

One important issue for PICs is the transmission and the receiving of optical signals to and from optical fibers. The mode size of InP-based waveguides is usually of the order of microns and is elliptical, whereas single mode fibers have a circular mode size of 10 μm. A mode mismatch can cause coupling losses of 10 dB. In Fig. 1.3 a MZI module is coupled to four lensed fibers [5]. It is not hard to imagine that the alignment of such fibers to PIC waveguides is a complicated step.

Another problem arises from the spot size mismatch of a single mode fiber and the high refractive index contrast InP material system. The standard single mode fiber (SMF) has a circular spot size of 10.4 μm (Fig. 1.4(a)), whereas an InP

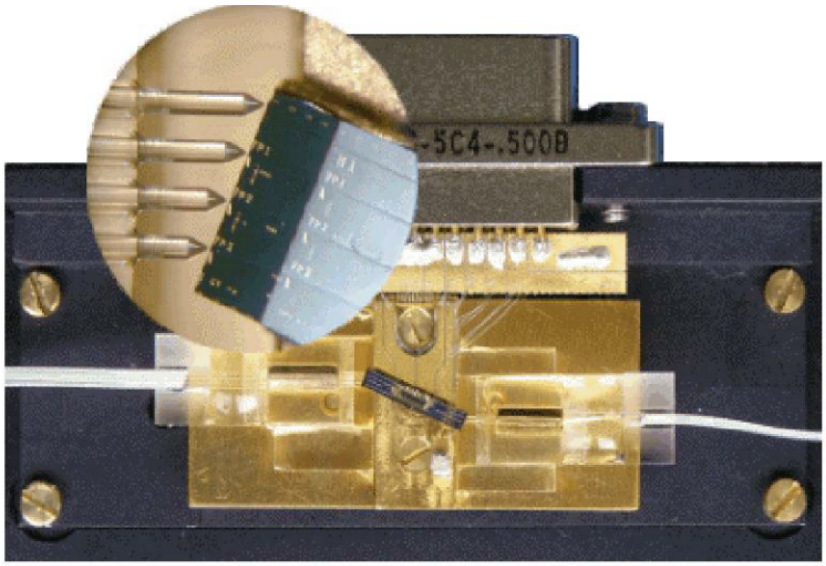


Figure 1.3: *Photograph of an integrated Mach-Zehnder-Interferometer (MZI) module coupled to lensed fibers [5].*

waveguide usually has an elliptical spot size only a few microns large. An example for a semiconductor laser is displayed in Fig. 1.4(b). The spot size of 2.4 μm (horizontal) and 1.0 μm (vertical), resulting in mismatch losses of 11 dB for direct coupling into a cleaved SMF. Approaches to improve the fiber coupling efficiency by microlenses or lensed fibers [17, 18] to modify the field size have been shown. However, to match the mode shape is still difficult. Furthermore tight alignment tolerance between fiber and III-V waveguide makes packaging an expensive step.

On-chip integrated spot size converters offer the opportunity to improve the fiber coupling efficiency and simplify the fiber alignment step. Therefore, the total cost of the device can be reduced.

In this thesis a brief introduction to the optical waveguide theory is given in the second chapter. Several approaches to integrated SSC are shown and their advantages and disadvantages explained in Chapter 3. In Chapter 4 the coupling mechanism in two vertically separated waveguides is analyzed. Furthermore, a method for improving the fabrication tolerance of resonant coupling is found. It will be shown in Chapter 5 how the birefringence in a passive asymmetric twin waveguide enables a polarization filter and splitter mechanism. The following chapter shows fabricated polarization filters and their measurements. Polarization insensitive spot size con-

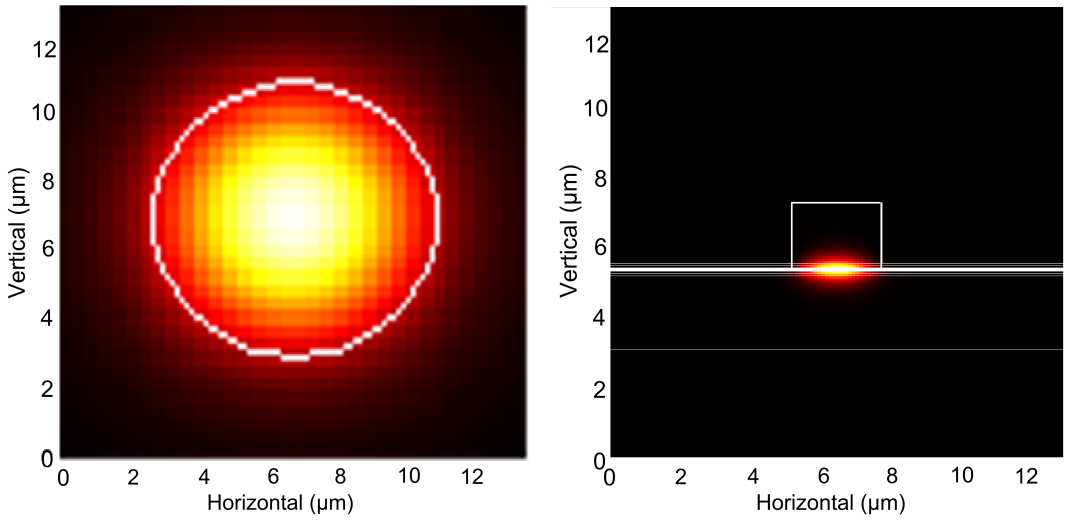


Figure 1.4: *Intensity of the TE-polarization. (a) 10.4 µm diameter circular spot size of a single mode fiber. (b) 2.4 (horizontal) and 1.0 µm(vertical) spot size of a 1.55 µm laser*

verters for a PIN-photodiode are designed in the Chapter 7 and the key influences on absorption efficiency are investigated. The refractive index of InGaAsP epi-layers is found to be the most critical factor. Because of this, in Chapter 8 the refractive indices of two different InGaAsP compositions are measured and the spot size converter layout for the afore-mentioned PIN-photodiode is adjusted taking these measurement into account. An important aspect of this thesis is the fabrication of an asymmetric twin waveguide. Different concepts for fabricating such a structure are outlined in Chapter 9. Problems that occurred during the processing are described and how they are solved. An inductively coupled plasma process based on the $Cl_2/CH_4/H_2$ is developed and the passivation properties of CH_4 are shown. Vertical and smooth sidewalls for the upper and lower waveguide can be obtained. Additionally, the upper waveguide can be down tapered to a width of 1 μm.

It is shown here theoretically and experimentally for the first time that an asymmetric twin waveguide can be used as a polarization filter. Although the bandgap wavelength of the epi-material was not as intended a power extinction ratio of the TE- relative to the TM-polarization of (3.1 $\pm$ 0.4) dB was measured at 1610 nm.

Chapter 2

Brief Overview of Optical Waveguide Theory and Simulation Methods

The intention of this chapter is to prepare the fundamental basis for the following chapters. The fully analytically solvable asymmetrical slab waveguide schema is used as a starting point. For this example the geometrical approach is shown and then further expanded to solving the Maxwell‘s equations. The limits of the analytic method are discussed and simulation methods described that are suitable for calculating the propagating field in any kind of waveguide design. For a more detailed view, the reader may refer to the literature [19, 20, 21, 22].

2.1 Optical Waveguide Theory

The ray optics or geometrical optics concept is the simplest theory of light propagation. Nevertheless it is suitable for a variety of optical problems, such as problems of the visible wavelength domain. Therefore, it can describe adequately most of your daily experiences with light. However ray optics is an approximate theory. As a result important phenomena, such as diffraction, interference, polarization or absorption, cannot be explained by ray optics. Therefore the basic concept of wave equations obtained from Maxwellt's equations is explained.

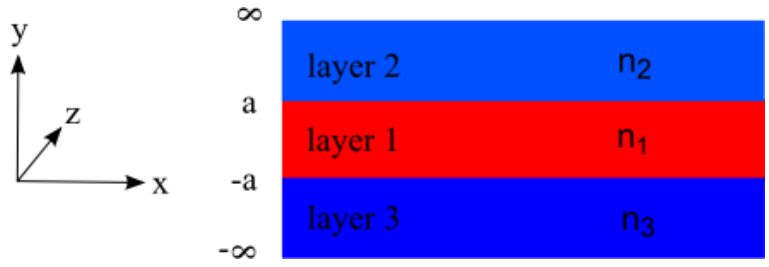


Figure 2.1: *Schematic of a slab waveguide*

2.1.1 Slab Waveguide

The simplest possible optical waveguide is the dielectric slab waveguide. Its simplicity makes it possible to describe the problem, relative to guided and radiation modes, by simple mathematical expressions. Because of that the study of slab waveguides and their results gives a better understanding of more complex waveguides and their properties. In Fig. 2.1 a slab waveguide is sketched. It consists of three layers. n stands for the refractive index of the material. In order to achieve mode guidance the refractive index of the core layer, n_1, has to be large than n_2 and n_3. If $n_2 = n_3$ the structure is called a symmetric slab waveguide, otherwise ($n_2 \neq n_3$) the structure is referred to as an asymmetrical slab waveguide. The electric and magnetic fields can be expressed by plane-waves (Eq. 2.1.2). β denotes the propagation constant. Since the waveguide is homogeneous along the x-direction the x-variation can be set to zero($\partial\overrightarrow{E}/\partial x = 0$, $\partial\overrightarrow{H}/\partial x = 0$). The following monochromatic electromagnetic plan waves $\overrightarrow{E'}$ and $\overrightarrow{H'}$ are used as an ansatz:

$$\overrightarrow{E'} = \overrightarrow{E}(x,y)e^{i(\omega t-\beta z)} \tag{2.1.1}$$

$$\overrightarrow{H'} = \overrightarrow{H}(x,y)e^{i(\omega t-\beta z)} \tag{2.1.2}$$

ω is an angular frequency of the sinusoidally varying electromagnetic field with respect to time. Inserting these field into Maxwell's source free equations leads to two independent sets of equation.

First there is the transverse electric (TE) mode that satisfies the wave equation 2.1.3. The electric field component along the propagation direction (z-axis) E_z is zero for the TE mode. Therefore, the electric component lays only in the transverse

direction.

$$\frac{d^2E_x}{dy^2} + (k_0^2n^2 - \beta^2)E_x = 0 \tag{2.1.3}$$

with

$$H_y = \frac{\beta}{\omega\mu_0}E_x \tag{2.1.4}$$

$$H_z = -\frac{i}{\omega\mu_0}\frac{\partial E_x}{\partial y} \tag{2.1.5}$$

$$E_y = E_z = H_x = 0 \tag{2.1.6}$$

k_0 stands for the wavenumber in a vacuum. Second, the transverse magnetic (TM) mode with its wave equation 2.1.7 is obtained. In this case only the magnetic field lays in the transverse direction.

$$\frac{\partial^2H_x}{\partial x^2} + (k_0^2n^2 - \beta^2)H_x = 0 \tag{2.1.7}$$

with

$$E_y = -\frac{\beta}{i\omega\epsilon_0n^2}H_x \tag{2.1.8}$$

$$E_z = \frac{1}{i\omega\epsilon_0n^2}\frac{\partial H_x}{\partial y} \tag{2.1.9}$$

$$E_x = H_y = H_z = 0 \tag{2.1.10}$$

In both cases homogeneous non magnetic, dielectric materials with permittivity ($\epsilon = \epsilon_0 n^2$) and permeability ($\mu = \mu_0$) are assumed. Since the optical field is only guided in the core layer (layer 2), an exponentially decaying ansatz for E_x and H_x in the cladding regions can be chosen. In the core region the solution of a harmonic oscillator fulfills the equation. The wavenumbers along the y-direction in the core and claddings κ, σ, ξ are defined by the following equations:

$$\kappa = \sqrt{k^2n_2^2 - \beta^2}, \qquad \sigma = \sqrt{\beta - k^2n_1^2}, \qquad \xi = \sqrt{\beta - k^2n_3^2} \tag{2.1.11}$$

At the interface boundaries (-a, a) the tangential magnetic as well as the tangential electric field components are continuous. Finally, one eigenvalue equation is obtained for each polarization. Here only the equations for the TE-polarization (Eq. 2.1.3)

are shown [21].

$$u = \frac{m\pi}{2} + \frac{1}{2}\tan^{-1}(\frac{w}{u}) + \frac{1}{2}\tan^{-1}(\frac{w'}{u}) \qquad (m = integer) \qquad (2.1.12)$$

$$\phi = \frac{m\pi}{2} + \frac{1}{2}\tan^{-1}(\frac{w}{u}) - \frac{1}{2}\tan^{-1}(\frac{w'}{u})) \qquad (2.1.13)$$

with the normalized transverse wavenumbers $u = \kappa a$, $w = \xi a$ and $w' = \sigma a$ and ϕ the phase term. For the symmetric case ($n_1 = n_3$) Eqs. 2.1.12 and 2.1.13 simplify to

$$u = \frac{m\pi}{2} + \tan^{-1}(\frac{w}{u}) \qquad (2.1.14)$$

$$\phi = \frac{m\pi}{2} \qquad (2.1.15)$$

The propagation constants of the symmetric slab waveguide can be obtained qualitatively in a graphical way. The u and w relationship of Eq. 2.1.14 is plotted in Fig. 2.2. The values of u and w should also satisfy the relation with the normalized

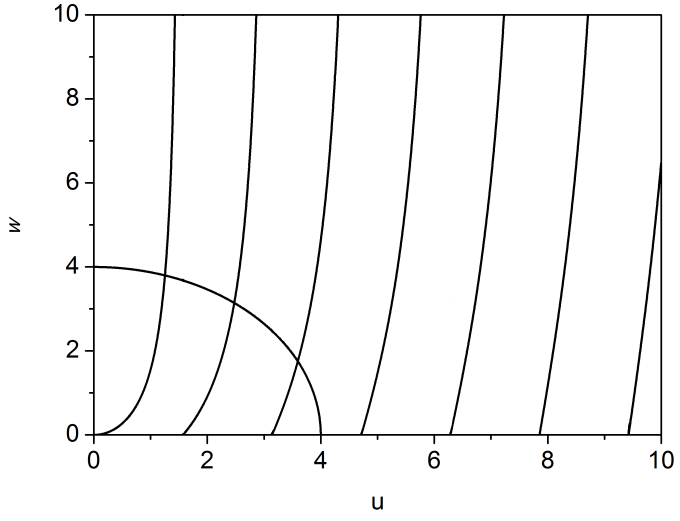


Figure 2.2: *$u - w$ relationship in a symmetric slab waveguide.*

frequency v ($u^2 + w^2 = v^2$). This relation is plotted for a value of $v = 4$. The solutions of the equations are then given as the crossing points of both graphs (Fig. 2.2). For example, the transverse wavenumbers u and w of the fundamental TE mode are the values at the crossing point of the quarter circle and m = 0. The propagation constant β can be finally calculated with Eq. 2.1.11. If $v < \frac{\pi}{2}$ there was only one crossing point and the waveguide would be a single mode waveguide.

The normalized frequency v is defined as [21]

$$v = k_0 a \sqrt{n_1^2 - n_3^2} \tag{2.1.16}$$

When the normalized frequency v is used, the propagation characteristics of the waveguides can be treated independent of each waveguide structure.

A second parameter, the normalized propagation constant, is introduced, which is defined as

$$b = \frac{n_{eff}^2 - {n_3}^2}{{n_1}^2 - {n_3}^2} \tag{2.1.17}$$

n_{eff} is the effective refractive index, it is related to the propagation constant by $n_{eff} = \beta/k$. With the normalized propagation constant b guided modes can be expressed by

$$0 \leq b \leq 1 \tag{2.1.18}$$

and the cut-off condition is expressed as

$$b = 0 \tag{2.1.19}$$

With these two parameters Eq. 2.1.12 can be rewritten as

$$v\sqrt{1-b} = \frac{m\pi}{2} + tan^{-1}\sqrt{\frac{b}{1-b}} \tag{2.1.20}$$

In the case of an asymmetrical slab waveguide ($n_2 \neq n_3$) a measure of the asymmetry of the cladding refractive indices is required

$$\zeta = \frac{n_3^2 - n_2^2}{n_1^2 - n_3^2} \tag{2.1.21}$$

In the asymmetrical waveguide ($n_3 > n_2$) the higher refractive index n_3 is used as the cladding refractive index, because the cut-off conditions are determined when the normalized propagation constant coincides with the higher cladding refractive index. Following, the following dispersion equation for the TE modes is obtained [21]

$$2v\sqrt{1-b} = m\pi + tan^{-1}\sqrt{\frac{b}{1-b}} + tan^{-1}\sqrt{\frac{b+\zeta}{1-b}} \tag{2.1.22}$$

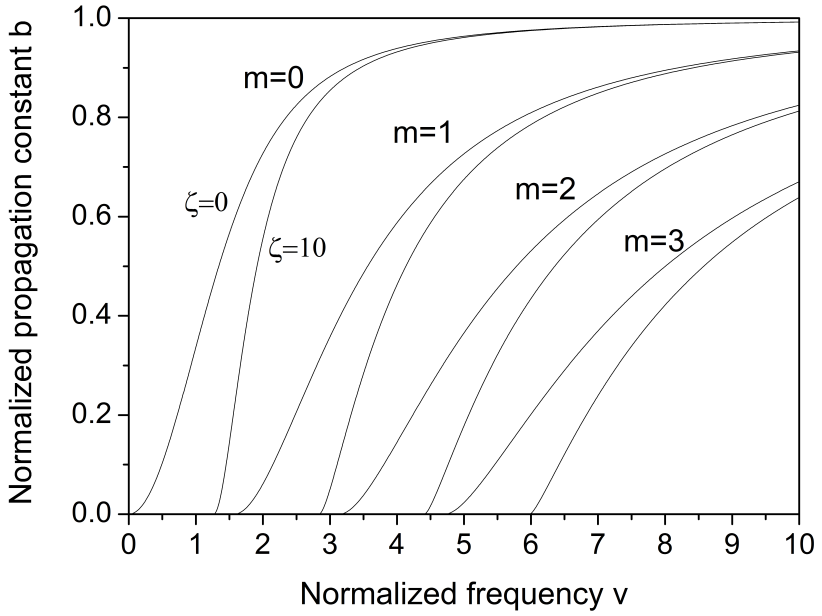


Figure 2.3: *Dispersion curves for the TE modes in the slab waveguide.*

The normalized propagation constant b is calculated for each normalized frequency v. Fig. 2.3 shows the $v - b$ relationship for the TE modes. This relationship is called dispersion curve. The mode number is expressed by the subscript m. The parameter ζ in Fig. 2.3 is the measure of asymmetry. It is know that there is no cut-off for the lowest TE(m=0) mode in a symmetrical waveguide ($\zeta = 0$).

2.1.2 Coupled Mode Theory

As earlier mentioned light propagates in a waveguide in the form of modes. The complex amplitude of the optical field is generally a superposition of these modes. Here we focus on the case when two waveguides are brought closely together (Fig. 2.4). The eigen modes in each waveguide are denoted $\vec{E}_p, \vec{H}_p (p = 1, 2)$ and satisfy

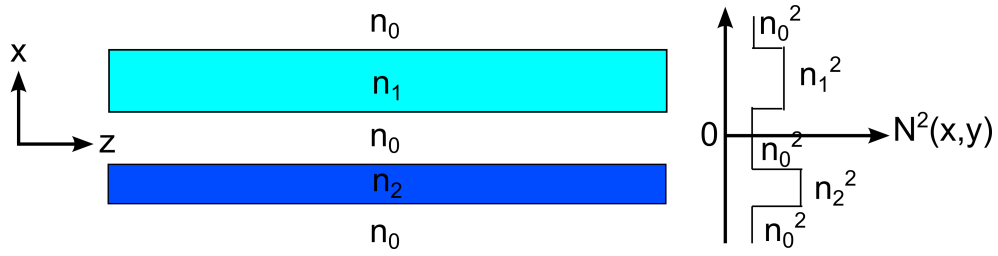


Figure 2.4: *Directionally coupled optical waveguides.*

Maxwell's equations. The electromagnetic fields of the coupled waveguides can now be expressed as the sum of the eigen modes in each waveguide

$$\vec{E}' = A(z)\vec{E}_1' + B(z)\vec{E}_2' \tag{2.1.23}$$

$$\vec{H}' = A(z)\vec{H}_1' + B(z)\vec{H}_2' \tag{2.1.24}$$

These fields, $\vec{E}$ and $\vec{H}$ also need to satisfy Maxwell's equation. Using Eqs. 2.1.23, 2.1.24 with Maxwell's equations and separating the transvers and axial dependence of the electromagnetic fields

$$\vec{E}_p' = \vec{E}_p \, exp(-i\beta_p z) \qquad (p = 1, 2) \tag{2.1.25}$$

$$\vec{H}_p' = \vec{H}_p \, exp(-i\beta_p z) \tag{2.1.26}$$

finally leads to [21]

$$\frac{dA}{dz} + c_{12}\frac{dB}{dz}\, exp[-i(\beta_2 - \beta_1 z] + i\chi_1 A + i\kappa_{12} B exp[-i(\beta_2 - \beta_1] = 0 \tag{2.1.27}$$

$$\frac{dB}{dz} + c_{21}\frac{dA}{dz}\, exp[+i(\beta_2 - \beta_1 z] + i\chi_2 B + i\kappa_{21} B exp[+i(\beta_2 - \beta_1] = 0 \tag{2.1.28}$$

where

$$\kappa_{pq} = \frac{\omega\epsilon_0 \int_{-\infty}^{\infty}\int_{-\infty}^{\infty}(N^2 - N_q^2)\vec{E}_p^* \cdot \vec{E}_q \, dx \, dy}{\int_{-\infty}^{\infty}\int_{-\infty}^{\infty}\vec{u}_z \cdot (\vec{E}_p^* \times \vec{H}_p + \vec{E}_p \times \vec{H}_p^*) \, dx \, dy} \tag{2.1.29}$$

$$c_{pq} = \frac{\int_{-\infty}^{\infty}\int_{-\infty}^{\infty}(N^2 - N_q^2)\vec{E}_p^* \cdot \vec{E}_q \, dx \, dy}{\int_{-\infty}^{\infty}\int_{-\infty}^{\infty}\vec{u}_z \cdot (\vec{E}_p^* \times \vec{H}_p + \vec{E}_p \times \vec{H}_p^*) \, dx \, dy} \tag{2.1.30}$$

$$\chi_p = \frac{\omega\epsilon_0 \int_{-\infty}^{\infty}\int_{-\infty}^{\infty}(N^2 - N_p^2)\vec{E}_p^* \cdot \vec{E}_p \, dx \, dy}{\int_{-\infty}^{\infty}\int_{-\infty}^{\infty}\vec{u}_z \cdot (\vec{E}_p^* \times \vec{H}_p + \vec{E}_p \times \vec{H}_p^*) \, dx \, dy} \tag{2.1.31}$$

and the pair of p and q are either $(p, q) = (1, 2)$ or $(2, 1)$, respectively. β_p is the propagation constant. $\vec{u}_z$ is the unity vector in z-direction. $N^2(x, y)$ denotes the refractive index distribution in the entire coupled waveguide, $N_p^2(x, y)$ represents the refractive index distribution of each waveguide.

c describes the butt coupling coefficient between two waveguides. In the case where waveguide 1 exists only in the region $z < 0$ and waveguide 2 in $z \geq 0$. The eigen mode $(\vec{E}_1, \vec{H}_1)$ propagates from the negative z-direction to $z = 0$. At this point the eigen mode $(\vec{E}_2, \vec{H}_2)$ is excited. This excitation efficiency is considered to be c_{12}. χ_p is much smaller than κ_p when two waveguides are sufficiently separated. Therefore, χ_p can be neglected. In most of the conventional analysis of the directional couplers, c_{pq} and χ_p were neglected and they are assumed to be $c_{pq} = \chi_p = 0$. The optical power carried by the eigen mode in the waveguide is expressed [21]

$$P_p = \frac{1}{2}\int_{-\infty}^{\infty}\int_{-\infty}^{\infty}(\vec{E}_p \times \vec{H}_p^*) \cdot \vec{u}_z \, dx \, dy \tag{2.1.32}$$

Therefore, the denominators of Eq. 2.1.29-2.1.31 are equal to $4P_p$. Henceforth, it can be assumed that the eigen modes in both waveguides are normalized to satisfy the condition:

$$\int_{-\infty}^{\infty}\int_{-\infty}^{\infty}\vec{u}_z \cdot (\vec{E}_p^* \times \vec{H}_p + \vec{E}_p \times \vec{H}_p^*) \, dx \, dy = 4P_p = 1 \tag{2.1.33}$$

Taking the optical power in the entire waveguide to be:

$$P_p = \frac{1}{2}\int_{-\infty}^{\infty}\int_{-\infty}^{\infty}(\vec{E}_p' \times \vec{H}_p'^*) \cdot \vec{u}_z \, dx \, dy \tag{2.1.34}$$

together with Eq. 2.1.27, 2.1.28, neglecting c_{pq}, χ_p and assuming loss-less waveguides (dP/dz = 0) leads to two coupled first-order differential equations [21]:

$$\frac{dA}{dz} = -i\kappa_{12}B\, exp[-i(\beta_2 - \beta_1)z] \tag{2.1.35}$$

$$\frac{dB}{dz} = -i\kappa_{21}A\, exp[+i(\beta_2 - \beta_1)z] \tag{2.1.36}$$

The solution of codirectional couplers ($\beta_1 > 0, \beta_2 > 0$) are assumed in the forms

$$A(z) = [a_1 e^{i\gamma z} + a_2 e^{-i\gamma z}]\, exp(-i\delta z) \tag{2.1.37}$$

$$B(z) = [b_1 e^{i\gamma z} + b_2 e^{-i\gamma z}]\, exp(i\delta z) \tag{2.1.38}$$

where γ is an unknown parameter to be determined and $\delta = (\beta_2 - \beta_1)/2$ describes the difference of the propagation constants between waveguide 1 and 2. Constants a_1, a_2, b_1 and b_2 satisfy the initial conditions

$$a_1 + a_2 = A(0) \tag{2.1.39}$$

$$b_1 + b_2 = B(0) \tag{2.1.40}$$

For the most practical case, in which light is initially only in waveguide 1 at $z = 0$ (A(0)=A_0), then the optical power flow along the z-direction is given by [21]

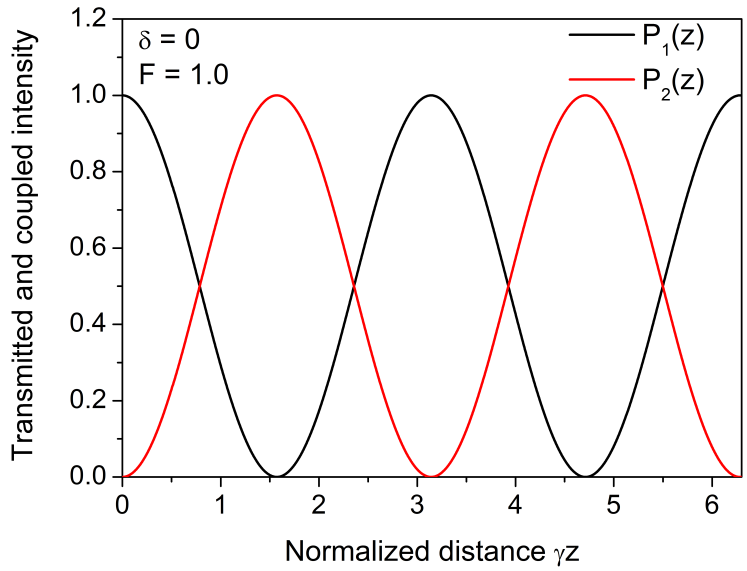
$$P_1(z) = \frac{|A(z)|^2}{|A_0|^2} = 1 - F\, sin^2(\gamma z) \tag{2.1.41}$$

$$P_2(z) = \frac{|B(z)|^2}{|A_0|^2} = F\, sin^2(\gamma z) \tag{2.1.42}$$

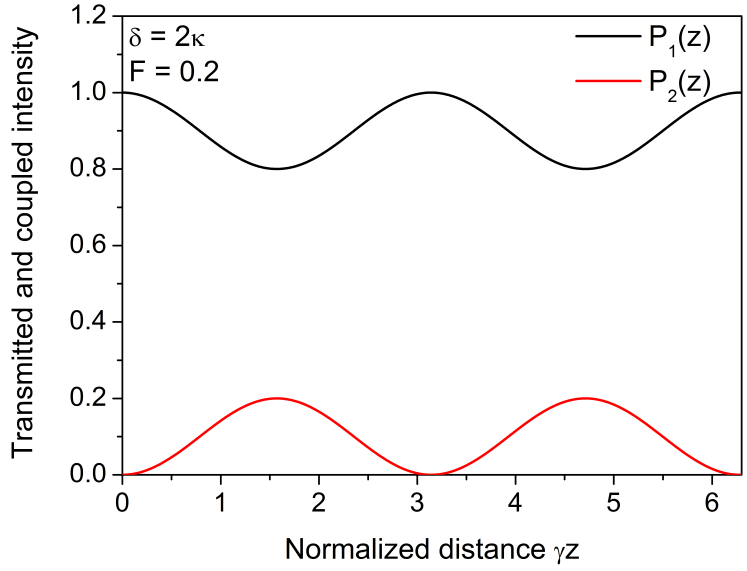
$\gamma = \sqrt{\kappa^2 + \delta^2}$ with $\kappa = \sqrt{\kappa_{12}\kappa_{21}}$. F denotes the maximum power-coupling efficiency, defined by

$$F = \left(\frac{\kappa}{q}\right)^2 = \frac{1}{1 + (\delta/\kappa)^2} \tag{2.1.43}$$

Therefore, the power is exchanged periodically between the two waveguides. Fig. 2.5 shows the power distribution between the two waveguides relative to the normalized length γz. It can seen that in Fig. 2.5(a) the complete optical field is transferred from one waveguide to the other. This is only possible if both waveguides have the same propagation constants and $\delta = 0$. In Fig. both propagation constants are different (2.5(b) $\delta \neq 0$) therefore the optical field couples only partially from



(a)



(b)

Figure 2.5: *Optical power in a codirectional coupler with (a) $F = 1.0$ and $\delta = 0$ and (b) $F = 0.2$ and $\delta = 2\kappa$.*

waveguide 1 to waveguide 2. A key issue to enable high coupling efficiency is to have waveguides with similar propagation constants.

The power-coupling efficiency from waveguide 1 to waveguide 2 reaches maximum

at

$$z = \frac{\pi}{2\gamma}(2m+1) \qquad (m = 0, 1, 2, ...) \tag{2.1.44}$$

The length z at $m = 0$ is called the coupling length.

2.2 Simulation Methods for Optical Waveguides

Although slab waveguides can be solved analytically, a purely analytical solution is not available for more complicated structures such as ridge waveguides. In such a case approximation and numerical methods are required to find the guided modes.

A well established method that allows an analytical solution for rectangular waveguides is the Marcatili [23] method. In the Marcatili method a three-dimensional rectangular waveguide gets split into nine different rectangular sections. In the center is the core guiding layer. That layer is surrounded by a cladding with a homogeneous refractive index. It is assumed that the electromagnetic field of well guided modes decays rapidly in each of the four corners. Therefore, it can be neglected in those sections. Under the assumption that one of the magnetic field components can be set to zero, two sets of wave equations are obtained. These sets of equations can be solved using the boundary conditions of the four adjacent regions.

Waveguides with non-homogeneous cladding around the core layer (e.g. ridge waveguide with air beside the upper cladding) cannot be analyzed by Marcatili's or further improved methods such as Kumar's method [24]. The effective index method is an analytical approach applicable to solving more complicated structures such as ridge waveguides. The basic assumption of the effective index method is that the electromagnetic field can be expressed by a separation of variables. This approach is suitable if there is no interaction between the two coordinates in a 2-D waveguide. Two independent differential equations relative to a single coordinate are derived and can be solved by using the general boundary conditions.

The previously described waveguide analyses are only usable for homogeneous-core planar optical waveguides and optical fibers. However, in structures like 3-dB couplers, taper designs with two vertical waveguides where mode coupling plays an

important role, a numerical solution is necessary to predict the behavior of electromagnetic waves.

Several numerical methods exist to solve nearly any given waveguide problem. Among the most common commercially available ones are the finite element (FEM) method [25, 26], the finite difference beam propagation (BPM) method [27], and finally the film mode matching (FMM) combined with eigenmode expansion method.

The FEM method is widely applicable for general physical problems (e.g. temperature, stress, etc.) and not only for waveguide problems. The basic principle of the FEM method is to discretize to geometry into smaller, e.g. triangular, sections. In this section the problem is approximated by either the variational or the Galerkin implementation of FEM. In the variational method a functional for each section can derived out of a small variation to the solutions of Maxwell‘s equations. The total functional is the sum of the functional of each section with the right boundary condition. The solution of the wave equation is obtained as the solution of the variational problem which satisfies the stationary condition of the functional. The Galerkin Method gives the same eigenvalue matrix equation. However, the starting point is an approximation solution that gives a small error. That error, the so called residual must be zero for a real solution. The FEM method is known for its accurate approximation. Nevertheless, a large number of elements is required for complicated geometries. This results in huge calculation times.

In the FD-BPM method the electric field is divided into a slowly varying envelope function and a very fast oscillatory phase term. The slowly varying function in the resulting differential equations is discretized relative to its coordinates. The propagating field can be expressed in a recurrence form from the staring point. A solvable tridiagonal matrix equation can finally be obtained with the right boundary conditions.

The commercially available software package that has been used in this thesis is Fimmwave and Fimmprop [28]. It makes use of the mode matching method [29] to find the modes in a given waveguide structure. A waveguide (Fig. 2.6) is split into several films and according to its geometry into slices. Each slice has a constant refractive index and permittivity. Each film has a set of film modes with mode

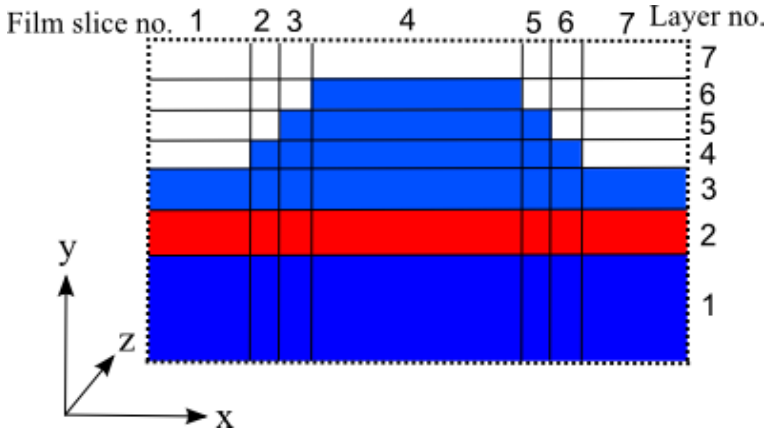


Figure 2.6: *Semiconductor ridge waveguide, represented by a number of slices and layers their in.*

functions $\varphi_k^{(m)}$ such that in layer n of film m

$$\frac{\partial^2 \varphi_k^{(m)}}{\partial y^2} + (\epsilon^{m,n} k_0^{(m)2} - k_k^{(m)2})\varphi_k^{(m)} = 0 \tag{2.2.1}$$

The eigenvalues $k_k^{(m)2}$ of Eq. 2.2.1 can be found with piecewise trigonometric/hyperbolic mode functions. The mode in one film is then expanded in film mode functions that fulfil the boundary condition at each slice interface. The modes with the same propagation constant in each film are collected and the field distribution at the film slice interfaces is matched by adjusting the modal amplitudes in each film. Only for certain values of the propagation constant can a set of non-zero film mode amplitudes with matching distributions at the slice interfaces can be found. The continuous set of substrate modes is discretized by the introduction of artificial boundaries such as electric or magnetic walls. Symmetry in a waveguide structure can be used to reduce the required calculation area, e.g. the horizontal symmetry in Fig. 2.6 can used to reduce the slice number to four, starting at the center of the ridge.

The propagating optical field behavior for any kind of geometry can be calculated by splitting the waveguide into only slightly changing waveguides along the propagation direction. In each waveguide the optical modes are obtained by the FMM method. The total electromagnetic field in each section is expanded by all calculated modes therein. Afterwards, the scattering matrix at each interface between different waveguides is calculated. The amplitude value for every calculated mode is then adjusted accordingly. The FMM method offers a high accuracy and

a reasonable compute time. In addition, it enables the simulation of a bidirectional optical field (e.g. reflections). This is not possible in the FD mechanism. Because in each section all guided modes can be calculated, FMM with eigenmode expansion is an accurate approach to find the resonance point of two different waveguide and enable or disable power transfer among the modes.

Chapter 3

Spot size converter concepts

The intention of this chapter is to give the reader a basic overview of the research that has already been done on spot size converters (SSCs). SSCs help to improve the direct fiber coupling to optical semiconductor devices. Since there has already been a large research interest over the past decades and various approaches for different material systems (e.g. silicon on insulater or InP) have been published, only the main approaches are shown. Different concepts such as grating couplers, taper couplers, antiresonant reflecting optical waveguides, silicaoxyinitride waveguides and polymer couplers are outlined. The asymmetric twin waveguide (ATG) design is explained and it is outlined why that design is used for the following studies.

3.1 The grating coupler

Gratings play an important role in optical devices. Periodic gratings offer a wide range of implementation possibilities for semiconductor devices. Gratings are widely used in distributed feedback (DFB) and distributed Bragg-reflector (DBR) lasers [30, 31, 32, 33, 34, 35, 36]. In such devices either the whole resonator consists of a grating where Bragg reflection occurs (DFB) or the laser has two grating as end mirrors (DBR). Separately a grating can enable improved coupling to and from optical fibers to SOI waveguides.

In this section examples of grating couplers are shown. General problems, such as bidirectional diffraction, and their solution concepts are outlined.

3.1.1 Applications of Grating Couplers in Silicon on Insulator Systems

Here the silicon on insulater (SOI) system is presented because grating couplers play an important role in the SOI system to improve fiber coupling. The SOI grating couplers acted also as starting point to transfer the concept to InP devices. The material system of SOI provides several advantages. It shows the potential of fabrication of low cost photonic integrated circuits (PICs) and optoelectronic devices. On one hand, there is also the significant refractive index difference between silicon (n = 3.5 at 1.55 μm) and silica (n = 1.47). That enables the creation of small waveguide features with highly confined optical modes. On the other hand, the silicon processing technology is well controllable and established. That makes it possible to fabricate the required waveguide relatively easily. Nevertheless, the low loss in- and out-coupling into and from SOI waveguides remains a key problem. Waveguide gratings have shown to be a good option to handle that problem.

A output coupling efficiency to free space of 70 % was reported for a rectangular grating with a period of 0.4 μm and a grating height of 0.14 μm [37]. To obtain such a high output efficiency the film thickness and the grating height have to be optimized. Taillaert et al. [38] designed a 13 μm long and 12 μm wide grating coupler for coupling in between SOI waveguides and optical fibers. To match the Gaussian mode of a fiber a non uniform grating was chosen. The groove widths and spacings were modified so that the output beam has a Gaussian mode profile. To reduce the previously mentioned losses to the substrate a two pair Bragg reflector was introduced. A theoretical coupling efficiency to a fiber of 92 % was reported for the TE-polarization. The smallest groove width was 30 nm. Nevertheless, the coupler was polarization dependent. For the TM-polarization the coupling efficiency was less than 1 %. A fabricated grating coupler with a period of 610 nm, 50 nm etch depth and 50 % duty cycle has been presented [6] with various wavelength division multiplexing (WDM) components, such as ring resonators, arrayed waveguide gratings and cascaded Mach-Zehnder interferometers. The input waveguide after the grating coupler was tapered down laterally so that the mode matches the SOI

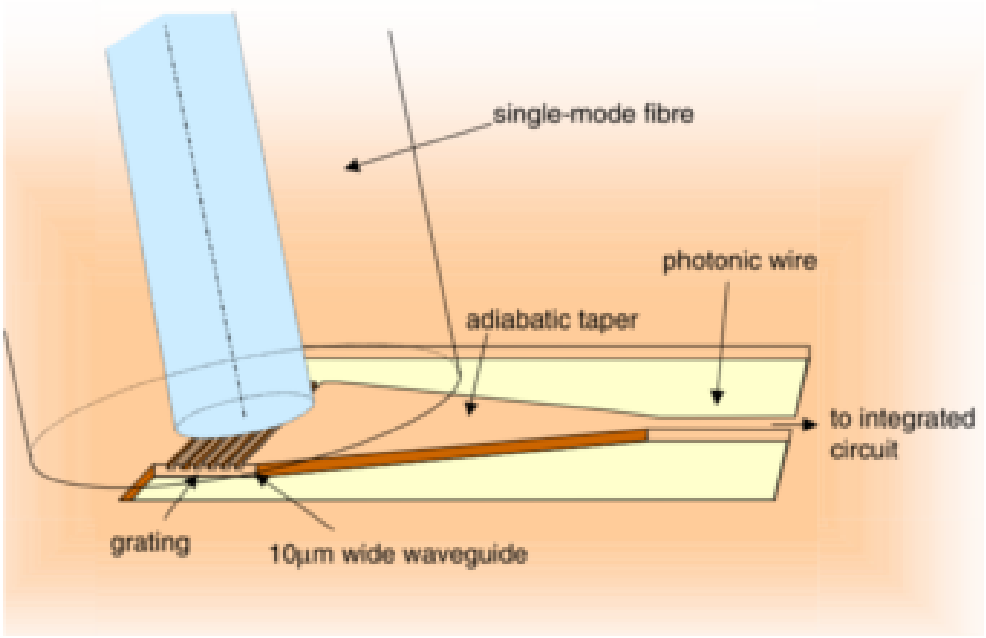


Figure 3.1: *Grating coupler for coupling between a SOI photonic wire and an optical fiber [6].*

waveguide mode. 20 % of the TE-polarized light of the fiber reached to photonic wire. For a fabricated SOI waveguide with a Bragg bottom mirror a coupling efficiency to a optical fiber of 69.5 % has been measured [39]. A grating with adjusted gap and bar width and with the gap etch through the silicon layer has shown a coupling efficiency of 35 % [40]. Making use also of a non uniform grating design a maximum coupling efficiency of 64 % to a single mode fiber has been observed [41]. The non uniformity of the grating was realized by the lag effect for inductively coupled plasma reactive ion etching. The lag effect describes the dependence of the etch rate on the feature size in a dry etching process.

In general grating couplers are well suited to couple light into and out of silicon based waveguides. A high coupling efficiency can be achieved over a short distance.

3.1.2 Applications of Grating Couplers for InP Systems

Implementing gratings for III-V based material system is more challenging, because the refractive index difference is a lot smaller and therefore there is not a large vertical mode confinement. Therefore, the SOI concept cannot be easily transferred

to InP or similar systems.

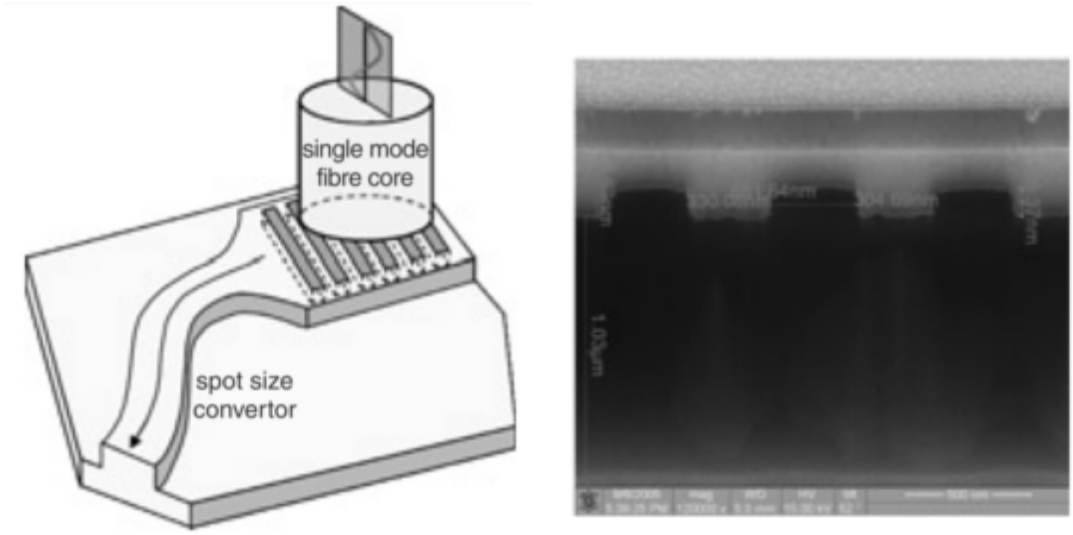
During the 1970s it became popular to use gratings to couple the emitted light of semiconductor lasers with a horizontal cavity out of the surface. Several of those grating coupled surface emitting lasers (GCSELs) in InGaAs-AlGaAs have been reported [42, 43, 44, 45, 46]. The lasers were either optically [44] or electrically pumped. Alferov et al. [43] and Zory et al. [44] used a centered grating outcoupler in a cleaved facet resonator. Burnham et al. [45] applied a buried DFB structure and Reinhart et al. [46] utilized one grating for feedback and outcoupling.

Since GCSELs possess several advantages, such as wafer level processing, on-wafer testing and monolithic integration with optical as well as electronic elements [47], they have been studied for InP systems. Wu et al. [48] have demonstrated an optically pumped surface-emitting InGaAsP/InP DFB laser (λ_g = 1.3 μm). A second order circular grating has been implemented to realize the cavity and to emit light out of the surface. The grating had an inner and outer diameter of 29 μm and 280 μm respectively. The grating was patterned by E-beam lithography.

Choa et al. [49] fabricated an InGaAsP/InP GCSEL at the telecommunication wavelength of 1.55 μm. For a DFB laser a top/edge output power ratio of 15 % was measured. Regrowth steps were necessary to fabricate the device.

Although out-coupling by a grating has already been demonstrated, in-coupling on the other hand, essential for any PIC, was not shown.

A first attempt to demonstrate a bidirectional grating coupler for an InP system was made with an InP-membrane (Fig. 3.2) [7]. A 300 nm thick layer of InP was grown on an InP substrate with an InGaAsP etch stop layer. The grating was defined by E-beam lithography. The parameters were: period = 660 nm, filling factor = 0.5, etch depth = 120 nm and benzocyclobutene (BCB) thickness = 1.18 μm. Afterward, the chip was bonded upside down onto a GaAs substrate covered with BCB. The polymer guaranteed a high refractive index contrast. Finally the InP substrate and the etch stop layer were removed. The back reflection of the fiber end was avoided by tilting the fiber by 10 °. After applying an Al_2O_3 anti-reflecting coating a coupling efficiency of 30 % was measured for the TE-polarization. The difference to the theoretical value of 54 % was explained by a deviation between the



(a) **(b)**

Figure 3.2: *(a) Sketch of grating coupler. (b) Cross-section of fabricated structure with AR-coating [7].*

fabricated and the targeted structure.

Grating couplers for InP devices offer advantages such as coupling out of the device without cleaving a facet. Therefore on-chip testing is possible. Furthermore, gratings can be realized without any regrowth step. However, fabrication of a polarization insensitive grating with unidirectional light beam is a challenging issue that requires special equipment and processing steps. In general, no InP based grating has shown a high coupling efficiency ($<$ 1 dB loss) to an optical fiber yet.

3.2 Taper Assisted Spot Size Converters

A widely used concept for mode adapters is to taper one or more waveguides. Since the mode coupling is analyzed in more detail in chapter 4, only the important aspects are listed briefly. One important aspect of a taper is its length. Less than 10 % of the power of the input mode should be transferred to higher order modes to enable an adiabatic transfer. To reduce the power losses of a mode a minimum taper length is required. In general that length can be several hundred microns. Therefore, the SSC can take a significant percentage of the whole size of the photonic device. The second important aspect is the taper width. To couple from one waveguide to

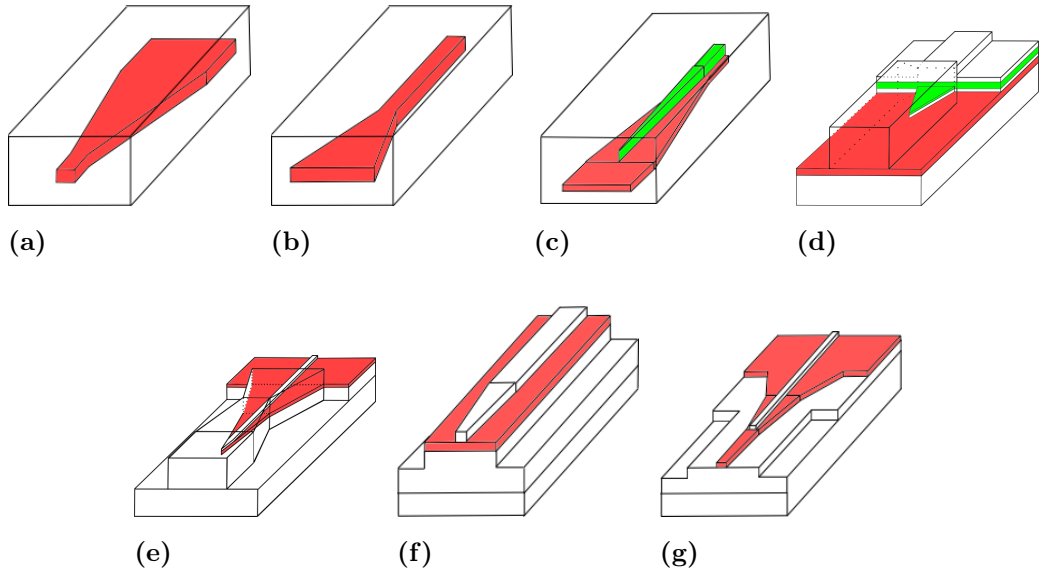


Figure 3.3: *Lateral taper designs: (a) Laterally down-tapered buried waveguide (b) Laterally up-tapered waveguide (c) Dual lateral overlapping buried waveguide taper (d) Dual lateral overlapping ridge waveguide taper (e) Nested waveguide taper transition (f) Single lateral taper transition (g) Multisection taper transition [8].*

another the width of one waveguide has to reduced to a width at which the starting waveguide does not guide any more modes. That width can be in the range of several hundred nanometers and is a critical aspect for processing.

To describe the most common taper concepts, Moerman et al. [8] is used as a guideline. The basic issues of each concept are described. The ways in which these concepts were experimentally realized and what challenges occurred are explained.

The taper designs can be combined to three different groups. First there is the lateral taper, followed by a vertical taper and finally a combined taper.

3.2.1 Lateral Tapers

In Fig. 3.3 the different main approaches to lateral tapers are displayed.

Fig. 3.3(a) shows a buried waveguide with a down-tapered ridge [50, 51]. Electron beam (E-beam) lithography and reactive ion etching (RIE) were used to define the taper. Five growth steps in a low pressure MOVPE system were necessary.

Fig. 3.3(b) displays a laterally up-tapered buried waveguide [52]. A circular mirror facet on the up-tapered side acts as a resonator. Selective chemical etching

and mass transport were used for fabrication. Such up-tapers are usually applied for high power laser diodes or semiconductor amplifiers [53].

The dual lateral overlapping waveguide taper for a buried waveguide (3.3(c)) is a popular approach [54, 55, 56, 57, 58, 59, 60]. The width of the upper waveguide becomes continuously smaller along the taper terminating in a very narrow end, whereas the width of the lower waveguide increases along the taper. E-beam lithography and regrowths are usually required to fabricate such structures. A disadvantage of this type of taper is the need for a sharp termination point of the upper waveguide. This complicates the taper fabrication process.

The taper design of Fig. 3.3(d) [61, 62, 63] is similar to the previous one. Instead of a buried waveguide, a ridge waveguide is laterally tapered from a narrow ridge with a thick strongly guiding layer, to a wide ridge with weakly guiding layer. Three epitaxial regrowth steps were usually carried out during the fabrication. .

In Fig. 3.3(e) the incoming narrow rib waveguide is converted into a fiber matched rib waveguide by means of two nested waveguide tapers [64]. The device should not only be applicable to laser-fiber coupling but also to passive fiber-optoelectronic integrated circuits for the entire wavelength range of 1.3–1.55 μm. The taper dimensions need to be accurate and therefore require high resolution fabrication technologies.

A different concept is presented in Fig. 3.3(f). The optical field is transferred from the thin ridge waveguide to an underlying, low refractive index contrast, fiber matched waveguide [65]. In the tapered section, the width of the upper ridge is sufficiently decreased so that the optical mode in the upper ridge is at cut-off near the taper facet and only a wide optical mode, defined by the lower ridge, is supported. Since the upper ridge waveguide has to be at cut-off at the facet, the upper ridge needs to be tapered to rather small dimensions (< 1 μm). The fabrication of the device required only a single growth step and standard lithography could be used. .

Fig. 3.3(g) shows a similar design as Fig. 3.3(f) [66]. The difference is that the taper is split-up into several sections.

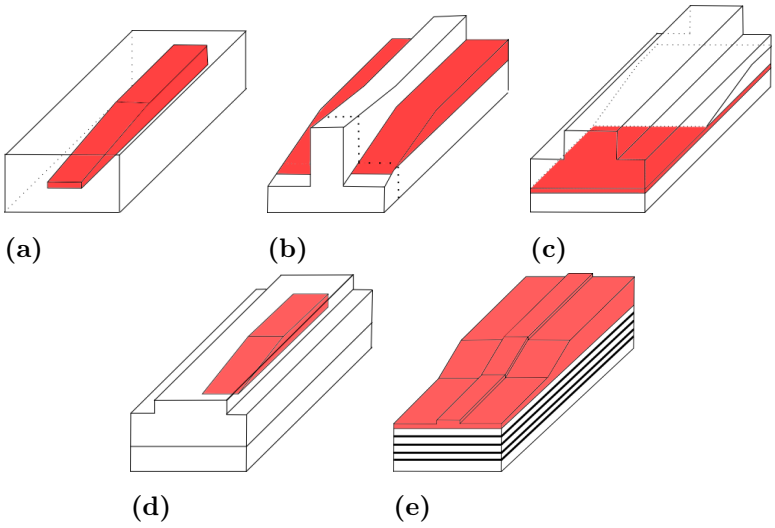


Figure 3.4: *Vertical taper designs: (a) Vertical down-tapered buried waveguide. (b) Vertical down-tapered ridge waveguide. (c) Vertical overlapping ridge waveguide. (d) Vertical overlapping taper transition from a buried waveguide to a fiber-matched waveguide. (e) Vertical overlapping waveguide taper transition from a ridge waveguide to a fiber-matched waveguide [8].*

3.2.2 Vertical Tapers

The second taper concept is based on a vertical taper instead of a lateral taper. A wide variety of technologies have therefore been developed to gradually change the thickness of a guiding layer. Examples of one dimensional vertical tapers are given in Fig. 3.4(a) for a buried waveguide structure [67, 68, 69] and in Fig. 3.4(b) for a ridge waveguide structure [70, 71, 72, 73]. The vertical taper shadow mask growth (SMG) [74] technique was required to form the taper. Because of the reduction of the quantum well thickness and because of compositional variations during SMG the band gap was increased and the taper behaved like a transparent window. In general the devices needed up to four growth steps.

In the ridge waveguide structure (Fig. 3.4(b)), diffusion limited wet chemical etching was used to obtain a vertical down tapered core layer [70]. The next step was a selective area regrowth of the upper cladding layer. Selected area regrowth in that case results in cladding with gradually increasing thickness. A facet needed to be cleaved at the position of the dashed line.

Also for vertical tapers several designs exist that make use of overlapping waveguides. Fig. 3.4(c) shows that the tapering is achieved by reducing the thickness of the upper guiding layer until it disappears completely near the end facet. The fabrication of the vertical taper included dip-etching [75].

In Fig. 3.4(d) a narrow buried waveguide is converted to a wide, fiber-matched ridge waveguide by vertically tapering the buried guiding layer . The circular spot of a fiber mode is thus transformed into the small elliptical mode of the chip waveguide. The taper was realized by depositing a vertical Al_2O_3 mask with a shadow mask and using ion-milling to transfer the profile into the semiconductor material [76]. One regrowth step was needed for the InP top layer.

The final vertical taper design Fig. 3.4(e) offers a way of making a vertical taper with one 2.7 μm regrowth step [77]. Three stair case sections were patterned by RIE and wet chemical etching. The mode expands vertically into the thin guiding layers of a fiber matched diluted waveguide.

A similar vertical ramp approach was used to fabricate a spot-size converter for a high speed p-i-n photodiode (PD) [78]. A large spot size waveguide acted as input for the optical field of a cleaved fiber. On top of that waveguide a second waveguide layer is vertically expanded to 1 μm. By introducing an optimized vertical shape of the taper a quasi-adiabatic spot size conversion with a conversion efficiency of nearly 95 % was realized [79].

3.2.3 Combined Tapers

In a combined taper, both the lateral and the vertical dimensions of the guiding layer(s) are changed. Fig. 3.5(a) shows a design in which the thickness and the width of a ridge waveguide are up-tapered toward the end facet [80]. Generally the thickness of a guiding layer is reduced to spread the optical mode, resulting in a waveguide which operates near cut-off. In this design the thickness of the guiding layer is increased, leading to a multimode waveguide. When the taper is adiabatic, the intermode coupling is minimal and the waveguide at the end facet behaves single mode. The taper fabrication was based on selective, low-pressure MOVPE through a dielectric growth mask. No regrowth step was necessary and because of the thick

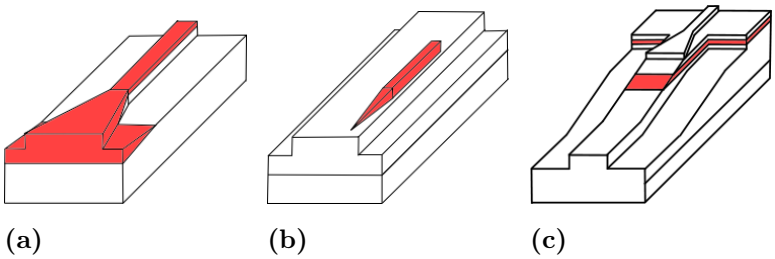


Figure 3.5: *Combined vertical and lateral taper designs: (a) Combined lateral and vertical ridge waveguide taper. (b) 2-D overlapping waveguide taper transition from a buried waveguide to a fiber-matched waveguide. (c) Overlapping waveguide taper transition with two sections from a ridge waveguide to a fiber matched waveguide [8].*

guiding layer the fabrication tolerance was higher compared to a thin guiding layer.

The design in Fig. 3.5(b) is a two-dimensional overlapping waveguide taper transition from a buried waveguide to a fiber matched waveguide [81]. The structure consists of two types of waveguide cores, a narrow core for guiding light with a small spot size and a second one with a wide core which symmetrically surrounds the small waveguide. The wider waveguide is constructed so that the mode size matches the mode of single mode fiber. The vertical taper is fabricated by a selective wet-etch technique, using the InP layer as an etch stop. After the lateral tapers are fabricated by dry-etching, the structure is overgrown.

The final figure, Fig. 3.5(c), shows another two-dimensional overlapping waveguide taper design [82]. The SSC consists of four different sections. A small spot strip loaded waveguide on the right hand side is transformed to a fiber matched rib waveguide on the left hand side. The transformation takes place over a lateral and vertical tapered section. In the fiber matched rib waveguide the fundamental mode is excited by the light that is launched into the device by a butt-coupled fiber. The fiber matched part has a highly doped InP substrate. The mode transformation in the vertical direction takes place in the vertical tapered region. In this region, high refractive index material from the graded index and quaternary layers appears at the top of the rib. No regrowth was required to fabricate the device. However, a special ion beam shadow etching technique was developed to obtain the vertical taper. Tab. 3.1 shows the coupling losses of each design and the corresponding

fabrication technique.

Table 3.1: *Best coupling result of each taper design.*

Lateral tapers			
	wavelength (nm)	Coupling loss (dB)	Fabrication technique
Laterally down-tapered buried waveguide Fig. 3.3(a) [51]	1550	2.8	Stepper litho., five growth steps
Laterally up-tapered wave-guide Fig. 3.3(b) [52]	1300	–	Selective chemical etching
Dual lateral over-lapping buried wave-guide Fig. 3.3(c)[59]	1530	1.1	Direct E-beam writing, RIE, Regrowth
Dual lateral over-lapping ridge wave-guide taper Fig. 3.3(d)[62]	1550	2.3	Direct E-beam writing, RIE
Nested waveguide taper transition Fig. 3.3(e)[64]	1300-1550	4	RIE, regrowth
Single lateral taper transition Fig. 3.3(f)[65]	980	0.9	Direct E-beam writing, reactive ion beam etching
Multisection taper transition Fig. 3.3(g)[66]	1550	3.3	RIE
Vertical tapers			
Vertical down-tapered buried wave-guide Fig. 3.4(a)[68]	1300	0.94	Selective area growth

continued on the next page

Vertical down-tapered ridge waveguide Fig. 3.4(b)[72]	1300	3	Diffusion limited etching
Vertical overlapping ridge waveguide Fig. 3.4(c)[75]	1530	1.7	Dip etch, regrowth
Vertical overlapping taper-transition Fig. 3.4(d)[76]	1550	2	Oxide shadow etching, regrowth
Vertical overlapping waveguide taper transition Fig. 3.4(e)[77]	1550	–	Shadow mask RIE
Combined tapers			
Combined lateral and vertical ridge waveguide taper Fig. 3.5(a)[80]	1540	3	Selective area growth, RIE
2-D overlapping waveguide taper transition Fig. 3.5(b)[81]	1550	0.4	Stepped etching Cl_2 dry etching, regrowth
Overlapping waveguide taper transition with two sections Fig. 3.5(c)[82]	1550	1.5	Direct shadow etching, ion beam etching, wet selective etching

3.3 Asymmetric Twin Waveguides

Another coupler concept that has shown good prospects, is the asymmetric twin waveguide (ATG) principle. To explain this concept significant development mile-

stones are outlined.

The integrated twin-guide (ITG) in an AlGaAs system can be taken as the starting point for ATGs [9]. Two waveguides with the same propagation constants are placed on top of each other (Fig. 3.6). The upper waveguide has two mirrors

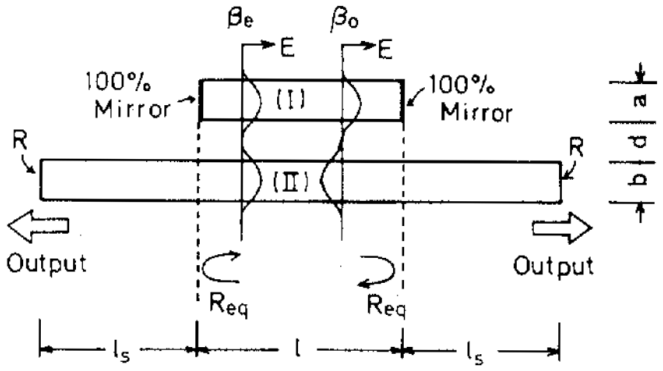


Figure 3.6: *Model for the ITG laser [9].*

on each side and acts as a laser. The underlying waveguide is transparent and passive. The laser is optically pumped and the threshold density was reported to be two times higher than that of a single waveguide laser. Since both waveguides are phase matched, the structure has similar properties to a directional coupler. Each of the waveguides has only a single vertical mode, therefore the combination of both waveguides has an even and an odd mode. It has been calculated [83] that both modes have a similar confinement factor and gain. Because of this, both modes are excited and mode beating is always present. The active region has to vanish right at the point where the optical field is in only the lower, passive waveguide to enable maximum coupling efficiency. A low tolerance of several microns is required. Furthermore, if a mismatch is supposed between the two waveguides the coupling efficiency to the lower waveguide is reduced. In the case of a mismatch of the propagation constants, one mode is highly confined in the active waveguide, whereas the second mode is mainly in the passive part. Therefore, a mismatch will reduce the coupling to the passive waveguide. In general it has been shown that even a simplified ITG is unpredictable in terms of threshold current or coupling efficiency. The coupling is significantly sensitive to the refractive indices and the thickness variation.

Nevertheless, an ITG offers the notable advantage of integrating several different active components with a passive waveguide in a single epitaxial growth step. Xu et al. introduced an absorbing layer in between the active and passive waveguide to avoid the disadvantages of an ITG [10]. A 100 Å InGaAs layer is placed at the center of the spacing layer. The even mode has a factor of 10 higher confinement factor than the odd mode in that layer (Fig. 3.7). This results in higher losses of

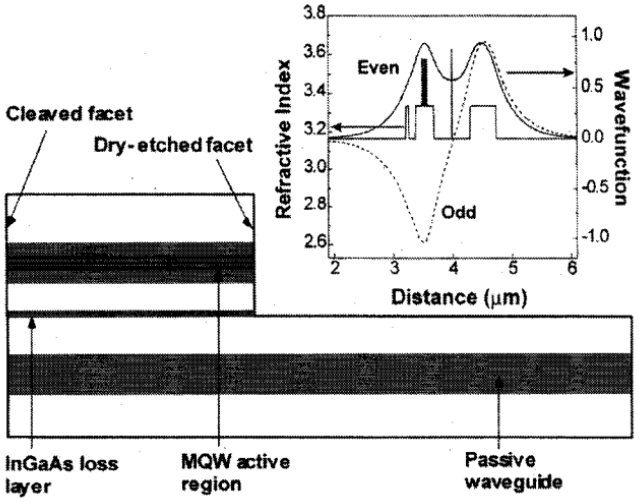


Figure 3.7: *Schematic diagram of the twin waveguide structure with passive waveguide. Inset: Refractive index and calculated mode profiles in the TG structure with InGaAs loss layer [10].*

the even mode, therefore the odd mode reaches the lasing condition at lower current and hence will be favored. The intensity in both guides is nearly equal, allowing a theoretical output coupling of 50 % in the passive waveguide.

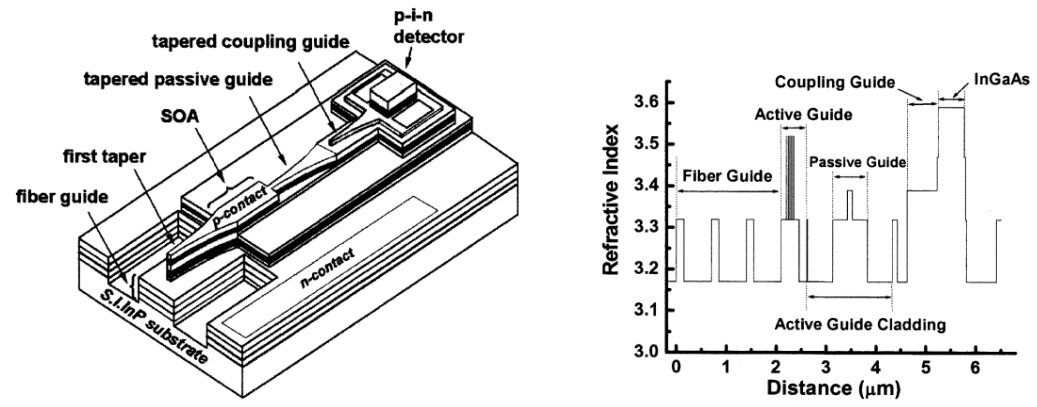
Although the absorbing layer was well suited to suppress the even mode in a laser,the absorption of the layer was not sufficient to remove the even mode in other applications (e.g. traveling-wave optical amplifier). As a result, the asymmetric twin guide (ATG) approach was introduced [84]. The thickness of the passive waveguide layer was increased compared to the symmetric twin-guide. As a result the even and odd modes are split unequally between the two guides. The odd mode has a dominant overlap with the active guide, whereas the even mode is strongly confined in the passive waveguide. Because of that the odd mode is significantly more amplified than the even mode for a sufficiently long amplifier. The even mode can be

neglected and the mode interference effects can be reduced.

Since the transition losses of up to 6 dB were significant, the previously shown, well established lateral taper design was implemented to reduce the coupling losses [85].

The ATG structure was also used to integrate a DBR in a single growth step process [86]. The same 125 μm long tapers as before were implemented to couple the optical field into the small spot size passive waveguide. The first order Bragg reflectors are located shortly after each taper.

On the receiver side the ATG has also shown its usefulness by integrating a PIN-photodiode [87].



(a) **(b)**

Figure 3.8: *(a) Three-dimensional schematic view of the integrated ATG SOA/p-i-n chip. (b) Index profile of the SOA/p-i-n epitaxial structure. . The tapered section of the passive guide joins these two parts together [11].*

Integration of an optical mode transformer, a semiconductor optical amplifier (SOA) and a high-bandwidth waveguide coupled photodiode based on ATG has been demonstrated (Fig. 3.8) [11]. The optical field was coupled among the different components by three adiabatic couplers. The fiber waveguide and the active waveguide were similar to those in [86]. The upper cladding of the active guide itself consists of a passive waveguide. Since the effective index of the active waveguide is always larger than the passive guide, the optical field is coupled into the active guide. Therefore, a negligible amount of light travels in the passive guide.

The ATG concept has shown monolithic integration of several active and passive components. Additionally, only a single epitaxial growth step is necessary and standard processing techniques can be used.

3.4 Antiresonant Reflecting Optical Waveguides

A further mode transformer method that is also related to two vertically separated waveguides makes use of the anti resonant reflecting optical waveguide (ARROW). ARROWs were first demonstrated in SiO_2-Si multilayer waveguides [88]. In Fig. 3.9 the principle of an ARROW is displayed. The waveguide core is the upper layer, and the thin layer d_2 acquires the transmission characteristics of a Fabry-Pérot

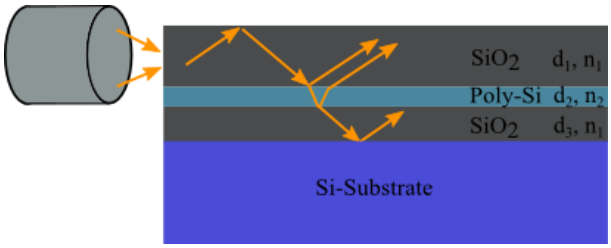


Figure 3.9: *Waveguide scheme using antiresonant reflection.*

cavity. High reflectance occurs at the antiresonant wavelengths of this cavity. This structure does not support guided modes. It is a kind of leaky waveguide with an effective single-mode behavior because of the high losses in the high-order modes and the low losses in the fundamental mode. While the resonances of a Fabry-Pérot cavity occur over a narrow band of wavelengths, the antiresonances are spectrally broad. Therefore, the ARROW works over a wide wavelength region. The thickness of the layers can be calculated by the following antiresonant conditions:

$$\begin{aligned} d_2 &= \frac{\lambda}{4n_2}(2N+1)\left(1-\frac{n_1^2}{n_2^2}+\frac{\lambda^2}{4n_2^2d_1^2}\right) \\ d_3 &= \frac{d_1}{2}(2M+1) \qquad (N,M=0,1,2...) \end{aligned} \tag{3.4.1}$$

where λ is the vacuum wavelength. The loss of the fundamental TE-mode has been calculated to be 0.225 dB/cm at 1.3 μm, whereas the first and second higher order modes have a loss of 99.2 dB/cm and 21.64 dB/cm respectively. On the other hand

the TM loss is very high since the TM reflections are always lower due to the same phenomenon which gives rise to the Brewster angle. A loss of < 0.8 dB/cm was measured for the TE-mode compared to 80 dB/cm for the TM-mode.

For ARROWs operating at a wavelength of 0.633 μm a transparent TiO_2/SiO_2 interference cladding has been employed to reduce the propagation loss [89]. A minimum loss value of 0.3 dB/cm was measured at a TiO_2 thickness of 0.08 μ for the TE-mode. Two uncoupled, stacked ARROW waveguides were realized by using a $TiO_2/SiO_2/TiO_2$ intermediate cladding.

A new type of antiresonant reflecting optical waveguide (ARROW-B) was proposed to reduce the polarization dependence [90]. In this case the refractive index of the first cladding is lower than the core in contrast to the previous ARROW concept where the refractive index of the cladding was higher. If the cladding is thick enough total internal reflection is possible. However, the cladding is thin and the evanescent field reaches the second cladding layer. In the case of the second cladding layer thickness being half of the core layer, the even modes satisfy the antiresonant condition, whereas the odd modes satisfy the resonant condition. Thus, the reflection is a kind of interference reflection. The polarization dependence is reduced, because the total internal reflection at the first interface dominates the overall reflection. The reported loss values were 0.5 dB/cm and 0.7 dB/cm for the fundamental TE- and TM-mode at a wavelength of 0.633 μm. The higher order modes still had a loss of more than 10 dB/cm.

The ARROWs exhibit very attractive features, like large mode size, low loss for the fundamental modes, high discrimination of the remaining modes and ease of fabrication. Therefore, the ARROW concept has been transferred to InGaAsP/InP waveguides and used for integrated spot size converters [91]-[92].

Koch et al. demonstrated that low loss ARROWs can be fabricated for wavelength ranges that are strongly absorbed in the adjacent InGaAsP reflector layers [91]. A 4.3 μm thick InP core was placed on two 0.24 μm layers of InGaAsP separated by 2.2 μm of InP. In the double reflector the thickness of the second InP layer was chosen to also be antiresonant [93]. The bandgap of InGaAsP was at 1.542 μm. The loss values were in the range of 0.9 dB/cm at a wavelength of 1.67 μm and up

to 6.5 dB/cm at 1.515 μm.

An ARROW design can also be used to enable lasing in the high index InGaAsP (λ_g = 1.35 μm) layers and couple light in to the large InP layer [12]. A 6.9 μm InP core layer was grown on two 0.33 μm InGaAsP reflectors separated by 3.3 μm of InP. Since both reflectors support modes with higher propagation constants than the ARROW, coupling between these waveguides was initially not possible. However, the interference pattern of two 1.06 μm laser beams incident at an angle to the surface formed a grating and enabled optical pumping. The carrier density change caused a change in the refractive index of mainly the top InGaAsP, resulting in an optical grating. In such a way the laser light can be coupled to the InP ARROW and finally measured at a detector.

Despite the use of the ARROW principle initially to confine the optical field vertically, Mamst et al. demonstrated a single mode laser with a lateral ARROW confinement [94]. In AlGaAs/GaAs a large spot size (4 - 8 μm) single mode laser was fabricated by placing three quarter wavelengths high-index cladding layers besides a 4 or 8 μm ridge. In such a way the fundamental mode can nearly be guided without losses, whereas the higher order modes are suppressed by their loss. A two-step MOCVD growth step was required for that structure.

A design of an InGaAsP-InP tapered ridge SSC with underlying ARROW coupling guide has shown theoretically improved coupling by a factor of 5.6 dB [95]. A 2 μm wide ridge waveguide (n_{core} = 3.29, d_{core} = 0.2 μm, 0.5 μm upper InP cladding) was placed over an ARROW, consisting of two InGaAsP reflection layers (λ_g = 1.3 μm, d = 0.32 μm), a 2.54 μm InP spacer and a 4.8 μm InP core layer. The ridge waveguide was linearly down-tapered to 0.5 μm over a length of 500 μm. The estimated power loss was 0.14 dB for the taper. After an optimization procedure the taper length was reduced to 315 μm with losses of 0.11 dB for TE- and 0.21 dB for TM-polarization. The calculated overlap integral of the ARROW modes to a SMF achieved a coupling efficiencies of 56 % (TE) and 53 % (TM).

A design similar to the previous one has been used to improve the fiber coupling of a 1.55 μm InP-InGaAsP laser [13]. A multi quantum well (MQW) laser was placed on an ARROW with a 5 μm InP core and two 0.32 μm InGaAsP (λ_g =

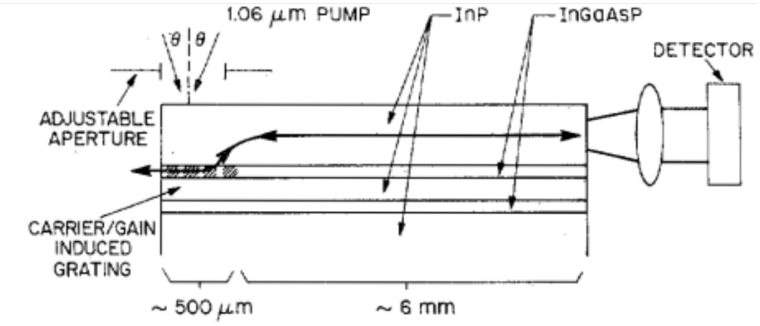
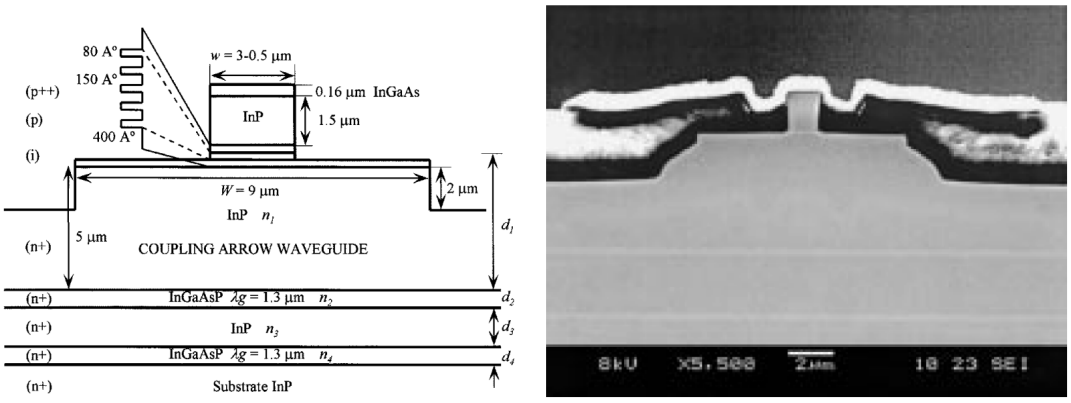


Figure 3.10: *Scheme of the optically pumped/optical grating InGaAsP/InP ARROW with active and passive region [12].*



(a) **(b)**

Figure 3.11: *Schematic drawing and SEM images of a laser and an integrated ARROW [13].*

1.3 μm) reflectors (Fig. 3.11). The laser mode was coupled adiabatically to the ARROW by three linear tapers.

Further investigations were carried out to reduce the thickness of the cladding layers [96]. By assuming a taper length of 300 μm and an allowed leakage loss of 0.1 dB/cm the total cladding thickness was reduced by 2.12 μm to 1.12 μm.

Galarza et al. have demonstrated that the antiresonant effect can also be used for lateral and vertical confinement [13, 97]. The intention for implementing the antiresonant effect for lateral confinement was to simplify the fabrication and avoid an alignment step. It is not necessary to form a mask and etch the wider ridge for the ARROW waveguide. The vertical expansion of the coupling waveguide is limited by the fact that lateral antiresonant confinement is reduced relative to the

InP thickness.

The effect of resonant coupling (Chapter 4.1.3) has been used to reduce the taper length for the InGaAsP-InP laser with vertical ARROW coupling [92]. The first taper was reduced from 3 to 1μm over a short distance of 20 μm. This caused partial power transfer from the fundamental to the first order mode. In a 173 μm long taper section from 1 to 0.81 μm, mode beating occurs. The mode beating couples the optical field to the lower waveguide. A final 100 μm taper (0.81 to 0.3 μm) prevents back coupling to the previous waveguide. The taper length was reduced by 177 μm compared to the adiabatic design. However, the fabrication tolerance is tighter.

To summarize, it can be concluded that the ARROW design is a good opportunity to improve fiber coupling. An ARROW structure can be grown in a single growth step. Furthermore, standard processing techniques with a good fabrication tolerance can be applied. Nevertheless, although the polarization insensitivity of ARROWs has been addressed in some cases, it still remains an issue, especially for III-V materials.

3.5 Polymer and Silicon Oxynitride Waveguides

A concept that is not directly based on semiconductor materials is that of waveguides made of polymers. Nevertheless, it offers the possibility of integration with semiconductor devices.

The advantage of polymer waveguides are the cheap cost compared to III-V materials. One of the main challenges for polymer waveguides is to find materials with a large refractive index difference and low absorption at the desired wavelength. For wavelengths in the range of 630 nm mode size transformation has been demonstrated by changing the refractive index difference between core and cladding [98]. The change of the refractive index was achieved by exposing a polyimide with different electron beam doses. The mode size diameter ($1/e^2$) was increased by a factor of two to more than 12 μm.

Polymer waveguides have received research attention for monolithically integrat-

ing photonic devices since the early 1990s. The polymer waveguides offer the capability of preparation of active and passive components on III-V wafers with already processed devices. Coupling from a buried ridge laser at 1.3 μm wavelength to a polymer waveguide has been demonstrated [99]. The polymer waveguide consisted of a Poly(methylmethacrylate) (PMMA) cladding and a core layer of polystyrene. The device was fabricated in two steps. First the laser was manufactured with standard semiconductor processing techniques. Then, the polymer waveguide was realized by spin coating, conventional photolithographic patterning and reactive ion etching (RIE). Furthermore, the waveguide showed absorption losses of less than 1 dB/cm at the telecommunication wavelengths of 1.3 and 1.55 μm.

Borges et al. [14] demonstrated coupling simulations from a single mode fiber into a thin film AlGaAs/GaAs waveguide via a polymer. The SMF is butt coupled to the polymeric channel (Fig. 3.12). It is patterned atop a GaAlAs/GaAs/GaAlAs

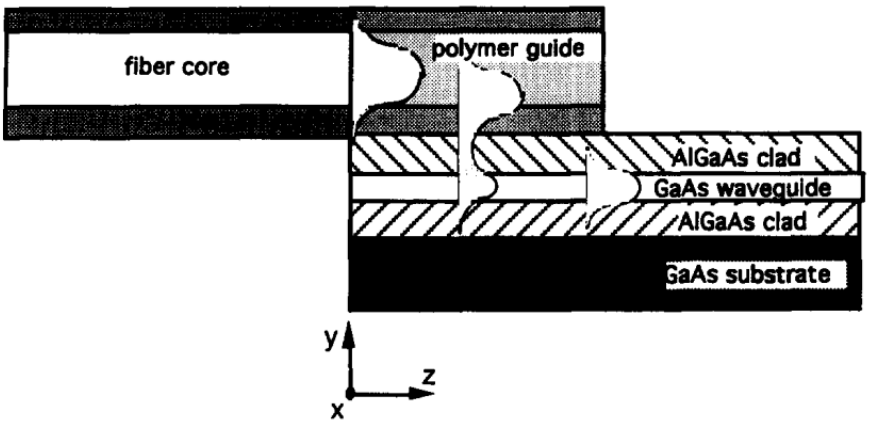


Figure 3.12: *Basic structure under consideration illustrating the transfer of power from the fiber to the polymer and then to the GaAs waveguide [14].*

waveguide. Then the field is transferred to the higher refractive index III-V waveguide.

Tapered polymer single-mode waveguide have been demonstrated that enable coupling from an InGaAsP laser diode to a fiber[100]. Four layers of the polymer Amoco Ultradel 4212 combined with DCM dye were spun onto a silicon substrate. The two center layers act as high refractive index guiding layers and are tapered. The tapering was achieved by masking and exposing the layers sequentially to UV

light. The areas that are exposed decrease in refractive index.

Although fiber coupling to III-V devices through polymer waveguides has been demonstrated and high refractive index polymers have been fabricated [101], certain challenges still remain before polymer waveguides reach the status of a standard technology. This birefringence of polymers is an issue that has to be addressed to enable polarization insensitive coupling. The birefringence is caused by two main sources: the inherent molecular structure and the processing history of the polymer.

Silicon-oxynitride (SiO_xN_y) is another promising approach that can offer similar properties to polymers. The refractive index of the SiO_xN_y can be adjusted between that of SiO_2 (1.46) and Si_3N_4 (2.0). A 0.1 μm thick and 2 μm wide Si_3N_4 core waveguide has been used to improve coupling of a channel mesa buried heterostructure laser (λ = 1.55 μm) to an optical fiber [102]. That core layer was surrounded by 4 μm thick and 7 μm wide phosphorsilicate glass. It acted as a core layer for a loose waveguide with a nearly fiber-matched mode size. The coupling between the small mode size Si_3N_4 and the loose waveguide was achieved by laterally down-tapering Si_3N_4 to zero over a distance of 1000 μm. The spot size converter was fabricated on a silicon wafer, but still needs a precise alignment step.

A similar SSC approach has been utilized to couple from a fiber into a chemo-optical sensor [103]. However, due to the smaller wavelength of 633 nm, a taper end width of less than 500 nm was necessary. Since a smooth vertical taper was not an option for them, a step-wise lowered taper point was implemented.

A general problem for SiO_xN_y is the incorporation of hydrogen and the absorption of the overtones of its bonds (-Si-H, -N-H, -Si-O-H). This absorption is located in the range of 1.4-1.5 μm. It has been demonstrated that the hydrogen bonds can be driven out of the material by keeping it for 3 h at a temperature of 1100 °C [104, 105]. However, to reduce the absorption losses below 0.1 dB/cm the chips have to be at 1200 °C for 12 h[106]. Although the absorption losses can be minimized, cracks can occur on the chip.

Hoffmann et al. [107] have demonstrated fiber-matched low-loss waveguides at 1.3 and 1.55 μm with 1x8 power splitters and wavelength division multiplexers (WDM). A 350 nm core layer of SiO_xN_y (n = 1.496) were fabricated by Plasma-

enhanced chemical vapor deposition (PECVD) at 400 °C. That core was embedded in a 17 μm layer of SiO_2. Because the core layer was thin and its refractive index was close to SiO_2 the optical field was mainly located in the cladding. As a result, the absorption losses were reduced to 0.2 dBcm^{-1} at 1.3 μm and 0.4 dB/cm at 1.55 μm. Low-pressure chemical vapor deposition (LPCVD) has a total hydrogen content of approximately 4 % compared to 22 % for PECVD [108]. Therefore, LPCVD technology is preferable to PECVD for reduced absorption.

Another aspect that needs to be considered is the birefringence caused by stress. Woerhoff et al. [109] have shown that it is possible to realize a polarization independent SiO_xN_y waveguide. It was found that for a certain thickness and width of the higher refractive index core the waveguide was polarization independent. For only a single width value the birefringence can be reduced to $|\Delta N_{TE-TM}| < 5 \cdot 10^{-5}$.

Silicon-oxynitrides have proven to be suitable for fabricating low-loss waveguides for improved fiber coupling. It is possible to integrate several components such as power and polarization splitters, MZIs and WDMs. However, so far the waveguide structures have generally been prepared on silicon wafers. To make an integrated SSC for III-V devices it has to be possible to transfer the SiO_xN_y technique from silicon to InP. However, due to the different heat expansion and thermal conductivity coefficients of InP and SiO_2, Si_3N_4 and SiO_xN_y stress is induced. Therefore, cracks can occur in the structure (Chapter 8). That makes it hard to realize low-loss waveguides. Furthermore, the required high temperature treatment is also not possible with the present fabrication facilities at Tyndall National Institute.

3.6 Conclusion

A large variety of different concepts to improve fiber coupling for semiconductor based waveguides has been shown. Gratings require sophisticated processing steps, such as E-beam lithography or holographic interference and special etching techniques. Polymer and siliconoxynitride SSCs offer cheap fabrication cost. However, certain processing equipment, e.g. high temperature ovens, is necessary that is not always available. Additionally, the optical field has to already be in a pas-

sive waveguide before it is coupled via a polymer/siliconoxinitride waveguide into a fiber. That leaves as a first step coupling from an active InP-InGaAsP waveguide to a passive one. This process has been intensively investigated by introducing tapered waveguides. The lateral taper design has advantages because of its standard fabrication step. The ARROWs and ATGs have the significant benefit of a single epitaxial growth steps. Additionally, lateral tapers can be used to transfer the optical field between different vertically separated waveguides. ATGs are preferable to ARROWS because of their negligible polarization dependent losses. Last but not least, ATGs are by far easier to simulate with the utilized simulation package Fimmwave/Fimmprop. Since the thin reflection layers of the ARROW also support modes, a large number of modes must be calculated before the main guided modes can be found. That increases the calculation time and effort for waveguides with changing geometry, where for each different section the modes and their overlap integral at each intersection must be calculated.

These are the reasons why the main topics of the following chapters are ATGs and their properties.

Chapter 4

Optical Coupling between Waveguides

Because the coupling of the optical field between different waveguides is one of the main subjects of this thesis, this chapter describes the key issues that have to be taken into account to enable low loss power transfer between two waveguides. The general case investigated here is a ridge waveguide. However, due to the complex boundary conditions, analytical solution of Maxwell's Equations is not possible. Therefore, an approximation method has to be used. All the simulations were done with the previously mentioned software package Fimmwave and Fimmprop.

In the following sections important aspects such as the resonance point and cut-off point are explained. Examples are shown. Using the knowledge of these points the principles of adiabatic and resonant coupling are illustrated. Finally, the parameters that effect the coupling efficiency and a technique for improving the fabrication tolerance of a resonant coupler are outlined.

4.1 Coupling between Two Vertically Separated Waveguides

The following design rules for an ATG suitable for direct fiber coupling are obtained in this chapter.

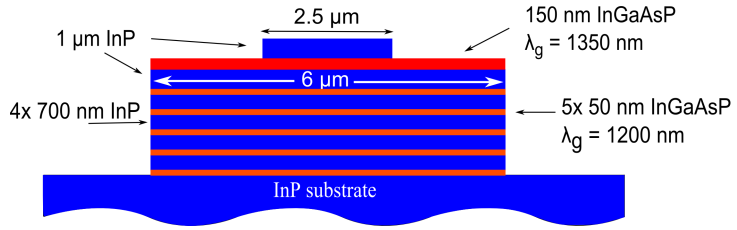
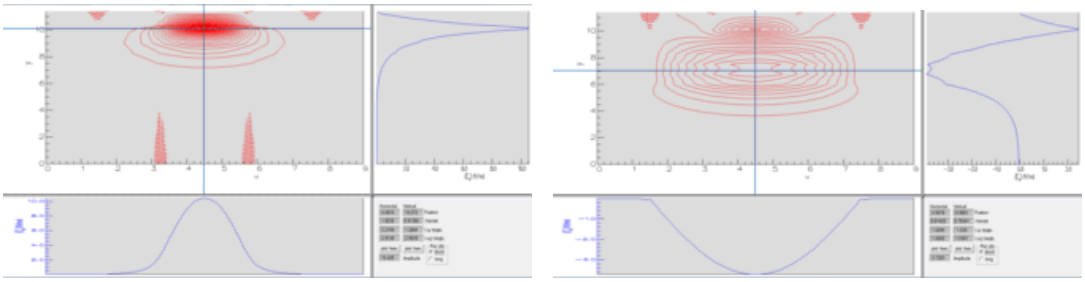


Figure 4.1: *Schematic cross-section of the ATG with the diluted lower waveguide*

- The first step is to design a large spot size single mode lower waveguide suitable for low loss fiber coupling.
- Then an ATG is required that is a single mode waveguide for both polarizations at the achievable minimum upper waveguide width.
- The propagation constants of the fundamental modes at this width must be close to the propagation constants of the lower waveguide. In such a way mode mismatch losses are reduced.
- Second, the modes must be calculated at the maximum desired upper waveguide width.
- Following, the propagation constants need to be calculated between this extrema to obtain the resonance points.

Implementing an additional vertically separated, large spot size waveguide into a photonic chip enables improved fiber coupling and simplified packaging. As outlined in Chapter 3, the ATG concept is well suited for this intention. Because an ATG consists of at least two different vertically separated waveguides, such a structure is investigated. In Fig. 4.1 the waveguide is shown. The lower waveguide has five 50 nm layers of InGaAsP (λ_g = 1200 nm, n(InGaAsP) = 3.33 at 1550 nm) interspersed with 700 nm thick layers of InP (n(InP) = 3.17 at 1550 nm). This waveguide is a so called diluted waveguide [110]. Epitaxially growing layers of InGaAsP several microns thick by an MOVPE is complicated and a homogeneous layer is hard to realize. Several parameters, such as the gas flow rate or the substrate temperature, have to stay constant over several hours. The diluted waveguide principle overcomes that problem. Only quaternaries of several tens of nanometers are necessary. These

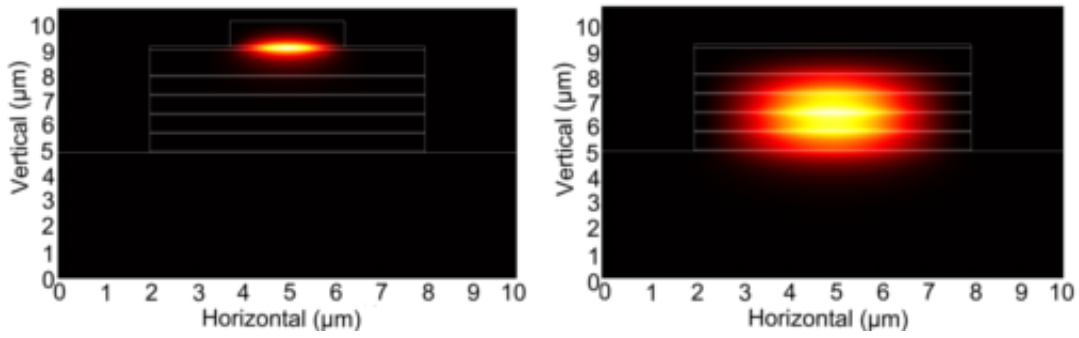


(a) **(b)**

Figure 4.2: *E_x profile at an upper cladding width of 2.5 μm, (a) for the even TE-mode, (b) for the odd TE-mode.*

higher refractive index layers combined with the thicker lower refractive index InP layers act as a single waveguide. A main criterion for an input waveguide (from an optical fiber) is that the waveguide must be a single mode waveguide for both polarizations. If multiple modes are guided in a waveguide, the input mode would excite these modes. This results in mode beating and as a result permanent coupling to an upper waveguide is difficult to do. This diluted waveguide is designed such that it only guides the fundamental TE- and TM-polarization with a propagation constant of 12.866 μm^{-1} and 12.862 μm^{-1} respectively.

The upper waveguide has a different InGaAsP (λ_g = 1330 nm) composition for the core layer. The bandgap of 1330 nm has a refractive index of 3.40 at a wavelength of 1550 nm for a material lattice matched to InP. In chapter 7 the physical details of the refractive index, the bandgap and the InGaAsP composition are described in more detail. In Fig. 4.1 the ATG is shown with a maximum upper waveguide width of 2.5 μm. This width corresponds to the usual width of ridge lasers fabricated at our research institute. The structure now guides two modes, the fundamental and first higher order mode, for each polarization. The fundamental mode is called the even mode (Fig. 4.2(a)). The first order mode is referred to as the odd mode (Fig. 4.2(b)). By reducing the upper InP cladding (Fig. 4.2(a)) width the ATG is modified to a single mode waveguide. The intensity profile of the fundamental TE-mode at an upper waveguide width of 2.5 μm and without a ridge can seen in Fig. 4.3(a) and (b).



(a) **(b)**

Figure 4.3: *TE mode intensity profile, (a) ridge width 2.5 µm, lower waveguide width 6 µm: optical field width ($1/e^2$) horizontal: 2.2 µm, width vertical ($1/e^2$): 1.2 µm, (b): lower waveguide width 6 µm: optical field width ($1/e^2$) horizontal: 4.6 µm, width vertical ($1/e^2$): 4.3 µm,*

The structure is passive to reduce any further influences on the coupling. It consists of a large lower waveguide with a circular spot size of nearly 4.5 µm and upper waveguide with an elliptical spot size of around 2.2 µm x 1.2 µm. An overlap integral [111] is used to calculate the butt-coupling efficiency for two Gaussian beam shapes. The coupling efficiency of a SMF with a spot size of 10.4 µm to the upper waveguide is 9 %. The large spot size waveguide (Fig. 4.3(b)) improves the coupling efficiency to 52 % because the large spot size optical field increases the fiber overlap.

4.1.1 Resonance and Cut-off Points

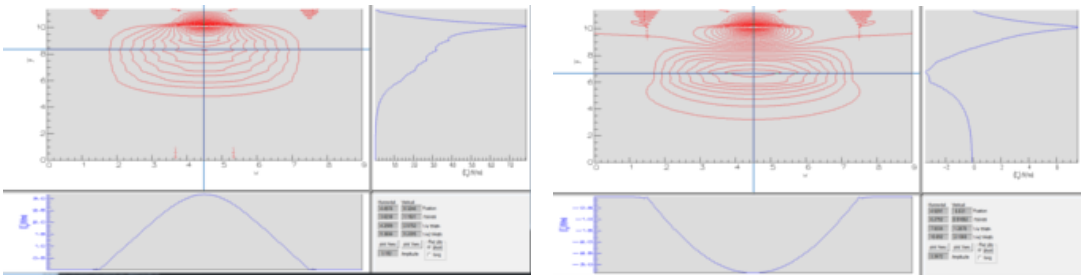
ATGs are the most suitable concept for integrating a mode adapter with different active or passive devices using standard fabrication techniques. To fulfill the different requirements, such as confinement factor, polarization sensitivity, single mode operation, high-quality electrical contacts, etc., each waveguide typically has a different propagation constant. This means that each waveguide has a different solution of Maxwell's equations. Therefore, a mode of one waveguide is not guided by the other waveguide. Additionally, if the effective indices in both waveguides are largely different each mode is only confined in its waveguide and does not expand into the other waveguide.

To enable power transfer from one waveguide to another, the propagation con-

stant, and therefore the effective refractive index, n_{eff}, of at least one waveguide has to be modified. The most appropriate way in the sense of simplified fabrication is to change the width of the waveguide. A wider/narrower waveguide results in a higher/lower propagation constant.

In the case of the simulated structure (Fig. 4.1) only the width of the upper waveguide cladding is altered. The 150 nm InGaAsP waveguide core is unchanged. Since the lower waveguide is 6 μm wide and designed for single mode operation, the waveguide needs to be several microns larger to result in a significant propagation constant increase. The propagation constant difference of the first order TE mode located in the lower waveguide, is 0.005 μm^{-1} if the lower waveguide width is changed from 6 μm to 8 μm with a 2.5 μm wide upper cladding. On the other hand, a change of the width of the upper cladding from 1 to 2.5 μm causes a change of the fundamental TE-mode propagation constant from 12.87 μm^{-1} to 12.91 μm^{-1} (difference 0.04 μm^{-1}). Therefore, the width of the upper waveguide is tapered to couple between the two waveguides.

The principal aspects that need to be considered when modifying the upper waveguide width are the resonance point and the cut-off point. The resonance point is the width at which both waveguides have more or less the same propagation constants. At that point the optical field of the even and odd modes is nearly equally split between both waveguides (Fig. 4.4). Combined, both waveguides now act as a



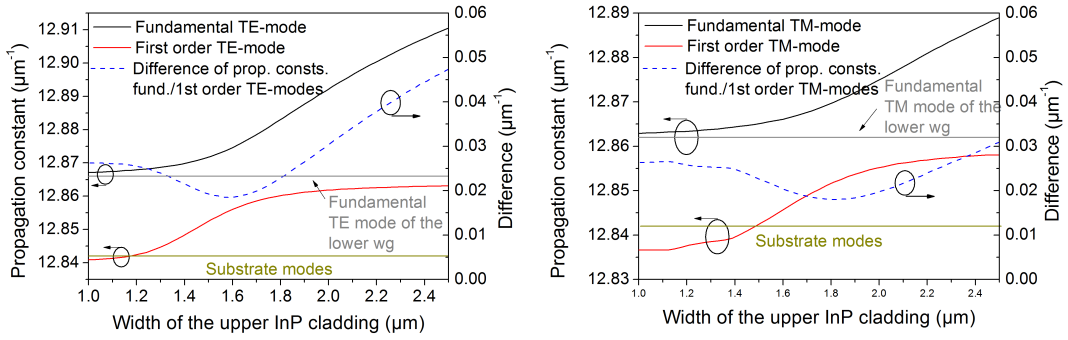
(a) **(b)**

Figure 4.4: *E_x profile at an upper InP cladding width of 1.6 μm, (a) for the even TE-mode, (b) for the odd TE-mode.*

single waveguide that supports two modes. If the width of the upper waveguide is wider than the resonance width the fundamental mode is mainly in the upper waveg-

uide and the first higher order mode is mainly in the lower waveguide. If the width of the upper waveguide is smaller, both modes are mainly in the lower waveguide. This effect can be explained by the following model. When the upper waveguide width is wider than the resonance width, the lower waveguide is the cladding of the upper waveguide. When the ridge width is decreased, the propagation constant is reduced as well and the mode starts to expand into the lower cladding. In the other case with a width narrower than the resonance width, the upper waveguide acts as a cladding for the lower waveguide with the same effect.

At the resonance point the spatial overlap of the even and odd mode is at its maximum. Therefore, a small modification of the waveguide causes power transfer from the fundamental mode to the next higher order mode. It is crucial to know the resonance point to control the power transfer effect. A technique to find this point can be seen in Fig. 4.5. The propagation constants of the even and odd



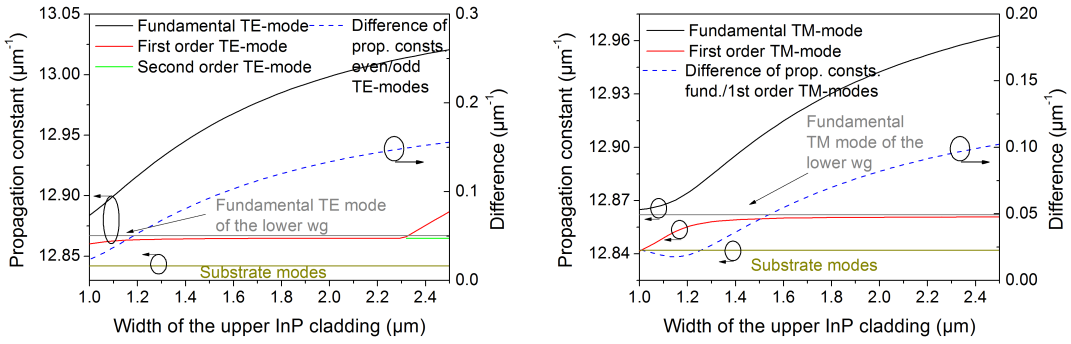
(a) **(b)**

Figure 4.5: *Propagation constants (n(upper wg) = 3.40) and its difference for the (a) TE-polarization (b) TM-polarization.*

mode of the TE- and TM-polarization are plotted for an upper waveguide cladding width from 1.0 μm to 2.5 μm and core layer thickness of 150 nm. It can be observe that for a width between 2.0 μm to 2.5 μm there is only a small change in the propagation constant of the first higher order TE-mode and the difference between the two modes is large (Fig. 4.5(a)). This means a steep taper angle can be chosen and no power is transferred from one mode to the other. For the TM-polarization (Fig. 4.5(b)) the difference is generally smaller. Only in a width range between 2.3

μm to 2.5 μm is the difference of the propagation constants larger than 0.025 μm^{-1}. For both polarizations in these ranges the propagation constants are large enough that the optical field is mainly confined in the upper waveguide. At 1.8 μm and at 1.6 μm, the differences of the propagation constants of both TM- and TE-modes are at their respective minima. These widths can then be identified as the resonance points for each polarization. A qualitative explanation for this conclusion can be given by assuming the ATG takes the form of a single waveguide that guides two modes, whereas for different widths two different waveguides are present. Another important point is the crossing of the first order mode propagation constants with the substrate mode line. The substrate mode line indicates a propagation constant with an effective index of InP. If any propagation constant is below this line, the mode is a substrate mode and not anymore guided in the waveguide. Therefore, the crossing for the first order TE-mode at $\approx$ 1.2 μm and $\approx$ 1.5 μm for the first order TM-mode shows the upper cladding width at which the ATG becomes a single mode waveguide. Then the optical field is mainly in the lower waveguide.

Fig. 4.6 shows the resonance points shifting to narrower widths for a higher



(a) **(b)**

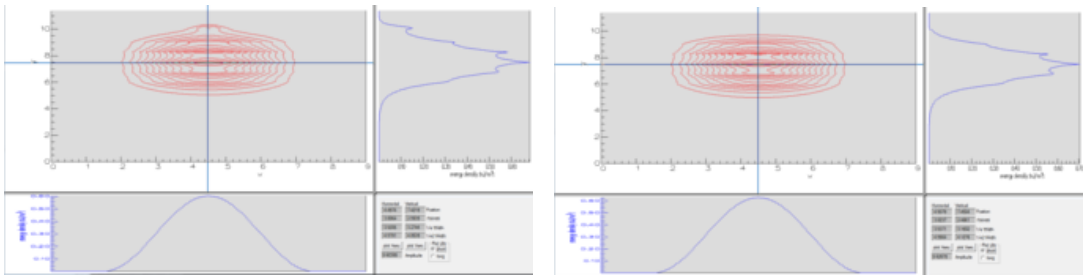
Figure 4.6: *Propagation constants (n(upper wg) = 3.50) and its difference for the (a) TE-polarization (b) TM-polarization.*

refractive index difference in the ATG. For the TM-polarization this width is $\approx$ 1.15 μm, whereas for the TE-polarization it is smaller than 1.0 μm. Another waveguide property can be seen at widths larger than 2.3 μm in Fig. 4.6(a). After this point the upper waveguide guides two lateral modes. Therefore, the odd TE-mode in the

ATG is the second higher order mode. For the first and second higher order (odd) TE-modes it can be observed (Fig. 4.6(a)) that the propagation constant change is negligible for a width > 1.0 μm. For the first higher order (odd) TM-mode the width is > 1.3 μm. The lower waveguide does not "recognize" the upper waveguide.

Additionally, the difference in the propagation constants results in no power transfer in the width range of 2.5 to 1.0 μm. Alternatively, an initial smaller refractive index difference shifts the resonance points to wider ridge widths.

A second important quantity is the cut-off point. The cut-off point is the width at which a waveguide does not guide modes anymore. The minimum width is limited by the deep ultra-violet (UV) mask aligner resolution. The available MA 6 mask aligner from Karl Suess offers a maximum resolution of 0.5 μm. Therefore, the upper waveguide in the investigated structure has to be designed in such a way that no additional modes are guided before that width and the optical field is mainly located in the lower waveguide (Fig. 4.7. As discussed a general problem can occur if the



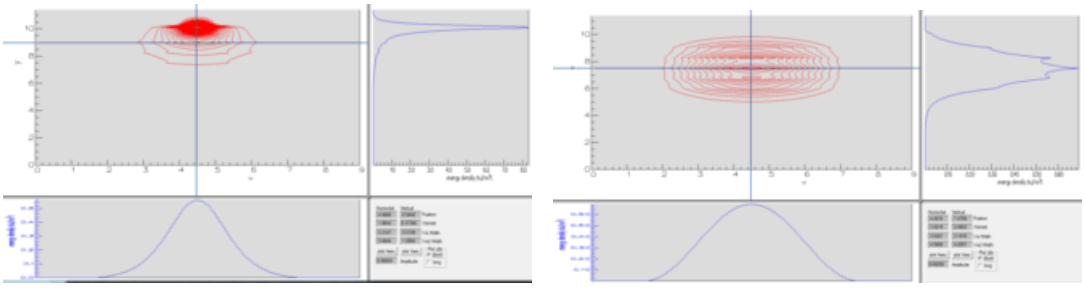
(a) **(b)**

Figure 4.7: *Intensity profile of the TE-polarization (a) at a upper cladding width of 1.0 μm, (b) only the lower waveguide is present, the upper cladding is removed.*

propagation constant values of the upper waveguide are too large. In Fig. 4.6 the propagation constants do not reach the propagation constant of the lower waveguide (β(TE) = 12.867 μm^{-1} and β(TM) = 12.862 μm^{-1}) for a refractive index value of 3.5 in the 150 nm core layer.

Furthermore, the waveguide still guides the even and odd transverse modes. The first order mode does not achieve its cut-off point and the fundamental TE-modes remains mainly in the upper waveguide. In this a case a low loss coupling to the lower waveguide is not possible because of the significant mode mismatch at the

boundary between the ATG (Fig. 4.8(a)) and the lower waveguide (Fig. 4.8(b)). A recognizable amount of the optical field remains in the upper waveguide. This



(a) **(b)**

Figure 4.8: *Intensity profile of the TE-polarization (a) at a upper cladding width of 1.0 µm, (b) only the lower waveguide is present, the upper cladding is removed.*

amount does not overlap with the optical field at the lower waveguide and is lost.

In general, in the design phase of an ATG care has to be taken, to ensure that the resonance and cut-off points are at an appropriate ridge width to achieve low loss coupling and polarization insensitivity.

4.1.2 Adiabatic Coupling

In the previous section it has been outlined that the upper waveguide width has to be reduced to transfer the optical field from the upper to the lower waveguide. Now it will be explained how a width change over a certain propagation distance affects the coupling. The tapering of the waveguide has to guarantee that losses are low and the total distance is short.

If scattering losses such as surface and volume scattering and absorption losses are ignored, losses in a taper are due to mode mismatch. The change of the geometry, e.g. the width reduction, of the waveguide causes a different mode distribution in a waveguide. If there is not an optimum mode overlap of the fundamental mode with itself at each section boundary, the power is partially coupled to the next higher order guided mode in the discrete set of all guided modes. If there already is power in the highest order guided mode, that power will be transferred to the continuous set of radiation modes.

In an intuitive approach one would expect that loss increases with increasing taper angle. That leads to the conclusion, that loss can be kept at a minimum as long as the taper angle is small enough. However, there is a practical limit to the smallest taper angle that can be achieved over a certain distance. This limitation is set by the lithography resolution. A reasonable approximation was given by Galarza et al. [97] with a width change of 90 nm over a length of 100 μm. A taper with negligible power losses of the fundamental mode as it propagates along the taper is called adiabatic. The optical field is then adiabatically coupled from one waveguide to another.

Criteria to calculate the necessary taper length to ensure adiabatic coupling are derived following Love et al. [112]. The first criterion can be concluded from the physical argument that the local taper length scale must be much larger than the coupling length between the fundamental mode and the coupling mode to reduce power loss. Denoting the taper angle Ω, the taper width w_t and the taper length z_t, we can conclude the following correlation

$$\Omega(z) = \tan^{-1}\left|\frac{dw_t}{dz_t}\right| \tag{4.1.1}$$

Since in practice $\Omega(z) \ll 1$, the equation can be approximated as:

$$z_t \approx \frac{w_t}{\Omega} \tag{4.1.2}$$

The local coupling length between the two neighboring modes is taken to be the beat length z_b between the fundamental and first order mode.

$$z_b = \frac{2\pi}{\beta_1 - \beta_2} \tag{4.1.3}$$

β_1 and β_2 are the propagation constants of the fundamental and first order mode respectively. If $z_t \gg z_b$ along the taper, then negligible coupling between the modes will occur. The fundamental mode will propagate adiabatically with negligible loss. Conversely, if $z_t \ll z_b$ significant coupling to the second mode takes place. Consequently, it can be said that the condition $z_t = z_b$ provides an approximation for adiabatic and lossy tapers. Using the length scale criterion for the modes of the previous ATG with an upper waveguide of 2.5 μm yields an adiabatic taper length of

133 μm for the TE-polarization ($\beta_1^{TE} = 12.910\ \mu\text{m}^{-1}$, $\beta_2^{TE} = 12.\ 863\ \mu\text{m}^{-1}$) and 203 μm for the TM-polarization ($\beta_1^{TM} = 12.889\ \mu\text{m}^{-1}$, $\beta_2^{TM} = 12.858\ \mu\text{m}^{-1}$). Although this gives an approximation for the taper length, one further aspect cannot be neglected. The propagation constants of all modes are a function of the propagation distance z ($\beta = \beta(\text{z})$). Therefore, the taper length changes with the propagation distance difference. As shown in Fig. 4.5 the difference is at a minimum at a width of 1.6 μm (1.8 μm) for the TE-polarization (TM-polarization). Taking the propagation constants at these points gives a taper length of 338 μm (TE-polarization) and 349 μm (TM-polarization). These changes require knowledge of the propagation constant along the taper for an accurate calculation.

An alternative approach to calculating the taper length for an adiabatic coupling is the weak power transfer criterion. In this criterion the loss from the fundamental mode due to tapering can be calculated by expressing the field along the taper as a superposition of the local guided and cladding modes. A set of coupled local-mode equations which relate the amplitude of each mode has to be solved. It can be assumed that the coupling is predominantly to the mode with a propagation constant closest to that of the fundamental mode. A coupling coefficient C for these two modes with propagation constants β_1 and β_2 can be derived [112]:

$$C = \frac{1}{2}\frac{k}{\beta_1 - \beta_2}\frac{dw}{dz}\frac{1}{n_{co}}\frac{\iint_{A_\infty}\psi_1\psi_2 dA}{\sqrt{\iint_{A_\infty}\psi_1^2 dA \iint_{A_\infty}\psi_2^2 dA}} \tag{4.1.4}$$

where n_{co} is the core index, $w = w(z)$ is the local core width, k is the free-space wavenumber, A_∞ is the infinite cross-section and ψ_1, ψ_2 are the scalar wave equation fields for the fundamental and first order local modes.

Another method to optimize the length of an adiabatic taper was shown by Xia et al. [113]. It was assumed that the width variation of a ridge waveguide is usually small. This leads to a spatially dependent permittivity $\epsilon_r(\overrightarrow{r})$, where $\overrightarrow{r}$ is the position vector. The time-independent optical field at $\overrightarrow{r}$ can be derived from the unperturbed field by adding a perturbation to the permittivity. The obtained wave equation can then be solved by a Fourier transformation of the field into momentum space. Following this the scattering rate per unit length is calculated. Finally, the

following equation is obtained for the taper length

$$z = A \int_{W_i}^{W} \frac{|d \langle m1 \,|\, \epsilon_r \,|\, m0 \rangle}{\Delta k_z} \tag{4.1.5}$$

$|mi\rangle$ is the field distribution in the x-y plane of mode i. Given the total taper length, tip width W_i, and the end width W_f, the scale factor A can be found, thus determining the optimal shape.

Although this method was used to calculate an optimized taper in an ATG photodiode layout, it only showed an improvement for the case of a 85 : 15 asymmetric waveguide. This means 15 % of the optical power is in the fiber matched waveguide and 85 % is in the coupling waveguide. For the case of 95:05 the optimized taper transfer efficiency is lower than the two-section taper. Furthermore, the field distribution of each mode changes along the taper. Therefore, the distribution must be calculated at each z point.

Several methods exist to determine the minimum length of an adiabatic taper. However, all of them require approximations such as only two modes present and only a small width variation. Therefore, the approach chosen here, that of finding the resonance point by the simulated propagation constants, is equally applicable. Furthermore, to investigate the amount of power transferred in a highly asymmetric waveguide structure among several modes, including guided and radiation modes, the method used in this thesis is advantageous.

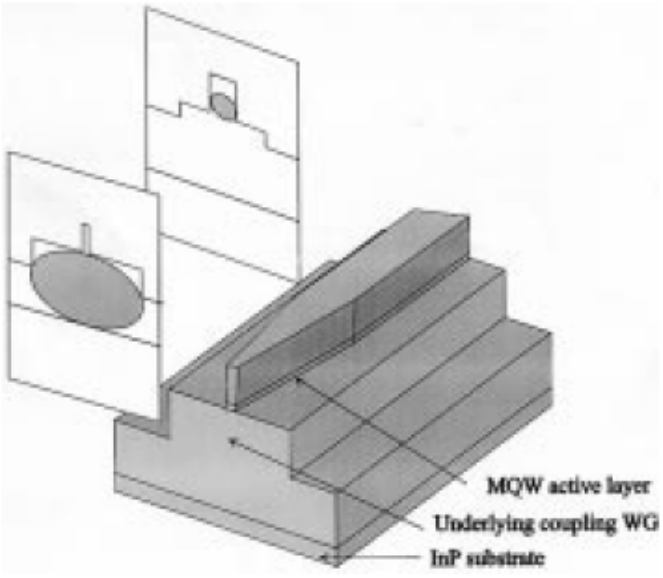
4.1.3 Resonant Coupling

In addition to adiabatic coupling a second field transfer method can be utilized to couple the field between two vertically separated waveguides. The second method is the resonant coupling mechanism [9]. In the case of resonant coupling two modes, referred to as supermodes, are excited in the waveguide and the field transfer from one waveguide to the other is caused by mode beating. Resonant coupling is regularly used to couple optical fields between laterally separated waveguides. Two similar single mode waveguides are placed closely to each other. The optical fields are then a superposition of the even and odd modes with slightly different propagation constants, β_e and β_o. These superposition fields will change their relative phase

as they travel along the directional coupler. If the field were in-phase at $z = 0$, they will be out-of-phase at $z = L = \pi/(\beta_e - \beta_o)$ [114]. The light power that initially started in one waveguide is coupled to the other waveguide after a distance L. For example, in dual-channel waveguide electro-optic modulators an applied voltage signal allows to switch the optical field output between the two waveguides [115]. Nevertheless, resonant coupling in vertical direction is more complicate to achieve.

A theoretical study was carried out to resonantly couple a 1.55 μm InGaAsP laser to an underlying fiber coupling waveguide [116]. Originally the laser beam was coupled adiabatically to the lower waveguide. However, a 500 μm long taper with a start and end width of 2 and 0.3 μm was required for a low loss transition. Although the taper length was reduced by 300 μm it was outlined that the phase matching condition critically depends on the refractive indices and the dimensions of the waveguides. A tapered active section was proposed to guarantee a single power transfer to the lower waveguide. However, the total taper length was 3000 μm and the ridge was tapered down from 2.0 to 0.1 μm. These are dimensions that are hardly realizable with standard processing techniques.

The same group fabricated the proposed resonant coupler [15]. A 2 μm wide



(a)

Figure 4.9: *Schematic diagram of the resonantly coupled-mode expander [15].*

ridge is exponentially reduced to 1.4 μm over a distance of 100 μm. Afterwards, a 100 μm long linear taper to 0.3 μm is used (Fig. 4.9). That taper caused an increase of the laser threshold from 28 mA to 36 mA. The laser only operated in pulsed mode. The coupling efficiency to a SMF was 3.8 dB with a coupling loss in the device of 0.6 dB.

4.2 Improving the Fabrication Tolerance for Resonant Couplers in an Asymmetric Twin Waveguide

Resonant coupling has the significant advantage of a shorter coupler length. Nevertheless, power has to be interchanged between the two guided modes. This effect causes a tighter fabrication tolerance because too much or not enough power transfer results in non optimum mode beating and coupling between the waveguides. Furthermore, the field distribution in both waveguides must be nearly symmetrical to enable maximum coupling efficiency, i.e. both waveguides must be in resonance.

4.2.1 Analysis of the Loss Factors for Adiabatic and Resonant Couplers

In a first step, divergences of the main factors such as refractive indices and waveguide width from their ideal values are analyzed relative to the coupling efficiency in a passive asymmetric twin waveguide (ATG). The coupling efficiency from the upper input to the lower output waveguide is simulated for resonant and adiabatic coupling.

The same ATG base structure as Fig. 4.1 is used. The underlying larger spot size waveguide is designed to be single mode and was mainly optimized for the TE mode. In Fig. 4.10(a) and Fig. 4.10(b) the adiabatic and resonant coupling waveguide dimensions can be seen. Both couplers have a 2.5 μm wide upper waveguide as their starting point. The total length for the adiabatic coupler is 450 μm and for the resonant coupler 211 μm. These two structures were also designed with simulation

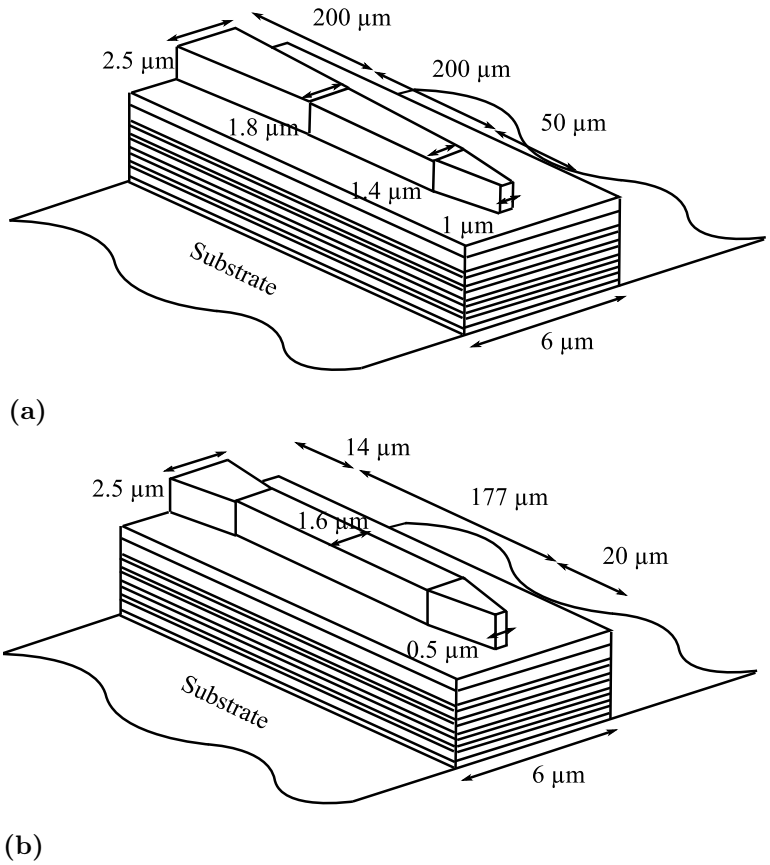


Figure 4.10: *Layout of the (a) adiabatic coupler and (b) the resonant coupler*

results obtained with Fimmprop. The input and output mode profiles for a TE mode are similar to Fig. 4.3. The difference of the propagation constants of the even and odd ($\Delta\beta = 0.048\ \mu\text{m}^{-1}$) mode is chosen to be large, so the even (fundamental) mode is initially mainly in the upper waveguide. In this case the underlying waveguide does not have a significant effect on the optical field in the upper waveguide. For example, the characteristics of a laser such as confinement factor and reflection at the mirrors is not affected by a lower large spot size waveguide. A side view of the field transition for a 450 μm long adiabatic coupler is shown in Fig. 4.11. Fig. 4.11 shows the transition of the field from the upper to the lower waveguide for an adiabatic transition. The coupler design of Fig. 4.10(a) is used. The coupler is split

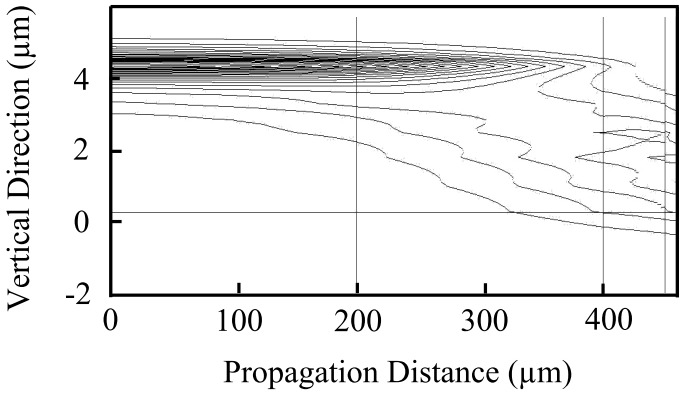


Figure 4.11: *Side view of the adiabatic coupler, contour plot of the field intensity distribution. The vertical lines correspond to section boundaries.*

into three different sections. In the first section (0 - 200 μm), the taper angle can be large, since the mode overlap of the even and odd mode is low. When the mode overlap increases (200 - 400 μm), the taper angle has to be small to prevent power transfer to the odd mode. The last taper (400 - 450 μm) can be steeper again. The width of the upper waveguide has to be reduced so that it does not support a mode anymore. In the output (450 - 460 μm) section, the upper cladding is removed and only the single mode lower waveguide remains. In Fig. 4.12 it can be observed that the transition loss is 1 % (0.04 dB). Although nearly 5 % of the power of the even mode is transferred to the odd mode when the two waveguides are at resonance, this power is not enough to cause recognizable mode beating, therefore this coupler is adiabatic.

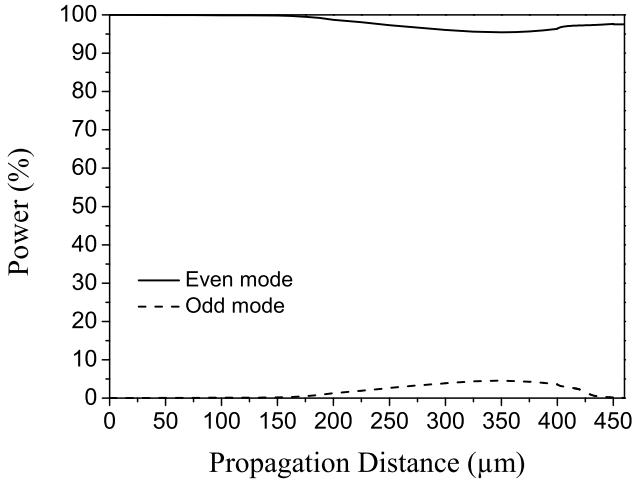


Figure 4.12: *Power distribution between even and odd mode for the adiabatic coupler. The power is in the even mode initially*

The resonant coupler design can be seen in Fig. 4.10(b). In Fig. 4.13 the field intensity distribution for the resonant coupler is shown. The device is divided into

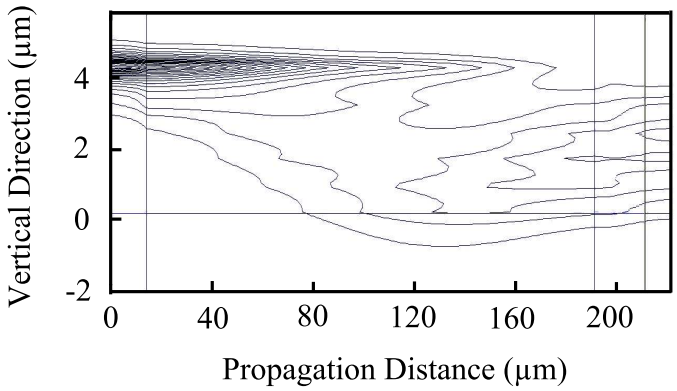


Figure 4.13: *Side view of the resonant coupler, contour plot of the field intensity distribution. The vertical lines correspond to section boundaries.*

three different sections. The first steep taper (0-14 μm) enables a power transfer from the even input mode to adjacent odd mode of nearly 30 % (Fig. 4.14). These two modes interfere in the straight mode beating section (14 - 191 μm), where the two waveguides are in resonance. The last taper (191 - 211 μm) guarantees that the upper waveguide is not supporting a mode at the end and that the mode power is transferred to the fundamental TE mode. In the resonant coupler the coupling from

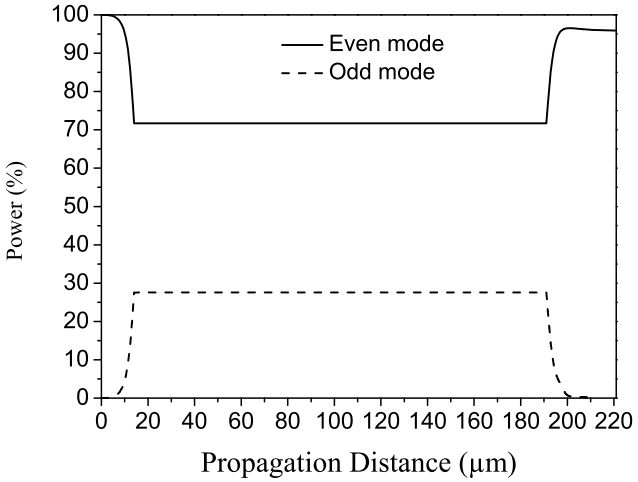


Figure 4.14: *Power distribution between even and odd mode for the resonant coupler. The power is in the even mode initially*

the smaller upper to the larger lower waveguide is accomplished by mode beating. The length of the resonant coupler (211 μm) can be shorter than the adiabatic one (450 μm) for our layer structure. Nevertheless, 96 % of the input power ends up in the output mode. For the adiabatic coupler this value is 98 %. In both cases an ideal waveguide with no additional losses, e.g. through surface roughness or impurity scattering, was assumed. In both simulations, the adiabatic and the resonant one, the back reflection at the interfaces is on the order of 10^{-9} and can be neglected.

A typical fabrication problem is a variation in the desired width of the waveguides. This can be caused by the lithography step or by the etching step of the waveguide. Therefore, the whole waveguide can be expected to be affected the same way. In Fig. 4.15 the remaining power of the fundamental TE/TM output mode for adiabatic and resonant coupling is displayed, with respect to a variation of the width of the upper waveguide. Resonant coupling allows only a width variation of $\pm$ 50 nm for the TE mode, otherwise the coupling efficiency is significantly reduced. For a ridge narrower than the ideal width, more power is transferred from the fundamental mode such that the transition of the optical field from the upper to the lower waveguide takes place in a shorter length. As the coupler is now longer than desired, some of the power is transferred back to the upper waveguide. If the ridge

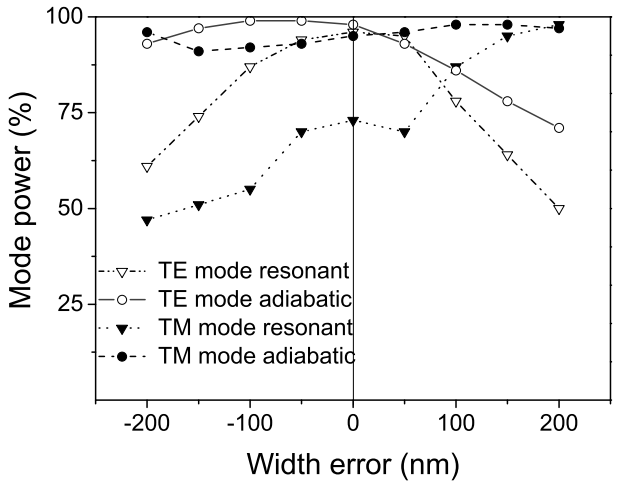


Figure 4.15: *Mode power in the output mode regarding to a upper waveguide width variation*

is wider than the ideal width, not enough power is transferred to the odd mode (Fig. 4.16). The field transition takes place only along the last taper and is not the result of mode beating (Fig. 4.16).

On the other hand, the adiabatic coupler is relatively insensitive to a narrower ridge. However, a wider ridge reduces the efficiency. This reduction is due to the fact that power remains in the upper waveguide and is lost at the transition to the output section. Nevertheless, the loss is not as high as for the resonant coupler. A further aspect that needs to be taken into account is possible errors in the refractive indices of the quaternaries. This depends on the compositions and, as the epitaxy of quaternaries is a challenging task with slightly different compositions, results in layers not having the intended refractive indexes. Here a deviation of the refractive index of the lower, diluted waveguide is analyzed. It can be seen from Fig. 4.18 that a small refractive index difference can cause large losses in the resonant case as both waveguides are no longer in resonance. The adiabatic coupler is nearly unaffected by such a change of the refractive index. For cases where the refractive index is three or more percent lower, large losses take place. This is caused by the diluted waveguide being close to cut-off and therefore the fundamental mode overlapping with radiation modes.

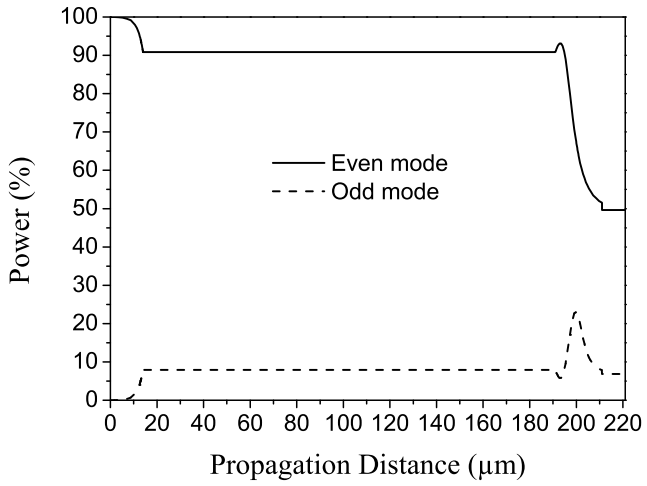


Figure 4.16: *Power distribution between even and odd mode for the 200 nm wider resonant coupler*

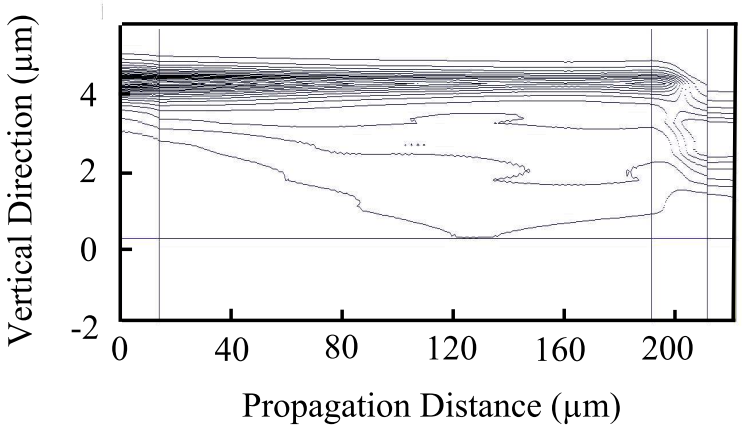


Figure 4.17: *Side view of the 200 nm wider resonant coupler, contour plot of the field intensity distribution. The vertical lines correspond to section boundaries.*

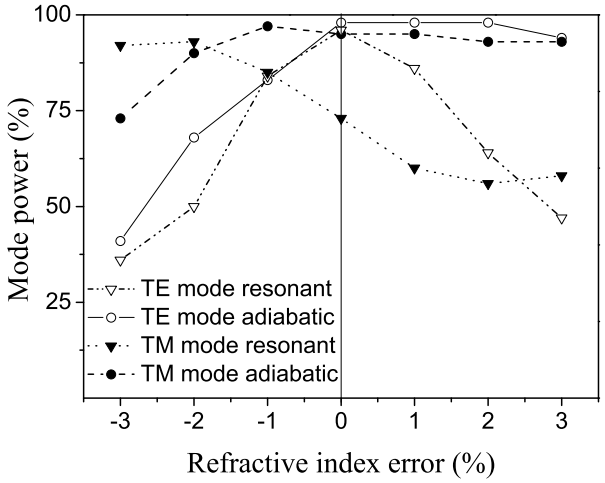


Figure 4.18: *Mode power in the output mode regarding to a lower waveguide refractive index variation*

4.2.2 Tapering the Mode Beating Section

Before resonant coupling can be practically used in PICs, the fabrication tolerances need to be improved. For a given layer composition, tapering the mode beating section was proposed [97]. In that case the taper slope is intended to be kept as small as possible. The fabrication minimum slope is considered to be 90 nm/100 μm. A taper with a starting width of 1 μm and an end width of 0.81 μm was shown. Additionally, the whole taper length needed to be increased from 143 μm to 173 μm.

Different slopes for the mode beating section from an initial and final width difference (ΔW_d) of 200 nm to 700 nm were investigated in [117]. The length of the mode beating section still was at 177 μm. The coupling efficiencies of the straight and slightly sloped (ΔW_d = 200 nm) resonant couplers are shown in Fig. 4.19. An improvement in tolerance can be realized by introducing the tapered mode beating section. In a first step the efficiencies of different ΔW_ds, the difference between the start and the end width of the mode beating section are investigated. In Fig. 4.20 the coupling efficiency for different taper start and end width differences for the intended design and for width variations of $\pm$ 100 nm is shown. It can be determined that a waveguide design that tapers by 500 nm results in the best fabrication

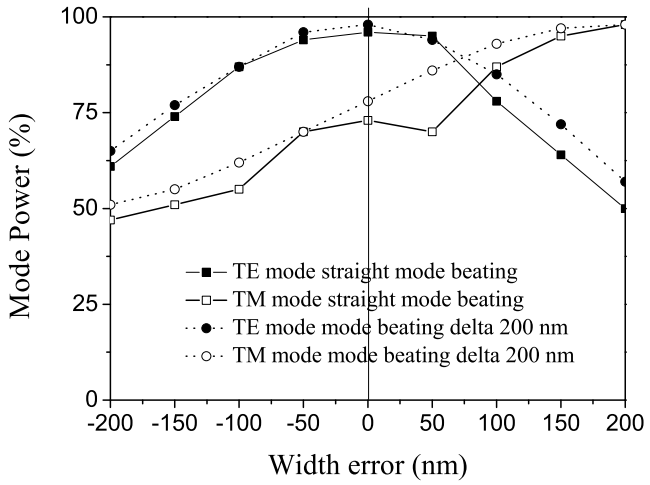


Figure 4.19: *Comparison of the mode power of the output mode of a straight resonant coupler to one with* ΔW_d *= 200 nm*

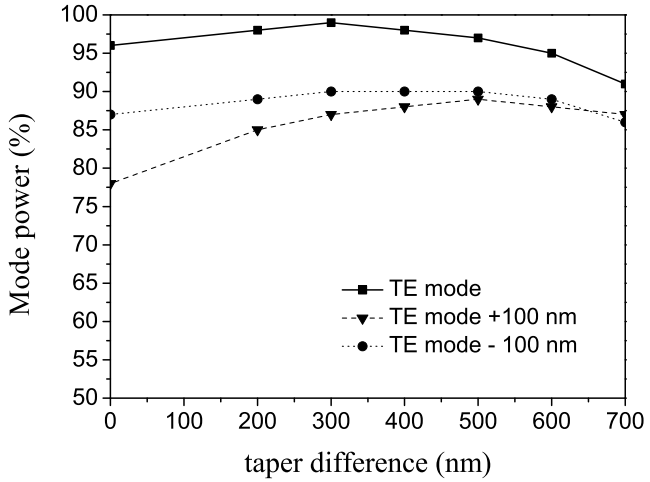


Figure 4.20: *Mode power of the output mode for different* ΔW_d*s. The ideal case and a* $\pm$*100 nm variation are displayed*

tolerance without affecting the efficiency for the intended waveguide dimensions. By looking at the power distribution between the even and odd mode (not shown), it can be observed that power is transferred along the whole device. In Fig. 4.21 the minimal taper difference of 200 nm is compared to the difference of 500 nm. It can be seen that the fabrication tolerance relative to a width error can be improved. Assuming the ΔW_d = 500 nm design, the tolerance relative to the refractive index

deviation can also be improved (Fig. 4.22).

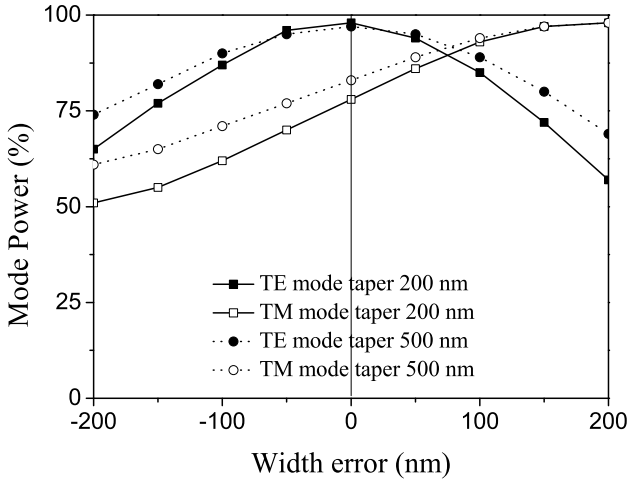


Figure 4.21: *Mode power of the output mode for ΔW_d = 200 and 500 nm*

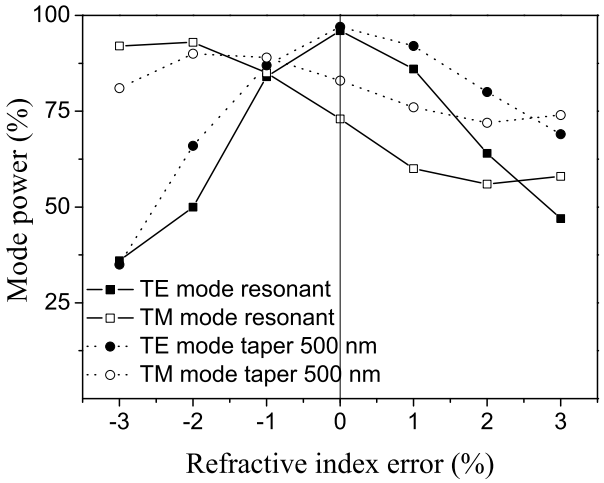


Figure 4.22: *Mode power of the output mode regarding to a lower waveguide refractive index variation for a straight and a ΔW_d = 500 nm mode beating section*

4.3 Conclusion

The methods of adiabatic and resonant coupling have been explained. Techniques have been outlined to design an optimum shaped adiabatic taper. It was set out how the resonance points of a taper can be found by plotting the propagation

constants of the two guided modes. This facilitates to adjustment of the taper length to either allow or avoid power transfer along the taper. It was shown that resonant coupling is more sensitive to deviations during the fabrication process (e.g. refractive indices, waveguide widths) than adiabatic coupling. An improvement of the fabrication tolerance for resonant coupler was demonstrated by tapering the mode beating section.

Chapter 5

Polarization Filter and Splitter

In this chapter it is explained how resonant coupling enables a polarization filter mechanism in the previously shown ATG structure. The concept can be further expanded to a polarization splitter. In this chapter modelling results obtained with Fimmwave/Fimmmprop are shown. In the following chapter fabricated polarizers are characterized.

5.1 Data Communication and Photonic Integrated Circuits

The demand for increased bandwidth in optical communication systems has pushed the need for higher information spectral densities. The adoption of polarization shift keying [118] and polarization diversity multiplexing [119] has created the need for polarization handling and manipulation in semiconductor waveguides. Different approaches to designing TE- and TM-pass polarizers have already been demonstrated. One way to realize a polarizer is to make use of the high birefringence of a material. Polarizers based on lithium niobate [120] or polymers [121] have been demonstrated (Tab. 5.6). For InGaAsP/InP based systems different designs of polarization splitters have been shown. Soldano et al. [122] demonstrated a polarization splitter based on a Mach-Zehnder interferometer (Tab. 5.2). The optical field was split into two arms by a 3-dB multi-mode interference (MMI) coupler. A

relative phase shift of π was introduced only to the TM-polarization in one arm by loading it with a dielectric (SiO_2) and a metal layer on top. The phase shift causes the TM-polarization to exit a second 3-dB coupler from a different port than the TE-polarization. However, for photonic integrated circuits (PICs), multiple

Table 5.1: *Polarizer properties at a wavelength of 1.55 μm*

Material system				
$LiNbO_3$ [120]				
Polarizer type	PER (dB)	Prop. loss (dB)	Length (μm)	Coupling loss (dB)
TM-pass	26	1.2	1500	not mentioned
Material system				
Polymers [121]				
Polarizer type	PER (dB)	Prop. loss (dB)	Length (μm)	Coupling loss (dB)
TM-pass	35	≈ 0.5	6200	2.7 to 4.0
TE-pass	40	1.2	7000	2.7 to 4.0

Table 5.2: *Polarization splitter properties at a wavelength of 1.55 μm*

Material system			
InGaAsP/InP [122]			
Polarization type	PER (dB)	Insertion loss (dB)	Length (μm)
TE	16	1.2	2610
TM	13		

components have to be easily integrable with InGaAsP/InP systems to simplify and therefore reduce the cost of packaging. The asymmetric twin waveguide (ATG) offers a good opportunity for direct fiber coupling and integration of different active components such as semiconductor optical amplifiers, lasers and photodiodes (Chapter 2.3).

Here, the birefringence present in an ATG and resonant coupling are used to implement a polarization filter. A modelled power extinction ratio (PER) of 20 dB for the TE mode and more than 10 dB for the TM mode are obtained for a TE/TM filter with a length of less than 400 μm. The filter could be repeated several times to improve the selectivity. A concept is shown of how the polarizer can be modified into a beam splitter by introducing an S-bend into the upper cladding and into the lower waveguide. Additionally, the concept is based on the already outlined ATG with one waveguide designed to improve fiber coupling.

5.2 Asymmetric Twin Waveguide and Resonant Coupling

The layer configuration of the ATG, starting from the substrate, is similar to the previously explained structure (Fig. 4.1). The lower, nearly 5 μm spot size, waveguide enables enables low loss butt coupling from and to a lens-ended or cleaved single mode fibers. The waveguide acts as a single mode waveguide. Additionally, the waveguide is configured to support only the fundamental TE- and TM-modes.

The upper waveguide has a higher effective refractive index than the diluted waveguide for an upper cladding width of 2.5 μm. The upper waveguide by itself is also a single mode waveguide. Therefore, both waveguides together guide the even and odd modes for both polarizations. The effective refractive index of the upper waveguide can be reduced by decreasing the width of the upper cladding. The width at which both waveguides, taken separately, have the same propagation constant is the resonance point. At that point the difference of the even and odd mode propagation constants is minimal. Furthermore, the spatial overlap of the even and odd modes is at a maximum. Therefore a small change of the waveguide geometry results in power transfer from the even to the odd mode. That effect is intended for resonant coupling, because the mode beating of both modes transfers the optical field from the lower to the upper waveguide and vice versa. Since the ATG is birefringent, the resonance point for the TE- and the TM-modes is reached at different widths of the upper waveguide, namely 1.6 μm for the TE- and 1.8 μm

for the TM-polarization. Finally, the width of the upper waveguide can be so small that it no longer guides modes. In that case the structure is a single mode waveguide and the optical field is mainly in the lower waveguide. At a width of 1 μm a low loss transition of the optical field to the output section, where the upper cladding is removed, is possible.

5.3 TE/TM-Pass Polarizer

Fig. 5.1 shows a schematic of a TM-pass polarizer. The section without the

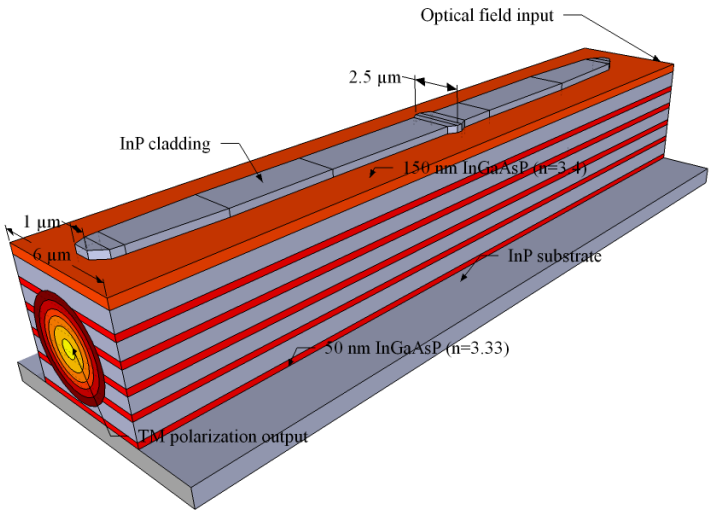


Figure 5.1: *Schematic of the TM-pass polarizer*

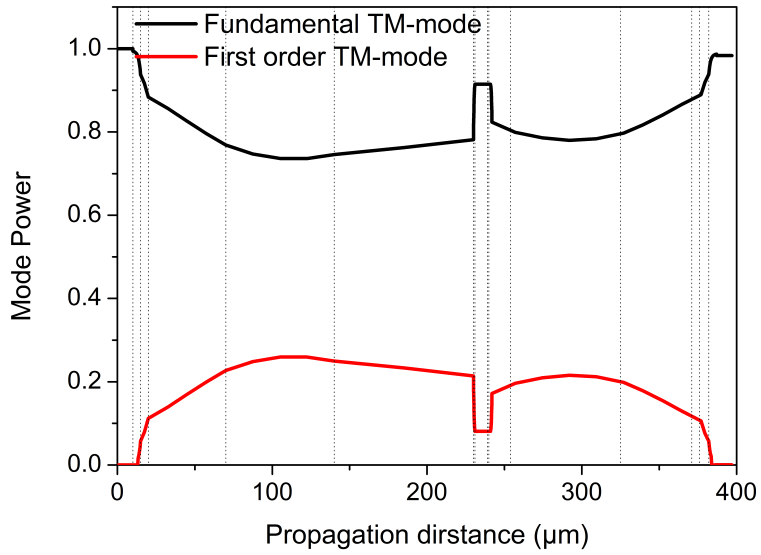
upper cladding is the input section for a randomly polarized optical field. The design principle has to guarantee that the TM-polarization couples to the upper waveguide and then back to the lower waveguide. On the other hand the power of the TE-polarization has to be transferred to substrate modes instead of the fundamental mode in the output section. This can be achieved by the lateral tapering of the upper waveguide cladding as listed in Tab. 5.3.

The coupler is designed such that for the TM-polarization only around 30 % of the input power is transferred to the first order mode by step tapers at a z-distance of 100 μm (Fig. 5.2(a)). The resonance point for a width of 1.8 μm lies roughly at this distance. For the TE-polarization on the other hand, the first steep taper, with an end width of 1.55 μm, and the second taper causes a power transfer of more than

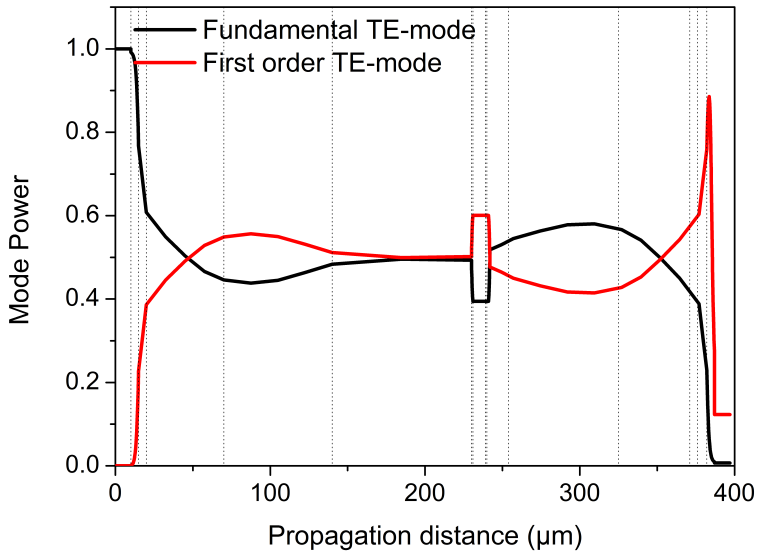
Table 5.3: *Configuration of the 372 μm long TM-pass polarizer.*

section no.	start-width (μm)	end-width (μm)	length (μm)
1	1.00	1.55	5.00
2	1.55	1.65	5.00
3	1.65	1.80	50.00
4	1.80	1.95	70.00
5	1.95	2.10	90.00
6	2.10	2.50	1.00
7	2.50	2.50	3.00
8	2.50	2.10	1.00
9	2.10	1.95	17.00
10	1.95	1.80	70.00
11	1.80	1.65	50.00
12	1.65	1.55	5.00
13	1.55	1.00	5.00

55 % to the first order mode (Fig. 5.2(b)). This results in a shorter coupling distance to the upper waveguide for the TE- than for the TM-polarization. Fig. 5.3 shows that the TM-field couples upwards and then smoothly downwards into the output waveguide. However, the TE-field is already in the upper waveguide at the center of the up-tapered section, couples back to the lower waveguide at the maximum width of the upper ridge, then couples a second time to the upper waveguide and finally is coupled to radiation modes (5.4). This larger power transfer can be explained by the resonance point being at a width of 1.6 μm. The step increase to this point enables a significant power transfer since the fundamental and first order TE-modes have a large spatial overlap. It can be observed that the TM-polarization couples to the upper waveguide at the center of the polarizer and back to the lower waveguide at the right end. 98 % of the input power of the TM-polarization reaches the right



(a)



(b)

Figure 5.2: *Power distribution along the TM-pass polarizer. The vertical lines correspond to the section boundaries of Tab. 5.3, additional there is a 10 µm long in- and output section. (a) Input: fundamental TM-mode, (b) Input: fundamental TE-mode.*

output. For the TE-polarization, on the other hand, the optical field is in the upper waveguide before the last taper. The steep last taper (no. 13) causes the power to be transferred into the first higher order mode and finally to substrate modes (Fig.

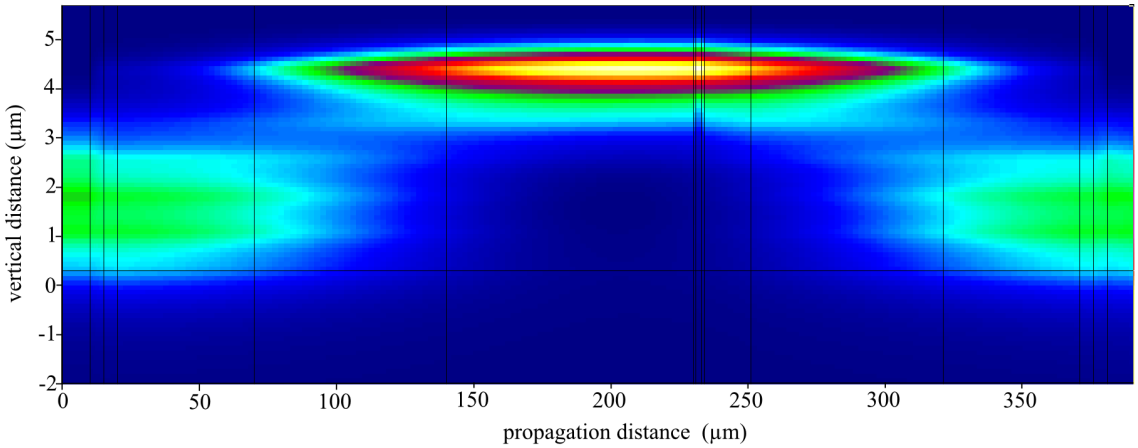


Figure 5.3: *Side view of the intensity distribution of the TM-field, the input is on the left side in the lower waveguide. The vertical lines correspond to section boundaries.*

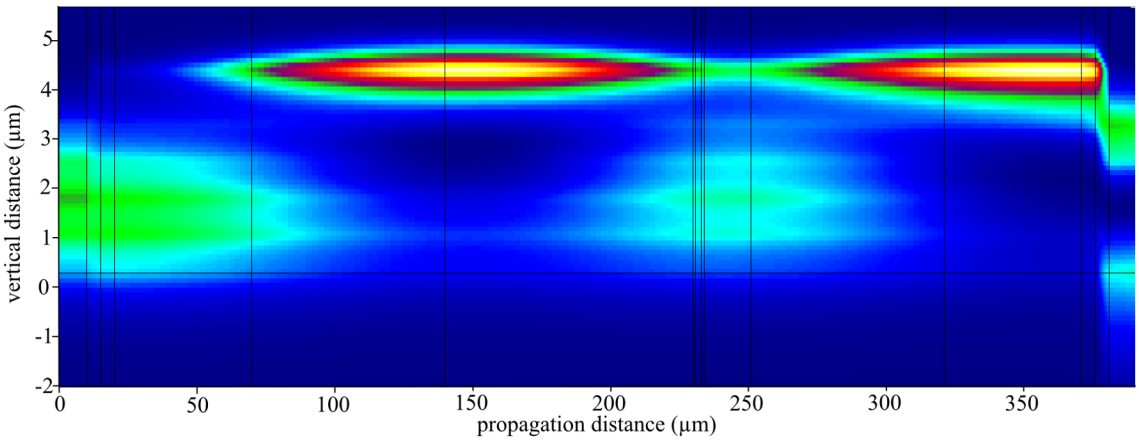


Figure 5.4: *Side view of the intensity distribution of the TE-field, the input is on the left side in the lower waveguide. The vertical lines correspond to section boundaries.*

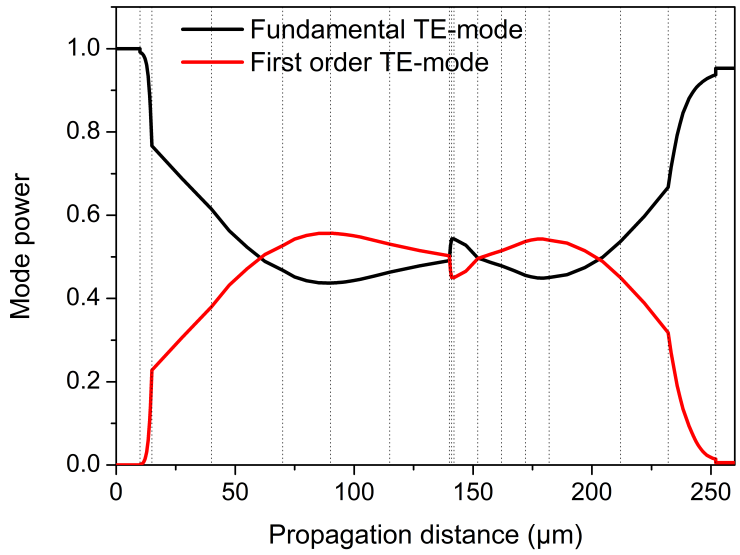
5.2. Only 1 % of the input power stays in the fundamental TE-mode at the output for a 372 μm long device.

The same principle can be used to construct a TE-pass polarizer (Tab. 5.4). The shorter coupling length of the TE- relative to the TM-polarization can now be

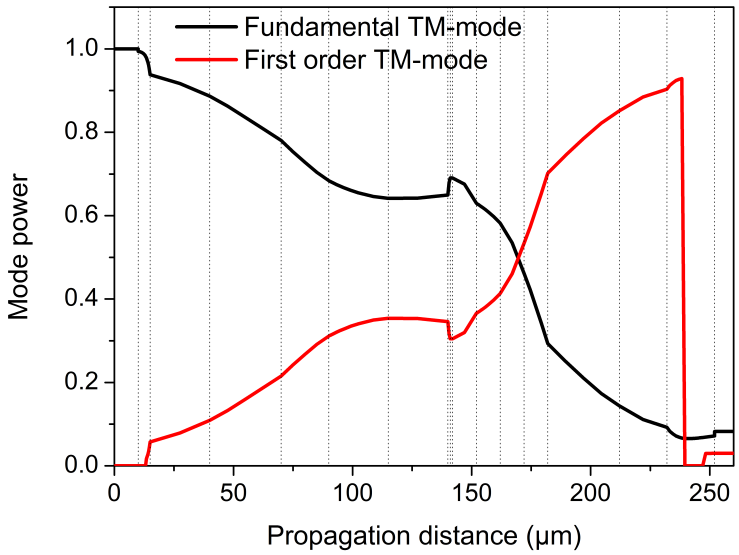
Table 5.4: *Configuration of the 242 μm long TE-pass polarizer.*

section no.	start-width (μm)	end-width (μm)	length (μm)
1	1.00	1.55	5.00
2	1.55	1.65	25.00
3	1.65	1.80	30.00
4	1.80	1.95	20.00
5	1.95	2.10	25.00
6	2.10	2.20	25.00
7	2.20	2.50	1.00
8	2.50	2.50	1.00
9	2.50	2.20	10.00
10	2.20	2.10	10.00
11	2.10	1.95	10.00
12	1.95	1.80	10.00
13	1.80	1.65	30.00
14	1.65	1.55	20.00
15	1.55	1.00	20.00

utilized to couple the TE-field back to the output waveguide, whereas the TM-field remains in the upper waveguide. The power transfer for the TE-polarization (Fig. 5.5(a)) is similar to the TM-pass polarizer. However, around the resonance point of the TM-polarization the taper is now steeper and further power transfer is provoked (Fig. 5.5(b)). By a reduction of the total coupler length and by a decrease of the



(a)



(b)

Figure 5.5: *Power distribution along the TE-pass polarizer. The vertical lines correspond to section boundaries. (a) Input: fundamental TE-mode, (b) Input: fundamental TM-mode.*

power in the fundamental TM mode, the coupling efficiency to the fundamental TM output mode is reduced. Figure 5.6 illustrates that TE-polarization couples efficiently to the fundamental TE output mode. On the other hand, the TM-field remains in the upper waveguide before the last taper section is reached (Fig. 5.7).

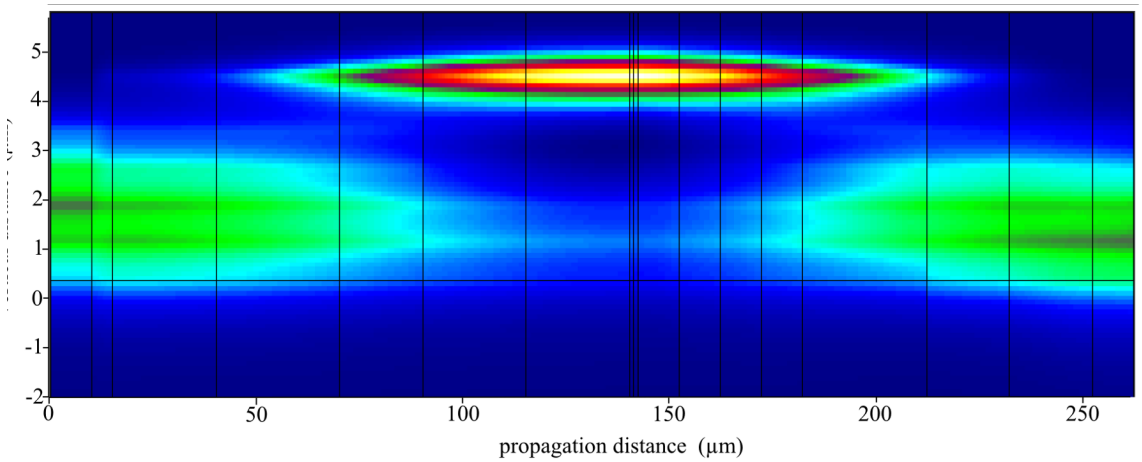


Figure 5.6: *Side view of the intensity distribution of the TM-field, the input is on the left side in the lower waveguide. The vertical lines correspond to section boundaries.*

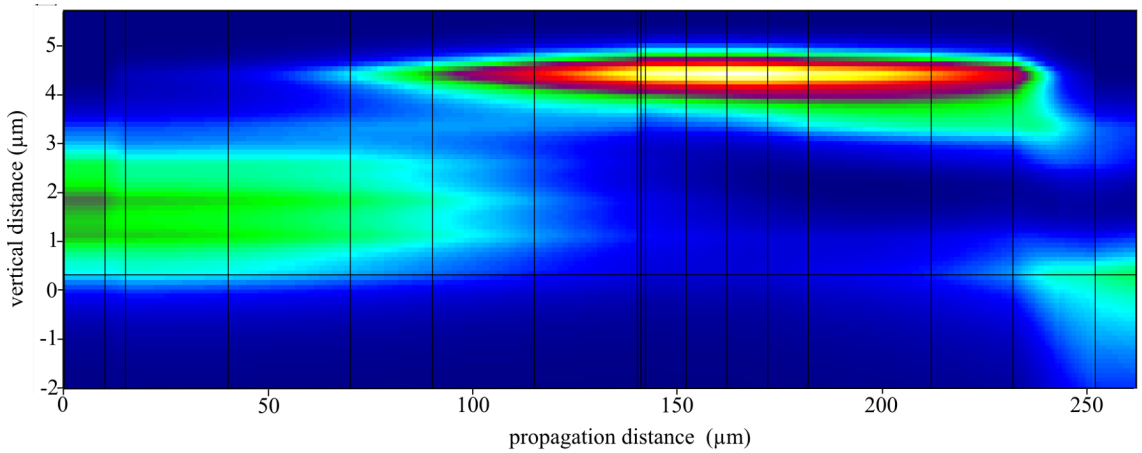


Figure 5.7: *Side view of the intensity distribution of the TM-field, the input is on the left side in the lower waveguide. The vertical lines correspond to section boundaries.*

Additionally, the TM-field power is mainly in the first higher order mode (Fig. 5.5(b)). Further power transfer from the fundamental to the first higher order mode is provake by the steep last taper. The first higher order mode has its cut-off point width in the last taper section and the TM-field power is finally coupled to substrate modes. For a 242 μm long taper section 95 % of the TE-input power reaches the output, whereas for the TM case the value is only 8 %. A larger difference between the cut-off widths of both polarizations should allow to improve the TE/TM power extinction ratio (PER) because a step taper for TM-polarization at its cut-off does have a reduced effect on the TE-polarization.

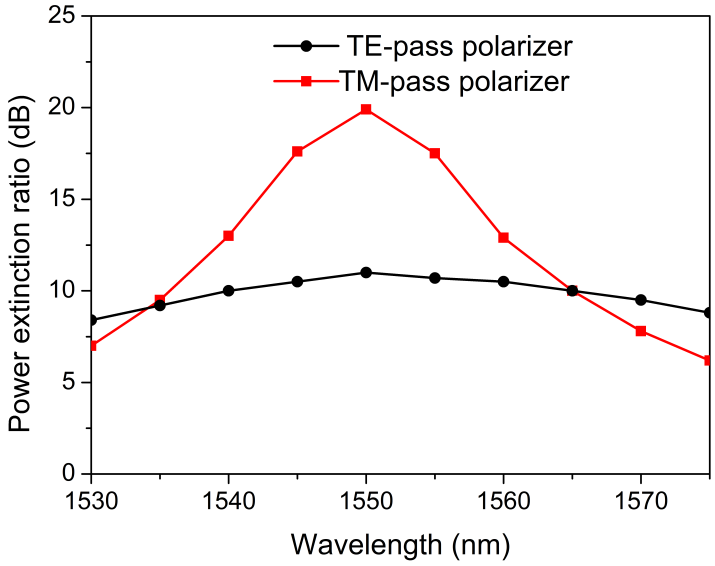


Figure 5.8: *Power extinction ratio for the TM- and TE-pass polarizer.*

In Fig. 5.8 a 10 dB PER from 1540 nm to 1565 nm can be seen for both polarizers. This makes the polarizers suitable at the telecommunication wavelength of 1.55 μm. An ATG with a larger birefringence and a larger difference of resonance points width of the upper waveguide should increase the bandwidth. Because a step taper around the resonance point, necessary for power transfer from the fundamental to the first order mode of one polarization, a key aspect of this filter mechanism, has a reduced effect on the other polarization.

Although the PERs are 20 dB (TM-pass) and 11 dB (TE-pass) for a single device, the structure can be easily repeated several times. A fivefold repetition of the TM-pass polarizer, length 379 μm, and a nine fold repetition of the TE-pass polarizer, length 242 μm, result in a PER of 100 dB over a total device length of less than 2 mm and 2.2 mm respectively. This is an improvement of the PER/length ratio of at least a factor of three compared to the references in Tab. 5.6.

5.4 Polarization Splitter

The fact that the two different polarization states are present in two different, vertically separated waveguides at the same point gives the opportunity to construct

a polarization splitter. The first section is similar to the TM-pass polarizer, but tapers from 1.0 μm to 1.35 μm and from 1.65 μm to 1.75 μm are inserted. The tapers to 2.5 μm are replaced by a 2.1 μm wide 120 μm long straight section, and the end width of the last taper is 1.45 μm Fig. 5.9. Furthermore, the section lengths are slightly modified. The maximum taper width of 2.5 μm was replaced by

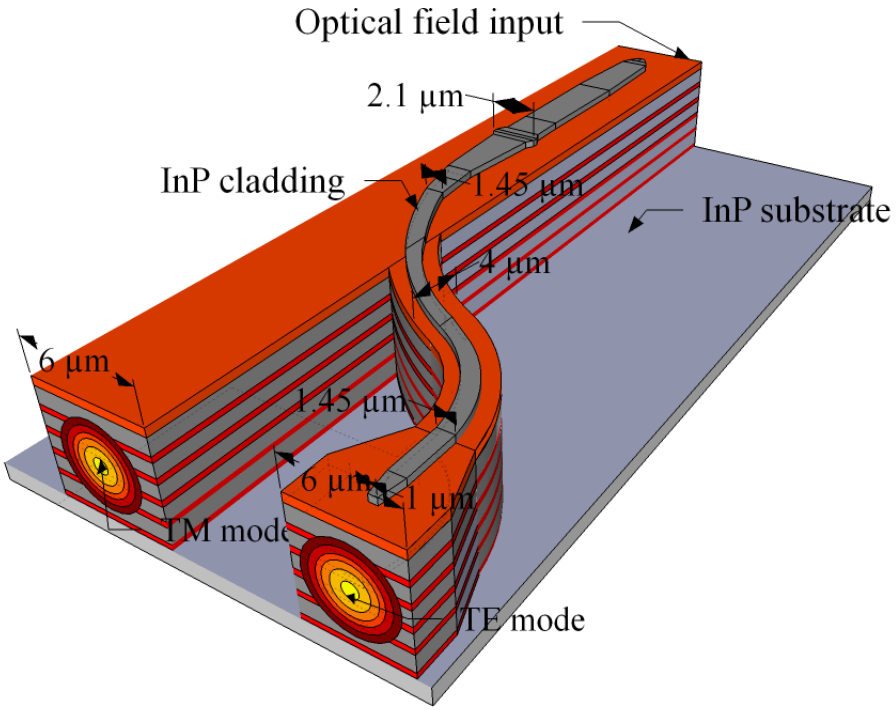


Figure 5.9: *Sketch of the polarization splitter*

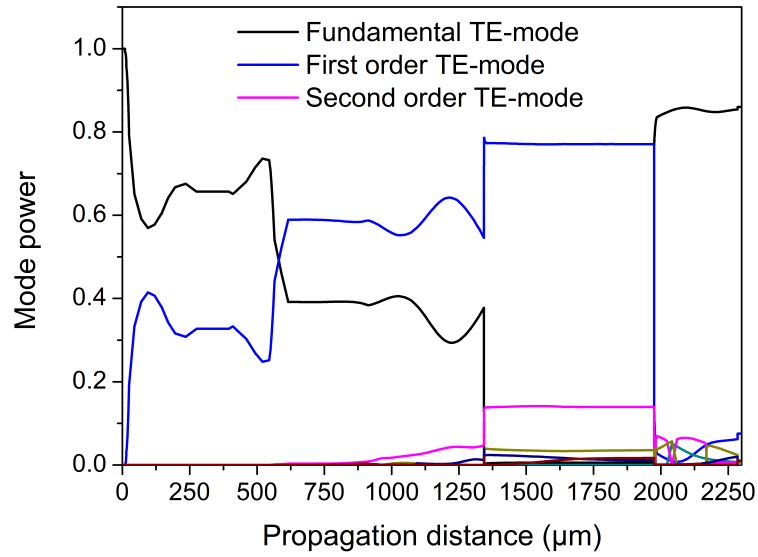
a width of 2.5 μm because the wider taper did not have any effect on the amount of power transferred from the fundamental to the first order mode. The amount of power transferred from the fundamental to the first higher order mode in the section tapered up from 2.1 μm to 2.5 μm, was back transferred in the following tapered down section (Fig. 5.2 and 5.5). In the straight section there is not any power transfer among waveguide modes. However, because power was already transferred previously, mode beating of the fundamental and first order modes occurs. The straight section allows to control the optical field position in the ATG. Power transfer from the fundamental mode to the first order mode for both polarizations is induced in the first sector of the device (Fig. 5.10). Nevertheless, for the TE-polarization this transfer is much larger. Furthermore, more power is in the first order mode than in the fundamental mode. The intensity of the first order mode is mainly located

Table 5.5: *Configuration of the 605 μm long first sector in the polarization splitter.*

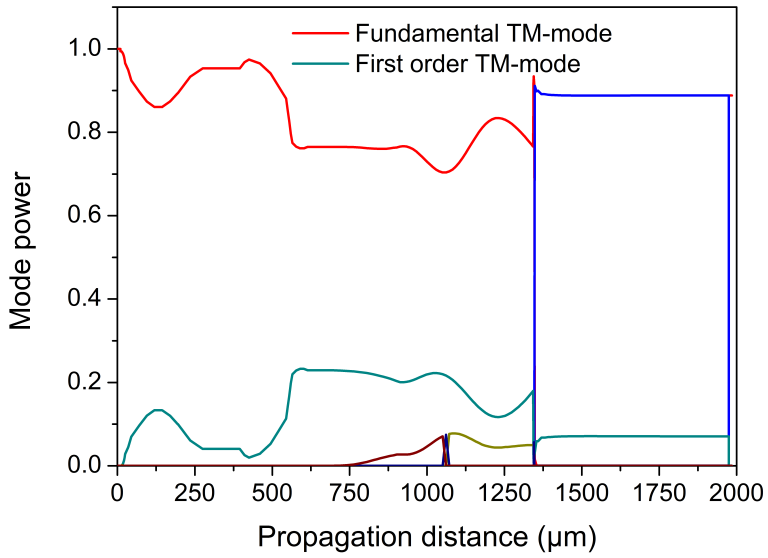
section no.	start-width (μm)	end-width (μm)	length (μm)
1	1.00	1.35	5.00
2	1.35	1.55	10.00
3	1.55	1.65	20.00
4	1.65	1.75	50.00
5	1.75	1.85	50.00
6	1.85	1.95	50.00
7	1.95	2.10	80.00
8	2.10	2.10	120.00
9	2.10	1.95	30.00
10	1.95	1.85	70.00
11	1.85	1.75	50.00
12	1.75	1.65	10.00
13	1.65	1.55	30.00
14	1.55	1.45	20.00

around the upper waveguide ridge (Fig. 5.11(b)), whereas for the TM-polarization the power is mainly in the fundamental modes. This simplifies the polarization splitting. After this point, the lower waveguide is split by an S-bend into a 4 μm wide branch port and a 6 μm wide straight port. The upper cladding of 1.45 μm follows the branch 4 μm port. As the splitting takes place over a long distance of 1360 μm, very little additional power is transferred among the modes. The increase of the width of the lower waveguide results in the creation of an even and odd mode profile in the horizontal direction as well (Fig. 5.11). This allows mode beating in lateral direction and a similar behavior as a directional coupler (Chapter 4.1.3).

The S-bend adds a lateral asymmetry to the waveguide. The TE-polarization



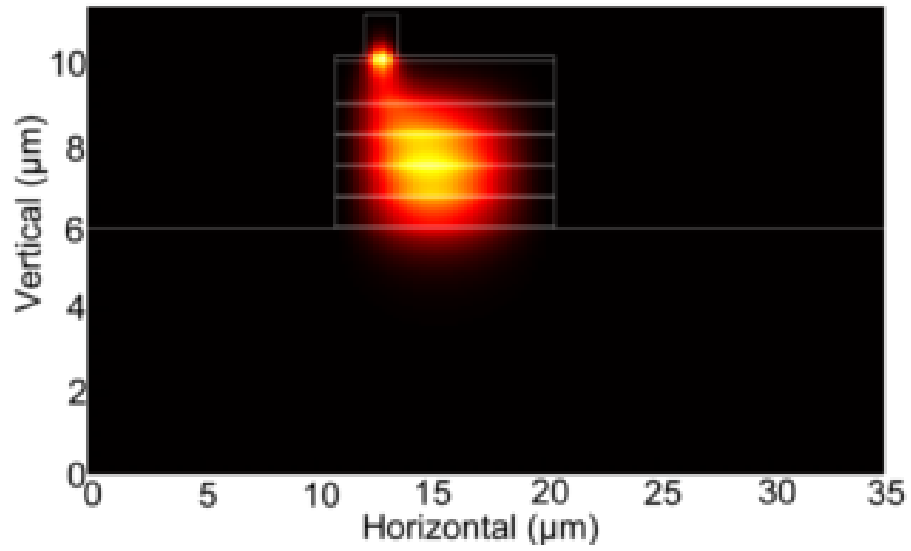
(a)



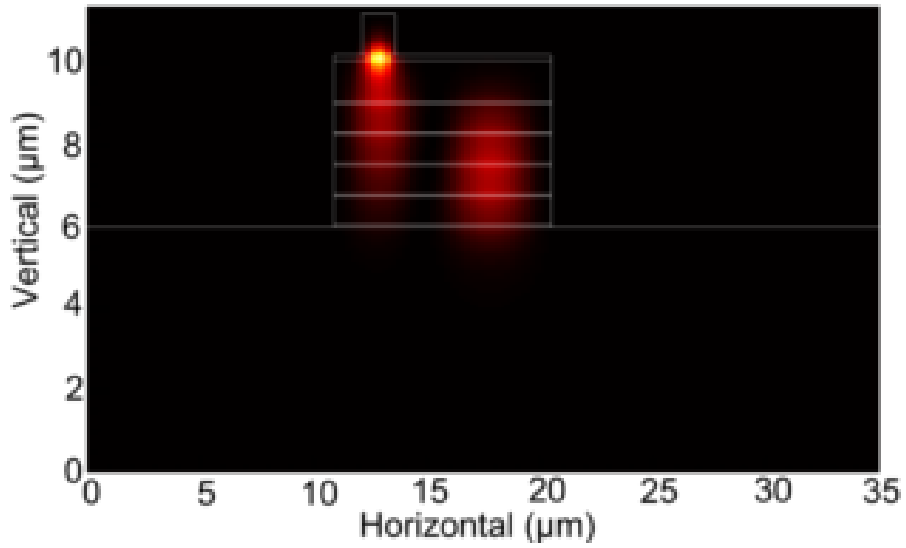
(b)

Figure 5.10: *Power distribution among the modes for the polarization splitter (a) Input is the fundamental TE-mode, (b) Input is the fundamental TM-mode*

located mainly in the 1.45 μm wide upper waveguide is guided by this S-bend, whereas the TM-polarization is mainly in the lower waveguide. Due to the different field position at the start of the S-bend and due to higher power in the first order mode of the TE-polarization, the TE-polarization can couple to the 4 μm wide port,



(a)



(b)

Figure 5.11: *Intensity distribution of the TE-polarization at a z-position of 690 µm in the splitter section (a) fundamental mode, (b) first order mode*

whereas the TM-polarization stays in the straight port. To have a similar output, the 4 μm wide port is tapered up to 6 μm, the upper cladding tapered down to 1 μm and then vanishes at the end. The change of the polarization order at 1360 μm is due to the simulation tool used. Only the position in the evaluated mode list changes when there are now two vertically separated waveguides present.

Figures 5.12 and 5.13 show the intensity distribution of the TE- and TM-polarizations. 85 % of the input TE- and only 6 % of the TM-polarization reach the upper output

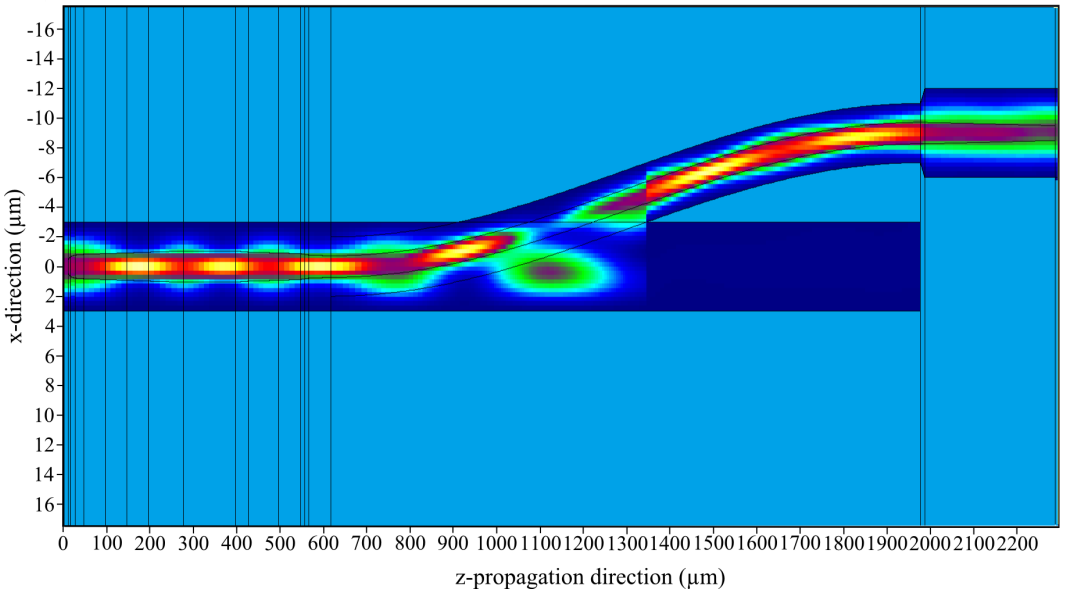


Figure 5.12: *Plan view of the intensity distribution for the TE-polarization*

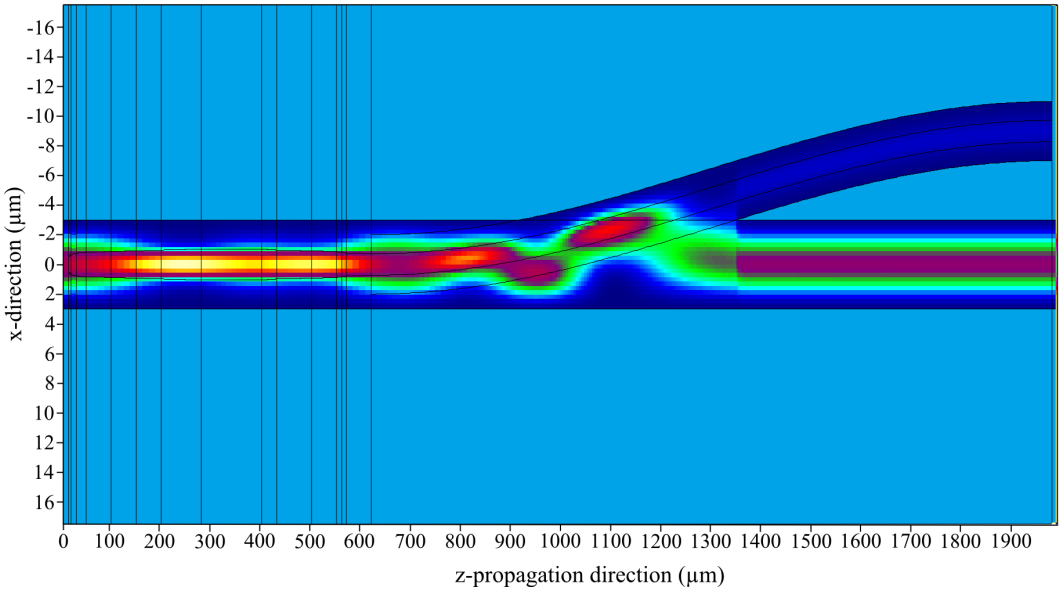


Figure 5.13: *Plan view of the intensity distribution for the TM-polarization*

port. At the lower port, 88 % of the TM- and 1 % of the TE-polarization remain according to the calculation. The total calculated losses along the device are 3 and 6 %.

In Fig. 5.14 a relative PER of 10 dB can be seen from 1530 nm to nearly 1560 nm for both polarizations. Because the lower waveguide has large dimension, all modes have only a small propagation constant difference and the beat length is

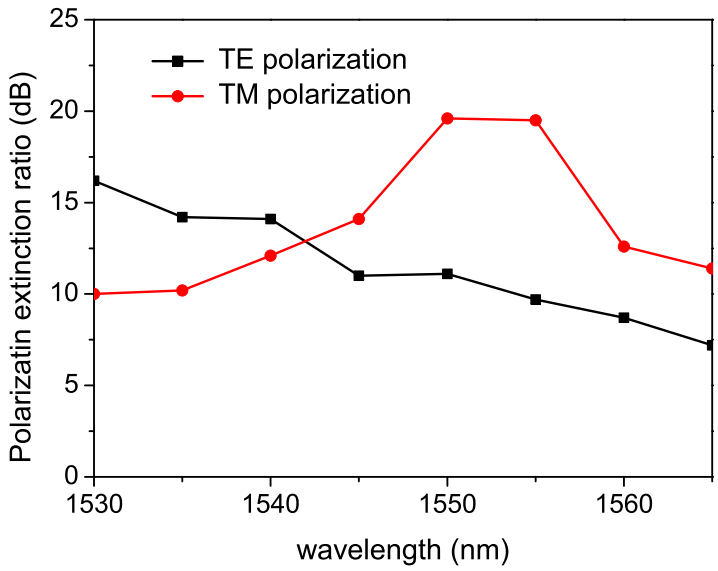


Figure 5.14: *Relative power extinction ratio versus wavelength for the polarization splitter*

long. However, the outlined principle can also be used in an ATG with two small spot size waveguides. This should reduce the length of the splitter. An additional polarizer (Section 5.3) at each output can further suppress the unwanted polarization state.

5.5 Conclusion

The birefringence in the analyzed ATG can be used to design polarizers with a length of less than 400 μm and a PER of 20 and 10 dB for the TE- and TM-polarization respectively. The integration of such a polarizer onto the input waveguide ridge is easy. Therefore, several of these polarizer can be placed one after another to increase the PER.

In Chapter 6 it will be shown that the polarizer principle based on resonant coupling in an ATG can be realized practically.

It is further explained that the same ATG also allows polarization splitting. Nevertheless, the practical realization of such a device is more complicated because of the slowly changing geometry and the small waveguide spacing at the splitting section.

Table 5.6: *Simulation results of the polarizers and the polarization splitter.*

Polarizers			
	PER (dB)	length (μm)	
TM-pass	20	372	
TE-pass	10	242	
bandwidth (PER >10 dB)	1540–1565		
Polarization splitter			
	TE-port (%)	TM-port (%)	length (μm)
TE-polarization	85	6	2300
TM-polarization	1	88	
bandwidth (PER >10 dB)	1530–1560		

Chapter 6

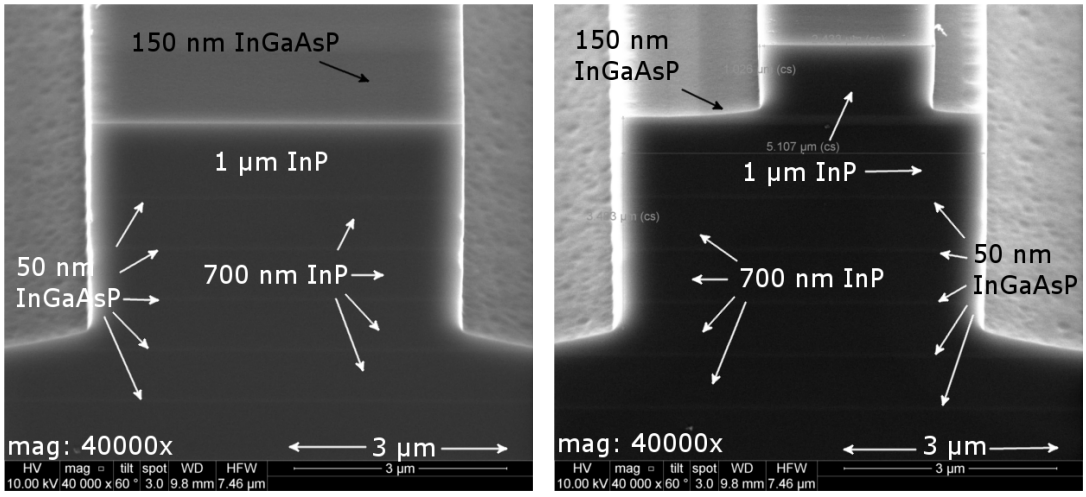
Characterization of the Polarization Filters

In Chapter 5, the simulation results of polarization filters were shown. In this chapter, the layout of the fabricated chip and the measurement setup are described. Finally, two polarization filters are presented, one of which worked as a TM-pass polarizer, and the other as a TE-pass polarizer at 1610 nm.

6.1 Layout and Fabrication Steps of the Polarizations Filters

The epi-structure (Fig. 6.1, growth A0887 (Appendix)) and the polarizer designs were intended to be identical to the simulated polarizers in Chapter 5. The designs of the TM-pass and TE-pass polarizers were shown in Tabs. 5.3 and 5.4 respectively. Two different regions were fabricated on a single chip. One region consisted only of TE-pass polarizers and the second consisted only of TM-pass polarizers. Each region was approximately 4 mm long. At both ends were 1 mm long regions with only the lower waveguide that permitted cleaving the chip at these locations.

Each TE- and TM-pass region was divided into four different subregions. In one subregion was a single polarizer. In the second subregion the polarizer was repeated a second time with a intended spacing of approximately 280 μm between them.



(a) **(b)**

Figure 6.1: *SEM cross-section images (a) of the single mode input waveguide, (b) of the ATG with an upper InP cladding width of 2.5 µm.*

The third subregion had also two polarizers. However, the spacing between both polarizer was intended to be around 1150 μm. The fourth and final subregion had four consecutive polarizers.

Each subregion was designed with different widths of the upper waveguide coupler. The ideal width was changed in 100 nm steps over a 600 nm range. The minimum width was 300 nm narrower and the maximum width 300 nm wider than the ideal case in Tabs. 5.3 and 5.4 respectively. Each coupler was labeled to identify its design (Fig. 9.37(a)).

Each width subsection had a single lower waveguide with the same length than the polarizers. This lower waveguide allowed to measure the waveguide losses.

Polarization filters were fabricated using the developed SAPSIOTIM fabrication steps (Chapter 9).

A waveguide similar to Fig. 6.1(a) was the input waveguide. Fig. 6.1(b) shows an ATG with an upper cladding width of around 2.5 μm. Although the upper cladding is laterally slightly misaligned, simulations showed that the propagation constants of the even and odd modes did not change significantly ($\Delta\beta(TEideal - TEmisalig.) \approx 0.002\mu m^{-1}$). Therefore, this misalignment has only negligible effect on the polarizer.

However, variations of the bandgap properties of the quaternaries with those

intended occurred. The PL measurements showed peaks at 1.06 eV (λ_g = 1170 nm) and 0.92 eV (λ_g = 1350 nm) with a full width at half maximum (FWHM) of 40 meV and 90 meV. The FWHM of the 50 nm thick InGaAsP (λ_g = 1170 nm) equals the standard values (Chapter 8). However, the wider bandgap of the 50 nm thick InGaAsP layer causes a reduction of the refractive index. The 150 nm thick InGaAsP (λ_g = 1350 nm) composition has a slightly lower bandgap, and significantly the FWHM at room temperature was more than twice the reported standard value (Chapter 8). Therefore, the refractive indices of the epi-material are different than intended. Furthermore, the lower waveguide width reduction of nearly 800 nm had a small effect on the propagation constants. The propagation constants of both polarizations were approximately reduced by 0.01 μm^{-1}. Consequently, the resonance widths of both polarizations are not at 1.6 and 1.8 μm anymore. This resulted in a different power transfer between the even and odd modes, different mode beating and a different filter performance.

Fimmprop simulation results of a TM-pass filter (Tab. 5.3) are presented in Figs. 6.3 and 6.2 with refractive indices adjusted to 3.30 and 3.45 for the 50 nm (λ_g = 1170 nm) and 150 nm thick InGaAsP (λ_g = 1350 nm) refractive indices. The refractive index of 3.30 corresponds to the refractive index measured in Chapter 8, whereas the second index is an approximation. Additionally, the waveguide dimensions were changed to values similar to Figs. 6.1 and 6.7.

In Fig. 6.2 it can be observed that the TE-polarization couples three times to the upper waveguide and finally couples to substrate modes. On the other hand the TM-polarization (Fig. 6.3) couples to the upper waveguide and starts to couple to the lower waveguide. Therefore, the TM-field can couple to the single mode output waveguide on the right. However, losses also occur for this polarization due to the TM-polarization is mainly in the upper waveguide when the steep tapers are reached. The steep tapers cause power transfer to substrate modes. This simulation showed a power extinction ration of the TE- relative to the TM-polarization (TE/TM-PER) of nearly 6 dB at a wavelength of 1610 nm.

A second simulation was done for the second polarizer. The widths of the upper waveguide of the second polarizer are similar to Fig. 6.12. The taper widths are

approximately 200 nm wider than in the previous case. The length of the device was similar to the first device. The results are shown in Fig. 6.4 and 6.5.

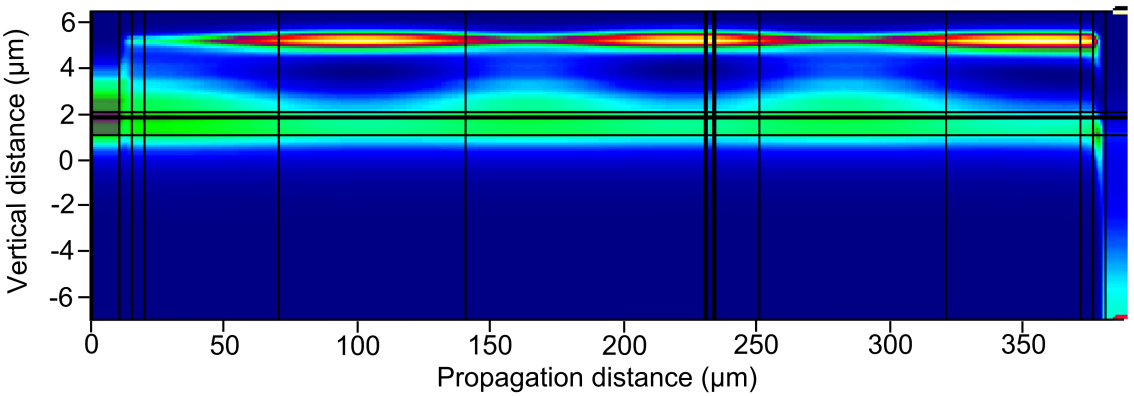


Figure 6.2: *Side view of the intensity distribution of the TE-field, the input is on the left side in the lower waveguide. The vertical lines correspond to section boundaries.*

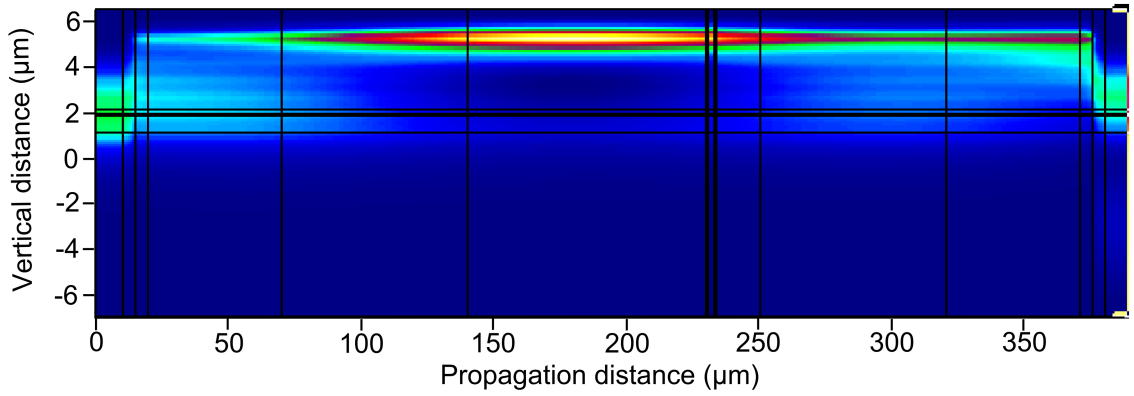


Figure 6.3: *Side view of the intensity distribution of the TM-field, the input is on the left side in the lower waveguide. The vertical lines correspond to section boundaries. In both cases the taper start width is 700 nm. The total taper width is reduced by 300 nm compared to the ideal case in Chapter 5.*

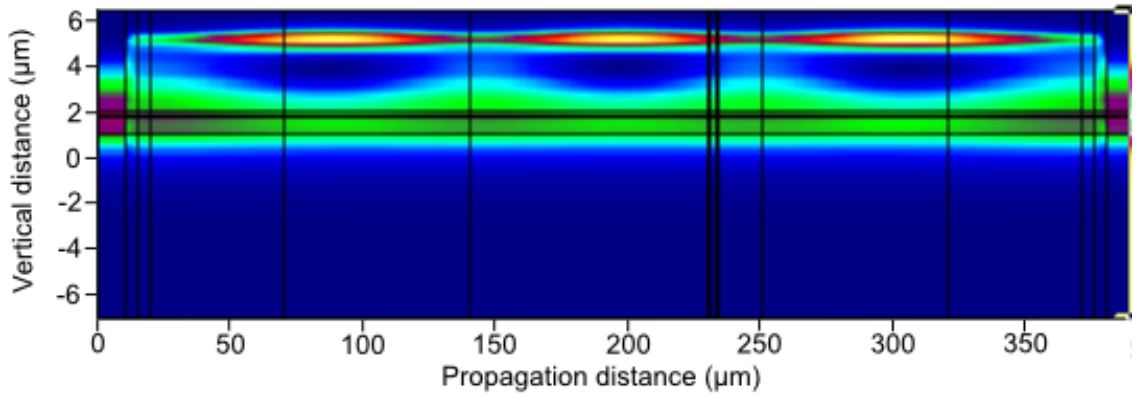


Figure 6.4: *Side view of the intensity distribution of the TE-field, the input is on the left side in the lower waveguide. The vertical lines correspond to section boundaries.*

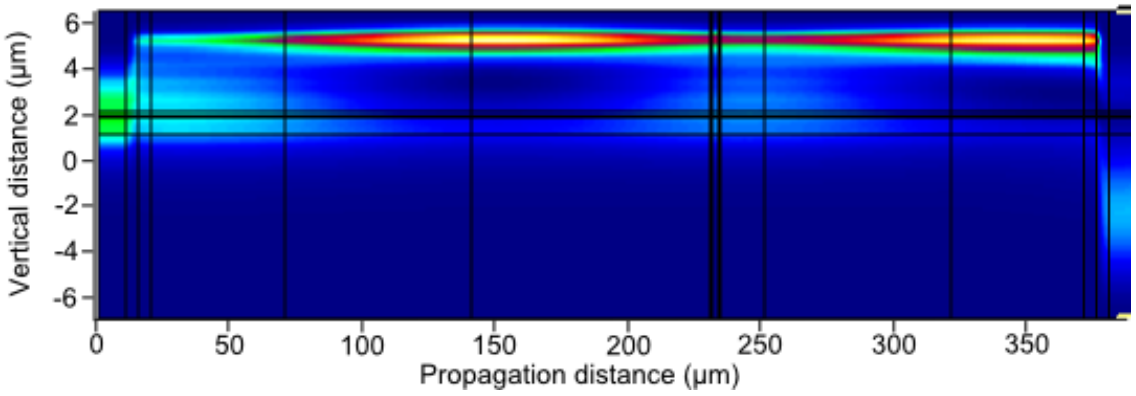


Figure 6.5: *Side view of the intensity distribution of the TM-field, the input is on the left side in the lower waveguide. The vertical lines correspond to section boundaries. In both cases the taper start width is 900 nm. The total taper width is reduced by 100 nm compared to the ideal case in Chapter 5.*

At a wavelength of 1610 nm 96 % of the TE-polarization reached the right end (Fig. 6.4), whereas for the TM-polarization this value is approximately 1 % and most of the power is in substrate modes (Fig. 6.5. The TE/TM-PER was calculated to be approximately 20 dB. This shows that a high TE/TM-PER is also possible.

6.2 Measurement Setup and Method

The transmission measurement of a polarization dependent single mode light wave was performed with the setup shown in Fig. 6.6. A tunable laser (TLS) with

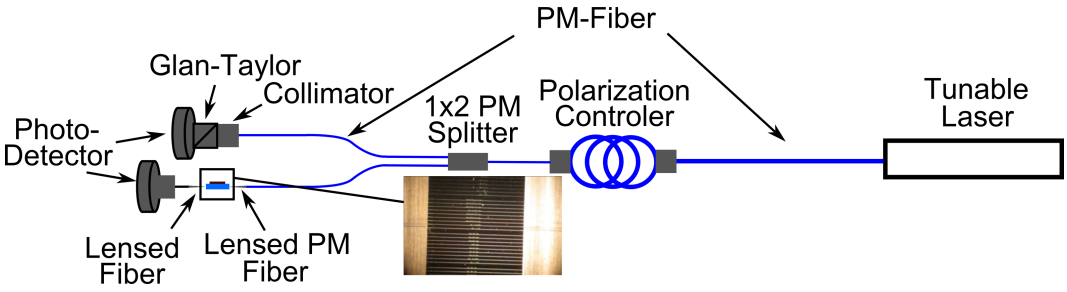


Figure 6.6: *Schematic of the measurement setup.*

a wavelength range of 1440 nm to 1640 nm acted as the light source. The light was coupled to a polarization maintaining (PM) single mode fiber. This fiber and all the other fibers were polarization maintaining to isolate the experimental setup from environmental factors and improve the accuracy of the results. The fiber from the TLS was connected to a free-space polarization controller. The polarization controller allowed the selection of either the TE- or the TM-polarization. Afterward this, a one by two PM 50 % to 50 % beam splitter was used, which allowed the simultaneous measurement of the polarization state and the light transmitted through the chip. The light from the upper branch was passed through a Glan-Taylor filter. This filter was aligned in such a way that only the TM-polarization was allowed to pass. The light transmitted through the Glan-Taylor was detected by an infrared photodetector. The polarization state was controlled by setting the photoresponse signal either to a maximum value (TM-polarization) or to a minimum value (TE-polarization) by adjusting the polarization controller. The second branch was connected to a PM AR-coated lensed fiber. The 6 μm spot size light beam was coupled into the fabricated chip. The optical field propagated through the chip. The output field on the left was coupled into an AR-coated 3 μm spot size fiber. The optical field intensity in this fiber was measured by another infrared photodetector.

Because both ends of the fabricated waveguides had cleaved facets, approximalty 30 % of the light is reflected at each facet allowing wavelength dependant Fabry-Pèrot spectra to be measured. The usage of the method proposed by Hakki and Paoli [123] facilitates the measurement of the waveguide loss. In this method a light beam makes transitions from one end of the sample to the other end. In each transition the beam looses power in a passive device. With the constructive and

destructive interference and the measured Fabry-Pèrot maxima and minima at a certain wavelength, an absorption coefficient α was calculated with the following equation [123]:

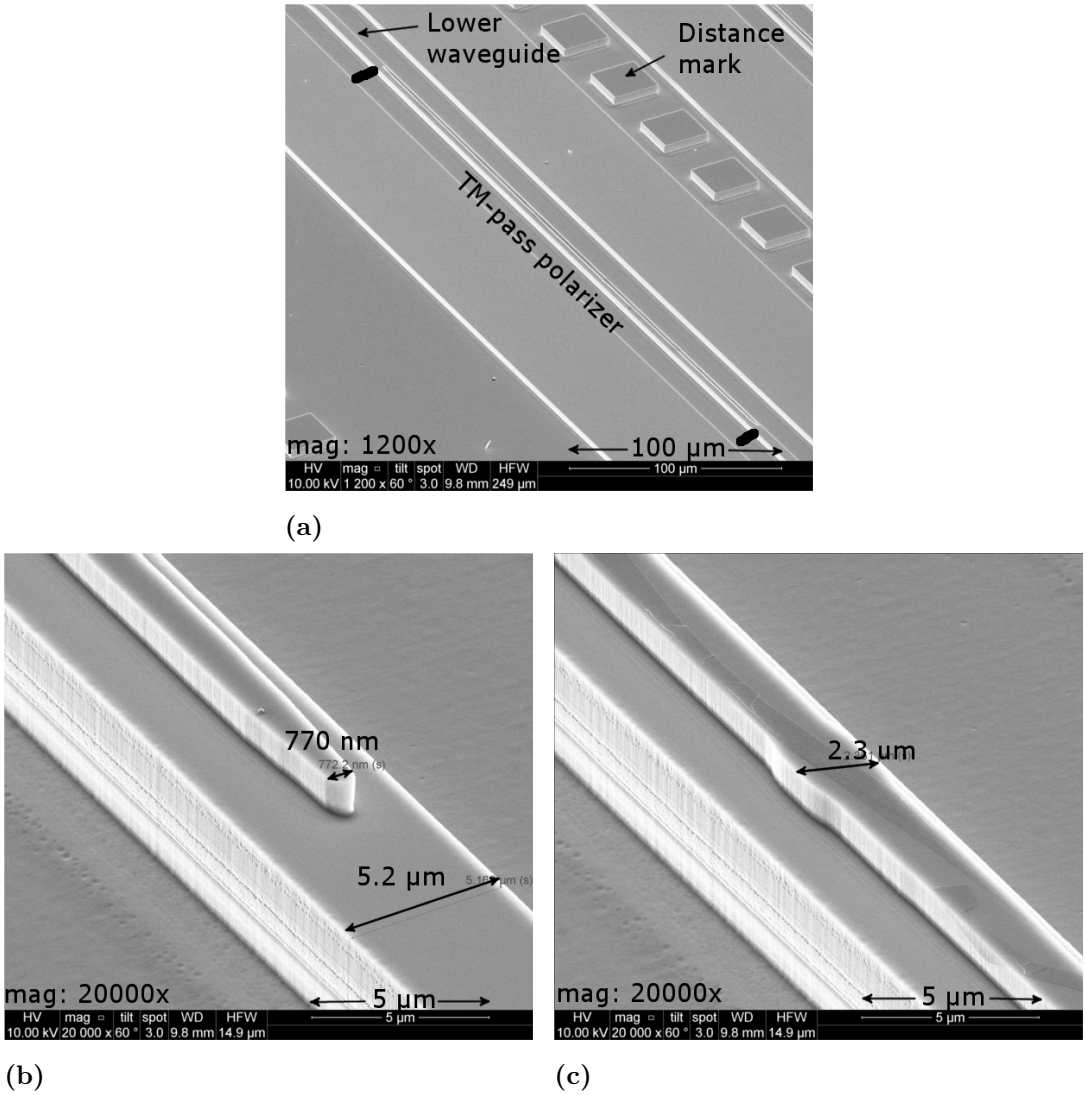
$$\alpha(\lambda) = \frac{1}{L} \ln \left\{ \frac{(P^+)^{1/2)} + (P^-)^{1/2}}{(P^+)^{1/2} - (P^-)^{1/2}} \right\} + \frac{1}{2L} \ln(R_1 R_2) \tag{6.2.1}$$

λ is the wavelength, P^+ the maximum intensity and P^- the minimum intensity respectively. The length L of the device can be measured by distance marks on the chip.

6.3 Measurements of the Polarizer Spectra

Fig. 6.7(a) shows a structure designed as a TM-pass filter at 1550 nm wavelength (Filter1). The layout is similar to Tab. 5.3, only the width of each taper is reduced by approximately 200 nm. In addition, each filter segment had a waveguide section consisting only of the lower input waveguide. With this waveguide it was possible to measure the waveguide losses. Because the input waveguide was a single mode waveguide the method proposed by Hakki and Paoli [123] was used to obtain the waveguide losses.

Fig. 6.8 shows the spectra of the lower waveguide for the TE- (Fig. 6.8(a)) and TM-polarizations (Fig. 6.8(b)) at 1550 nm. The length of this waveguide was 5400 μm. With this length and with the maxima and minima in the spectra a waveguide loss of (2.6 $\pm$ 0.4) dBcm^{-1} for the TE-polarization and (1.9 $\pm$ 0.3) dBcm^{-1} for the TM-polarization was calculated. A slight change in the polarization state on repeated measurements is recognizable in Fig. 6.8(b). The change in the polarization state was $<$15 % relative to the maximum photocurrent signal. This was observed in different spectra and is most probably related to the TLS. A small polarization rotation was also caused by the polarization controller and the environmental conditions. However, a rotating polarization for different wavelengths was also observed when the TLS was directly connected to the Glan-Taylor branch without a polarization controller. The rotating polarization was especially noticeable for the TE-polarization. However, the field mainly consisted of the TE-polarization



(a)

(b) **(c)**

Figure 6.7: *SEM cross-section images (a) of Filter1, (b) of the taper end of the polarizer, (c) of the center of Filter1.*

and the TM-polarization contribution only had a small effect on the measured PER. Therefore, the rotating polarization was ignored.

Fig. 6.9 shows similar measurements at a wavelength around 1610 nm. The photocurrent was reduced because of the lower output power of the TLS at longer wavelengths. The waveguide loss of the TE- and TM-polarizations are (3.6 ± 0.2) $\mathrm{dBcm^{-1}}$ and (3.0 ± 0.2) $\mathrm{dBcm^{-1}}$ respectively. The losses at 1550 and 1610 nm are used as references for the polarization filters (Tab. 6.1).

The spectral response of Filter1 (Fig. 6.7) is shown in Fig. 6.10. The original design had an upper waveguide 300 nm narrower than the ideal case. The taper

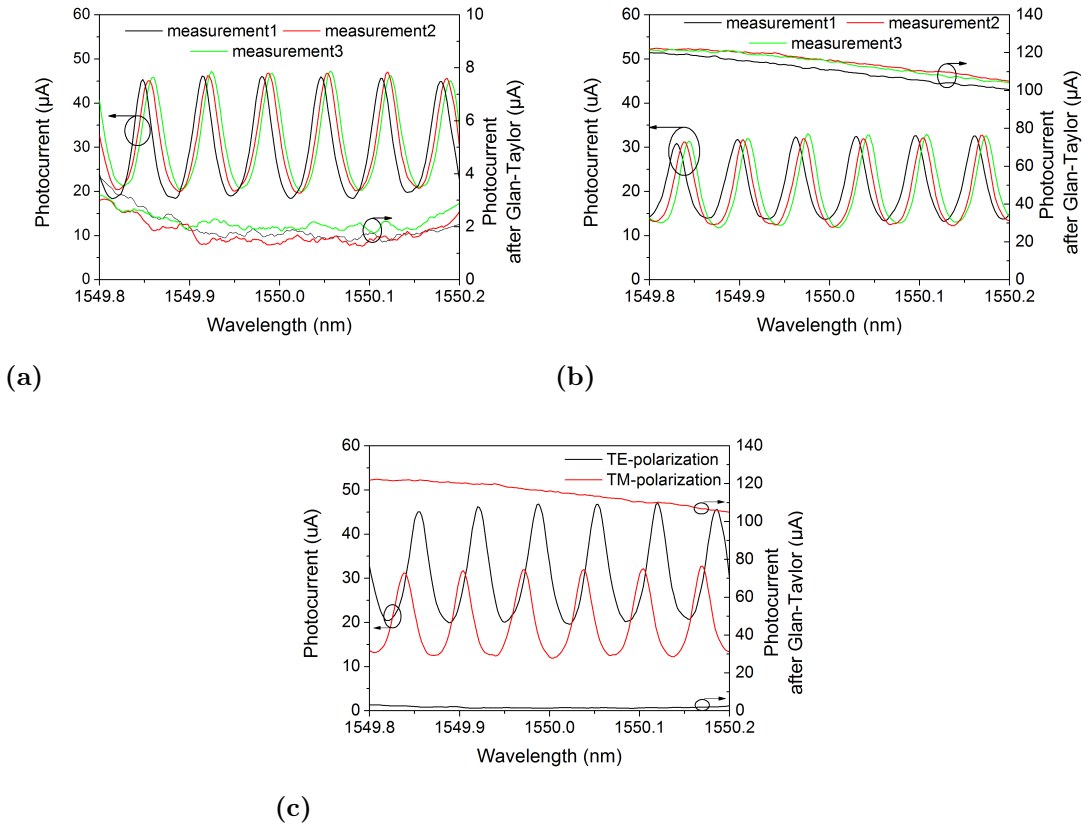


Figure 6.8: *Fabry-Pèrot spectrum (1550 nm) of the lower 5400 µm long waveguide and the polarization state of the TLS beam (a) for the TE-polarization, (b) and the TM-polarization, (c) Comparison of both polarizations.*

start width was designed to be 0.7 μm, and the width of the center of the TM-pass polarizer 2.2 μm respectively. The loss for the TE-polarization was (6.7 $\pm$ 0.5) dBcm^{-1}. This was an increase of (4.1 $\pm$ 0.6) dBcm^{-1} relative to the single lower waveguide. This increase can not be caused by additional waveguide losses, because both upper waveguides together had only an approximated length of 750 μm (Tab. 5.3) compared to a total length of 5400 μm. Therefore, insufficient coupling between the lower and upper waveguide was the reason for the higher loss. On the other hand the loss of the TM-polarization is only increased by (1.7 $\pm$ 0.4) dBcm^{-1}. Thus, a polarization effect was measured. Taking reference losses of (2.6 $\pm$ 0.4) dBcm^{-1} for the TE-polarization and (1.9 $\pm$ 0.3) dBcm^{-1} for the TM-polarization, the TE/TM-PER was calculated to be (0.8 $\pm$ 0.3) dB at 1550 nm. Spectra of Filter1 around a wavelength of 1610 nm are shown in Fig. 6.11. The TE-polarization loss was

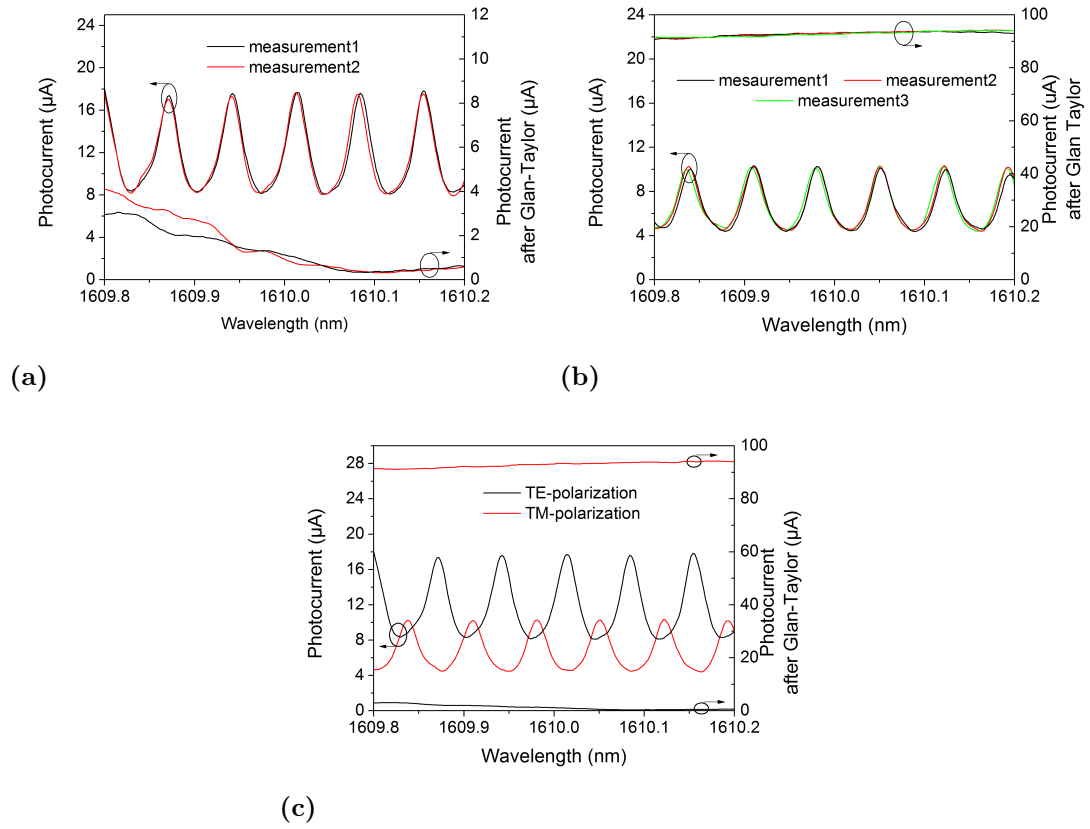


Figure 6.9: *Fabry-Pèrot spectrum (1610 nm) of the lower waveguide and the polarization state of the TLS beam (a) for the TE-polarization, (b) and the TM-polarization, (c) Comparison of both polarizations.*

(11.0 ± 0.6) dBcm^{-1} (Fig. 6.11(a)). The additional loss introduced by the filter was calculated to be (7.4 ± 0.7) dBcm^{-1}. The TM-polarization loss was (3.7 ± 0.7) dBcm^{-1} (Fig. 6.11(b)). The additional filter loss for the TM-polarization was only (0.7 ± 0.4) dBcm^{-1}. The TE/TM-PER was (3.1 ± 0.4) dB. Because the TM-pass polarizer was repeated a second time the PER for a single TM-pass polarizer is (1.6 ± 0.2) dB.

In Fig. 6.12 SEM images are shown of a second single TM-pass polarizer designed 100 nm narrower than the ideal case (Filter2). The taper widths of Tab. 5.3 are reduced 100 nm for this filter. The device length was the same than for the polarizer in Fig. 6.7(a).

Fig. 6.13(a) shows a TE- and TM-polarization loss at 1550 nm of (3.1 ± 0.4) dBcm^{-1} and (2.8 ± 0.2) dBcm^{-1} respectively. Both polarizations propagated along

Table 6.1: *Losses in the lower waveguide.*

		Loss ($dBcm^{-1}$)	
		TE-polarization	TM-polarization
Wavelength (nm)	1550	2.6 ± 0.4	1.9 ± 0.3
	1610	3.6 ± 0.2	3.0 ± 0.2

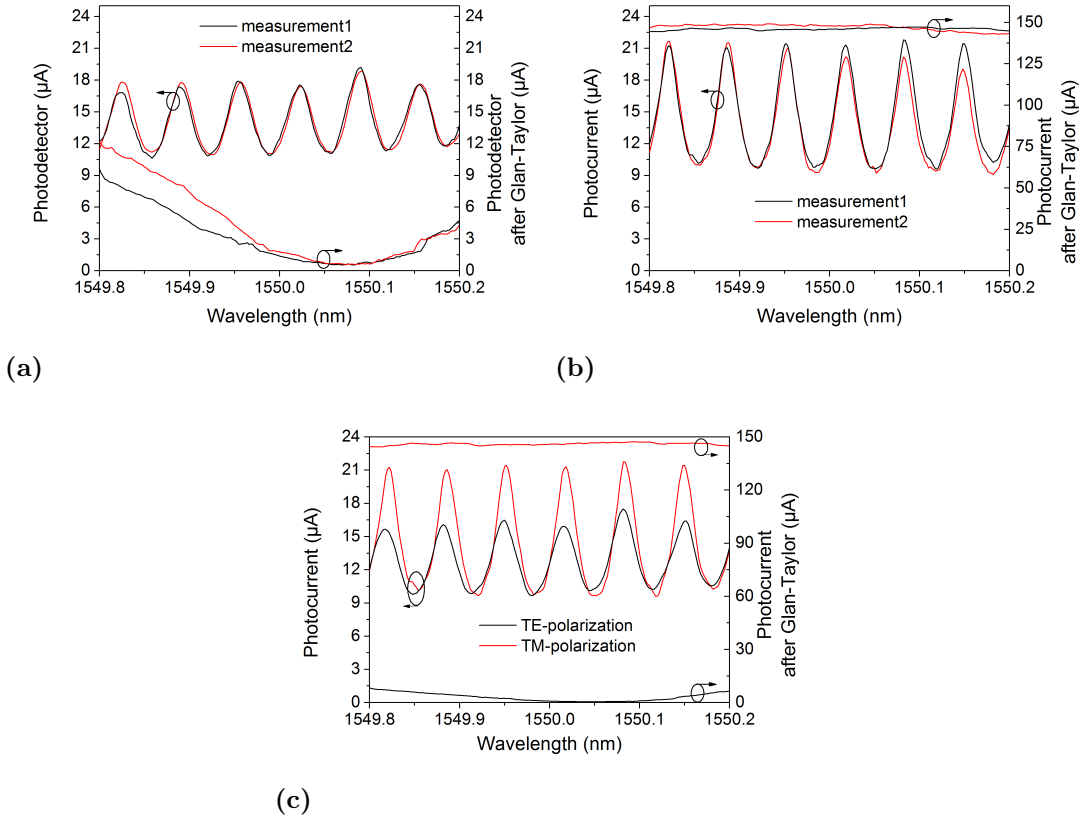


Figure 6.10: *Fabry-Pèrot spectrum (1550 nm) of Filter1 (cavity length: 5400 μm) and the polarization state of the TLS beam (a) for the TE-polarization, (b) and the TM-polarization, (c) comparison of both polarizations.*

the waveguide with low additional losses compared to a lower waveguide. In the case of the TM-polarization the loss is even lower for the lower waveguide. A possible explanation is a low loss coupling and propagating in the upper waveguide. Because only the cladding of the upper waveguide was etched, the sidewall roughness losses were reduced. The loss reduction of 9 % relative to the lower waveguide alone supports this assumption because the upper waveguide length is approximately 14

Table 6.2: *Waveguide losses in Filter1.*

		Loss ($dBcm^{-1}$)	
		TE-polarization	TM-polarization
Wavelength (nm)	1550	6.7 ± 0.5	3.6 ± 0.3
	1610	11.0 ± 0.6	3.7 ± 0.7

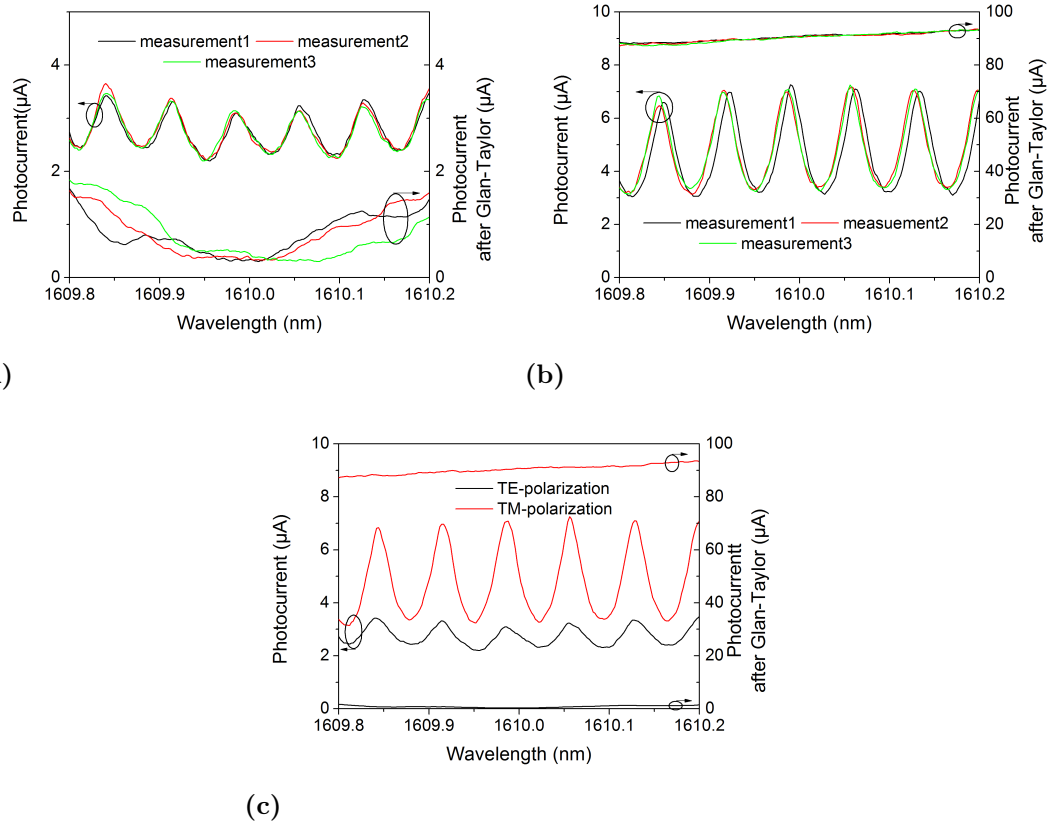
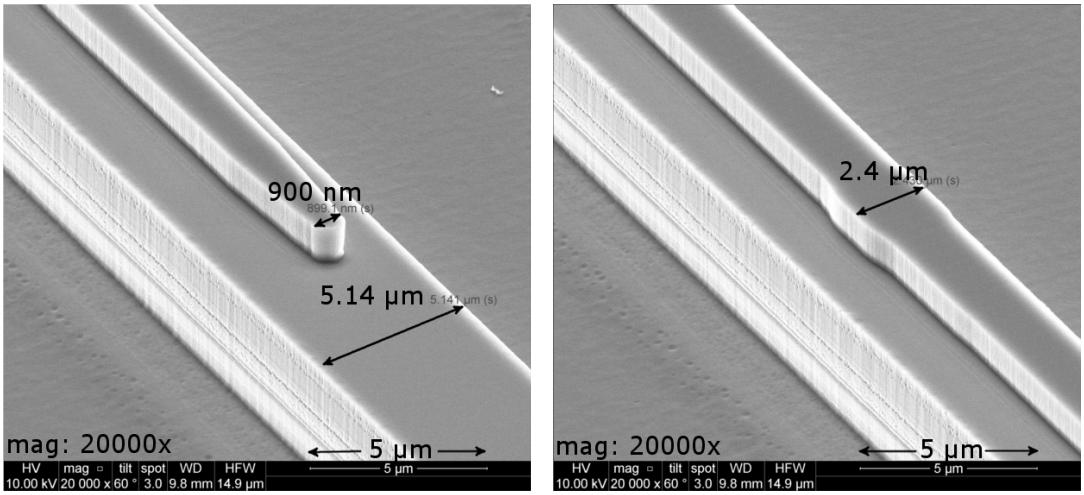


Figure 6.11: *Fabry-Pèrot spectrum (1550 nm) of Filter1 (cavity length: 5400 μm) and the polarization state of the TLS beam (a) for the TE-polarization, (b) and the TM-polarization, (c) comparison of both polarizations.*

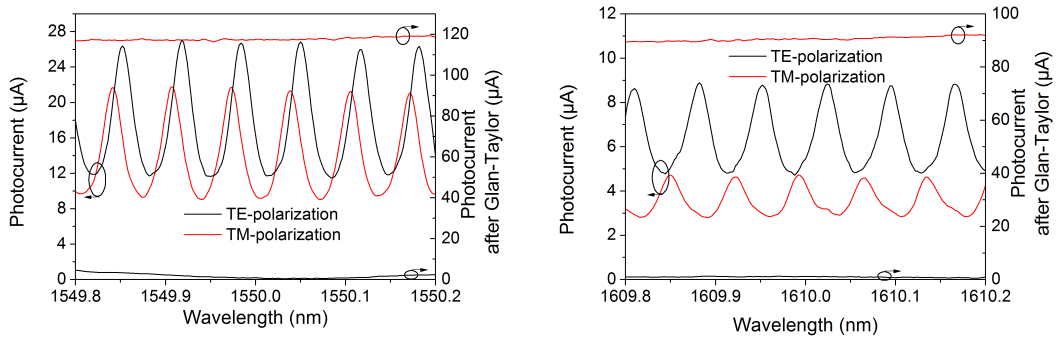
% of the whole waveguide structure.

Although this structure does not show any polarization filtering at 1550 nm, filtering can be observed at a longer wavelength of 1610 nm. Fig. 6.13(b) shows TE- and TM-polarization losses at 1610 nm of (5.4 ± 0.2) $dBcm^{-1}$ and (7.2 ± 0.4) $dBcm^{-1}$ respectively. The additional losses of the polarization filter were (1.8 ± 0.2) $dBcm^{-1}$ (TE) and (4.2 ± 0.4) $dBcm^{-1}$ (TM). The TM/TE-PER was (0.7 ± 0.2) dB



(a) **(b)**

Figure 6.12: *Cross-section SEM images of Filter2 (a) of the taper end of the polarizer, (b) of the center of Filter2.*



(a) **(b)**

Figure 6.13: *Fabry-Pèrot spectrum of Filter2 (cavity length: 5400 µm) for both polarizations and the polarization state of the TLS beam (a) at a wavelength of 1550 nm, (b) and a wavelength of 1610 nm.*

for a single polarizer (Tab. 6.4).

Table 6.3: *Waveguide losses in Filter2.*

		Loss ($dBcm^{-1}$)	
		TE-polarization	TM-polarization
Wavelength (nm)	1550	3.1 ± 0.4	2.8 ± 0.2
	1610	5.4 ± 0.2	7.2 ± 0.4

Table 6.4: *Power extinction ratio for a single stage of Filter1 and Filter2.*

	Filter1		Filter2	
Power extinction ratio (dB)	1550 nm	1610 nm	1550 nm	1610 nm
TE/TM	0.4 ± 0.2	1.6 ± 0.2	–	–
TM/TE	–	–	0.2 ± 0.1	0.7 ± 0.2

6.4 Conclusion

Resonant coupling with an ATG was used to obtain polarization filters for the first time. At a wavelength of 1610 nm a PER of (1.6±0.2) dB was measured for the TE-polarization in a single TM-pass polarizer. A TE-pass polarizer was demonstrated with a TM/TE-PER of (0.7±0.2) dB at 1610 nm. The low PER at a wavelength of 1550 nm was explained by variations in the refractive indices of the InGaAsP layers. If the epi-material refractive indices are well known, polarizers with higher PERs can be fabricated. A higher birefringence in the ATG and a larger difference in the upper waveguide width at the resonance points for both polarizations should enable an improved PER and a higher fabrication tolerance.

The large spot size input waveguide allowed simplified fiber alignment. Additionally, the short filter length of only a few hundred microns makes it possible to place several filters consecutively to get a high PER.

Chapter 7

Spot Size Converters for a PIN-Photodiode

In this chapter the previously explained spot size converter (SSC) concept based on asymmetric twin waveguides (ATGs) is integrated with a PIN-photodiode. The adiabatic field coupling in the device is shown. The principle of the matching layer is explained. The alignment tolerance of the coupling waveguide to the photodiode can be improved by a 400 nm wider coupling waveguide than the PD. Finally, a SSC concept is investigated that enables 88 % coupling efficiency from a single mode fiber. It is found that the field transition to the PD and therefore its absorption efficiency (AE) mainly depends on the refractive indices and hence the bandgaps of the different InGaAsP layers. The AE is calculated by comparing the total field power at the end of the photodiode to the total power at its starting point.

7.1 PIN-photodiode with a 5 μm Spot Size Input Waveguide

Photodiodes (PDs) are one of the key components in telecomms photonic integrated circuits. They convert received optical signals into electric signals. Side-illuminated waveguide PDs offer the advantage of decoupling the carrier collection length and the optical field absorption length. Because the carrier transition path

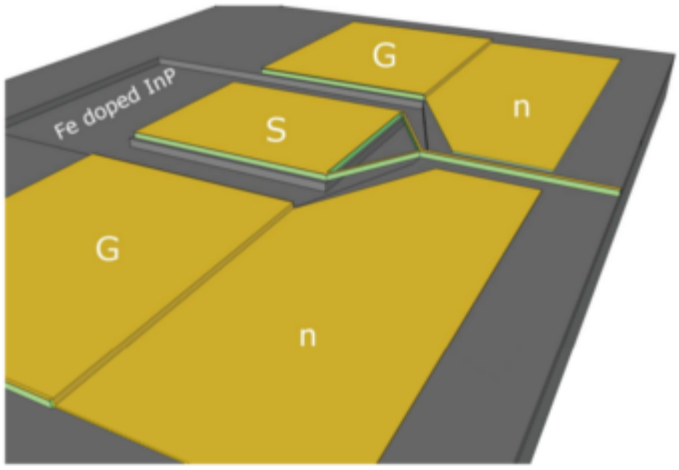


Figure 7.1: *Schematic drawing of dielectric-free ridge waveguide PD using isolated pedestal contact configuration [16].*

is perpendicular to the optical field a high efficiency and a short transit time can be achieved simultaneously [124]. A dielectric free fabrication of a waveguide photodiode operating up to 30 GHz was recently reported [16]. A compact, lumped element waveguide photodetector using a planar isolated pedestal ground-signal-ground (GSG) configuration with a 125 μm pitch was presented. The intention of that work was to reduce the parasitic capacitance due to the RF contacts without the usage of benzocyclobutene. In that approach the GSG contacts are planar with the ridge waveguide and are placed directly on the semiconductor. The signal contact is isolated from the rest of the device through a deep ICP etch into the semi-insulating substrate. The ground contact is formed through an angled n-metal evaporation, shorting the ground pedestal to the n-doped InP layer. The signal contact is connected to the ridge waveguide through a self-supported air bridge formed using a selective wet etch to undercut the n-doped InP (Fig. 7.1).

However, a mode mismatch between the large circular beam of a cleaved fiber and a small elliptical beam of the InGaAs PIN-photodiode (PIN-PD) results in losses of $>$10 dB and a resultant low responsivity. Several approaches were made to solve this problem. The evanescently coupled waveguide PD is one concept that enables high speed operation and high responsivity. The WG-PD consists of a WG-photodiode located on top of a passive waveguide [125]. Beling et al. demonstrated an InP based spot size converter operating with a 120-GHz bandwidth and a responsivity

of 0.5 A/W at 1.55 μm. A cleaved fiber butt-couples into a diluted input waveguide and the light is then transferred to the coupling waveguide by a vertical taper. The asymmetric twin waveguide (ATG) is a similar approach. However, the transfer to the coupling waveguide is caused by a lateral taper (Chapter 3.3). The responsivity and the bandwidth were reported as 0.75 A/W and 40 GHz [87]. A lensed fiber was used as the optical field input.

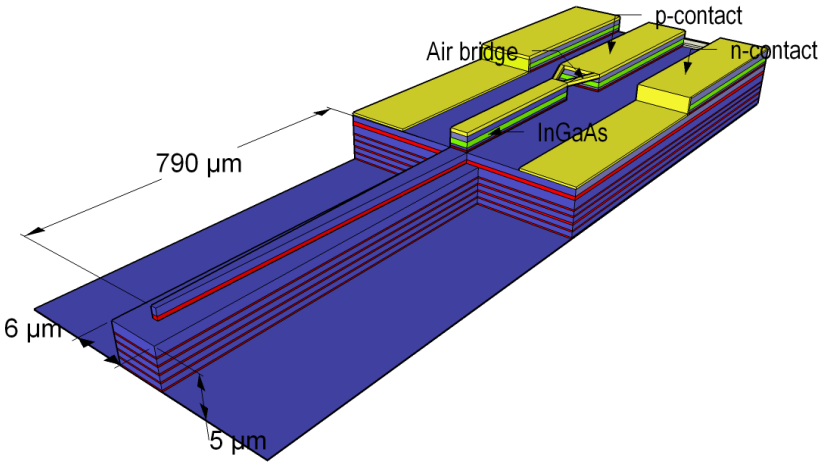
7.1.1 Photodiode and Spot Size Converter Layout

Here a structure is designed to improve the coupling efficiency to the dielectric free fabricated PD [16]. The intention to integrate a SSC is to increase the responsivity of the PD. Furthermore, the additional SSC permits cleaving of the chip at a designated section. The cleavage is not necessary through the PD. This allows to reduce the PD-length, and consequently increases the PD bandwidth.

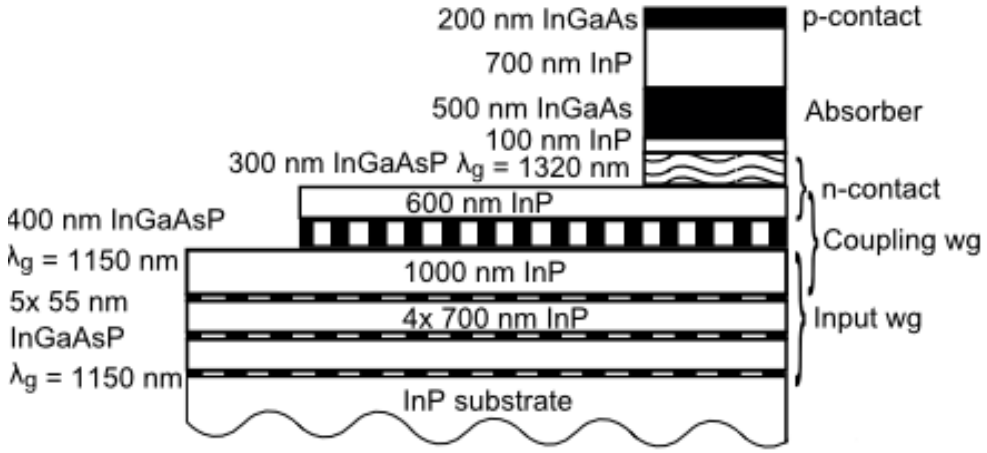
The single mode input waveguide with the five layers of InGaAsP is on the left (Fig. 7.2(a)). Following this, the upper waveguide is up-tapered from 1 μm to 3 μm over a distance of 790 μm. Tab. 7.1 shows the taper layout. This upper waveguide ends at the dielectric free fabricated PD and the optical field is absorbed in the 500 nm thick InGaAs layer. The length and width of the PD can be altered to analyze

Table 7.1: *Configuration of the spot size converter and the photodiode*

section no.	start-width (μm)	end-width (μm)	length (μm)
1	1.0	1.4	20.0
2	1.4	1.6	20.0
3	1.6	2.0	200.0
4	2.0	2.2	150.00
5	2.2	2.5	250.0
2	2.5	3.0	150.0
Photodiode	3.0	3.0	100.0



(a)



(b)

Figure 7.2: *(a) Three-dimensional schematic view of the photodiode and the waveguides. (b) Schematic cross-section side-view of the layer structure.*

the responsivity.

The layer characteristic of the spot size converter is similar to the previously outlined structures (Chapter 4 and 5). However, the InGaAsP layer thickness in the diluted lower input waveguide is adjusted from 50 nm to 55 nm. The measured refractive index was around 3.30 (Chapter 8) compared to the index of 3.33 in the simulations. The increase of the InGaAsP layer thickness resulted in an increase of the propagation constant from 12.857 μm^{-1} to 12.861 μm^{-1} for the TE-polarization. This value is closer to the value of 12.866 μm^{-1} in the first simulations. The smaller

difference of the propagation constants should improve the coupling to the ATG. In addition, the higher refractive index quaternary of the upper waveguide is replaced by a 400 nm thick layer of the same InGaAsP composition as the diluted input waveguide (Fig. 7.2(b)). This avoids the need of an additional composition and therefore reduces the complexity. The transfer from the input to the coupling guide is realized by adiabatic coupling.

The method explained in Section 4.1.1 was applied to design an adiabatic taper for both polarizations. The resonance points were found to be at widths of approximately 1.90 μm (TE-polarization) and 2.30 μm (TM-polarization). Therefore, the taper angles are small at these points (Tab. 7.1).

7.1.2 Optical Field Behaviour

Because the concept is based on evanescent coupling, a matching layer is required to improve the field overlap between the coupling waveguide (CWG) and the absorber [126, 127]. An increased field overlap helps to reduce the required PD length and therefore results in a higher PD bandwidth.

In Fig. 7.3 intensity cross-sections of three of the excited modes in the PD-section can be seen. The single mode input field arriving from the SSC section couples into the modes that relocated partially below the PD-ridge. The first two modes in Fig. 7.3(a) and (b) also have a slight overlap with the absorber, the third layer from the top. Therefore, the amplitudes of these modes decrease along the PD length. Nevertheless, modes, as shown in Fig. 7.3(c), are excited. These modes have very little overlap with the absorber. Consequently, the power in these modes does not get absorbed and does not contribute to an electrical signal. The matching layer refractive index and thickness are designed to minimize the power coupling into the low absorbing modes.

The adiabatic electromagnetic field coupling is visualized in Fig. 7.4. The fundamental TE-mode in the 6 μm wide input waveguide is transferred to the CWG by a 790 μm long taper section (Fig. 7.2). The coupling mainly occurs around the propagation distance range of 100 and 250 μm. Because the taper angles are small there is practically no power transfer from the fundamental input mode to

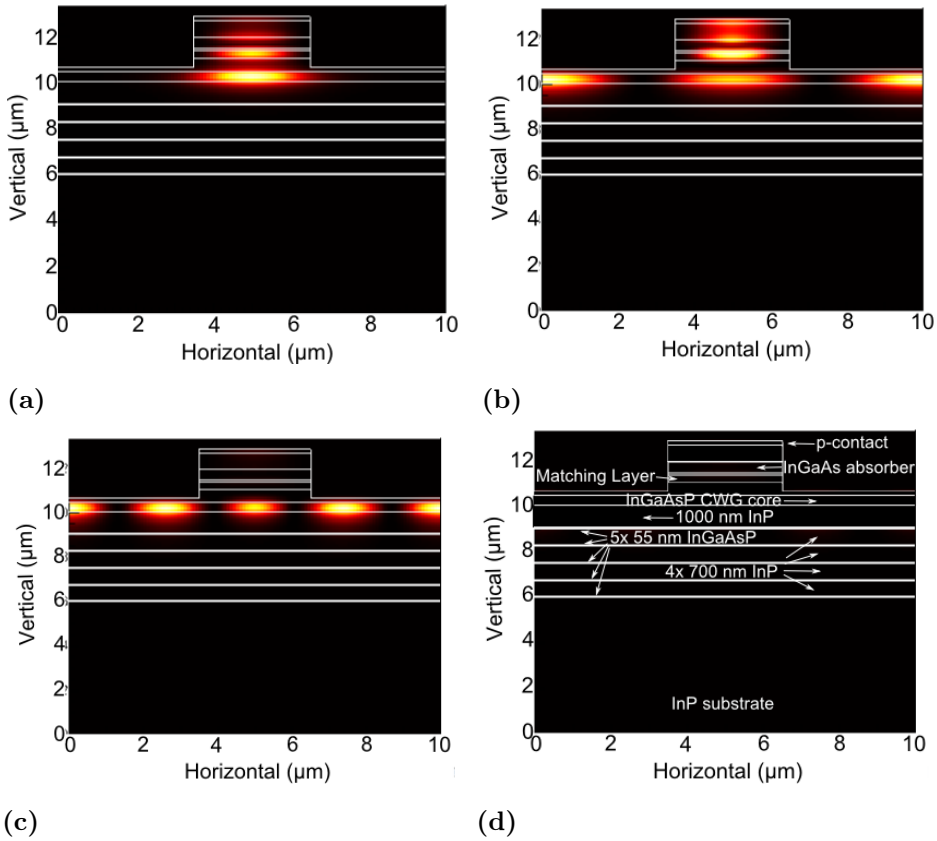


Figure 7.3: *Excited mode intensity distribution at the intersection SSC-PD (a) lowest order mode with an overlap between the CWG and absorber, (b) next higher order mode with an overlap between the CWG and absorber, (c) higher order mode with hardly any overlap between the CWG and absorber,(d) Cross section view of the layers of the SSC and PD.*

any higher order or substrate mode for both polarizations. Because the resonance point of the TM-polarization is at a wider waveguide width, the taper angles must remain small and hence the taper distances long to enable adiabatic coupling until the CWG reaches the PD width of 3 μm. The absorption efficiencies are 82 % for the TE- and 78 % for the TM-polarization. This value demonstrate the polarization insensitivity of the coupler.

The mode mismatch at the CWG-PD intersection causes power losses of 9 % for the TE- and 12 % for the TM-polarization respectively.

An important aspect of the SSC-PD fabrication process is the alignment of the CWG to the PD. Fig. 7.5(a) shows that the AE decreases to values of 76 % (TE-

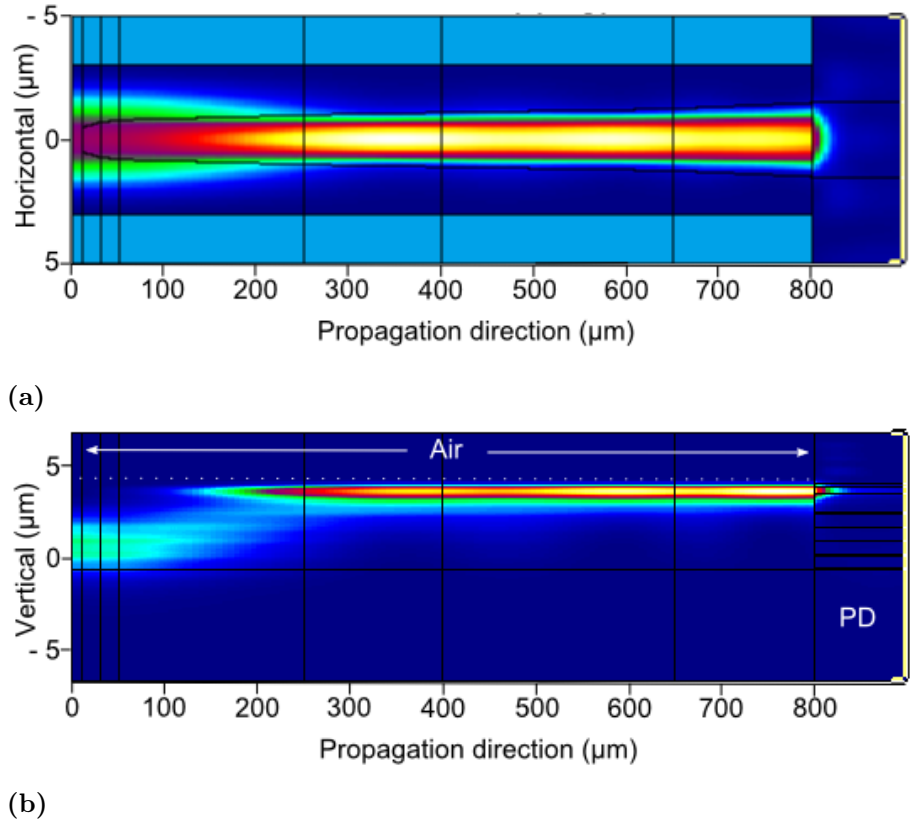


Figure 7.4: *Intensity distribution of the TE-polarization in the PD-SSC structure, (a) plan view, (b) side view.*

polarization) and 74 % (TM-polarization) for a misalignment of the CWG to the PD of 1000 nm. A 3.4 μm CWG ridge end, rather than a 3 μm CWG ridge end, is used to increase the alignment tolerance. In Fig. 7.5(b) the AE relative to a maximum misalignment of 1000 nm can be seen. A higher AE of 85 % is achieved for both polarizations in the ideal case of perfect alignment. Furthermore, the coupling loss is reduced to 6 % (TE-polarization) and 10 % (TM-polarization) at this point. Finally, the alignment tolerance is improved. Particularly, the AE of the TM-polarization remains at a higher level compared to the 3 μm wide ridge (Fig. 7.5(c)).

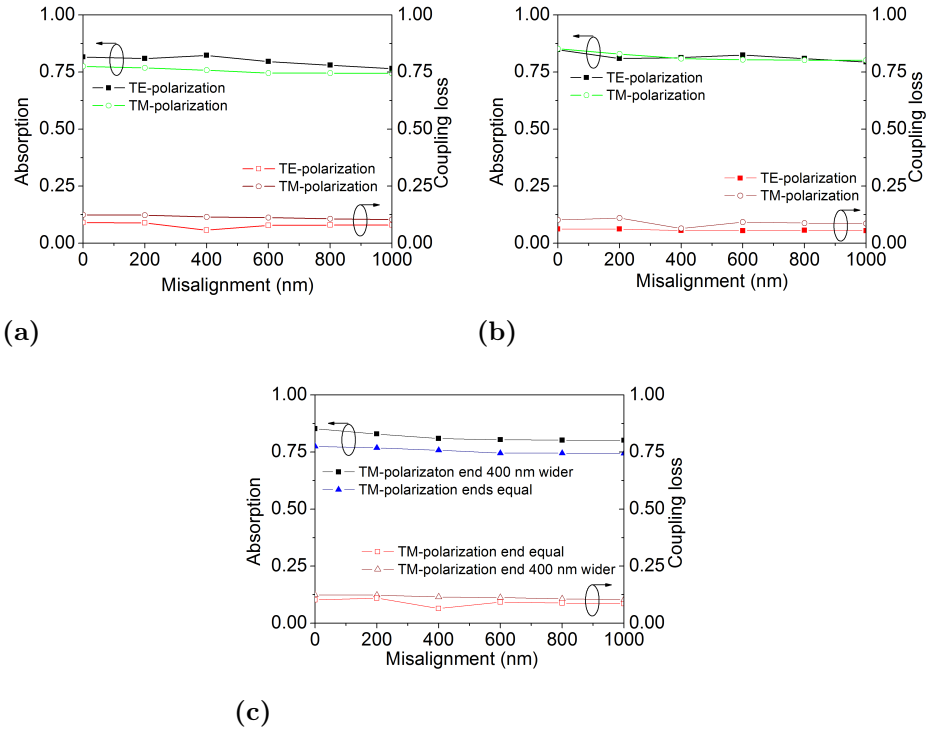


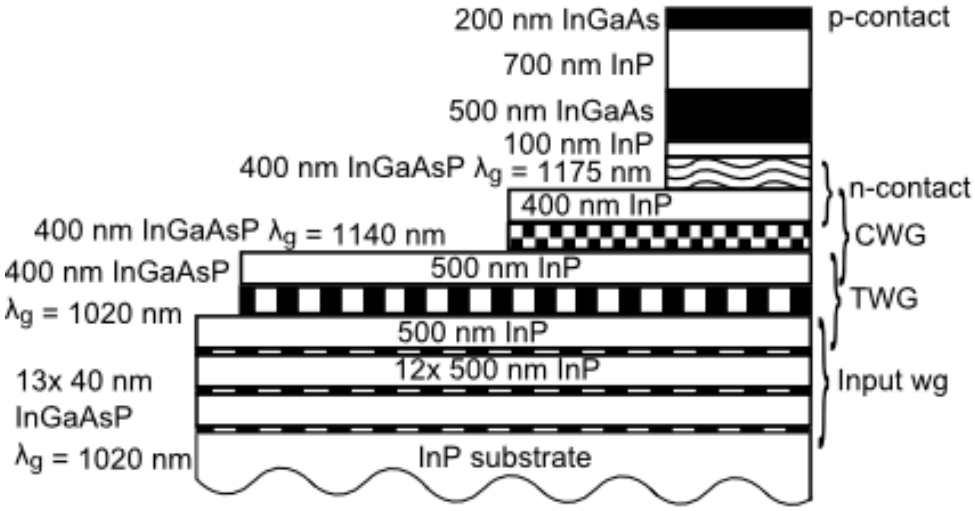
Figure 7.5: *Absorption efficiency relative to a misalignment of the PD (a) taper end width equals PD width, (b) taper end 400 nm wider than PD, (c) comparison of both cases for the TM-polarization*

7.2 PIN-photodiode with a 8 μm Spot Size Input Waveguide

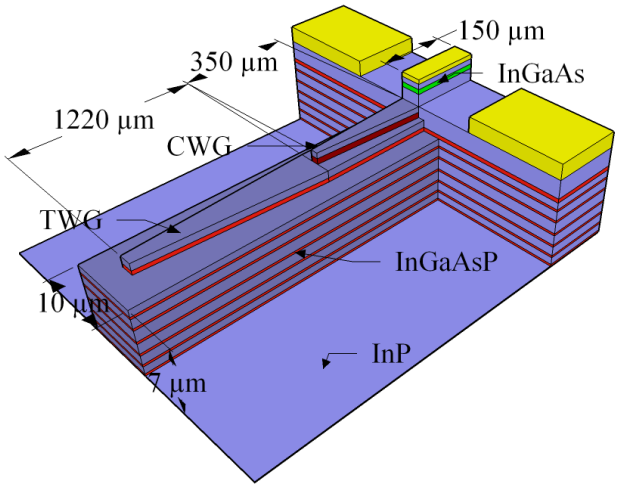
The previous SSC design (Chapter 7.1) achieves a theoretical coupling efficiency of 91 % for a 6 μm spot size lensed fiber. However, in the case of a SMF cleaved fiber the coupling efficiency drops to a value of 52 %. Here we show the design of a PIN-PD with an input waveguide with a spot size of 7.7 μm (horizontal) and 6.9 μm (vertical) suitable for direct cleaved fiber butt-coupling at the telecommunications wavelength of 1.55 μm. The large spot size input waveguide achieves a theoretical coupling efficiency of 88 % to a cleaved fiber. The input field is transferred insensitive of polarization to the small mode size coupling waveguide by a transition waveguide (TWG) with an effective index and a mode size in-between that of the lower input waveguide and CWG. The AE of the PD is simulated relative to waveguide misalignment, width variation in the waveguides, different refractive indices of the quaternaries and n-contact etch depth. It is found that the refractive indices of the different InGaAsP layers have the main effect on the AE.

7.2.1 Photodiode and Spot Size Converter Layout

Fig. 7.6(a) shows the epitaxial structure. The InGaAsP refractive indices are calculated with a modified single-effective-oscillator method (Chapter 8.1). Light from a cleaved SMF is coupled into the 10 μm wide and 7 μm deep waveguide having a $1/e^2$ spot size of 7.7 x 6.9 μm. A direct transfer of the field into the 3 μm wide coupling waveguide by a lateral taper is not possible, because the guided modes of the CWG do not have a field overlap with the input waveguide that results in low-loss coupling. Therefore, an additional TWG with a width of 5 μm is introduced. On top of this TWG is the CWG with an end width of 3 μm, similar to the PD width. Finally, the PD is placed onto the CWG. The PD has a 500 nm thick $In_{0.53}Ga_{0.47}As$ absorption layer, a 200 nm InGaAs p-contact and a 800 nm n-contact consisting of 400 nm InP and 400 nm InGaAsP (λ_g = 1140 nm). The 400 nm InGaAsP layer acts as a matching layer (7.1.2), improves the field overlap with the absorber and reduces the necessary PD length. Fig. 7.6(b) outlines the spot size converter design. At the



(a)



(b)

Figure 7.6: *(a) Schematic cross-section view of the layer structure. (b) Three-dimensional schematic view of the photodiode and the waveguides.*

input from the SMF there is the large spot size single mode input waveguide. The following taper layout can be seen in Tab. 7.2. The width of the TWG is increased from 1.0 μm to 5.0 μm over a total length of 720 μm. Subsequently, the TWG width is kept at 5.0 μm and the CWG width is increased from 1.0 μm to 3.0 μm over a total length of 350 μm. Finally, a 3 μm wide and 150 μm long InGaAs PIN-PD absorbs the optical signal.

The behavior of the TE-field is shown in Fig. 7.7. The fundamental TE-mode

Table 7.2: *Configuration of the spot size converter and the photodiode*

sector 1			
section no.	start-width (μm)	end-width (μm)	length (μm)
1	1.0	2	20.0
2	2.0	2.5	500.0
3	2.5	3.0	500.0
4	3.0	5.0	200.00
sector 2			
section no.	start-width (μm)	end-width (μm)	length (μm)
1	1.0	1.3	50.0
2	1.3	3.0	300.0
Photodiode	3.0	3.0	150.0

of the single mode input waveguide enters the first taper section. It is adiabatically up-coupled to the TWG. Following this, the TE-mode is transferred to the CWG to enable an optimum field overlap in the PD. An AE of 88 % (TE-polarization) and 85 % (TM-polarzation) was calculated.

Furthermore, both waveguides (TWG and CWG) could be theoretically replaced by different optical components such as semiconductor optical amplifiers (Chapter 3.4), multi mode interference couplers with a Mach-Zehnder interferometer [86] or polarization filters (Chapter 5.3). This allows for additional functionality required in PICs.

7.2.2 Fabrication Tolerance

The simulation results give a good indication of how a waveguide structure will work after it is fabricated. Nevertheless, the fabrication procedure can result in divergences from the ideal layout. Usually, each waveguide needs to be aligned to a subsequent waveguide. The alignment procedure of any manual mask aligner is a

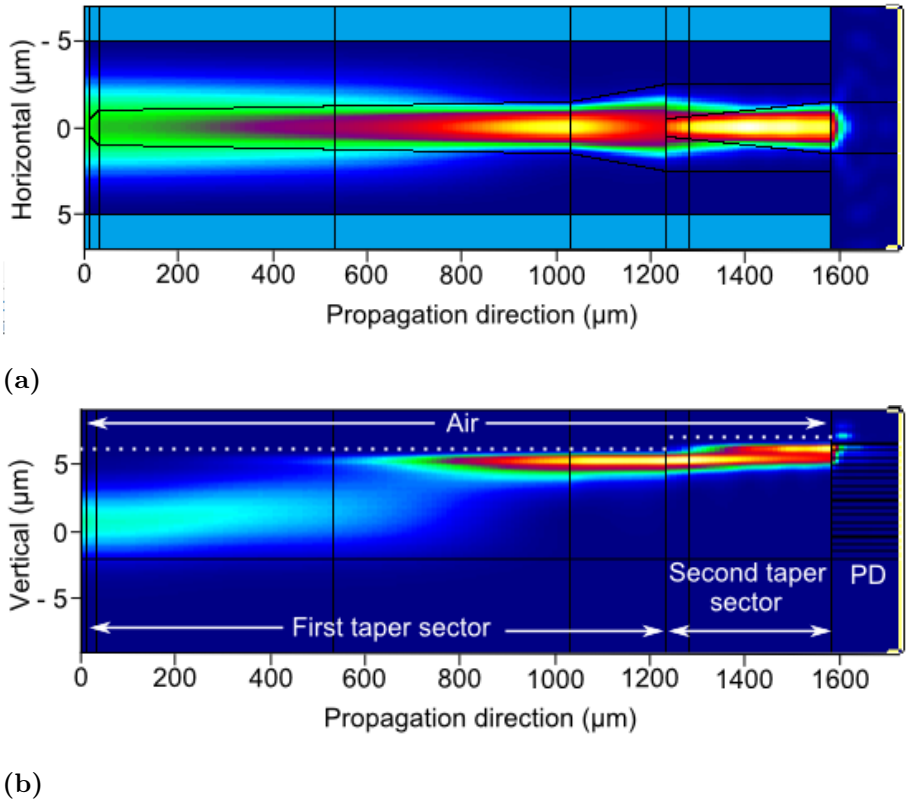


Figure 7.7: *Intensity distribution of the TE-polarization in the PD-SSC structure, (a) plan view, (b) side view.*

complicate series of steps. Misalignments in the range of several 100 nm are easily possible. Therefore, the AE relative to such misalignments is simulated. Fig. 7.8 shows the AE of both polarizations relative to a misalignment of up to 1.0 μm in 200 nm steps. Additionally, the coupling losses are indicated. The coupling losses are calculated by subtracting the total power in all modes at the start of the PD section from the 100 % input signal. In general the losses in both taper sections are in the range of 1 to 2 %. However, at the intersection between the second taper end and the beginning of the PD, mode mismatch losses higher than 10 % can occur. The 1-dB barrier relative to the AE in the ideal case is drawn to indicate a critical loss limit. The first possible misalignment is a lateral position shift of the TWG ridge. In Fig. 7.8(a), it can be seen that a lateral misalignment of the large spot size input waveguide to the TWG has little effect on the AE. A similar behavior can be observed for a misalignment of the TWG to the CWG (Fig. 7.8(b)). This can be explained by the fact that the propagation constants do not change significantly. At a TWG

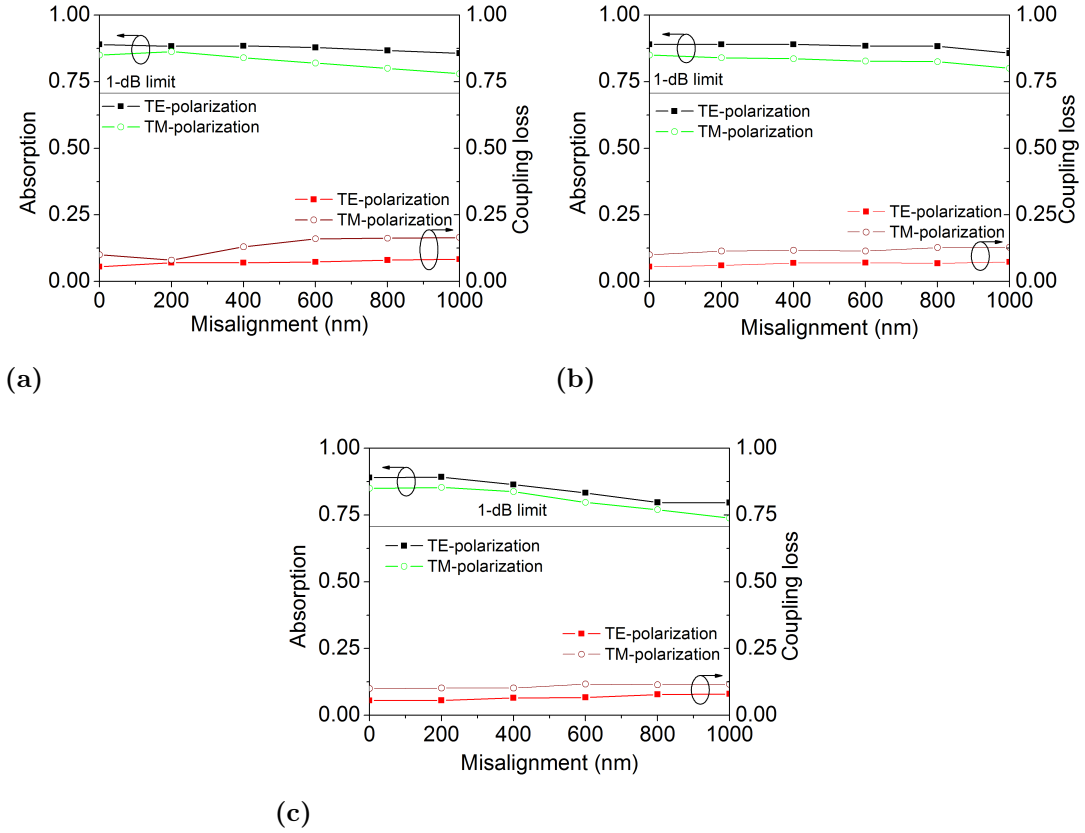


Figure 7.8: *Absorption efficiency relative to a misalignment (a) of the input to the transition waveguide, (b) of the transition to the coupling waveguide, (c) of the coupling waveguide to the photodiode.*

width of 2.0 μm the difference of the propagation constants of the fundamental and first order mode are $10.8 * 10^{-3} \mu m^{-1}$ for an ideally aligned coupler. In the case of the TWG misaligned by 1000 nm to the input waveguide the difference of the propagation constants is $10.6 * 10^{-3} \mu m^{-1}$ at the same position. Only a misalignment of the PD relative to the CWG results in a significant AE decrease. However, even at a misalignment of 1.0 μm the AE is not at the 1-dB limit.

A second fabrication issue is the actual waveguide width. Generally, an etch mask is defined by a lithography step and is used in a dry etch step to define the ridge. However, during the lithography, over or under exposure as well as over or under development can happen. Therefore, the ridge width might not be at its intended value. Fig. 7.9 shows the AE relative to a width variation in each of the three different waveguides. Because of the wider waveguide width, a variation of up

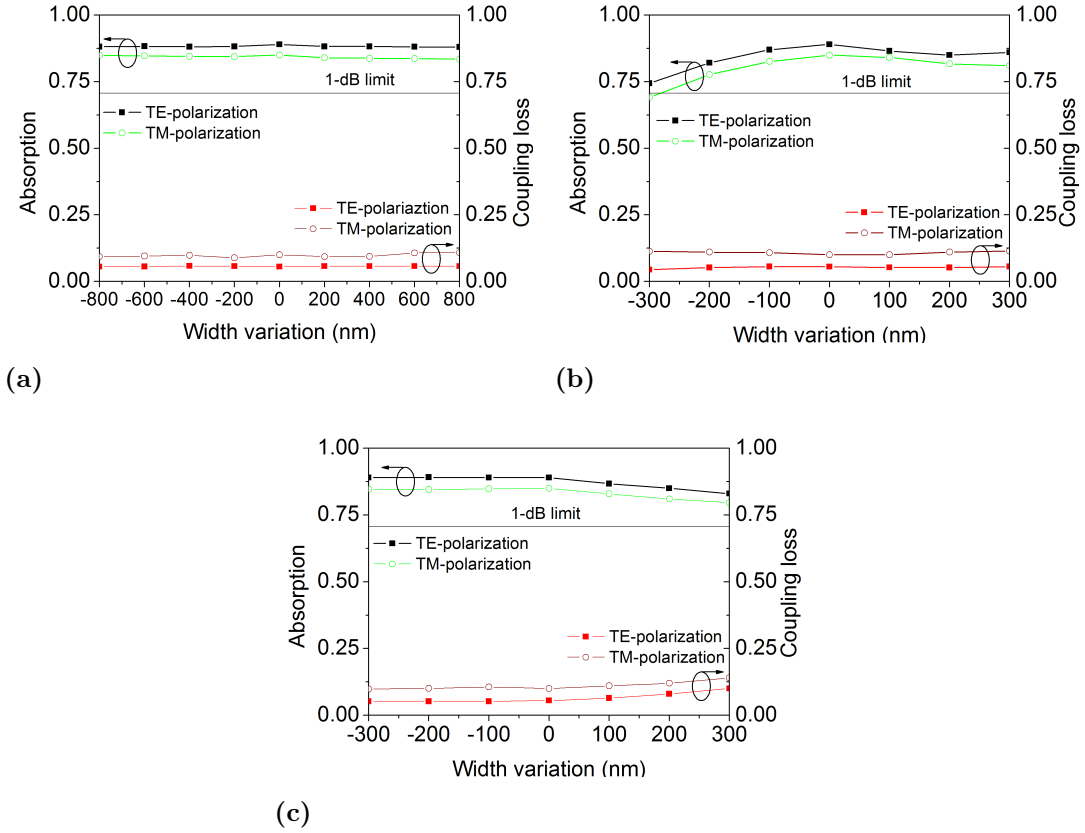


Figure 7.9: *Absorption efficiency relative to a width variation (a) of the input waveguide, (b) of the transition waveguide, (c) of the coupling waveguide.*

to ± 800 nm is simulated for the input waveguide 7.9(a). It can be seen that only a 300 nm narrower TWG introduces a loss close to 1-dB (Fig. 7.9(b)). A wider or narrower ridge width of the input waveguide or of the CWG does not significantly affect the AE (Fig. 7.9(a), (b)).

Metal organic vapor phase epitaxy (MOVPE) or comparable epitaxial systems are necessary to grow the different layer compositions. However, especially in the case of the InGaAsP quaternaries, several parameters such as the temperature, chamber pressure, gas flow and growth rate must be simultaneously controlled. This is very difficult, therefore a deviating composition can be easily obtained. A different composition results in a different bandgap and consequently in a different refractive index. Thus the AE relative to variations of the refractive indices of the three different quaternaries is simulated. Particularly, the quaternary in the input and coupling waveguide (InGaAsP(λ_g = 1020 nm)) allows for very little variation without result-

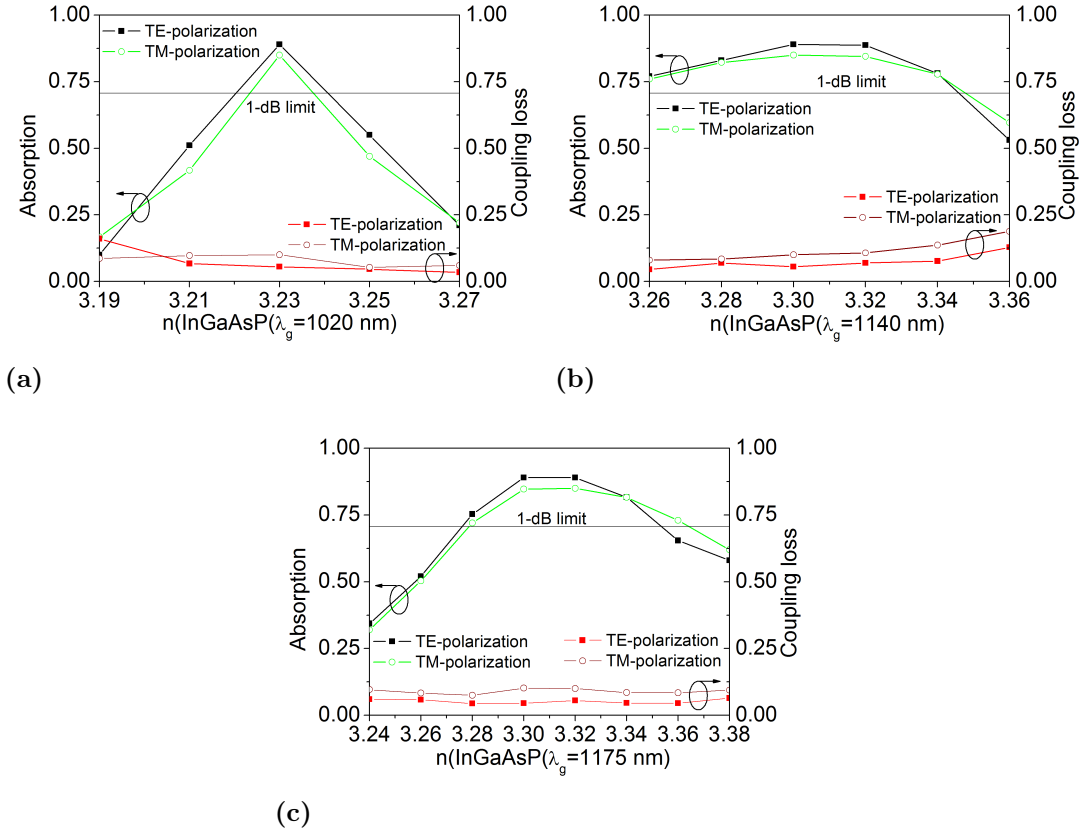


Figure 7.10: *Absorption efficiency relative to a refractive index variation of (a) InGaAsP (λ_g = 1020 nm), (b) InGaAsP (λ_g = 1140 nm), (c) InGaAsP (λ_g = 1175 nm).*

ing in > 1-dB decrease in AE (Fig.7.10(a)). If the refractive index is too low or too high either the electromagnetic field does not properly couple to the TWG or the resonance point is shifted to the steep taper and power is transferred from the fundamental mode. This causes mode beating and a reduced coupling efficiency to the TWG and further to the PD. On the other hand, the refractive index of the TWG can be at least 0.04 smaller and the AE is still above the 1-dB limit (Fig. 7.10(b)). Only for an index change of ± 0.06 is the coupling efficiency to the TWG, and hence the AE, reduced.

The InGaAsP composition in the matching layer improves the mode overlap between the CWG and the absorber. In an index range of - 0.04 to + 0.02 the AE stays over the 1-dB limit (Fig. 7.10(c)). The coupling is especially sensitive to lower index values, where a decrease of only 0.04 results in considerably reduced mode overlap and an AE of less than 35 % for both polarizations.

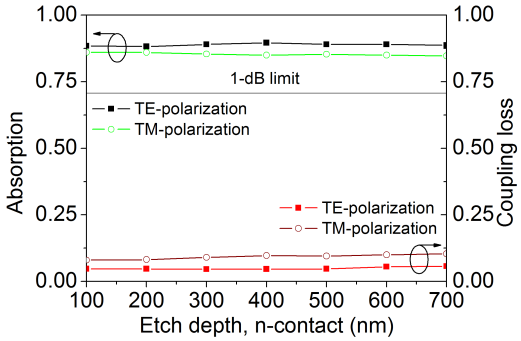


Figure 7.11: *Absorption efficiency relative to a difference in the n-contact etch depth*

A final effect that is considered is the etch depth to the n-contact. The etch must end in the n-doped region to enable an electric contact (Fig. 7.6(a)). Fig 7.11 shows that the n-contact etch depth has no influence on the AE.

7.3 Conclusion

The 6 μm wide and 5 μm deep SSC concept has been successfully integrated with a PIN-PD. Adiabatic coupling to the PD with an absorption efficiency of 82 % for the TE-polarization and 78 % for the TM-polarization has been simulated. It has been found that a 400 μm wider coupling waveguide ridge relative to the PD improves the absorption efficiency and additionally increases alignment tolerance of the coupling waveguide and the PD.

A polarization insensitive coupling from a fiber matched waveguide to a PIN-PD has been shown in the second section. A transition waveguide enables the optical field transition from the large spot size (8 μm) input waveguide to the small spot size photodiode. Critical alignment steps during processing do not affect the absorption efficiency of the photodiode spot size converter design. For adiabatic tapers the effect on the absorption efficiency of width variations, as can occur during lithography and etching, can also be neglected. The main factors that must be taken into account to guarantee an optimum absorption efficiency are the refractive indices and hence the bandgaps of the quaternaries.

Chapter 8

Determining the Refractive Index of $In_{1-x}Ga_xAs_yP_{1-y}$ Layers

$In_{1-x}Ga_xAs_yP_{1-y}$ is an important quaternary composition for InP systems. The importance is laid out in this chapter. Furthermore, a model is shown for how the refractive index of $In_{1-x}Ga_xAs_yP_{1-y}$ can be calculated in terms of its composition and a measurement method for the refractive index is outlined. Finally, this method is used to determine the refractive index of two different compositions.

8.1 Refractive Index of $In_{1-x}Ga_xAs_yP_{1-y}$ relative to the Composition

As previously outlined, the refractive indices of different $In_{1-x}Ga_xAs_yP_{1-y}$ compositions are an important criterion to fabricate low loss spot size converters and polarization filters. The great advantage of the $In_{1-x}Ga_xAs_yP_{1-y}$ material system is the ability to modify its bandgap and keeping the lattice constant matched to InP. Because of that it is possible to grow $In_{1-x}Ga_xAs_yP_{1-y}$ lattice matched to InP with different refractive indices. A modified single-effective-oscillator method [128, 129, 130] is described to calculate the dependency of the refractive index on the different concentrations of the four elements. Since the $In_{1-x}Ga_xAs_yP_{1-y}$ layers are implemented in passive devices, the material bandgaps are restricted to non-active

regions.

The lattice constant of $In_{1-x}Ga_xAs_yP_{1-y}$ has to be matched to the lattice constant of InP (a_0=5.8669 nm) to guarantee a minimum amount of defects. It has been shown that Vegard's Law can be utilized to set the gallium and arsenic mole fractions, x and y respectively, to ensure lattice matching [131].

$$x = \frac{0.452y}{1 - 0.031y} \tag{8.1.1}$$

The band energy of $In_{1-x}Ga_xAs_yP_{1-y}$ depends on x and y approximately as [132]

$$E_g(in\ eV) = 1.35 + 0.668x - 1.068y + 0.758x^2 - 0.069xy - 0.332x^2y + 0.03xy^2 \tag{8.1.2}$$

For the entire composition range of $In_{1-x}Ga_xAs_yP_{1-y}$ lattice matched to InP, neither a miscibility gap nor indirect bandgap semiconductor compounds exist, making this material ideally suited for optical sources and detectors in the infrared wavelength range. In our case the refractive index is restricted to the transparent region. With the single oscillator energies [128],

$$E_0(in\ eV) = 0.595x^2(1 - y) + 1.626xy - 1.891y + 0.524x + 3.391 \tag{8.1.3}$$

$$E_d(in\ eV) = (12.36x - 12.71)y + 7.54 + 28.91 \tag{8.1.4}$$

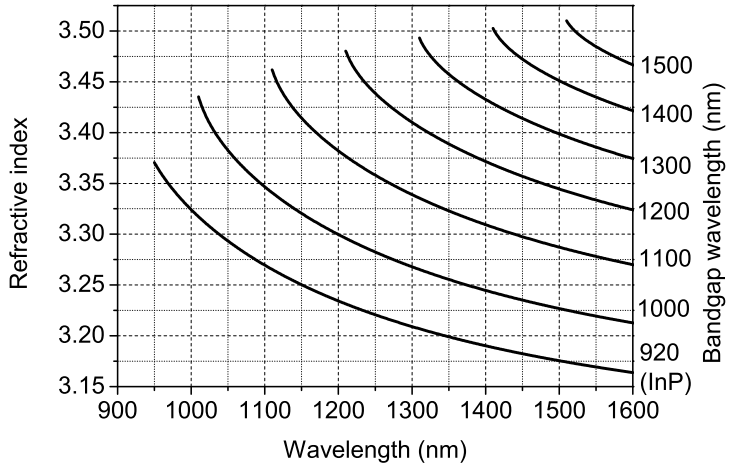
the refractive index for a photon energy E can be calculated:

$$n(E) = \sqrt{1 + \frac{E_d}{E_0} + \frac{E_d E^2}{E_0^3} + \frac{\eta E^4}{\pi} \ln \frac{2E_0^2 - E_g^2 - E^2}{E_g^2 - E^2}} \tag{8.1.5}$$

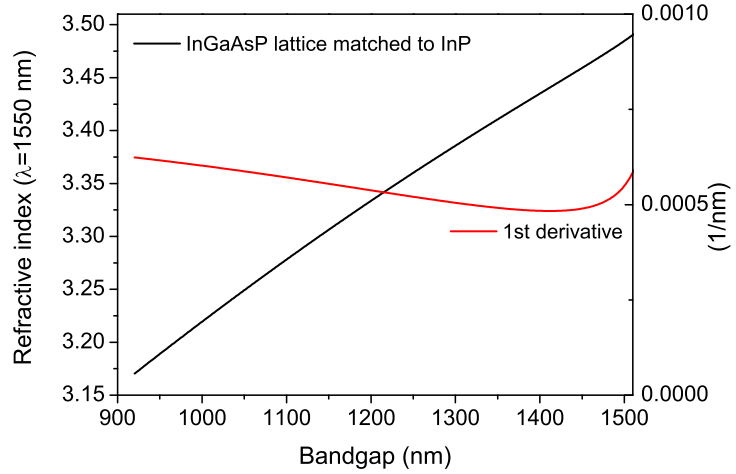
with

$$\eta = \frac{\pi E_d}{2E_0^3(E_0^2 - E_g^2)} \tag{8.1.6}$$

In Fig 8.1(a) the wavelength dependency of the refractive index for different bandgap wavelengths is displayed. As the bandgap wavelength increases, so too does the refractive index. In this thesis, the relevant wavelength is 1550 nm. The refractive index behavior at that wavelength relative to the bandgap can be observed



(a)



(b)

Figure 8.1: *Refractive index of InGaAsP lattice matched to InP (a) versus wavelength in the transparent region (b) versus bandgap wavelength for a fixed wavelength of 1550 nm*

in Fig 8.1(b). It can be noticed that the refractive index range is restricted between 3.17 (InP) and 3.50.

To obtain the refractive indices of the passive ATG (Chapter 4 and 5), 3.33 for the large spot size input waveguide and 3.4 for the small spot size upper waveguide at a wavelength of 1550 nm, equation 8.1.5 with the lattice matching condition (eqn. 8.1.1) are used. The two compositions are $In_{0.789}Ga_{0.211}As_{0.46}P_{0.54}$ and $In_{0.705}Ga_{0.295}As_{0.64}P_{0.36}$. The corresponding bandgap wavelengths are $\lambda_g = 1200$ nm $\lambda_g = 1330$ nm.

8.2 Measurements of $In_{1-x}Ga_xAs_yP_{1-y}$ Refractive Indices

In the last section it has been outlined how the $In_{1-x}Ga_xAs_yP_{1-y}$ composition can be adjusted to a desired refractive index. However, the metalorganic vapor phase epitaxy (MOVPE) growth is restricted to only a certain range around the desired composition. Therefore, an accurate refractive index measurement of the grown $In_{1-x}Ga_xAs_yP_{1-y}$ epi layers is important.

A method is described that enables refractive index calculations without the knowledge of the exact epilayer thickness. Since a measurement of the layer thickness, e.g. through SEM images, involves an uncertainty of several percent, the uncertainty gets transferred to the refractive index. The well established reflection spectroscopy technique avoids the thickness factor. This technique has been used to measure the refractive indices of different quarternaries.

8.2.1 Measurement Method

The chosen method, the reflection spectroscopy technique, is based on constructive and destructive interference and has been frequently used to measure the refractive index of different compositions [133, 134, 135, 136]. The reflection spectroscopy technique requires an up to 2 μm $In_{1-x}Ga_xAs_yP_{1-y}$ epilayer on an un-doped InP substrate. The epilayer forms a Fabry-Pèrot etalon on top of the substrate. Reflections

occur at two intersections. First, the incident beam is reflected at the air/epilayer interface. Secondly, the epilayer-substrate intersection causes an additional reflection beam. The two beams interfere destructively or constructively depending on the optical thickness. Extrema occur when the optical thickness equals an integral number of quarter-wavelengths:

$$n(\lambda_m)d = \frac{m\lambda_m}{4} \tag{8.2.1}$$

$n(\lambda_m)$ is the epilayer refractive index at the position of the extremum m. d is the thickness of the epilayer. If m corresponds to an integer even number of the wavelength the fringe minima represent the air/substrate reflection. The maxima are represented by odd numbers of m and represent a quarter-wavelength of the epilayer. The refractive index of the epilayer is then given by

$$n(\lambda_m)^2 = n_0 n_s \left(\frac{1 + r_s\sqrt{M_m}}{1 - r_s\sqrt{M_m}} \right) \tag{8.2.2}$$

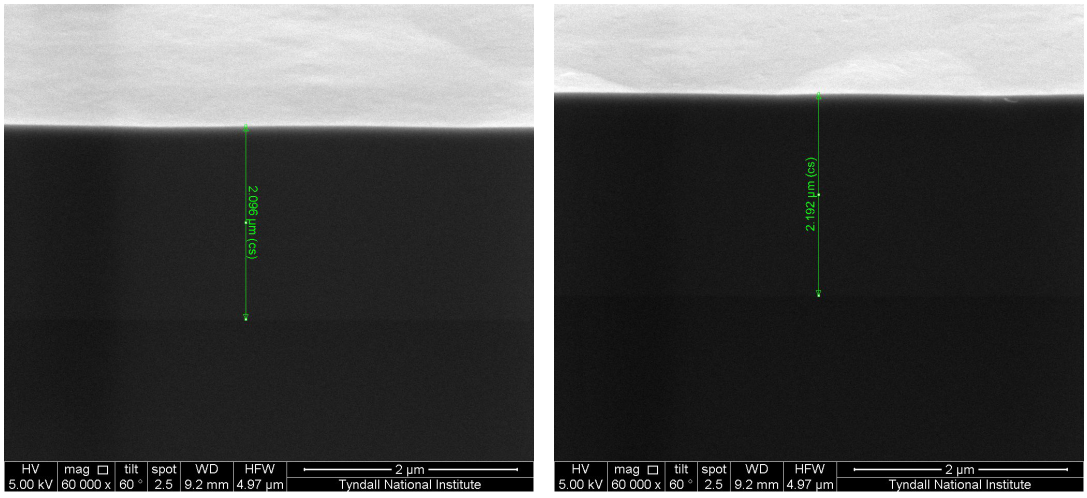
r_s is the amplitude reflection of the air/substrate interface. M_m is the fringe amplitude, the ratio of the local reflectivity minima and maxima. The fringe amplitude is calculated at every wavelength by interpolating between the two adjacent reflectivity extrema.

$$M_m = \left(\frac{R_{m-1} + R_{m+1}}{2R_m} \right)^{(-1)^m} \tag{8.2.3}$$

At the band edge of the epi layer, absorption occurs, and this method cannot be used. However, the investigated epimaterial is intended to be part in a passive waveguide. Therefore, the reflection spectroscopy technique is well suited to measure the refractive index.

8.2.2 MOVPE Growth A0983

The 50 nm high refractive index InGaAsP layer in the diluted 6 μm spot size input waveguide has been designed to have a refractive index of 3.33. Using the modified oscillator model (Sec. 8.1) leads to a composition of $In_{0.789}Ga_{0.211}As_{0.46}P_{0.54}$ with a bandgap of 1200 nm. The MOVPE growth, especially of quarternaries, requires the control of several parameters such as the gas flows and the temperature.



(a) **(b)**

Figure 8.2: *SEM images of run A0983: (a) InGaAsP epi layer on InP substrate at the center of the wafer (b) InGaAsP epi layer on InP substrate at the edge of the wafer*

Therefore, divergences in the obtained bandgap and in the composition might happen and the actual refractive index differ from the intended one. Since the refractive index is an important issue to guaranty good coupling efficiency to the upper, small spot size waveguide, the refractive index of the grown epimaterial has to be determined.

A 2 μm layer was epitaxially formed on a semi-insulating InP substrate. The wafer was cleaved into four 1/4 wafers and each of them was halved to obtain information about the epilayer thickness. In Fig. 8.2(a), a SEM image of the wafer center and in Fig. 8.2(b) a SEM image of the wafer edge are shown. It can be observed that the epi material is slightly thicker by 100 nm than the intended 2000 nm in the center of the wafer. Additionally, the epilayer is 2200 nm thick at the edges of the wafer. This indicates a higher growth rate at the edges than in the center. Also a closer look on the surface reveals an imperfectly homogenous morphology. The slight roughness can result in additional scattering losses in the reflection measurement. The non-uniformity in the epi-layer thicknesses also makes the reflection spectroscopy technique the best option to compute the refractive indices since the layer thickness is not required.

The reflection measurement were done with a Perkin Elmer Lambda 950 spec-

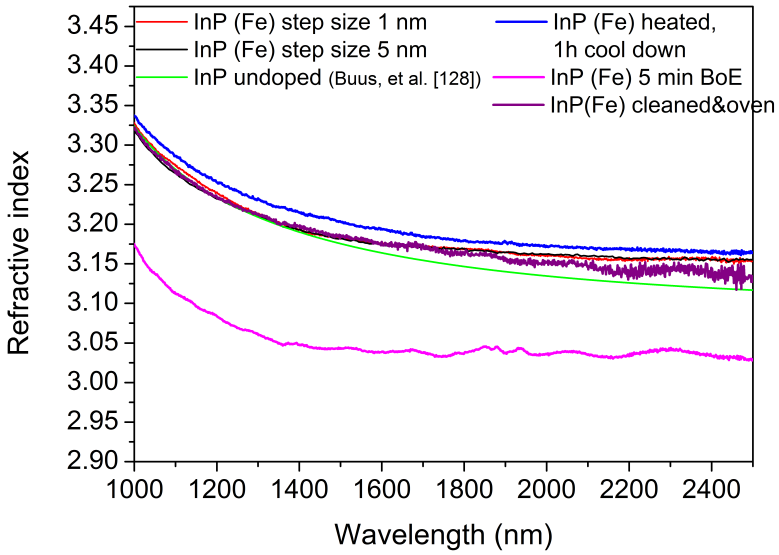


Figure 8.3: *Refractive indices of the InP substrate calculated from the reflection measurements*

trometer. This model is designed as a high precision measurement tool for wavelengths up to 3000 nm. Several samples were measured. The measurement position was either close to the center or to the edge of the wafer. The reflection of an unmodified piece of the semi-insulating InP substrate that was used for the growth run was recorded to get a reference point.

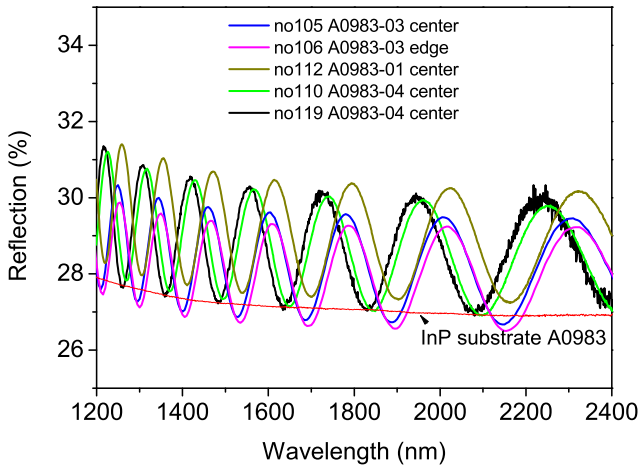
In Fig. 8.3 the calculated refractive indices of these measurements are displayed. Since the bandgap energy of the investigated wavelength region is lower than the bandgap energy, equation 8.2.4 can be used. n_{Air} has been set to 1.

$$R = \left(\frac{n_{InP} - n_{Air}}{n_{InP} + n_{Air}} \right)^2 \tag{8.2.4}$$

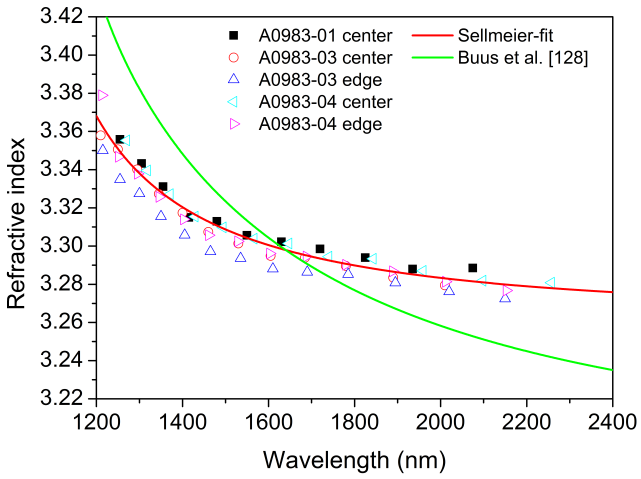
Several measurements at different times and positions were done to check the repeatability of the measurement. It can be seen that similar results can be obtained independent of the measurement time or step size. The chip was heated to 90 ° for one hour and was cooled down for another hour to determine if a small amount of moisture on the chip's surface might effect the results. A small shift to a higher index can be seen. This is most likely due to the fact that the sample had not reached room temperature and therefore the bandgap was decreased. The bandgap

decrease causes a slightly higher refractive index. Another issue that could disrupt the reflection measurement is the thin oxide layer on the InP-substrate. This layer is related to the natural oxidation of InP under atmospheric conditions. An oxide layer can be easily removed by diluted hydrofluoric acid. Hydrofluoric acid does not affect InP or InGaAsP. After dipping the substrate chip into the etchant for five minutes the chip was rinsed by deionized water. Nevertheless, the graph shows a reduction of the refractive index by more than 0.1 over the whole wavelength range. This can only be explained by some residuals remaining on the surface. This assumption is also confirmed by an additional measurement where the sample was rinsed again and heated in the oven up to 90 ° to remove any residuals. After this treatment nearly the same curve was recorded as in the previous measurements. A literature value of the refractive index of un-doped InP [137] is plotted for comparison. It can be observed that the calculated values match very well with the theoretical values in the range of 1100 to 1600 nm. The calculated refractive index is slightly higher (≈ 1 %) for longer wavelengths. This can be justified by a small index modification caused by the Fe dopants or by a negligible error in a wavelength region that is not important for the device, since the operating wavelength is at 1550 nm. Nevertheless, the calculated refractive index values were used for the following steps.

Fig. 8.4(a) shows the reflection measurements and Fig. 8.4(b) the resulting refractive indices of the 2 μm InGaAsP (λ_g = 1160 nm) layer. In Fig. 8.4(a) a dependency of the fringe wavelength position and of the reflection value can be observed. The minima of measurements 110 and 119 show a very good overlap with the InP substrate reflection. This corresponds well with previously outlined theory. Furthermore, the extrema positions and values of both scan nearly overlap. These measurements were taken at the center of the wafer. The center place is assumed to have the optimum growth conditions. As a result the lowest scattering losses are present there. Measurement numbers 105 and 106 on the other hand show reflection minima values that are lower than the InP substrate. This is an indication that additional scattering loses are present at these positions. Especially on the edge of the wafer the inhomogeneous growth could have caused more surface roughness. The roughness (shown in Fig. 8.2) is most likely the reason for the lower minima



(a)



(b)

Figure 8.4: *A0983: (a) Reflection measurements at different positions (b) Calculated refractive indices and Sellmeier-fit*

values. The reduced minima value at the center position of no. 105 might be due to roughness inflicted by chip handling. The increased reflection values in no.112 should be related to possible residuals on the sample's surface.

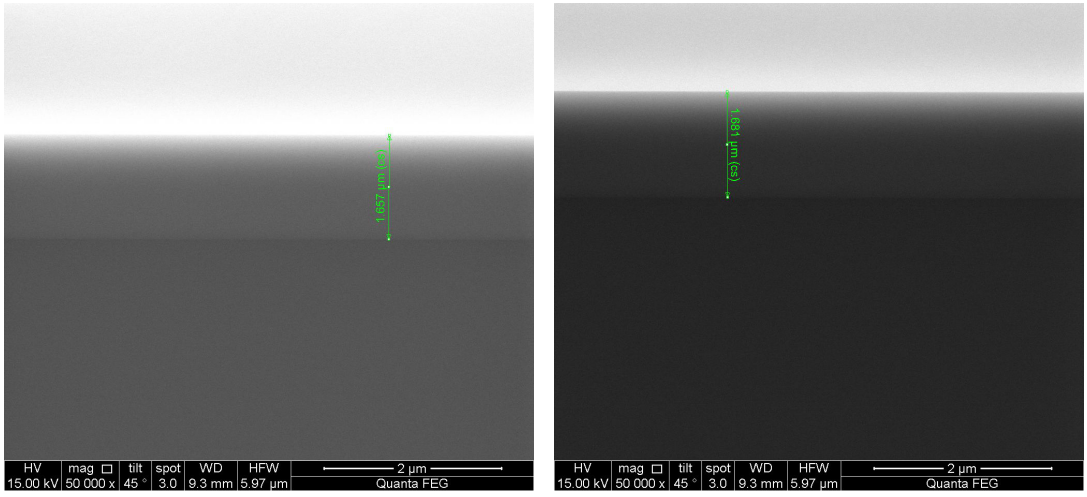
Now, the peak values and formulas 8.1.5 and 8.1.6 can be used to compute the refractive index at the corresponding wavelength points. Fig. 8.4(b) show these values. A modified, single term Sellmeier equation has been applied to fit the obtained refractive index points. Comparison of the fit with the theoretical refractive

index values for a composition of $In_{0.805}Ga_{0.195}As_{0.415}P_{0.585}$, obtained from XRD and PL measurements, confirms a good agreement (difference < 1 %) in the relevant wavelength region from 1400 to 1800 nm. The increasing difference at shorter and longer wavelengths can be caused by difference effects, such as defects, a not perfectly lattice matched layer or substrate effects. Nevertheless, at the telecommunication wavelength of 1550 nm the calculated index value of 3.30 can be taken as accurate and the quaternary layer thicknesses can be adjusted to this value.

8.2.3 MOVPE Growth A1034

The second $In_{1-x}Ga_xAs_yP_{1-y}$ composition that has been investigated is the composition of the matching layer in the design of the PD with the integrated SSC (Chapter 7.1). Because the matching layer improves the overlap of the InGaAs absorber with the coupling waveguide, knowing the matching layer's refractive index is crucial to design a structure with a high absorption efficiency and a short PD length.

The matching layer also acts as a n-contact for the PD. Therefore, the $In_{1-x}Ga_xAs_yP_{1-y}$ layer has to be doped and the effect of additional carriers on the bandgap has to be taken into account. Bennett et al. have outlined that three effects are the main contributors to the bandgap in InP/InGaAsP systems [138]. The three effects are bandfilling, band-gap shrinkage, and free-carrier absorption. Bandfilling and free-carrier absorption reduce the refractive index, whereas band-gap shrinkage always increases the index for energies below the bandgap. The contribution of the three effects dependes on the carrier concentration and similar for p- and n-type dopants. In our case the doping is around $2*10^{18}$ cm^{-3} and bandfilling is dominant over shrinking effects. Therefore, a reduction of the refractive index in the range of 10^{-2} has to be considered.

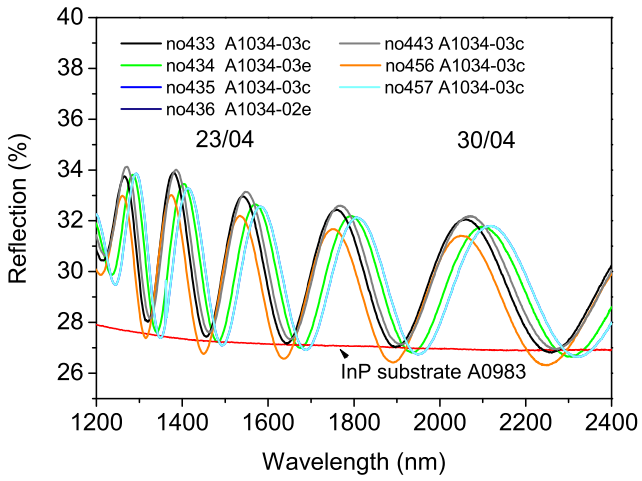


(a) **(b)**

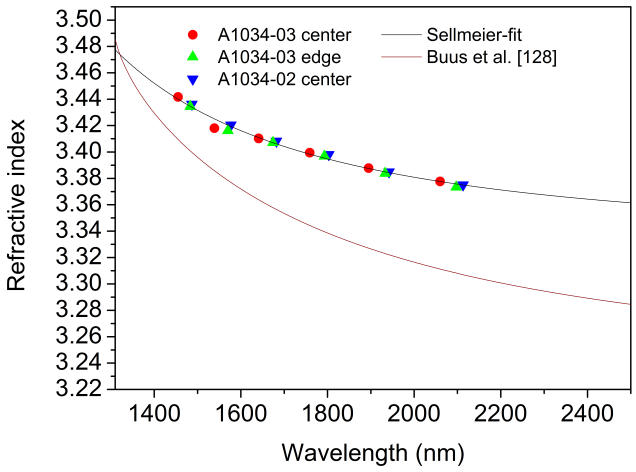
Figure 8.5: *SEM images run of A1034: (a) InGaAsP epi layer on InP substrate at the center of the wafer (b) InGaAsP epi layer on InP substrate at the edge of the wafer*

Fig. 8.5 shows SEM images of the single layer growth on InP semi-insulating substrate. It can be observed that the thickness is reduced by 15 %. The measured thickness is 1.7 μm. However, no height difference can be seen between the position at the center of the wafer and its edge. Furthermore, the roughness notice at growth run A0983 cannot be observed either.

Growth run A1034 has been done on semi-insulating polished substrate. The polished substrate results in an additional reflection at the substrate air interface. The measured reflection spectrum is now a superposition of the air/epilayer, the epilayer/substrate and the substrate/air reflection. To obtain reliable data the substrate/air reflection has to be incorporated or suppressed. The best option is to suppress this reflection. That has been done by roughening the polished substrate. The roughening was done with a PM5 lapping and polishing system provided from Logitech Ltd.. Al_2O_3 with a particle sice of 20 μm dissolved in water was the polishing solution. The measured roughness average roughness R_a and the root mean squared roughness R_q at measured with a Dektak stepper has been 1400 and 1700. Comparison of these values to the measured values of unpolished substrate (R_a = 900, R_q = 1100) justifies the assumption there is not anymore substrate/air reflection.



(a)



(b)

Figure 8.6: *A1034: (a) Reflection measurements at different positions (b) Calculated refractive indices and Sellmeier-fit*

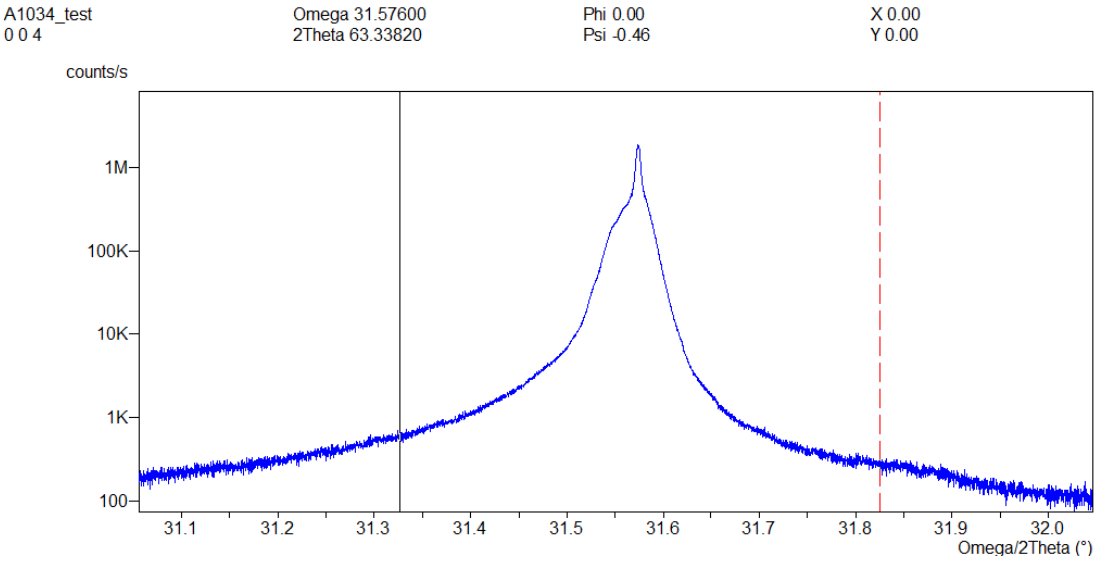


Figure 8.7: *Rocking curve of chip A1034*

Fig. 8.6(a) shows the reflection measurements. Two pieces from a halved 1/4 wafer have been measured. In all measurements except no. 456 the minima matches perfectly with the reflection obtained from an InP substrate. The reduced reflection values in no. 456 could be caused by a not well aligned chip on the spectrometer. Nevertheless, the rest of the measurements overlap reasonably well and can also be repeated.

Although the substrate of growth run A1034 is not exactly the same as in run A0983, it has the same specification. A measurement of a different semi-insulating substrate (Fig. 8.3 dark yellow line) shows the same reflection spectrum. Therefore, using the InP substrate values of run A0983 is justified.

The extrema positions can now be used to calculate the refractive index again. The index values and their Sellmeier-fit are displayed in Fig. 8.6(b). The theoretical value of an un-doped InGaAsP composition with the same bandgap value of 1300 nm lattice matched to InP is drawn as a reference. It can be noticed that the Sellmeier-fit lays above the theoretical refractive index values over the whole wavelength section. This result is contrary to the previously outlined effect of a dopant concentration of $2*10^{18}$ cm^{-3} and requires explanation. An increase of the refractive index can only be caused by modifications in the bandgap energy, assuming there are not any other pollution effects present. One way to get additional information

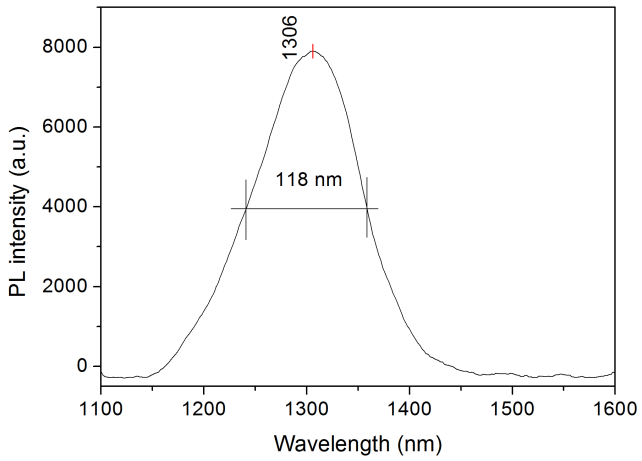


Figure 8.8: *Photoluminescent measurement of chip A1034.*

about the epilayer is by inspecting the x-ray diffraction (XRD) rocking curve. The rocking curve can be seen in Fig. 8.7. The InP substrate peak is the highest peak with a small bandwidth. However, the peak of the 1.7 μm thick InGaAsP epilayer can not be clearly seen, instead a broad peak overlapping with the substrate peak is shown. This broad XRD peak was caused by non-uniform strain in the material [139]. The assumption of non-uniform strain and defects lead to the conclusions that there was a large number of energy states in the bandgap structure or different compositions with different bandgaps are present. Furthermore, the room temperature photoluminescent measurement (PL) (Fig. 8.8) shows a peak value of around 1300 nm. However, the full width at half maximum (FWHM) was 90 meV ($\Delta(\lambda) =$ 118 nm). In general, FWHM values of 40 meV were reported for InGaAsP lattice matched to InP at room temperature [140].

These effects explain the calculated refractive indices. Therefore, a calculated refractive index of 3.42 can be used to design the final layer structure.

8.3 Conclusion

The reflection spectroscopy technique has been used to determine the wavelength dependent refractive indices of two different InGaAsP compositions. For the assumed composition $In_{0.805}Ga_{0.195}As_{0.415}P_{0.585}$ with a bandgap of 1160 nm (A0983)

a refractive index of 3.30 at a wavelength of 1.55 μm has been obtained. This value matches very well with the theoretical value of 3.31.

The refractive index of growth run A1034 does not agree well with the expected theoretical value. Nevertheless, the difference can be explained by possible strain and defects in the epilayer. Furthermore, the reproducibility of this composition is guaranteed even for several hundred nanometer layers. Therefore, the calculated refractive index value can be used for the matching layer in the final PD-SSC structure.

The refractive indices in the simulation of the PD-SSC structure have been adjusted to the obtained values. The layer thicknesses were modified to compensate for the difference in the refractive indices. The InGaAsP layer thickness in the diluted input waveguide has been increased from 50 to 55 nm. The matching layer thickness has been reduced from 300 to 200 nm. With these modifications absorption efficiencies of 85 % and 81 % for the TE- and TM-polarization respectively are achievable by a 3 μm wide and 100 μm long InGaAs-PD.

Chapter 9

Device Fabrication

The development steps necessary to obtain a repeatable process and a good asymmetric twin waveguide (ATG) structure are described. Several process steps needed to be developed and optimized to fabricate an integrated SSC based on an ATG. These development steps and the optimized fabrication are shown here.

The starting point was a process using a SiO_2/Si_3N_4 etch mask. First, the process steps are outlined. Following this, problems during the Si_3N_4 mask step such as a resolution limit of 0.5 μm and cracks on the Si_3N_4 surface are presented. It is shown that the inductively coupled plasma (ICP) recipes available in-house were not suitable for the fabrication of smooth and vertical sidewalls.

Because of the tight resolution and the poor Si_3N_4 quality, a new process with a SiO_2/Titanium mask was applied. These process steps are also outlined. The importance of the photoresist in obtaining a vertical SiO_2 etch mask is shown. This vertical etch mask was essential to eventually etch vertical and smooth InP/InGaAsP waveguides.

For the SiO_2/Titanium mask process the $Cl_2/CH_4/H_2$ ICP etch was intensively studied in a 2^k factorial Design of Experiment (DoE). A temperature dependent passivation effect of CH_4 was found. Finally, the $Cl_2/CH_4/H_2$ = 10/18/12 sccm chemistry permitted the etching of smooth and vertical sidewalls.

In the final part of Chapter 6, images of the optimized process steps for fabricating polarization filters are shown. In addition, the possibility of integrating a SSC with a photodiode is demonstrated using the optimized process steps.

The equipment used in this work is presented in Tab. 9.1. Standard processes were used to deposit SiN_x by plasma enhanced chemical vapor deposition (PECVD) and SiO_2 by either sputtering or PECVD. Furthermore, the metal evaporation steps were not modified. The patterning of the dielectrics was done with an ICP etch tool using a CF_4/CHF_3 based chemistry.

Table 9.1: *Process equipment used at Tyndall National Institute*

Process step	Equipment	Manufacturer
Lithography	Contact Mask Aligner MA6 Contact Mask Aligner MA1006	Karl Süss
Dielectrics	Sputterer Plasmalab System 400 PECVD	Oxford Instruments Surface Technology Systems
Metal evaporation	Electron beam evaporater	Temescal
Dry etching	310 PC Plasmalab System 100	Surface Technology Systems Oxford Instruments

9.1 Simplified Alignment Process with a SiO_2/Si_3N_4 Etch Mask

Fabrication of the previously simulated design is important to experimentally verify the simulation results. In this section the development steps and the critical aspects of the process run with a SiO_2/Si_3N_4 etch mask are explained. The process is designed in such a way that both etch masks are formed before any semiconductor etch. This simplifies the alignment and the lithography because the height difference is only in the range of several hundred nanometers instead of several microns. The first process runs were focused on fabricating the resonant coupler shown in section 4.2. An important issue is the waveguide width as already previously outlined. Special care must be taken to obtain a taper end width of 0.5 μm. The sidewall roughness must also be low to reduce the waveguide losses in the passive ATG structure.

9.1.1 Process Outline

The schematic of the simplified alignment SiO_2/Si_3N_4 (SIOSIN) process is shown in Fig. 9.1. The fabrication started with a deposition of a 250 nm SiN_x layer on the epi-material. This layer acts as an etch mask for the taper part of the ATG. Plasma enhanced chemical vapor deposition (PECVD) was used to deposit the 250 nm of Si_3N_4 layer. The process was at a temperature of 300 °C. The detailed process parameters for this and all the further steps are listed in Appendix B.

The next step was the patterning of the dielectric layer. For this, a photoresist pattern needed to be formed on top of the dielectric (Fig. 9.1(a)). This pattern enables removal of the SiN_x at the uncovered areas and preserves the SiN_x under the covered areas. Deep UV (DUV) photoresist and the corresponding MA6 mask aligner are necessary to pattern Si_3N_4 with a desired maximum resolution of 0.5 μm. The Si_3N_4 was etched in an inductively coupled plasma (ICP) system with a CF_4/CHF_3 chemistry.

After the SiN_x was patterned and the remaining resist was removed (Fig. 9.1(b)), a 400 nm thick layer of SiO_2 was deposited either by the PECVD or by sputtering. This layer underwent a similar lithography as the previous SiN_x. The 400 nm thick SiO_2 acted as an etch mask for the lower, large spot size waveguide (Fig. 9.1(c)).

The etch mask is an important step to form a 1 μm deep and 2.5 μm to 0.5 μm wide ridge waveguide on top of a 6 μm wide and 5 μm deep second waveguide ridge by dry etching. Since inductively coupled plasma (ICP) etches have a physical etch component the mask is also etched (indicated in Fig. 9.1(d)). Because of this the etch mask must have a certain minimum thickness. Because the etch mask must be patterned by photo-lithography, the mask maximum thickness is limited to half the photoresist thickness in order to obtain a vertical mask.

With the patterned 400 nm thick SiO_2 on top of the 250 nm SiN_x, the chip is now prepared to be etched to define both ridges. An ICP dry etch system was used to create vertical sidewalls in the semiconductor. A second etch option would have been wet chemical etching. However, only V- or $\wedge$-shaped ridges, depending on the crystal orientation, are obtained with this method. Furthermore, wet etches are isotropic and an undercut relative to the etch mask occurs. Therefore, the samples

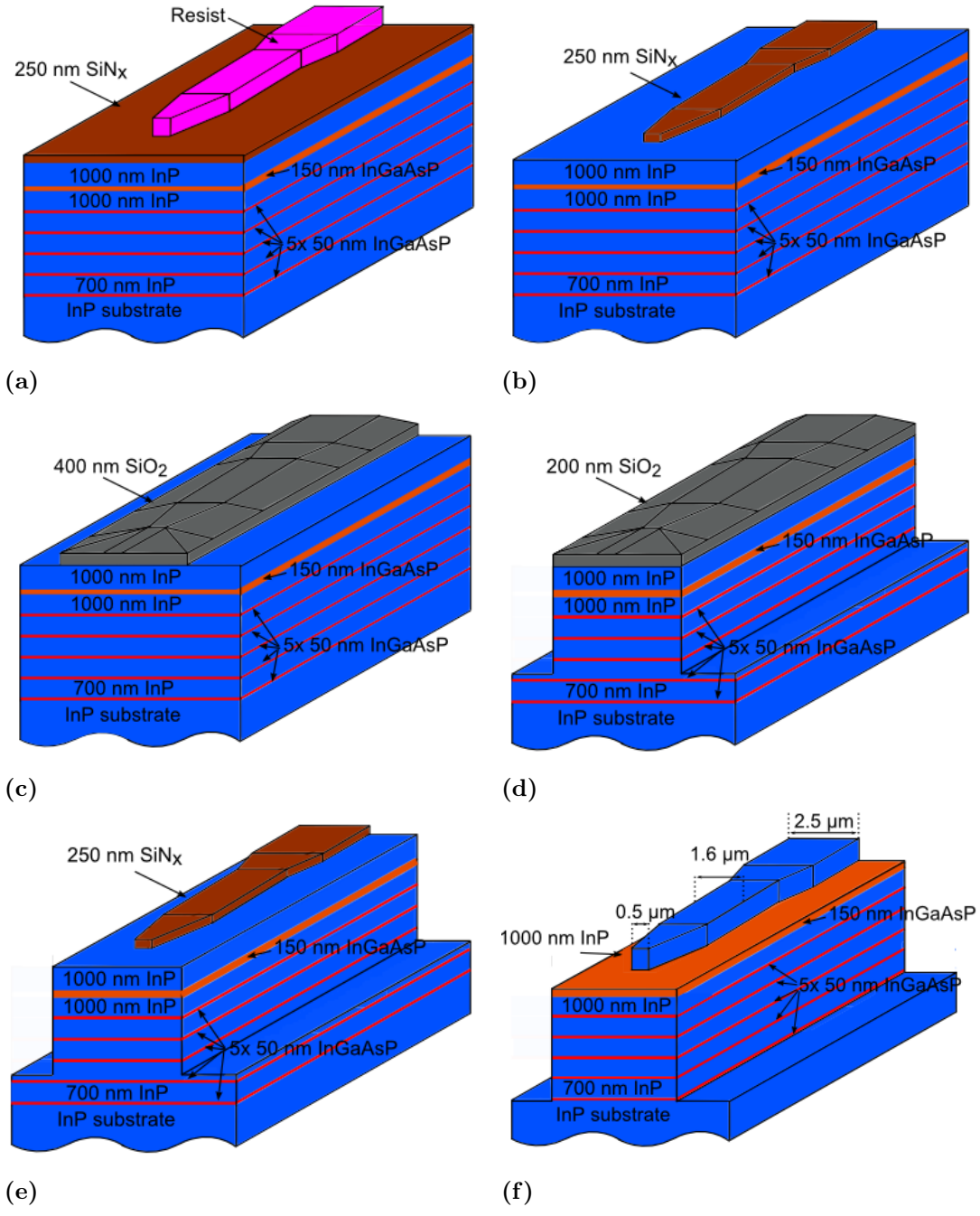


Figure 9.1: *Consecutive process steps used, (a) after the first lithography step, (b) after the SiN_x mask is patterned, (c) after the SiO_2 layer is patterned, (d) after the first 4µm deep III-V material ICP etch, (e) after the overlaying SiO_2 mask is removed by wet chemical etching, (f) the final ATG structure with the SiN_x mask removed.*

were dry etched. The required etch depth in the first etch step was around 4 μm (Fig. 9.1(d)).

Following this 4 μm deep etch the remaining SiO_2 must be removed without affecting the underlying SiN_x. Hydrofluoric acid (HF) is the primary choice for wet chemically removing SiO_2. However, HF also etches SiN_x. The chemical reactions are [141]:

$$SiO_2 + 6\,HF \longrightarrow H_2SiF_6 + 2\,H_2O$$

$$Si_3N_4 + 18\,HF \longrightarrow H_2SiF_6 + 2\,(NH_4)_2SiF_6$$

H_2SiF_6 and $(NH_4)_2SiF_6$ are soluble in water. Usually, HF is buffered to control the etch rate [142]. Here, such a buffered oxide etch (BOE) was used. Additionally, SiO_2 is etched significantly faster by BOE than SiN_x. In this case the etchant was further diluted by deionized H_2O. The rate of SiO_2 was usually around 0.6 nm/s, whereas the etch rate of SiN_x was roughly one order of magnitude smaller. Therefore, the SiO_2 was removable in principle without significantly etching the underlying SiN_x (Fig. 9.1(e)).

After the SiO_2 had been removed the chip was ready to undergo the second 1 μm deep ICP etch to define the upper waveguide ridge. Additionally, the large spot size lower waveguide etch depth was extended. When the ICP etch was finished a 60 s BOE dip was performed to dissolve the remaining SiN_x. This was the final step and an ATG as shown in Fig. 9.1(f) was fabricated.

9.1.2 Problems during the Si_3N_4 Patterning Step

The correct dimensions of the ATG are important to enable optimum coupling in between the two waveguides. Especially, in the case of resonant coupling, the fabrication tolerance is quite small (Chapter 4). Differently shaped couplers (Fig. 9.2) are fabricated to obtain information about what shapes and dimension of an ATG-based coupler can be obtained.

The first lithography and the following ICP etch are crucial steps to obtain the desired waveguide dimensions. Because the taper end width is 0.5 μm high

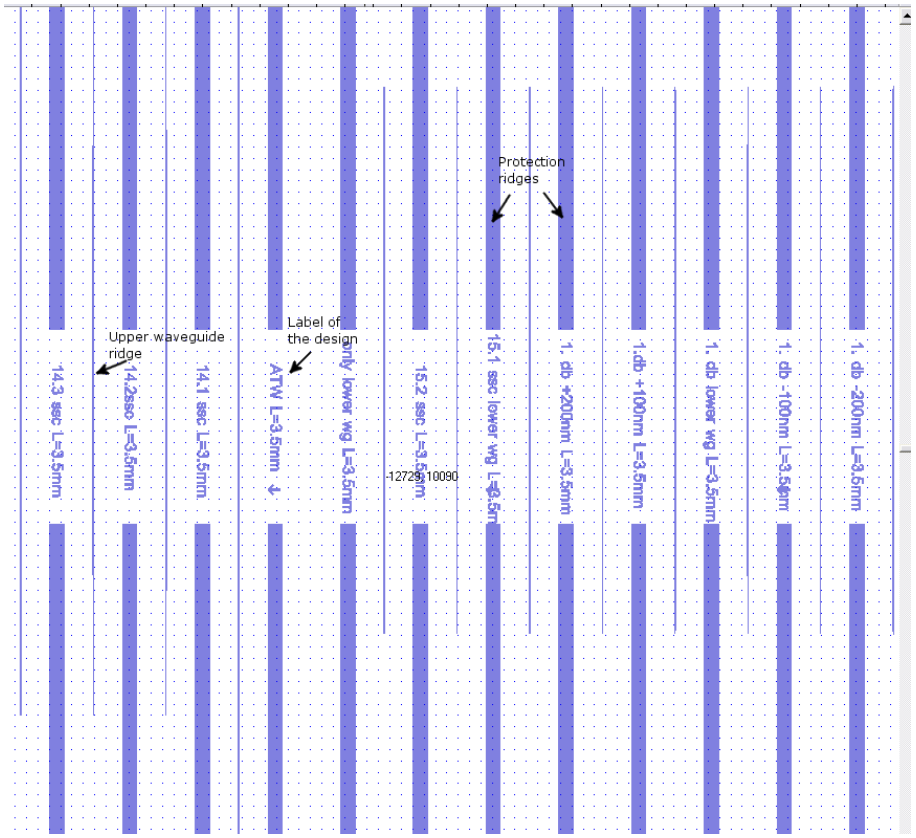


Figure 9.2: *Image of the first level lithography mask. A clear field mask is shown to define different shaped upper waveguides. This mask was used to obtain a resist pattern shown in Fig. 9.1(a).*

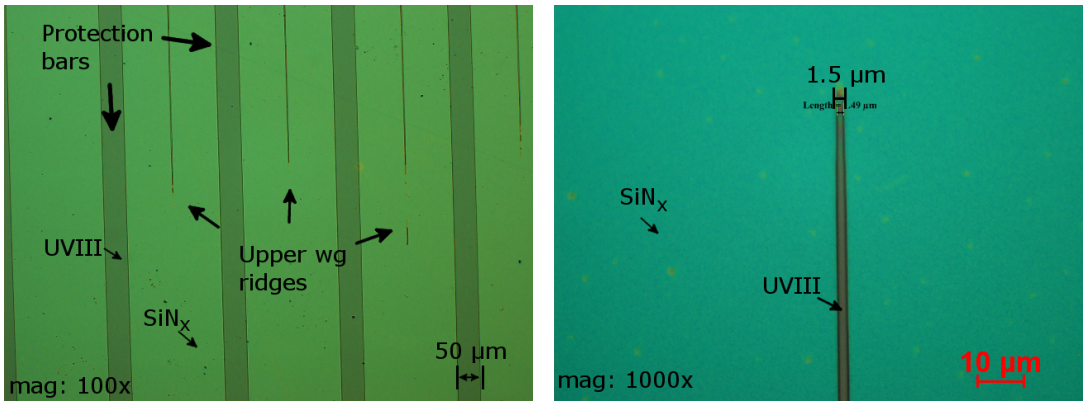
resolution deep ultraviolet (DUV) lithography is necessary. In the first test runs the resist UVIII from Rohm and Haas (Tab. 9.2) was used to define the mask for the SiN_x etch.

Because the lamp power of the mask aligner is mostly constant, the exposure time is modified to change the intensity on the resist. Microscope images of UVIII on SiN_x are shown in Fig. 9.3. The exposure time was 9.5 s. It can be seen that the exposure time was too long. The resist vanishes at a width of around 1.5 μm and the tapers do not have the intended length. Even at a exposure time of 3.5 s the expected minimum width of 0.5 μm was not possible. On the other hand an exposure time of 3 s was not enough to remove UVIII on the unwanted areas. Because of this, UVIII was replaced by the thicker DUV resist UV26.

Although the higher resist thickness prevents over-exposure at an exposure time

Table 9.2: *Photoresist properties [1, 2]*

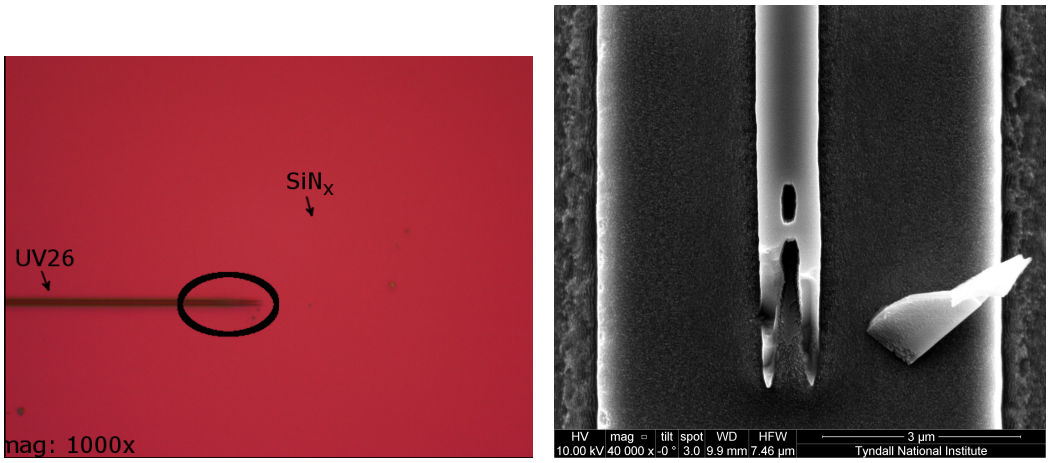
Photoresist	UVIII	UV26
Thickness (Å)	6000–8700	9700–25000
Minimum line spacing (μm)	0.25	0.35
Depth-of-focus (μm)	1.0	0.8



(a) **(b)**

Figure 9.3: *Microscope image of UVIII after an exposure of 9 s, (a) several ridges, (b) ridge end.*

of only a few seconds, several factors must be taken into account to enable a high resolution. One of those factors is the proximity of the chip to the exposure mask. If the mask is too far away an optimum exposure of the resist will not be possible. Either the resist ridges get wider than intended or diffraction occurs, especially at the 0.5 μm ridge ends (Fig. 9.4). The following reasons are responsible for a larger than desired spacing between the chip and the exposure mask. First, during the spinning of photoresist onto the chip, there is a build-up of material at the wafer edges. Because only a quarter wafer is used due to cost, the edge bead removal must be done manually and higher photoresist can remain at the edges than in the center. Second, dirt on the exposure mask has a similar effect. Third, the vacuum contact option of the mask aligner must be used to achieve close proximity between mask and sample. With this option, the chamber with the sample in it is evacuated. This guarantees a very short spacing between photomask and chip. However, also related to cost, four different mask elements are present on a single photomask. Therefore,



(a) **(b)**

Figure 9.4: *InP/InGaAsP chip, (a) microscope image after the first UV26 processing step (b) SEM image of a taper end of a poorly processed chip*

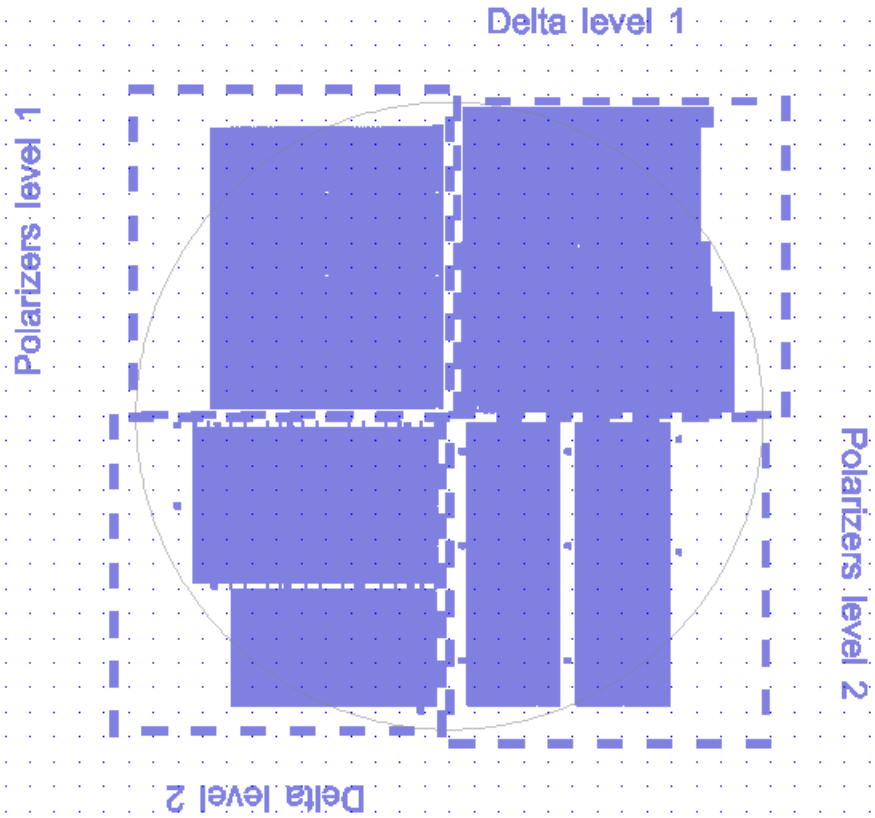


Figure 9.5: *Image of the 100 mm diameter two level polarization filter and two level delta mask. Four different mask elements are on a single mask.*

the sample cannot be at the designed position on the chuck (Fig. 9.6(a)). Instead,

the sample has to be off center. This causes holes that suck the sample onto the chuck to be uncovered. Because of this, additional chips must be placed on the chuck (Fig. 9.6(b)) to cover these holes and enable a good vacuum contact. The height



(a) **(b)**

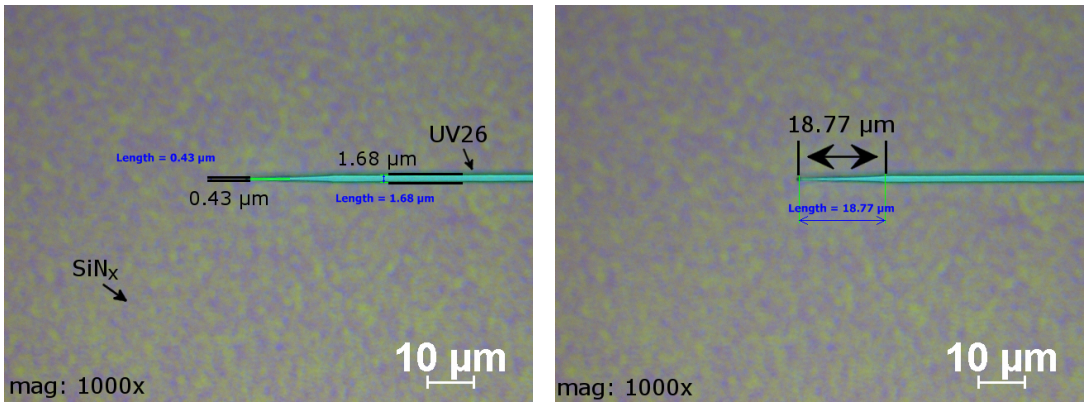
Figure 9.6: *Images of the MA 6 mask aligner, (a) quarter wafer chuck without a sample and with the indicated sample position (b) quarter wafer chuck with a sample and two cover chips*

of those cover chips must be smaller than the sample. However, if the height is too small the photomask might be slightly bent, resulting in a non optimum contact between the sample and the mask. Because not all of the holes are covered with a single chip it is hard to obtain a good vacuum in the sample chamber. A bad vacuum level also results in large mask/sample spacing.

In Fig. 9.7 it can be seen that a width of 0.5 μm is possible. The end width corresponds well, within the microscope tolerance, with the expected end width of 0.5 μm. The measured width of the mode beating section is only 100 nm wider than the intended width of 1.6 μm. Also, the measured length of around 19 μm matches the expected value of 20 μm.

However, many factors such as the resist quality, the edge bead removal, the cleanliness of the exposure mask, the vacuum contact quality and the exposure time correlated to the intensity of the mask aligner UV-lamp must be perfect to guarantee such a resolution. Therefore, the end width is increased to 1 μm to simplify processing.

The final reason why the SIOSIN process was eventually dismissed is related to



(a) **(b)**

Figure 9.7: *Microscope images of a properly processed InP test chip. The exposure time of UV26 was 11.5 s. (a) ridge width measurement, (b) taper section length measurement.*

the quality of the SiN_x mask. Cracks on the order of tenths of nanometers occurred in the SiN_x layer (Fig. 9.8). During the wet chemical SiO_2 removal, BoE will flow

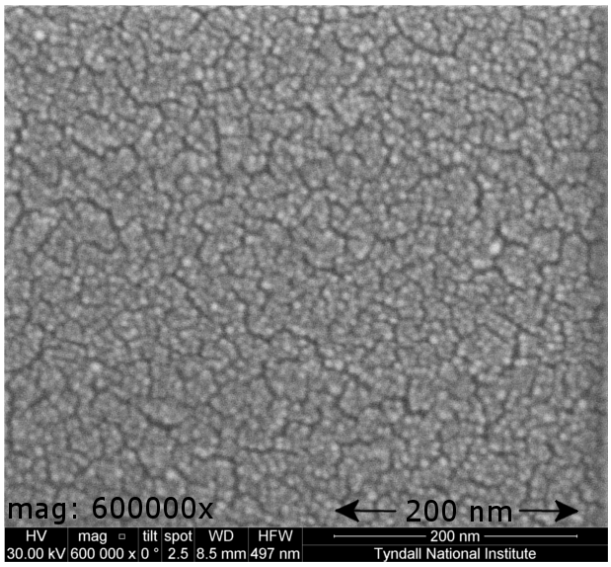


Figure 9.8: *PECVD deposited SiN_x on an InP chip.*

into those cracks. This causes an etch of the SiN_x mask, rough mask sidewalls and further a possible removal of the SiN_x mask at certain areas. This makes it nearly impossible to fabricate low loss waveguide tapers.

A possible explanation for the cracks can be found by focusing on the SiN_x deposition step. A PECVD process at 300 °C was used to deposit SiN_x. After this step the chip was cooled down rapidly to room temperature. However, InP

and SiN_x have different linear thermal expansion coefficients. At room temperature those coefficients are around 5*10^{-6} °C^{-1} (InP) [143] and 3.2*10^{-6} °C^{-1} (Si_3N4) [144]. The induced stress by different expansion coefficient during a fast cooling down could result in these cracks. The observed cracks are the reason why SiN_x was not used further.

9.1.3 Problems during the Inductively Coupled Plasma (ICP) Etch Step

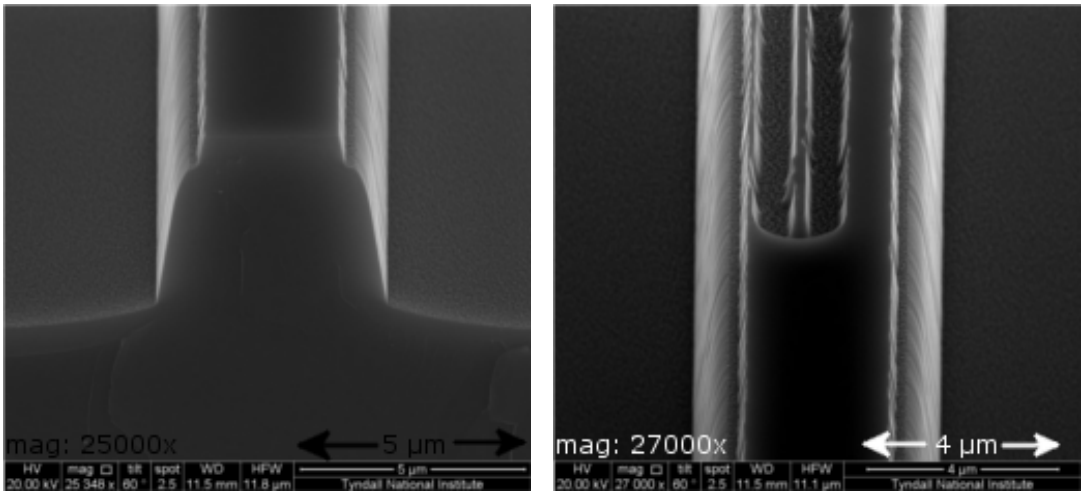
In house ICP recipes based on the CH_4/H_2 and Cl_2/N_2 chemistries were available (Tab. 9.3). However, an etch of 4 μm was not done before and the behavior of this etch was unknown.

Table 9.3: *Established ICP etch chemistries*

Chemistry	CH_4/H_2	Cl_2/N_2
Gas flow (sccm)	CH_4	Cl_2
	30	6
	H_2	N_2
	70	35
Platen power (W)	800	425
Coil power (W)	200	75
Pressure (mTorr)	25	95
Chuck temperature (°C)	90	170

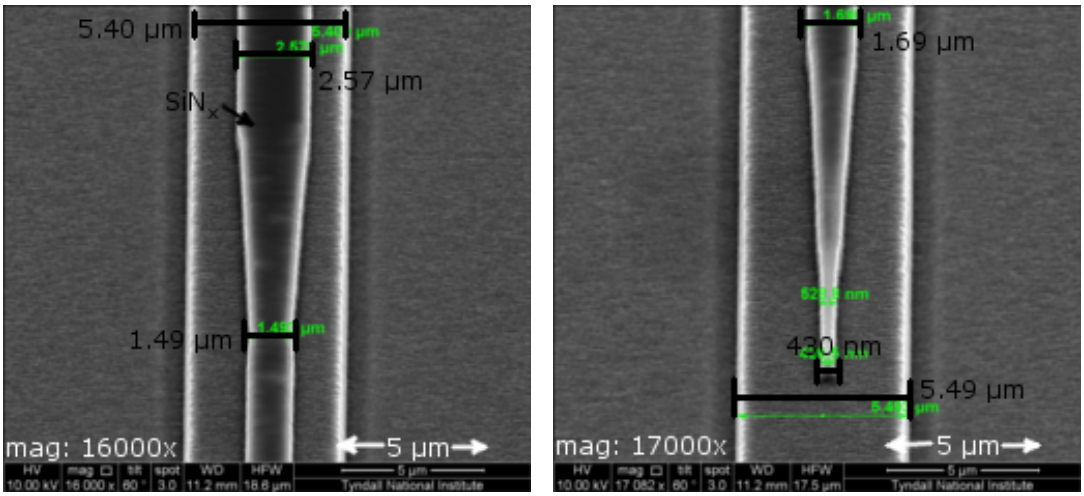
An InP test sample was prepared according to the process run in Fig. 9.1(a)-(c). The chip was etched for 10 min with the CH_4/H_2 chemistry. Fig. 9.9 shows SEM images of the InP-chip after the etch. It can be seen that the dielectric mask is completely removed (Fig. 9.9(a)) and that the upper waveguide ridge disappeared (Fig. 9.9(b)). Trenches were formed beside where the SiN_x mask might have been. The slow etch rate was related to the passivation properties of CH_4 explained later.

The Cl_2/N_2 chemistry was investigated as an alternative. Fig. 9.10 shows a resonant coupler after the upper waveguide etch (Fig. 9.1). The width of the upper



(a) **(b)**

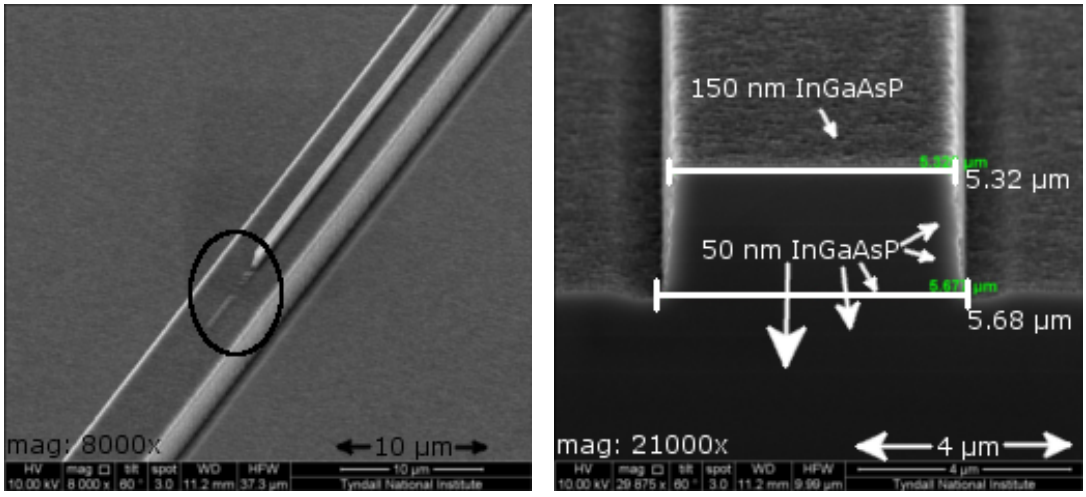
Figure 9.9: *Cross-section SEM images of an InP-chip after a 10 min CH_4/H_2 etch. (a) cross-section of the ridge, (b) top view.*



(a) **(b)**

Figure 9.10: *SEM images of a resonant coupler 200 nm wider than ideal after a 7 min 45 s and 2 min 45 s Cl_2/N_2 etch. (a) top view of the taper to the mode beating section, (b) top view of the end taper.*

waveguide was designed 200 nm wider than the ideal case. The taper from the wide upper waveguide to the mode beating section as well as the taper to a narrow end width can be seen. However, the upper waveguide width is reduced by roughly 200 nm compared to the value on the lithography mask. It is clear from the image that it is difficult to recognize the actual edge of the ridge. A different position of the

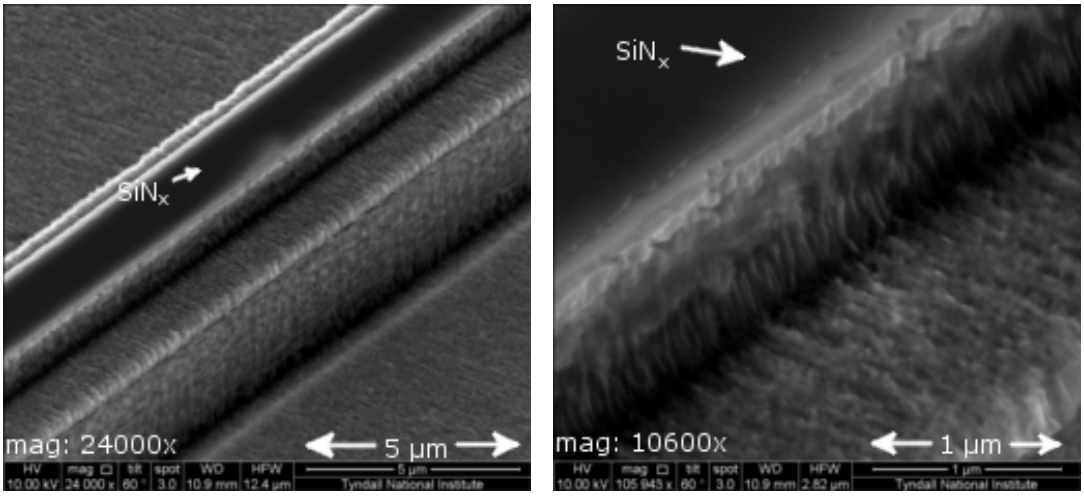


(a) **(b)**

Figure 9.11: *Cross-section SEM images after a 7 min 45 s and 2 min 45 s Cl_2/N_2 etch. (a) of a parabolically tapered down ridge, (b) front facet*

edge can cause a measurement difference of 200 nm for the mode beating section. The dark areas on the upper cladding ridge are related to remaining SiN_x. SiN_x starts to disappear and the ridge gets brighter towards the taper end (Fig. 9.10(b)). Furthermore, the removal of the etch mask towards the taper end results in a shorter and narrower last taper than intended. Fig. 9.11(a) shows a similar disadvantage of the Cl_2/N_2 chemistry. Originally, the upper cladding should have been parabolically tapered down to 0.5 μm over the same distance as the resonant coupler (211 μm). However, the upper ridge disappeared several microns before its intended end point. Additionally, the cross section in Fig. 9.11(b) demonstrate that the lower waveguide ridge is not quite vertical. The sidewall of an ATG is shown in Fig. 9.12. It can be seen that the sidewalls are very rough. This causes high waveguide losses.

The several hundred nanometer reduced width of the upper waveguide, the high temperature, and the sidewall roughness and its slope lead to the conclusion that the Cl_2/N_2 chemistry is also not an option for fabricating a low propagation loss ATG. Therefore, $Cl_2/CH_4/H_2$ is investigated as an alternative. This investigation and its results are shown in section 9.3.



(a) **(b)**

Figure 9.12: *Cross-section SEM images of a constant ATG after a 7 min 45 s and 2 min 45 s Cl_2/N_2 etch. (a) sidewall of the upper and lower waveguide , (b) sidewall of the upper waveguide.*

9.2 Simplified Alignment Process with a SiO_2 and Titanium Mask

Here, a second fabrication process scheme is discribed that fulfills the same requirements as the first one, such as simplified alignment, precise dimensions and smooth sidewalls. However, the ridge end width is now at 1.0 μm. Therefore, the maximum resolution of the mask aligner is not necessary, and the fabrication is simplified. In this process SiN_x is replaced by a Ti mask. Wet chemical etchants are only used in the last step. The simplified alignment process with a SiO_2 and Ti mask (SAPSIOTIM) is applied to fabricate polarization filters (Chapter 5 and Chapter 6) and eventually PDs with SSCs (Chapter 7).

9.2.1 Process Outline

This second process flow that avoids most of the previous problems (high resolution, SiN_x roughness) is shown in Fig. 9.13.

The starting point is a deposition of 200 nm of SiO_2 (Fig. 9.13(a)). The etch mask for the tapered upper waveguide now defined by a 'lift-off' mechanism. This

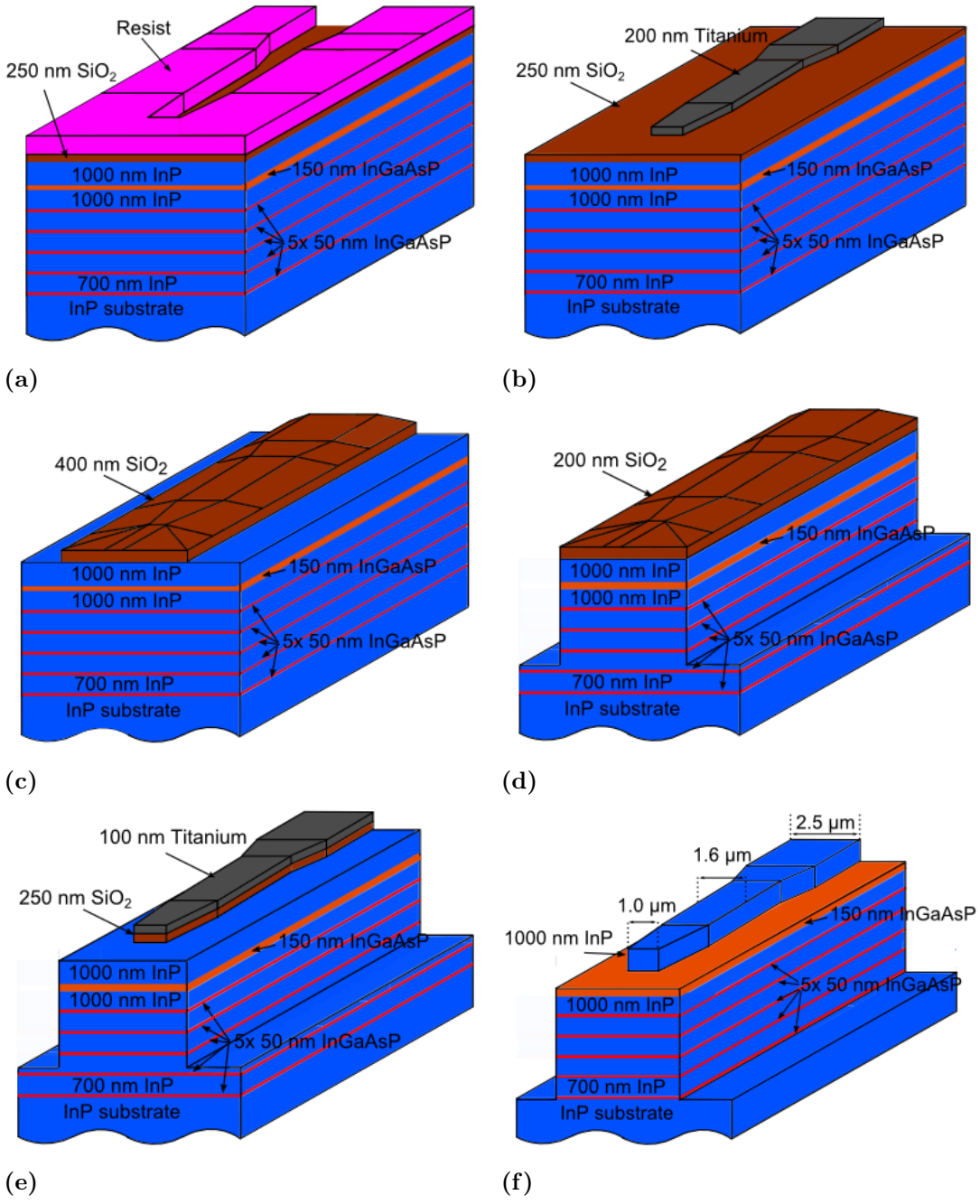


Figure 9.13: *Consecutive process steps scheme of the chip, (a) after the first lithography step, (b) after the Ti lift-off, (c) after the SiO_2 layers are patterned, (d) after the first III-V material ICP etch, (e) after the overlaying SiO_2 mask is removed by an ICP etch, (f) the final ATG structure with SiO_2/Ti mask removed.*

mechanism is generally used for metal contacts. First, a photoresist pattern is formed on the chip. The contact areas are not covered with resist. Afterwards, metal is evaporated on to the chip. After the evaporation the chip is placed in a photoresist

solvent. The resist with the metal on top is removed. The metal contacts remain on the areas previously covered with photoresist. In this passive ATG process a metal contact is not required for electrical purpose, therefore a single 200 nm thick Ti layer is suitable (Fig. 9.13(b)). Furthermore, Ti is easily removed by BOE.

The next steps in the fabrication sequence are similar to those previous outlined. 400 nm thick SiO_2 was deposited on the chip. The SiO_2 etch mask for the 4 μm deep etch was defined by lithography and a fluoride-based ICP etch (Fig. 9.13(c)). Following this is the deep semiconductor etch which was done with a $Cl_2/CH_4/H_2$ chemistry (Fig. 9.13(d)).

Now the SiO_2 mask for the deep etch must be removed without affecting the underlying taper etch mask. This time however, dry etching is used instead of BOE wet etching. This is also the reason why there is Ti on top of SiO_2. The Ti etch rate is much slower than the SiO_2 etch rate, therefore Ti acts as an etch mask to define the mask for the taper section(Fig. 9.13(e)).

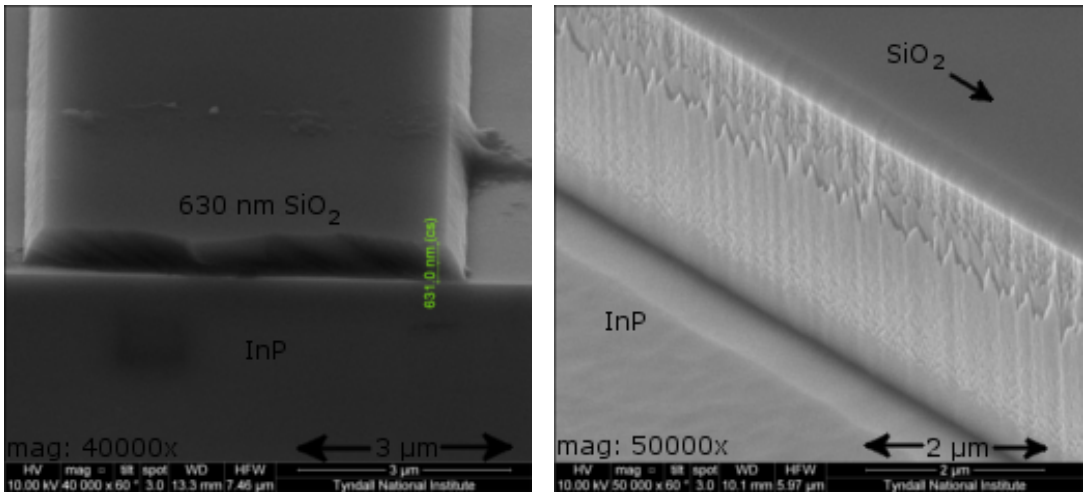
The second etch step is again a 1 μm deep etch. The upper tapered waveguide is defined with this etch and the ridge height of the lower waveguide is extended by etching all the way to the substrate. Finally, in the only wet chemical etch step, the remaining SiO_2/Ti mask is removed by BOE (Fig. 9.13(f)).

9.2.2 SiO_2 Etch Mask

The SiO_2 etch mask is an important part in order to obtain vertical and smooth sidewalls. Initially, UV26 resist was used to mask the SiO_2 for ICP etching. However, only in a few ICP etches was a smooth and vertical sidewall obtained. Because the etch mask quality affects the subsequent ICP step and results in undesired sidewall properties, the SiO_2 step was analyzed and improved.

In general a photoresist thickness twice the underlying dielectric thickness should suffice as an etch mask turning out with vertical sidewalls. The same photoresist, UV26, and the same mask aligner, MA6, was used as in the first lithography step to reduce the amount of possible process parameter fluctuations. The measured thickness of UV 26 was around 1.3 to 1.4 μm. Therefore, the thickness criterion was fulfilled for a 650 nm thick SiO_2 layer.

However, an inspection of the SiO_2 as shown in Fig. 9.14(a) revealed sloped sidewalls. Furthermore, etch results as shown in Fig. 9.14(b) can be correlated to a previously non optimum etch mask. Such a mask can cause 'scratch like' features

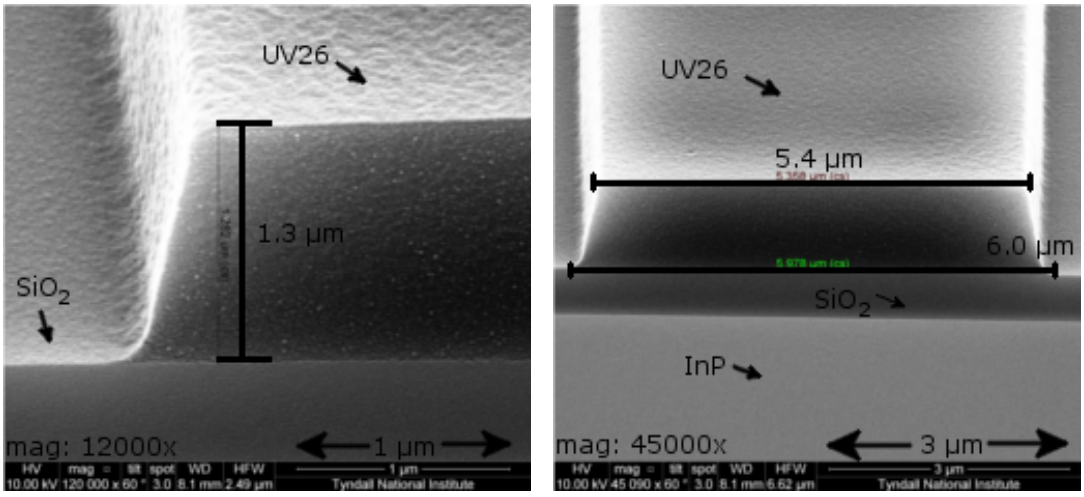


(a) **(b)**

Figure 9.14: *Cross-section SEM images of SiO_2 on InP. (a) before the InP etch, (b) after the InP etch.*

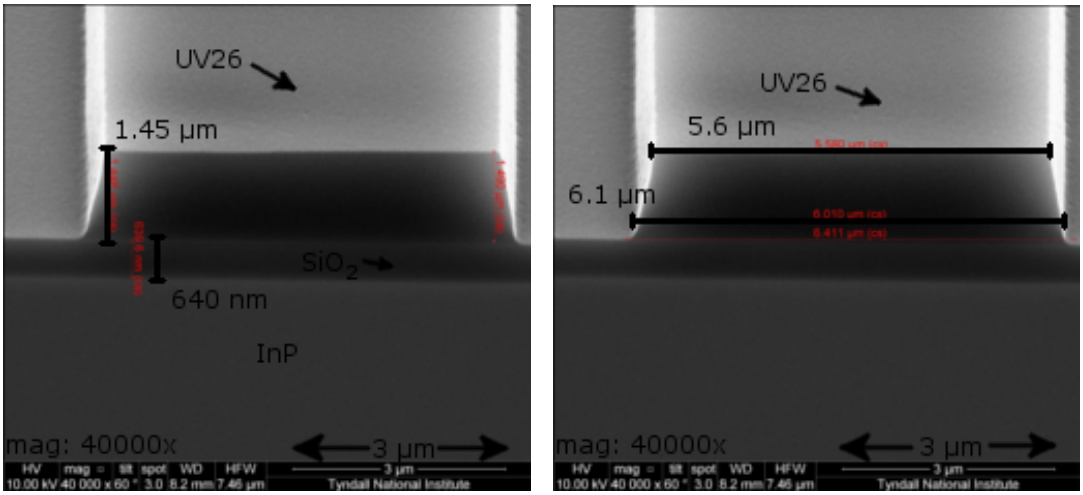
on the sidewalls. The etch mask starts to disappear before the etch is finished, and consequently the previously covered semiconductor parts are etched as well. Because a non vertical etch mask is most likely caused by a non vertical photoresist mask prior to the SiO_2 etching, the resist used with the previous parameters is inspected under the SEM. The cross-section of UV26 on SiO_2 can be observed in Fig. 9.15. Fig. 9.15(a) shows that the resist has twice the thickness of SiO_2, however the sidewall have roughly a 60 degree slope instead of 90 degree verticality. Only at the lower resist edge does the ridge has the same 6 μm width as the photomask (Fig. 9.15). The width at the upper part is reduced by 600 nm.

Several experiments were carried out to adjust the exposure and development time of the UV26. In Fig. 9.16 the exposure time was reduced to 5.5 s. The resist is slightly more vertical just above the SiO_2 mask. Additionally, the top part is wider than previously. However, the resist profile was still not usable to achieve the necessary SiO_2 verticality. Because shorter exposure and development times did not result in a vertical resist mask and the lower part of the resist ridge became several



(a) **(b)**

Figure 9.15: *Cross-section SEM images of UV26 exposed and developed for 9.5 s and 25 s respectively. (a) height measurement, (b) width measurement.*

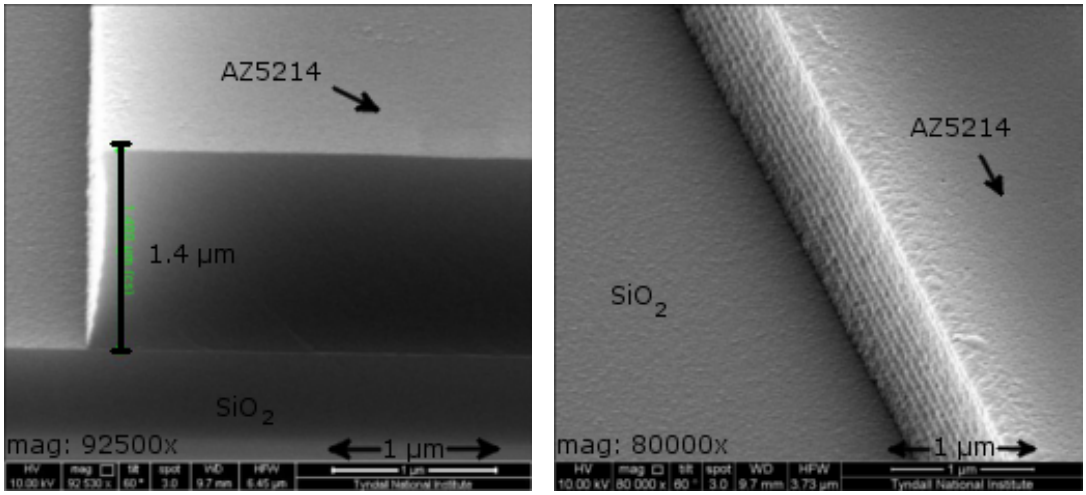


(a) **(b)**

Figure 9.16: *Cross-section SEM images of UV26 exposed and developed for 5.5 s and 25 s respectively. (a) height measurement, (b) width measurement.*

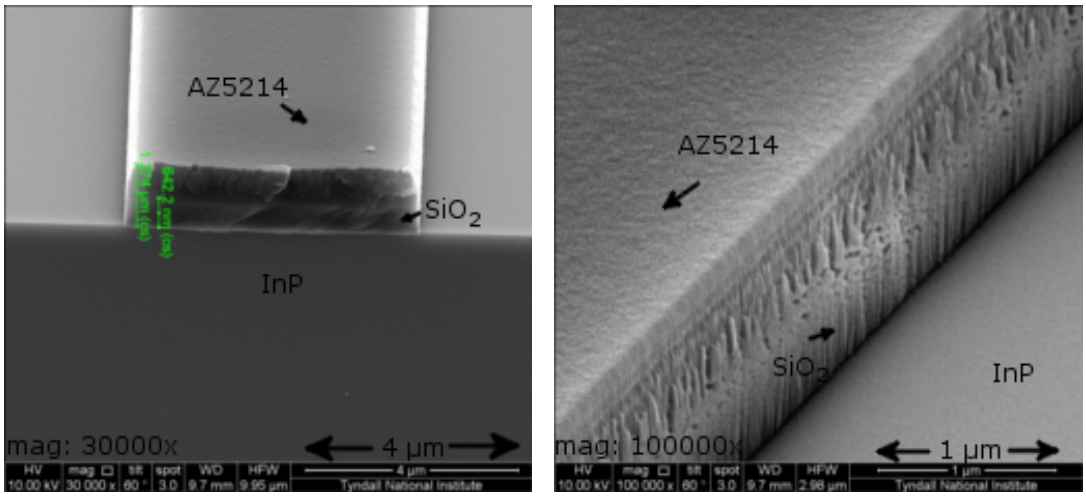
hundred nanometers wider than intended, UV26 was replaced by AZ5214.

In Fig. 9.17 a 1.4 μm thick AZ5214 resist with vertical sidewalls on top of SiO_2 is shown. This profile is suitable to eventually obtain a vertical SiO_2 mask. The results can be seen in Fig. 9.18. The SiO_2 sidewalls are vertical and smooth. However, it can also be seen that the resist lost its verticality. Only slightly above the SiO_2 does the resist remain vertical. This leads to the conclusion that AZ5214 can be used



(a) **(b)**

Figure 9.17: *Cross-section SEM images of AZ5214 exposed and developed for 7.5 s and 25 s respectively. (a) height measurement, (b) sidewall.*



(a) **(b)**

Figure 9.18: *Cross-section SEM images of AZ5214 after an SiO_2 etch. (a) front facet, (b) sidewall.*

to pattern SiO_2 with vertical and smooth sidewalls. However, this sidewall quality cannot be guaranteed for SiO_2 thicker than 650 nm.

9.3 Inductively Coupled Plasma Deep Etching using $Cl_2/CH_4/H_2$

Etching of deep waveguides is an important aspect to fabricate the ATGs presented in this thesis (Figs. 9.13(e) and (f)). For this, an inductively coupled plasma (ICP) etch with a high anisotropy is necessary. Furthermore, the sidewalls have to be smooth to minimize scattering losses. Previous investigations with a CH_4/H_2 and a Cl_2/N_2 chemistry did not show satisfying results (Section 8.1). However, test runs with $Cl_2/CH_4/H_2$ chemistry looked promising. Therefore, this latter etch is investigated more thoroughly here.

A significant research effort has already been put into the development of ICP etches of InP-based waveguides. Studies on Cl_2 based gas mixtures such as $Cl_2/Ar/N_2$ [145, 146], $Cl_2/Ar/H_2$ [147], $Cl_2/Ar/CH_4$ [148], Cl_2/H_2 [149], Cl_2/N_2[150, 151] and $Cl_2/CH_4/H_2$ [152, 153] have been reported. Cl_2 is the main etching gas. All of these processes have a similar drawback because of the low volatility of $InCl_3$, which can result in the formation of "grass" on the surface [154]. A high temperature (>150 °C) of the RF-biased electrode, and therefore on the sample, can help eliminate the "grass" effect. The addition of Ar increases the physical etch component in the ICP process and therefore increases the roughness. To enable smooth and vertical etching the sidewalls have to be passivated.

The undercut resulting from pure Cl_2 also requires sidewall passivation. By introducing either N_2 or CH_4 to the chemistry this passivation appears to be possible [155, 156].

Although several of these processes have shown good results in etch depth and sidewall roughness, the chuck usually has to be at temperatures higher than 150 °C. In such a way an In-rich surface with the "grass" side effect can be avoided. Nevertheless, time consuming preparations of our ICP system are required for temperatures >80 °C. A $Cl_2/CH_4/H_2$ etch of InP with an electrode temperature close to 25 °C is desired and has already been demonstrated [157]. However, the sidewalls have not shown the necessary smoothness and verticality required for low loss waveguides.

9.3.1 Experimental Conditions

The $Cl_2/CH_4/H_2$ etching processes were performed with an Oxford Instruments Plasmalab System 100 (Tab. 9.1). The coil power was kept at 1000 W, the platen power at 150 W, the chamber pressure at 3 mTorr and the electrode temperature at 20 °C. A 4-in silicon wafer was used as a sample carrier. The carrier was mechanically clamped by a quartz ring. The samples were not bonded to the carrier. Backside cooling was not used between the electrode and sample. The completely un-doped samples consist, starting from the top, of a 1 μm InP upper cladding, 150 nm InGaAsP (λ_g = 1330 nm), a 1 μm InP lower cladding and five 50 nm thick layers of InGaAsP (λ_g = 1200 nm) interspersed by 700 nm InP (Fig. 9.21(a)). The structure is similar to the ATG design described in Chapter 4 and 5. The etch time was 195 s. The etch masks were 650 nm of sputtered SiO_2. The mask is similar to Fig. 9.13(c), however because of the reduced complexity required the first etch mask was not defined. The SiO_2 mask was patterned by CF_4/CHF_3 etching in a Surface Technology Systems 310 PC. AZ5214 photoresist from AZ Electronic Materials exposed with a MA 1006 mask aligner from Suess MicroTech was used as an etch mask for the SiO_2 mask.

To determine the principal effects and the interaction of the different gases a 2^k factorial Design of Experiment (DoE) approach was chosen. Eight etches with the minimum and maximum gas flows in Tab. 9.4 were performed. The gas ranges were

Table 9.4: *Gas flows investigated*

Gas	-1, Minimum flow(sccm)	+1, Maximum flow(sccm)
Cl_2	4	10
CH_4	7	15
H_2	10	20

selected after an initial Cl_2 /CH_4/H_2 = 7/11/15 sccm etch with reasonable quality under the assumption that the optimum gas flows are in a roughly ± 40 % range. The DC bias of the etches was usually around 251 V. Minimum and maximum values of 248 V and 259 V respectively were observed for the $Cl_2/CH_4/H_2$ = 4/15/10 sccm

and the $Cl_2/CH_4/H_2$ = 10/15/20 sccm etch. After each etch, SEM images were taken to measure the etch depth at the ridges and the remaining SiO_2. The sidewall conditions observed at the SEM were qualitatively attributed to values from 1 (very smooth sidewall) 10 (very rough sidewall). Fig. 9.19 shows three different examples.

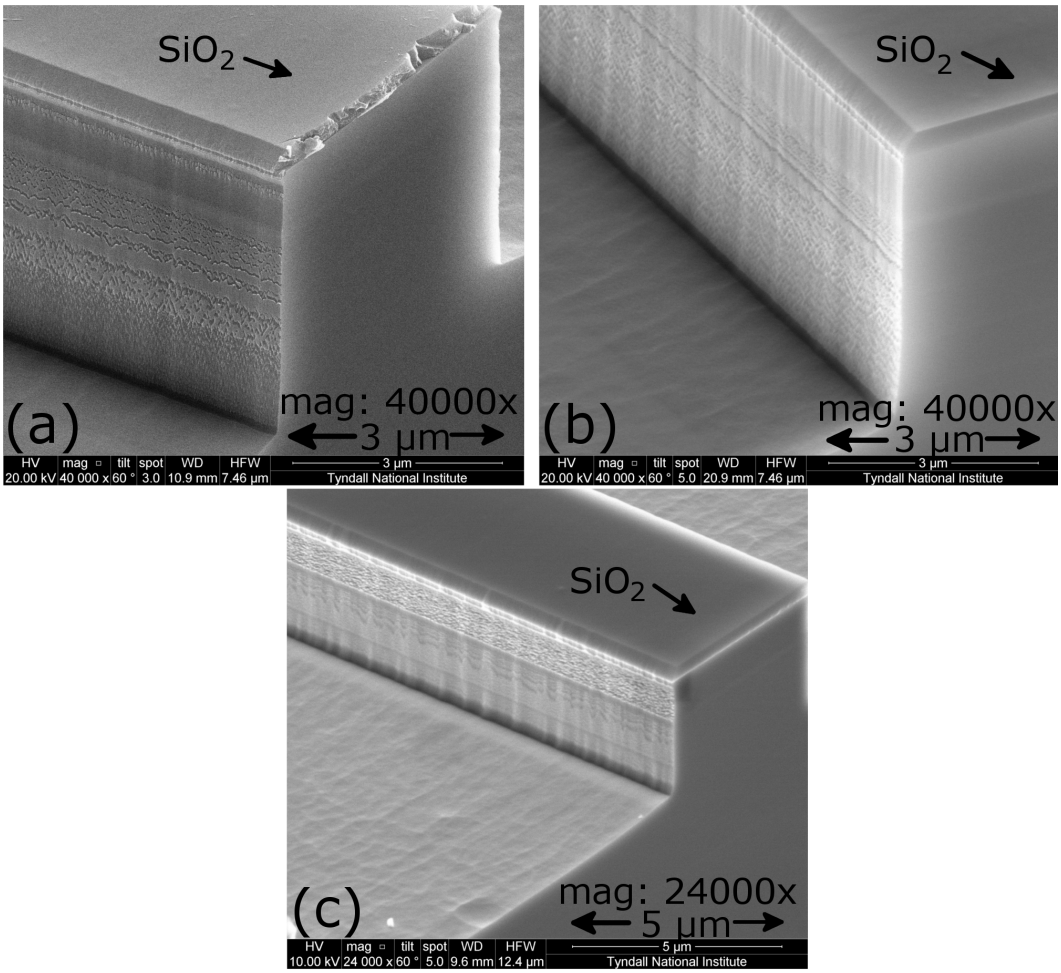


Figure 9.19: *Cross-section sidewall SEM images, (a) $Cl_2/CH_4/H_2$ = 10/15/20 sccm sidewall roughness value 3, (b) $Cl_2/CH_4/H_2$ = 4/7/20 sccm sidewall roughness value 5, (c) $Cl_2/CH_4/H_2$ = 4/15/10 sccm sidewall roughness value 7*

9.3.2 Etch Analysis

The eight etch runs performed as part of the DoE are analyzed using the 2^k factorial design [158, 159]. The effect, the interaction and the sum of squares of the three studied factors (Cl_2,CH_4, H_2) on the InP/InGaAsP etch rate, the selectivity of

InP/InGaAsP relative to SiO_2 and the sidewall roughness are investigated. The main effect plots are obtained by taking the mean response values (etch rate, selectivity, roughness) of the minimum and maximum level of each parameter (Cl_2-, CH_4-, H_2-flow). For example, the value of the etch rate for the minimum/maximum value of the Cl_2-flow is calculated by adding all etch rates where the Cl_2-flow is at 4/10 sccm and dividing it by the number of etches. In this case the number is four. The sign of the main effect shows the direction of the effect, i.e. if the average response value decreases or increases with an increasing parameter value. Steep lines in the main parameter plots show an important influence of the specific parameter. DoE also enables the determination of interactions between different parameters. The interactions can be visualized in an interaction plot. In the interaction plot of two parameters one parameter is kept at its minimum (or maximum) and the average response values are plotted with the other parameter at its minimum and maximum. Parallel lines in the interaction plots indicate that the two parameters do not influence each other.

In Fig. 9.20, a grass-like surface can be observed after an etch of $Cl_2/CH_4/H_2$ = 10/7/10 sccm. However, the grassy surface is mainly located close to the mesas.

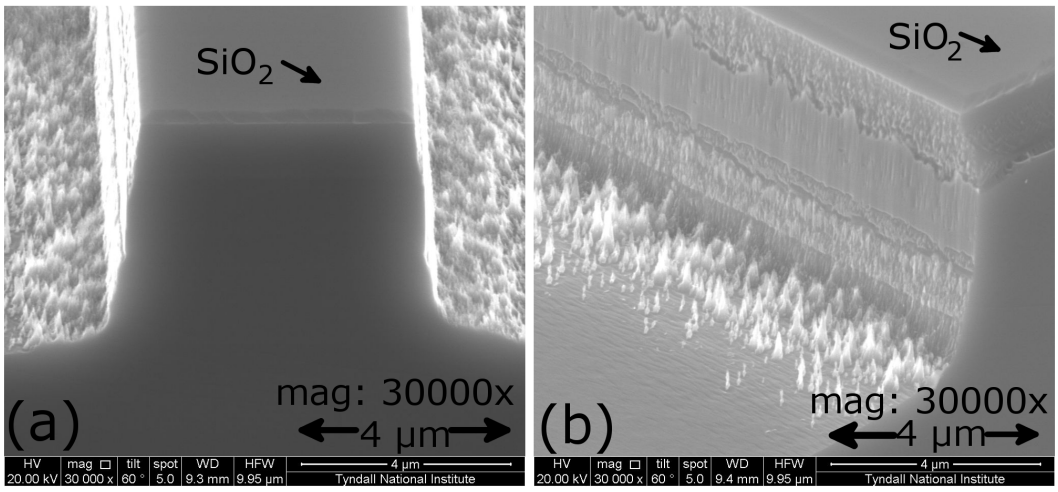


Figure 9.20: *Cross-section SEM images of the front facet and sidewall of the 195 s etch of $Cl_2/CH_4/H_2$ = 10/7/10 sccm.*

A possible explanation for this could be a shadowing effect by the mesa causing a reduced etchant concentration next to it. Nevertheless, the same result does not

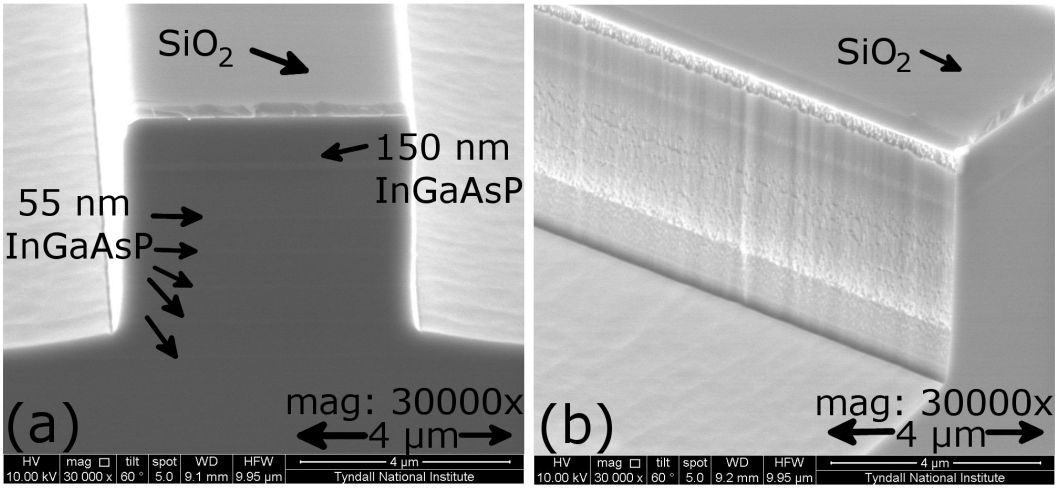


Figure 9.21: *Cross-section SEM images of the front facet and sidewall of the 195 s etch of $Cl_2/CH_4/H_2$ = 10/15/10 sccm.*

occur in any of the other seven etches. Therefore, it is possible to conclude that only for a high concentration of Cl_2 does the grass effect occur. By incorporating the right ratio of CH_4 into the etchant, a balanced removal of In and P atoms is possible because the etch product $In(CH_3)_3$ has a much higher volatility [160]. For the gas flow of $Cl_2/CH_4/H_2$ = 10/15/10 sccm, a relatively smooth sidewall can be recognized (Fig. 9.21) and it can be assumed a high CH_4 flow is important for smooth sidewalls. The etch rate relative to the low and high value for each gas is plotted in Fig. 9.22(a)-(c). Since Cl_2 is the main etchant, a high Cl_2 value increases the etch rate (Fig. 9.22(a)). It can also be seen that a high CH_4 flow reduces the etch rate (Fig. 9.22(b)). This indicates passivation properties of CH_4. The nearly straight line in Fig. 9.22(c) leads to the DoE conclusion that H_2 has only a small effect on the etch rate in the chosen flow ratio ($H_2/(Cl_2+H_2)$ = 0.60 - 0.83). For the $Cl_2/Ar/H_2$ chemistry a minimum etch rate of InP and InP/InGaAsP has been reported for a ratio of around 0.48 [148]. The InP etch rate increased for ratios up to 0.67, whereas the InP/InGaAsP etch rate reached an almost constant level. Figure 9.23 shows the three possible interactions of the gases. In Fig. 9.23(a) an interaction between Cl_2 and CH_4 on the etch rate can be seen. The nearly parallel lines in Fig. 9.23(b) indicate a weak interaction between Cl_2 and H_2 on the etch rate. A slightly higher, but still not significant interaction can be observed in Fig.

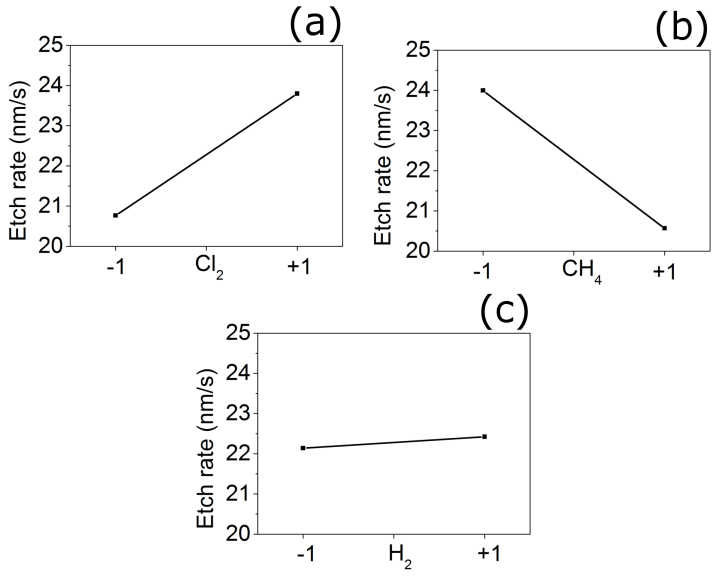


Figure 9.22: *Main effects plot for the etch rate of InP/InGaAsP, (a) main effect of Cl_2, (b) main effect of CH_4, (c) main effect of H_2.*

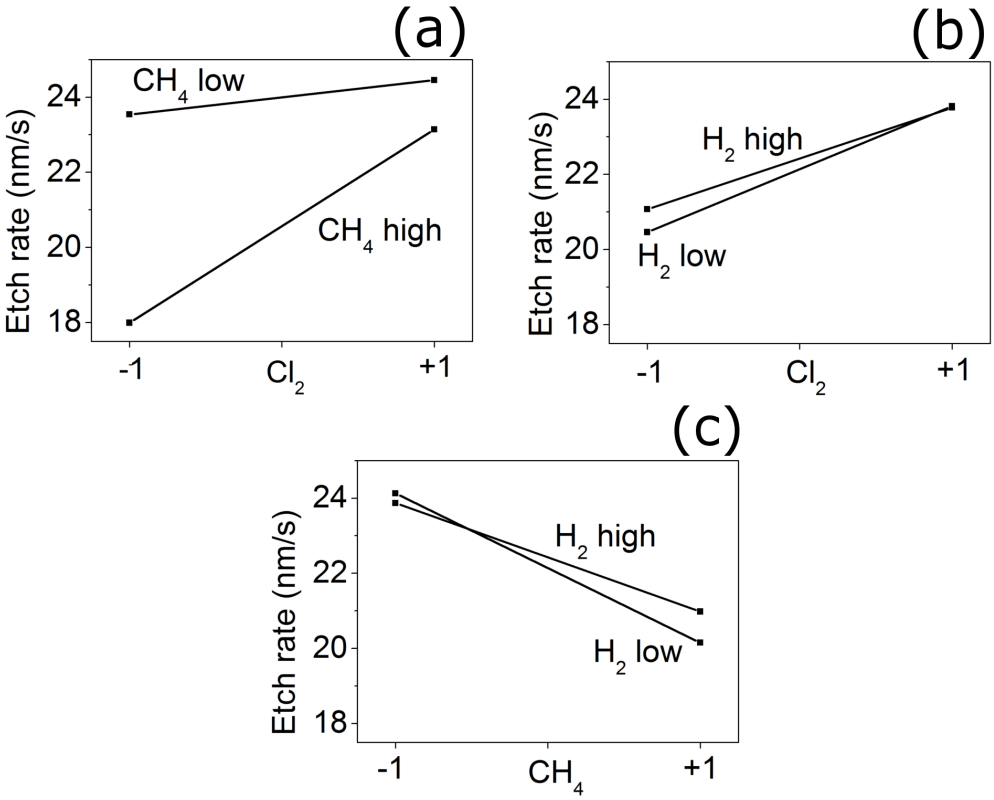


Figure 9.23: *Interaction plot for the etch rate of of InP/InGaAsP, (a) interaction between Cl_2 and CH_4, (b) interaction between Cl_2 and H_2, (c) interaction between H_2 and CH_4.*

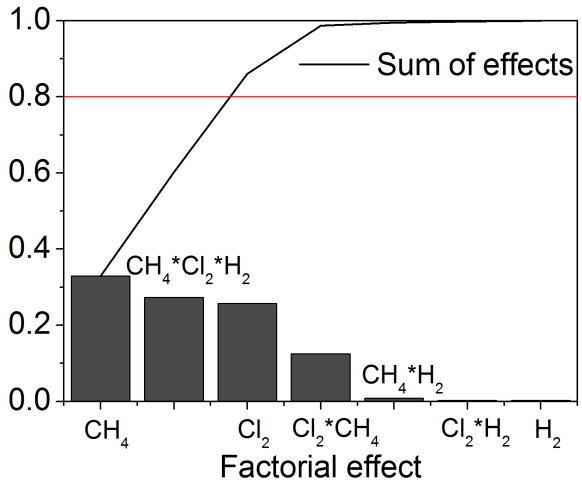


Figure 9.24: *Sum of squares percentages and the 80 % limit for the etch rate of InP/InGaAsP.*

9.23(c) between CH_4 and H_2. From the sum of squares percentage (Fig. 9.24) it can be seen that the CH_4 and Cl_2 flows, as well as the interaction of all three gases, have more than 80 % influence on the etch rate. The reduced etch rate caused by a high value of all three gases is related to the fact that H_2 and CH_4 were increased by a larger quantity than the main etchant Cl_2.

Another important aspect is the selectivity, that is, the ratio of semiconductor and SiO_2 etch rate. If the selectivity is known, it will be possible to adjust the required etch mask thickness. The only gas that contributes to a change in the selectivity is CH_4 (Fig. 9.25(a)). A high CH_4 flow reduces the selectivity. This is correlated to the reduced etch rate of the semiconductor. The SiO_2 etch rate is mainly physical and therefore unaffected by any change in the gas composition. The second effect is the CH_4/Cl_2 interaction (Fig. 9.26(a)). CH_4 decreases the semiconductor etch rate, while Cl_2 increases it. Therefore, the ratio of these gases has to be balanced to ensure a high selectivity. Fig. 9.27 outlines the fact that all other influences can be neglected.

Since the main objective of this ICP process is to etch optical waveguides, an important consideration for low loss waveguides is the sidewall roughness and how it can be improved. From Fig. 9.28(b) and (c) it can be seen that CH_4 and H_2 are main contributors to sidewall roughness. In both cases a high gas flow results in

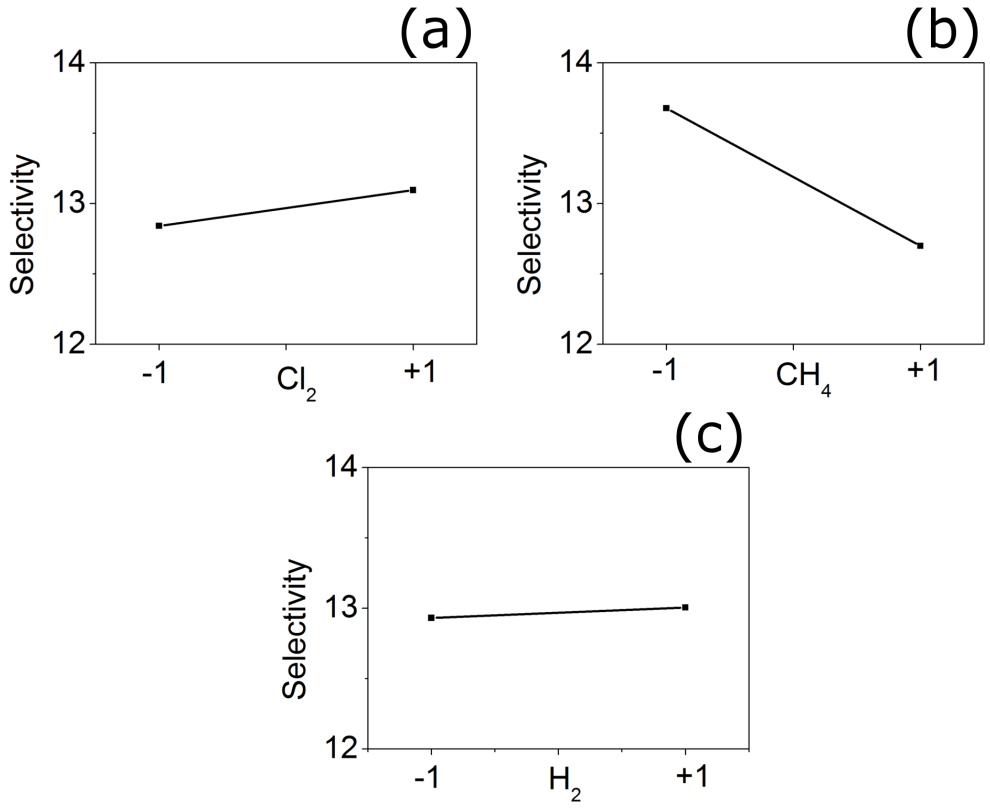


Figure 9.25: *Main effects plot for the selectivity, InP/InGaAsP to SiO_2, (a) main effect of Cl_2, (b) main effect of CH_4, (c) main effect of H_2.*

smoother sidewalls. As previously discussed, CH_4 might passivate the sidewalls and therefore contribute to smoother sidewalls. Cl_2 only affects the sidewall roughness in its interaction with CH_4 (Fig. 9.29(a)). The sum of squares plot (Fig. 9.30) further indicates that these three effects have more than 80 % influence on the sidewalls and that Cl_2 by itself can be neglected.

9.3.3 Optimized conditions

Taking the previously shown influences into account and focusing on the sidewall roughness, a simple linear regression equation was used to calculate optimized gas ratios. For a ratio of $Cl_2/CH_4/H_2 = 10/18/12$ sccm, the best results were obtained. To control the etch depth, etches of the InP/InGaAsP samples at 30 s intervals were done. Fig. 9.31 shows the evolution of the InP/InGaAsP etch rate with etch time for two runs. In the first 30 – 60 s only the top 1 μm InP layer was etched.

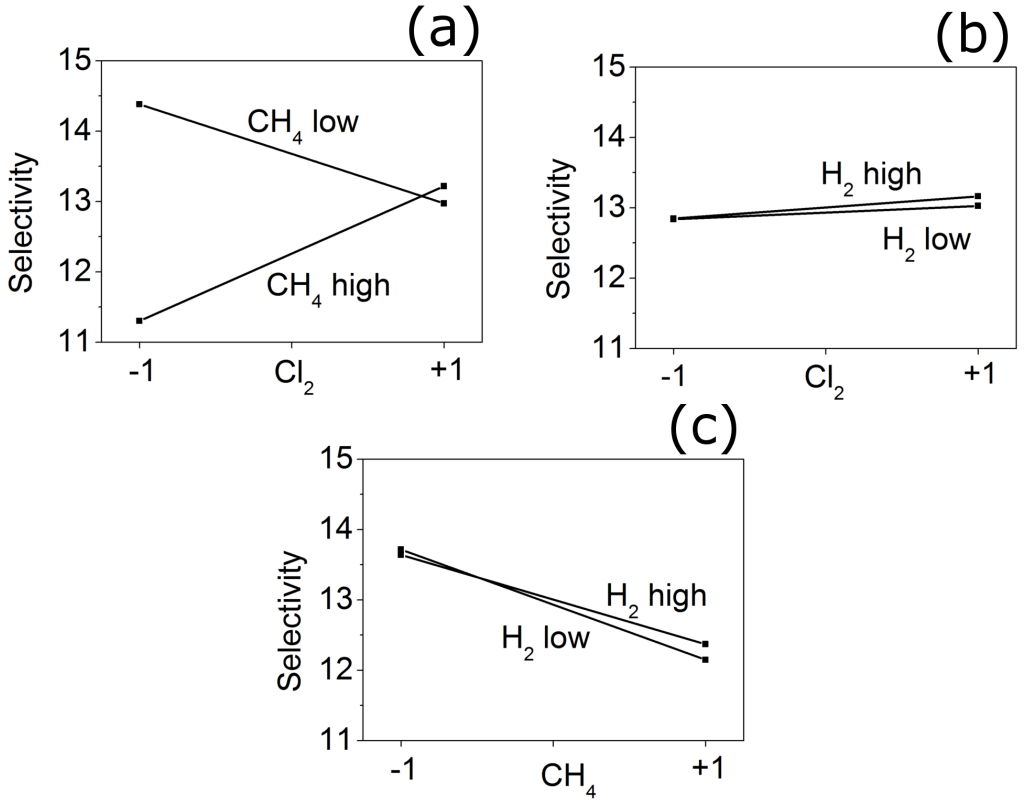


Figure 9.26: *Interaction plot for the selectivity, InP/InGaAsP to SiO_2, (a) interaction between Cl_2 and CH_4, (b) interaction between Cl_2 and H_2, (c) interaction between H_2 and CH_4.*

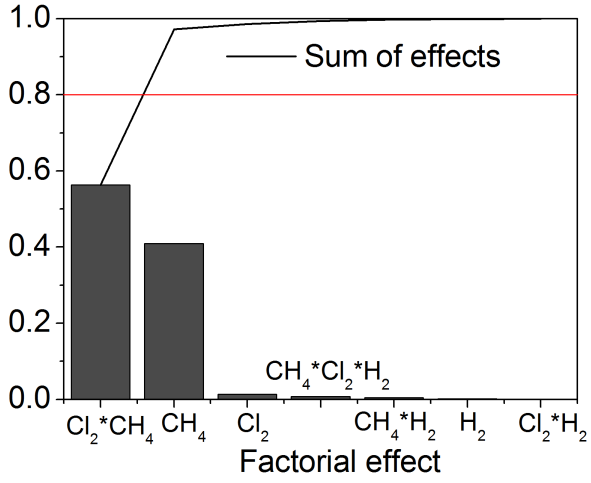


Figure 9.27: *Sum of squares percentage and the 80 % limit for the selectivity, InP/InGaAsP to SiO_2.*

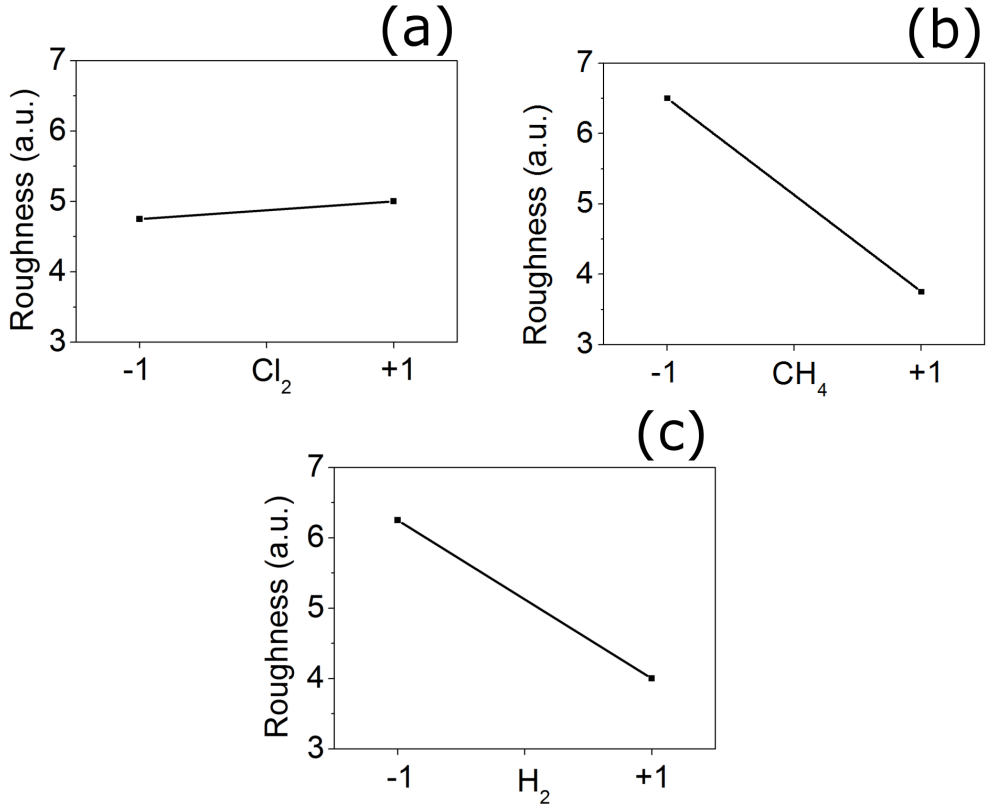


Figure 9.28: *Main effects plots for the sidewall roughness of InP/InGaAsP, (a) main effect of Cl_2, (b) main effect of CH_4, (c) main effect of H_2.*

Therefore, the etch rate is higher. The reduction in the etch rate for the 90 s was caused by the slower etch rate of the 150 nm InGaAsP layer. The 120 s etch finished just above the first 55 nm InGaAsP layer. The etch rate of run 2 starts to increase after 150 s and increases significantly at 180 s. For run 1 a similar increase can be observed. However the times of the increases are shifted to 180 s and 210 s. Since the periodic layer stack is reached after 120 s and the etch is still above the substrate after 210 s, the layer structure does not correspond to the increase in the etch rate. The temperature of the chip might play a role in the etch rate. Therefore, Testo temperature labels available in the range of 100 °C to 260 °C were put on a silicon test chip and etched to determine the effect of the etch time on the temperature [161]. Tab. 9.5 shows that a temperature of 166 °C is already reached on the Si-sample after a 30 s for the $Cl_2/CH_4/H_2$ = 10/18/12 sccm etch. The temperature increased to a value of 254 °C after 90 s and reached more than 260 °C at 120 s. For

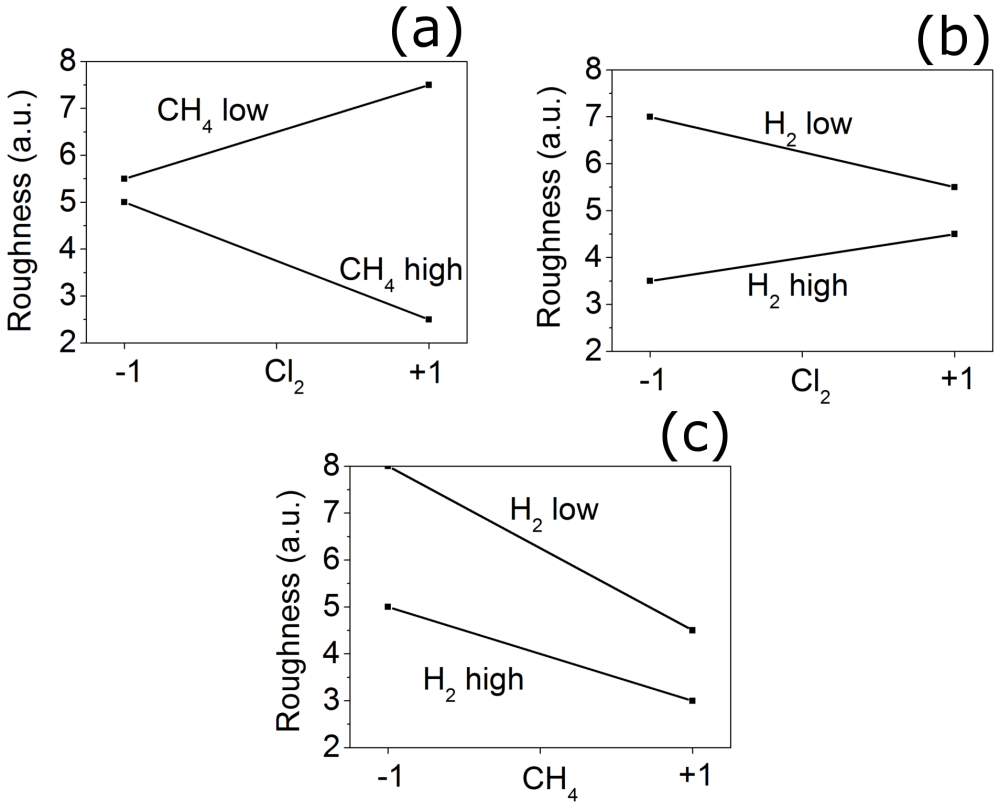


Figure 9.29: *Interaction plot for the sidewall roughness of InP/InGaAsP, (a) interaction between Cl_2 and CH_4, (b) interaction between Cl_2 and H_2, (c) interaction between H_2 and CH_4.*

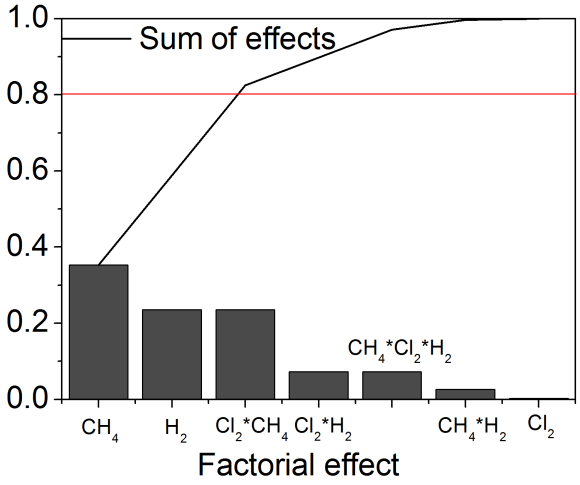


Figure 9.30: *Sum of squares percentage and the 80 % limit for the sidewall roughness of InP/InGaAsP.*

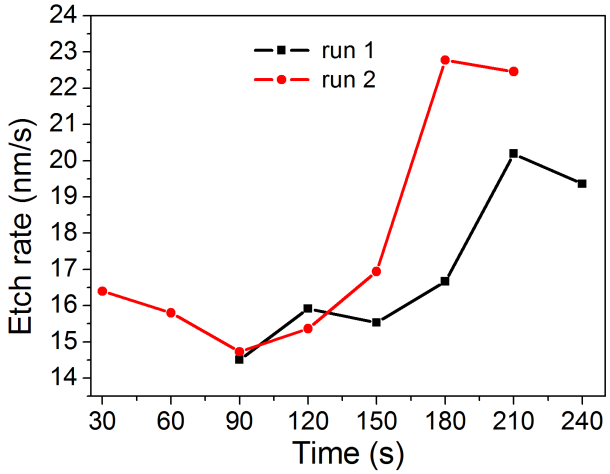


Figure 9.31: *Time dependent etch rate (InP/InGaAsP) of $Cl_2/CH_4/H_2$ = 10/18/12 sccm.*

Table 9.5: *Temperature relative to etch time.*

Etch time (s)	30	60	90	120
Temperature (°C)	166	204	254	260

longer etch times an ongoing increase of the temperature can be assumed. If the CH_4 exhibited a passivation effect, this effect might fail at a certain temperature and therefore the etch rate would increase significantly. The different times (run 1: 180 s, run 2: 150 s) are likely related to different chip sizes as the chip in run 2 was smaller. The chip sizes in run 1 were approximately 0.7 cm^2, whereas in run 2 the size was around 0.4 cm^2.

Etching for 120 s with Cl_2/H_2 = 10/12 sccm and $Cl_2/H_2/Ar$ = 10/12/18 sccm was done to further study the passivation effects of CH_4. Fig. 9.32(a) and (b) show that both etches result in notches right below the SiO_2-mask at the position of the 1 μm InP layer and also a rougher surface. The InGaAsP/InP etch rates were 27 and 29 nm/s for Cl_2/H_2 and $Cl_2/H_2/Ar$ respectively. The slightly higher etch rate is related to the additional physical etch component of the Ar ions. The notches have a width of 4.9 μm (Cl_2/H_2) and 4.8 μm ($Cl_2/H_2/Ar$), whereas the ridge width is 5.2 μm in both cases (not shown here). The notches show a strong lateral etch component in both chemistries especially right under the dielectric etch mask. On

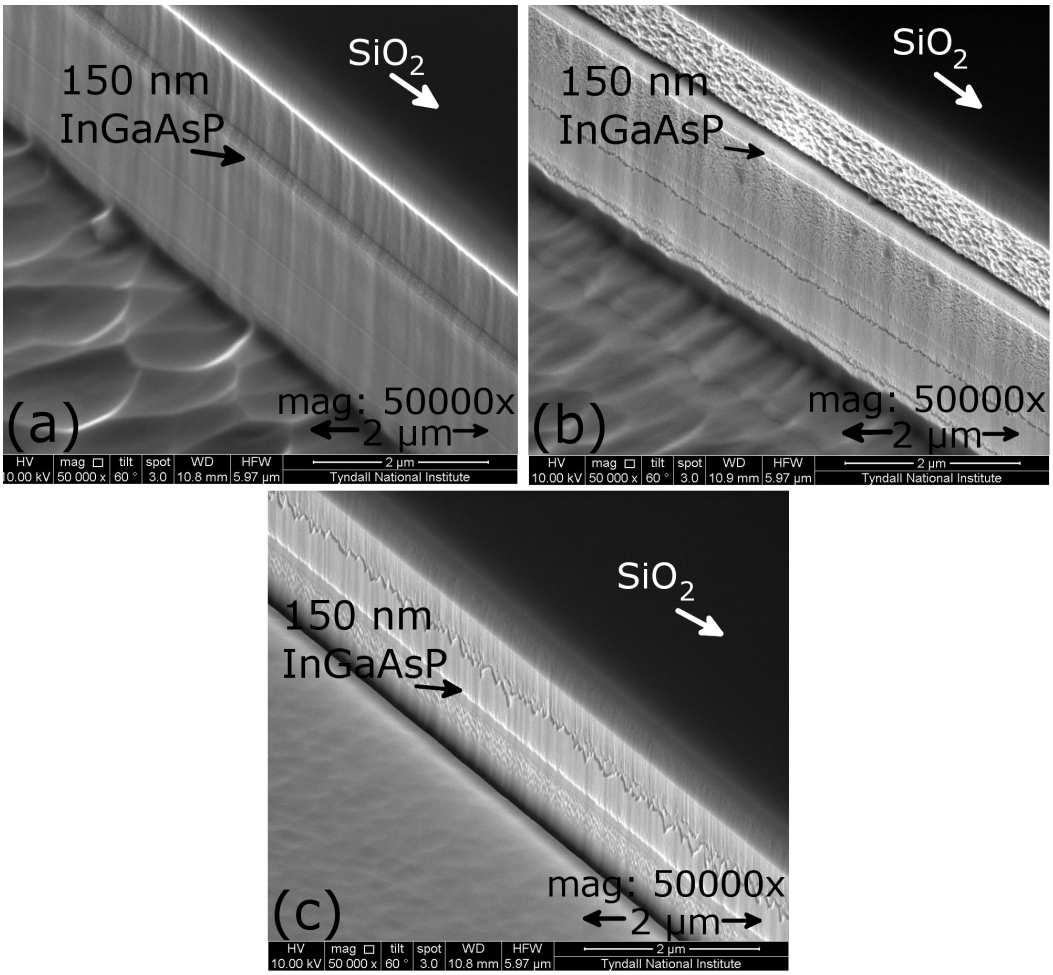


Figure 9.32: *Cross-section sidewall SEM images, (a) 120 s Cl_2/H_2 = 10/12 sccm, (b) 120 s $Cl_2/H_2/Ar$ = 10/12/18 sccm, (c) 120 s $Cl_2/CH_4/H_2$ = 10/18/12 sccm. The 'scratch' like line is most probably caused by an inferior SiO_2 mask.*

the other hand, the 120 s $Cl_2/CH_4/H_2$ = 10/18/12 sccm etch does not have notches. However, the etch rate is only 16 nm/s. The small rough line along the mesa is most likely caused by an inferior SiO_2 mask. Fig. 9.32(c) shows a less vertical edge of SiO_2 than in Fig. 9.32(a) and (b). Furthermore, the vertical mask width was 5.4 μm before the etches in Fig. 9.32(a) and (b), whereas the sloped mask width was 5.6 μm before the etch in Fig. 9.32(c).

Comparing the semiconductor etch rate to the SiO_2 etch rate gives the selectivity (Fig. 9.33). At 30 s the selectivity is low. This is due to the fact that the temperature is not yet at 170 °C and the InP/InGaAsP etch is mainly physical and therefore slow. Afterwards the selectivity stays more or less constant until the InGaAsP/InP etch

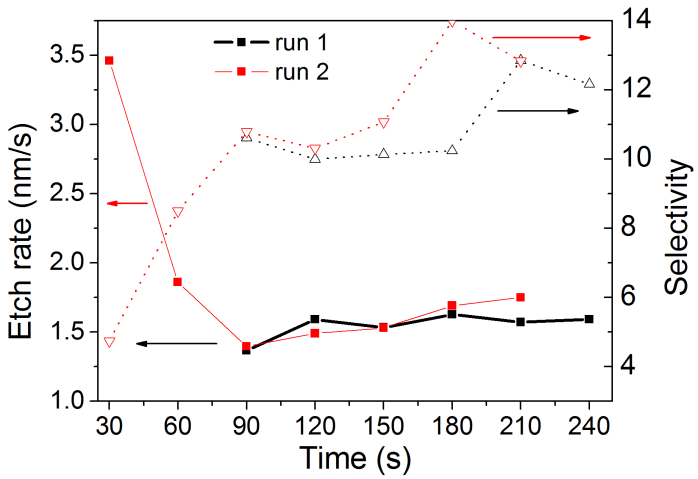


Figure 9.33: *SiO_2 etch rate and selectivity (InP/InGaAsP to SiO_2) of $Cl_2/CH_4/H_2$ = 10/18/12 sccm.*

rate increases. Therefore, the selectivity is mainly influenced by the semiconductor etch rate. In Fig. 9.34, an etch of about 3 μm depth with vertical and smooth sidewalls is shown. For the 180 s etch (Fig. 9.34(b)) the sidewalls are smooth and

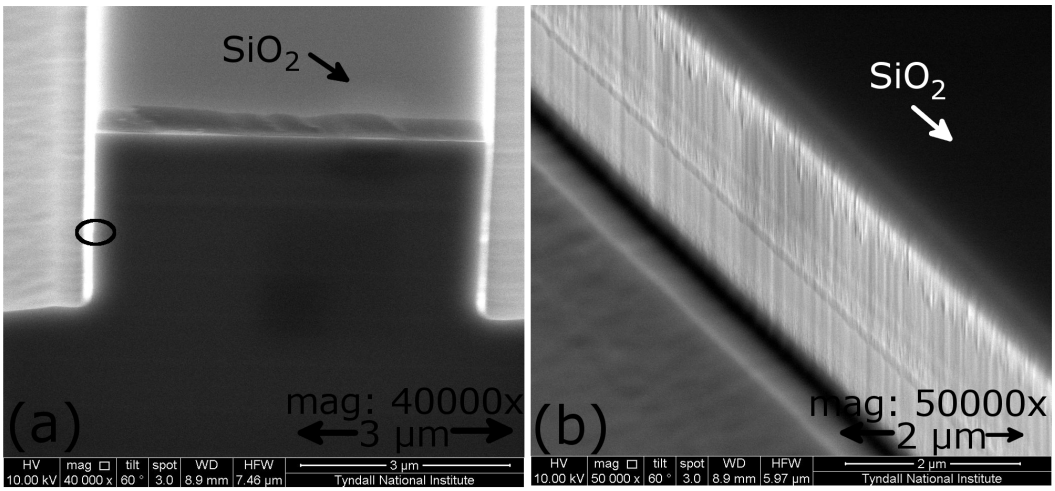


Figure 9.34: *Cross-section SEM images of the front facet and sidewall of the 180 s etch ($Cl_2/CH_4/H_2$ = 10/18/12 sccm, InP/InGaAsP).*

suitable for optical waveguides. The small line along the mesa can be observed as a small step in the mesa width ($\approx$ 30 nm, Fig. 9.34(a)). The line does not line up with any InGaAsP layers and therefore is most probably caused by a disappearing mask at the edges. It is similar to Fig. 9.32(c), however the mask was probably

smoother and therefore the line is straighter. Nevertheless, the sidewall remains smooth, supporting the observation of CH_4 passivation properties.

For etch times of 180 s (run 2, Fig. 9.35(a)) and 210 s (run 1, Fig. 9.35(b)) the sidewalls get rougher. A closer look at the lines along the mesa and on the etch mask reveals that the roughness at the top of the mesa is most probably caused by a gradual removal of the etch mask at the mesa edges. Supporting this is the fact that all the lines have a very similar appearance. They are also not along one

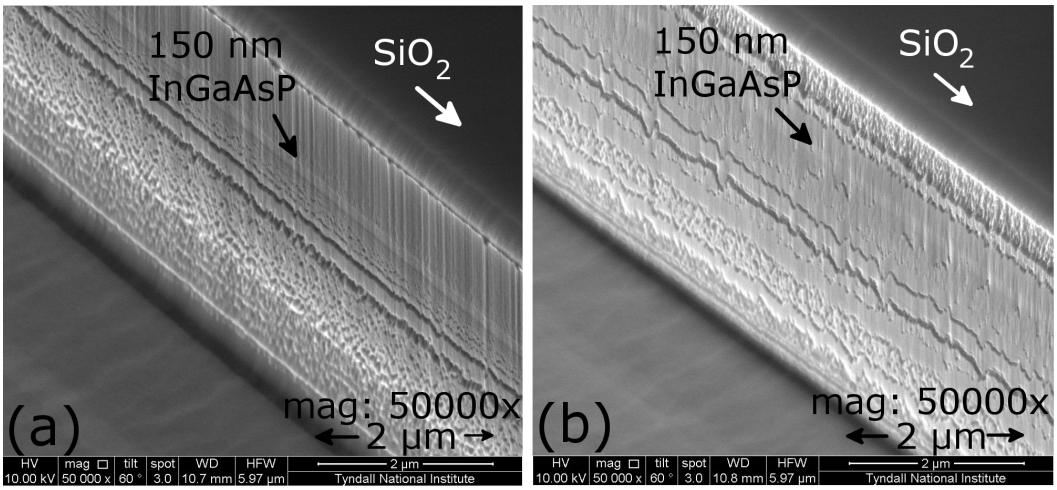


Figure 9.35: *Cross-section SEM images of the sidewalls, etch ($Cl_2/CH_4/H_2$ = 10/18/12 sccm, InP/InGaAsP), (a) run 2, 180 s, (b) run 1, 210 s. The 'scratch' like lines in (a) and (b) are most probably caused by an inferior SiO_2 mask.*

of the InGaAsP layers and the ridge gets slightly narrower from the bottom to the top especially where the lines appear. Furthermore, the edges of the SiO_2 mask are not vertical anymore and there is no undercut of the mask. Additionally, the comparison of the etch mask width before the ICP etch (5.6 μm, not shown here) to the SiO_2 mask width after the 210 s etch (5.4 μm, not shown here) indicate that the sidewalls were not properly protected by the mask. The upper rough part has a width similar to the etch mask, whereas the smoother lower part still has a width of 5.6 μm. The roughness at the bottom of the mesa, however, cannot be seen in any of the shorter etches. Because in both etches a higher etch rate was observed, it is highly likely that a temperature was reached where the suggested CH_4 passivation no longer occurs.

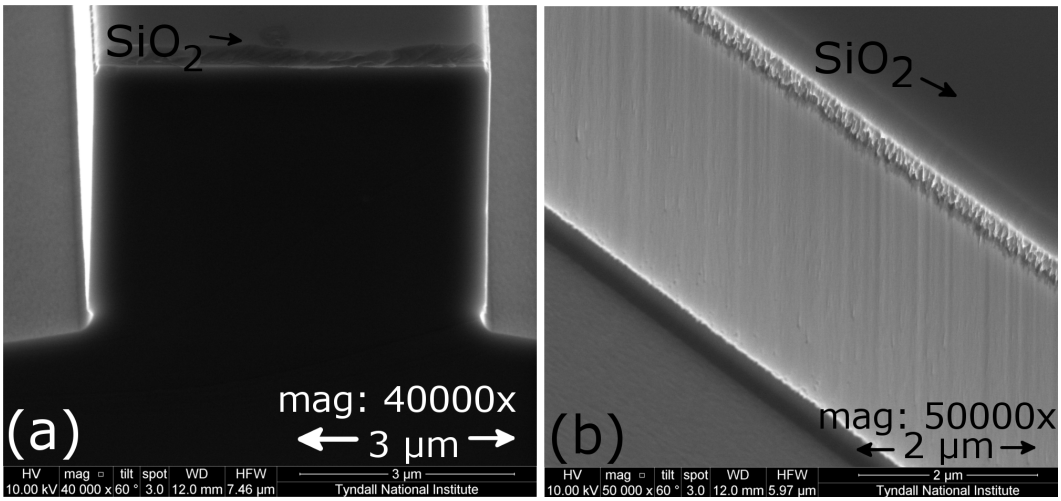


Figure 9.36: *Cross-section SEM images of the front facet and sidewall of the 190 s etch ($Cl_2/CH_4/H_2$ = 10/18/12 sccm , InP substrate).*

The DoE analysis, the reduced etch rate, the notches for the CH_4 free chemistries, the reduced mesa width and the rough sidewalls after a certain time all taken together form a strong indicator of the previously suggested passivation effect of CH_4. It is suggested that an interval etch consisting of etch times not longer than 150 s with several minutes cool down time in between each etch step should enable deeper etches with smooth sidewalls. Furthermore, it is critical to have a smooth and vertical SiO_2 mask.

The fact that deeper etches with smooth and vertical sidewalls are possible can be recognized in Fig. 9.36. A 190 s etch of semi-insulating InP (Fe-doped) with an etch depth of more than 4.7 μm has smooth sidewalls. The smooth sidewalls further indicate that the temperature at which the passivation failure of CH_4 occurs was not reached. The chip had a size of 1.0 cm^2, therefore a longer etch time was possible before the critical temperature level was reached. The higher etch rate compared to the InP/InGaAsP structure is related to the higher etch rate of pure InP. After an etch time of 60 s for the InP/InGaAsP material the 150 nm InGaAsP layer was most likely reached and the etch rate declined.

In summary, an InP/InGaAsP ICP etch process without electrode heating based on $Cl_2/CH_4/H_2$ was investigated using a full factorial DoE. The key influences and their effects on the etch rate (high value of CH_4 $\rightarrow$ low etch rate, high value of Cl_2

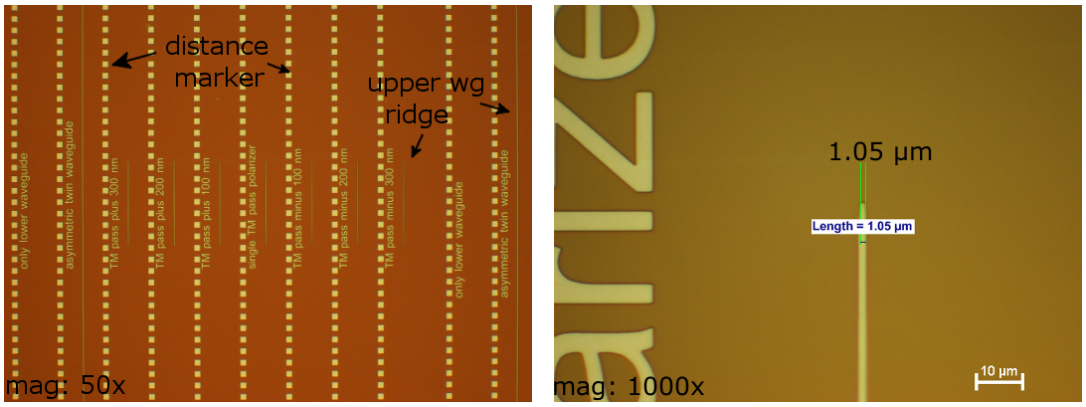
$\rightarrow$ high etch rate), selectivity (high value of CH_4 $\rightarrow$ low selectivity) and sidewall roughness (high value of CH_4 $\rightarrow$ low roughness, high value of H_2 $\rightarrow$ low roughness) are found. Finally, the chemistry is modified to $Cl_2/CH_4/H_2$ = 10/18/12 sccm. Smooth and vertical sidewalls are demonstrated for etch depths around 3 μm (InP/InGaAsP) and larger than 4.7 μm (InP). A strong indication of the passivation property of CH_4 is obtained by comparing the optimized $Cl_2/CH_4/H_2$ to the Cl_2/H_2 and Cl_2/H_2/Ar etch images. The low etch rate of the etches in section 9.1.3 is related to this passivation effect. The increased etch rate and roughness of the optimized etch can be explained by a passivation failure after a certain etch time due to a rise in the temperature of the sample. In general, the scratch like roughness along the sidewalls is most probably caused by a mask failure. Also the roughness right below the SiO_2 layer can be attributed to a similar cause, as the rest of the ridge is smooth. These two effects are avoidable by a perfect mask. On the other hand, there is the suggested passivation failure effect due to etch-induced high temperature on the sample. In this case the ridge is especially rough at its lower half. The etch duration must be adjusted to avoid this effect. For a quarter 2 inch diameter wafer, as usually used for processing, an etch depth of 4 μm should be possible, because the chip size is significantly larger than in these DoE runs.

9.4 Optimized Process Steps

Finally, the previously optimized process steps included in the SAPSIOTIM process were used to fabricate polarization filters which are characterized in Chapter 6. The process guidelines can be found in Appendix B. Here, images of the important process steps and the final process results are shown.

The first critical step is to fabricate an etch mask with a taper end width of 1.0 μm. For this the Ti-lift-off step was used. The upper waveguide width is varied from - 300 nm to + 300 nm in 100 nm steps to take into account a possible width variation during processing (9.37(a)). Fig. 9.37(b) shows that a Ti mask with a 1.0 μm width can be obtained.

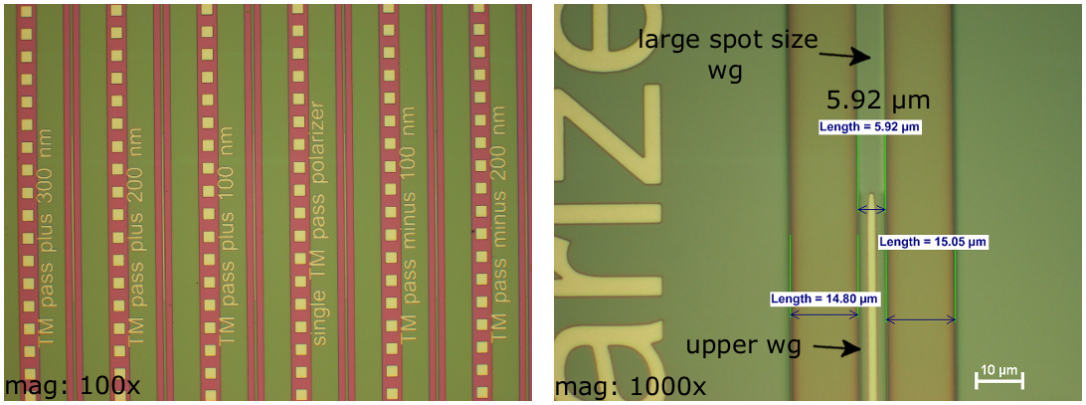
Another important aspect is the second etch mask. It was outlined that the



(a) **(b)**

Figure 9.37: *Microscope images after the Ti-lift-off step. (a) Section of a single TM-pass polarizers, (b) Taper end of a TM-pass polarizer with a designed width of 1.0 µm*

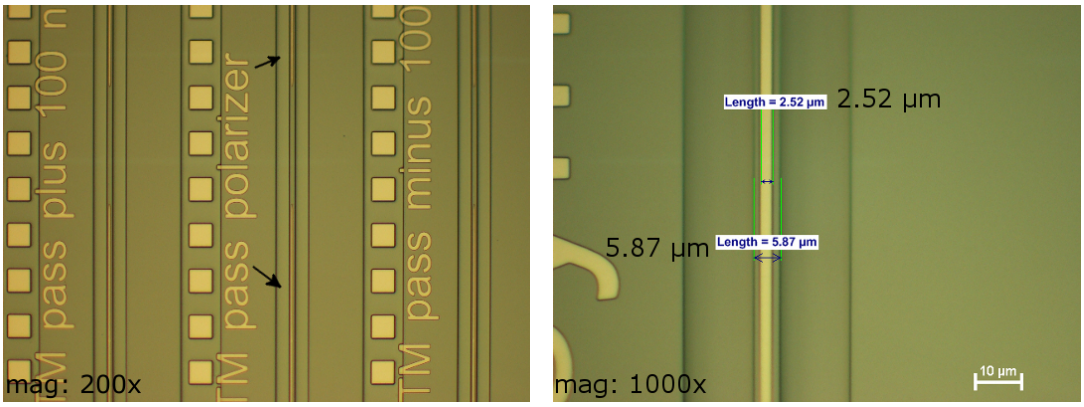
photoresist AZ5214 is a good choice to get the desired etch mask quality. The AZ5214 photoresist step is shown in Fig. 9.38. The width of the resist is as intended namely 6 μm.



(a) **(b)**

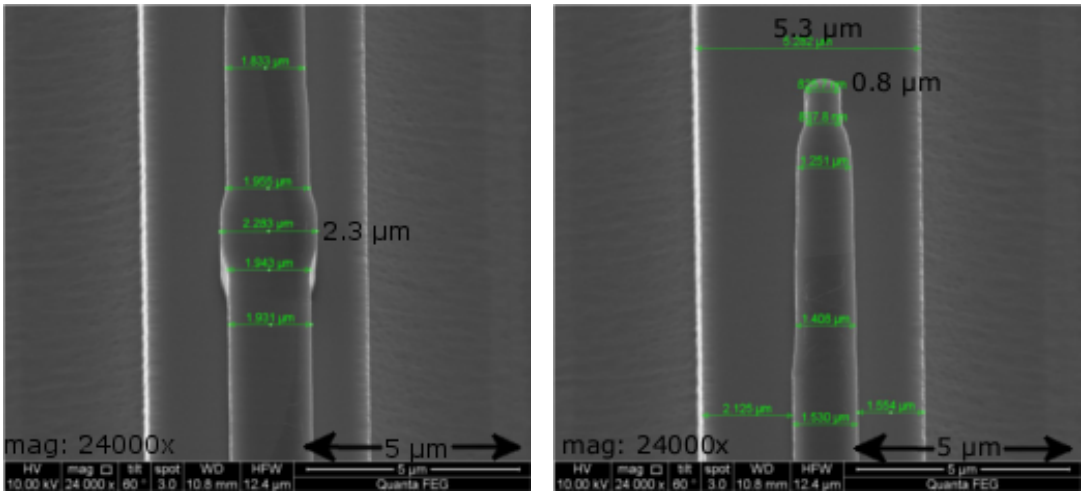
Figure 9.38: *Microscope images after the AZ5214 lithography step. (a) Section of a single TM-pass polarizers, (b) Taper end of a TM-pass polarizer with a designed width of 1.0 µm*

In Fig. 9.39 it can be seen that the SiO_2 mask that was used in the first $Cl_2/CH_4/H_2$ ICP etch was removed without affecting the underlying Ti mask. Figs. 9.40 and 9.41 show the finished polarization filter structure. The mesured width of the "300 nm narrower" TM-pass polarizer is just 100 nm wider than the intended 2.2 μm (Fig. 9.40). The 0.7 μm narrow taper end causes a slightly different taper shape than the design. However, this taper should not result in additional losses.



(a) **(b)**

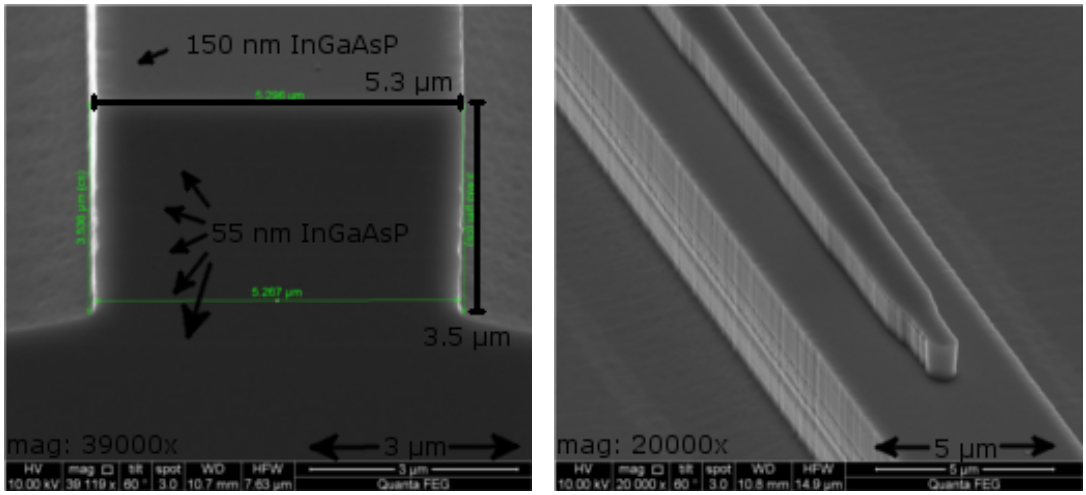
Figure 9.39: *Microscope images after the ICP removal of the second SiO_2 mask. (a) Section with two TM-pass polarizers, (b) unmodified ATG along the whole section.*



(a) **(b)**

Figure 9.40: *SEM cross-section images after the process run. (a) Middle section of a 300 nm narrower TM-pass polarizer, (b) Taper end of a TM-pass polarizer with an designed width of 0.7 µm.*

The main intention of a SSC is to improve direct fiber coupling. Therefore, a large spot size waveguide is required. Fig. 9.41(a) shows the input waveguide and its vertical sidewalls. The height and width of the waveguide are 3.5 μm and 5.3 μm respectively. The width is slightly reduced by 700 nm. However, it still is a large mode input waveguide. Because the width reduction is caused by a narrower than intended SiO_2 etch mask, the width of the photomask can be increased by several hundred nanometers to incorporate the expected waveguide width reduction.

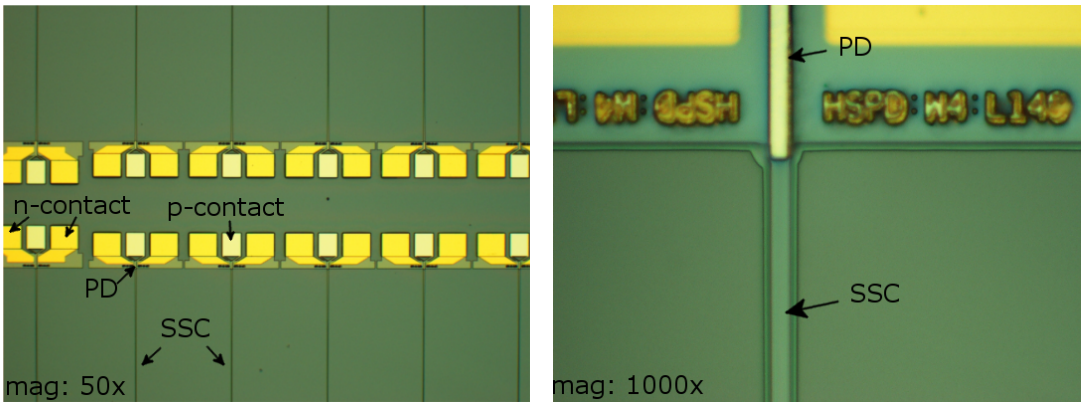


(a) **(b)**

Figure 9.41: *SEM cross-section images after the process run. (a) Front facet of the input waveguide, (b) sidewall of a 300 nm narrower TM-pass polarizer.*

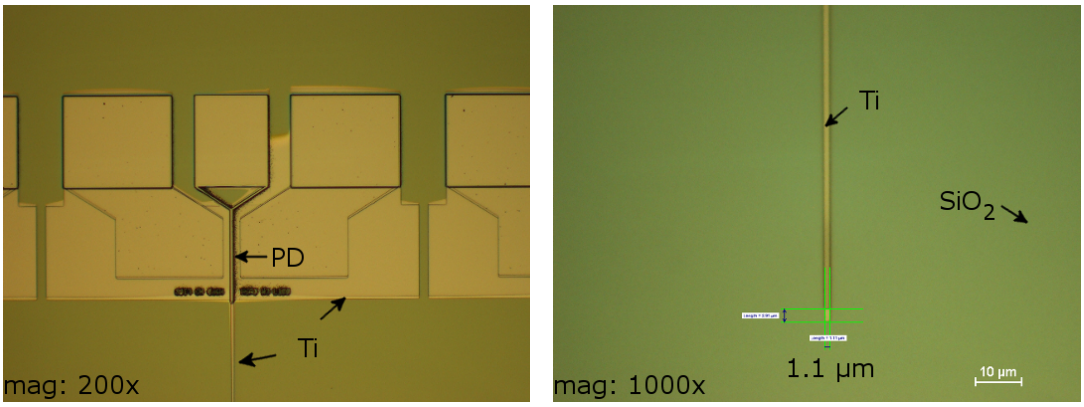
The $Cl_2/CH_4/H_2$ ICP developed etch provided smooth and vertical sidewalls (Fig. 9.41(b)). Nevertheless, a good vacuum contact during the AZ5214 photoresist remains as a critical issue. The linear scratch like features along the mesa in Fig. 9.41(a) are most likely related to a not perfectly vertical SiO_2 mask caused by a non optimum vacuum contact during the exposure of the photoresist mask.

The importance of SSCs lies in the ability to integrate them with other optical devices. In Chapter 7, SSCs together with PDs were design. In this chapter, it is demonstrated that the process enables the actual integration of a SSC with a PD. In Figs. 9.42 and 9.42 images of a process run on an InP wafer are shown. In Fig. 9.42 the PD structure is already defined, SiO_2 is deposited on the chip and UV26 is patterned for a Ti lift-off step. It is possible to align the upper waveguide ridge well to the PD. This ridge together with the PD must be covered by Ti for the following process steps. Fig. 9.43 shows the chip after the Ti-lift-off. Fig. 9.43(a) shows that the PD and its contacts are covered. Furthermore, in Fig. 9.43(b) a taper end width for the upper waveguide of 1.1 μm can be seen. Therefore, it is possible to obtain the desired waveguide dimensions. Nevertheless, the vacuum contact during the resist exposure remains a critical issue.



(a) **(b)**

Figure 9.42: *Microscope images of patterned UV 26 on an InP-test chip before the 200 nm thick Ti-evaporation. (a) multiple PDs with SSC, (b) SSC waveguide aligned to a 4 µm wide PD.*



(a) **(b)**

Figure 9.43: *Microscope images of an InP-test chip after the 200 nm thick Ti-lift-off. (a) PDs with SSC, (b) SSC upper waveguide end*

9.5 Conclusion

A process guideline based on a SiO_2/Ti etch mask has been analyzed and developed capable to fabricate an asymmetric twin waveguide with vertical and smooth sidewalls. Furthermore, the required taper end width of 1 μm for the upper waveguide has been repeatedly achieved. The importance of an appropriate photoresist to define a dielectric ICP etch mask has been shown. The etch rate, selectivity, and smoothness of a $Cl_2/CH_4/H_2$ inductively coupled plasma etch was analyzed in a design of experiment approach relative to the gas concentrations. The temperature

dependant passivation effect of CH_4 has been found. A $Cl_2/CH_4/H_2$ = 10/18/12 sccm etch has been obtained that allows to etch smooth and vertical sidewalls for InP and InP/InGaAsP systems.

Chapter 10

Conclusion

The purpose of this thesis was to obtain an integrable spot size converter for InP-based photonic systems. Standard fabrication techniques had to be used for the required fabrication steps. Furthermore, the fabrication of the structure had to be possible without epitaxial regrowth. To fulfill these requirements, an asymmetric twin waveguide design was investigated. The coupling mechanism in this asymmetric twin waveguide was simulated. The fabrication steps of an asymmetric twin waveguide were analyzed and optimized. The refractive indices of different InGaAsP compositions were measured. Spot size converters integrated with photodiodes were designed. Finally, polarization filters were fabricated and characterized.

10.1 Summary of Results

The waveguide structures analyzed in this thesis always consisted of a lower large spot size ($\approx$ 5 μm) diluted fiber coupling waveguide and higher refractive index smaller spot size upper waveguides.

Here the adiabatic and resonant coupling mechanism at 1550 nm was analyzed for such a passive asymmetric twin waveguide. A methodology was developed to first determine the resonance points in the structure, and then design the tapers around those points either to avoid or allow power transfer between the guided modes. It has been found that the fabrication tolerance of the asymmetric twin waveguide in this thesis can be improved by tapering the mode beating section by a width

difference (start/end) of 500 nm.

It has been shown that it is possible to use the resonant coupling mechanism in this asymmetric twin waveguide to design a TM- and a TE-pass polarizer. The simulated power extinction ratios were 20 dB (TM/TE) and 11 dB (TE/TM) respectively. Furthermore, it has been shown that a polarization splitter can be designed in this asymmetric twin waveguide. The asymmetric twin waveguide was split into two section. In the first section a tapered upper waveguide was introduced. This structure allowed a certain ratio of power transfer from the even to the odd mode for each polarization. In the section section the upper waveguide width was kept constant and the width of the lower waveguide increased. The wider lower waveguide caused in mode beating in the lateral direction. This mode beating resulted in split ratios of 85/6 for the TE- and 88/1 for the TM-polarization.

Following, measurement results of fabricated polarizers were shown for the first time. The polarizers were designed according to the simulation results of Chapter 5. The power extinction ratios were (3.1 $\pm$ 0.4) (TE/TM) and (1.4 $\pm$ 0.4) dB (TM/TE) at a wavelength of 1610 nm. Two couplers, each of them 372 nm long, were placed consecutively. The shift from 1550 nm to 1610 nm was caused by a different than designed epitaxial material and by a different width of the large spot size lower waveguide. The waveguide losses of the large spot size input waveguide were (2.6 $\pm$ 0.4) dB for the TE-polarization, and (1.9 $\pm$ 0.3) for the TM-polarization at 1550 nm.

In Chapter 7 the second InGaAsP composition in the upper waveguide was replaced by a layer consisting of the same InGaAsP material as in the diluted waveguide. This reduced the complexity of the growth step for the asymmetric twin waveguide. The modified asymmetric twin waveguide was integrated with an evanescent coupled PIN-photodiode. It has been shown that the alignment tolerance to a 3 μm wide photodiode can be improved by introducing a 3.4 μm wide end to the adiabatic taper of the coupling waveguide. 82 % of the TE- and 78 % of the TM-polarized were absorbed in the photodiode. An input waveguide with 88 % fiber coupling efficiency was demonstrated. The optical field coupling to the photodiode was achieved by introducing a transition waveguide between the input and the coupling waveguide.

The absorption efficiencies of the photodiode were calculated to be 88 % for the TE- and 85 % for the TM-polarization. Under the assumption of constant photodiode material it has been shown that only a variation of the refractive indices of the InGaAsP quaternaries to their ideal indices reduced the absorption efficiency by more than 1 dB.

The reflection spectroscopy technique was used to measure the refractive indices of an un-doped and n-doped InGaAsP composition. For the un-doped InGaAsP (λ_g = 1160 nm) material an index of 3.30 at 1550 nm was calculated. This value matched well with the theoretical value. For the $2 * 10^{18}$ cm^{-3} n-doped InGaAsP (λ_g = 1300 nm) a refractive index value of 3.42 at 1550 nm was calculated. The higher than theoretical value was explained by a non uniform strain in this layer. This non uniform strain was verified by the corresponding XRD rocking curve and the PL measurement.

Finally, in Chapter 9 the fabrication steps for asymmetric twin waveguide were analyzed and optimized. It has been shown that a process with a SiO_2 and Ti etch mask enabled the fabrication of an asymmetric twin waveguide. It was possible to fabricate a taper end width of 1 μm under the usual present facility conditions. The etch rate, selectivity, and smoothness of $Cl_2/CH_4/H_2$ inductively coupled plasma etches were analyzed in a design of experiment approach relative to the gas concentrations. The temperature dependant passivation effect of CH_4 was found. A $Cl_2/CH_4/H_2$ = 10/18/12 sccm etch was obtained that enabled to etch smooth and vertical sidewalls for InP and InP/InGaAsP.

10.2 Main Conclusion

In conclusion, the major findings of this thesis are:

- It has been shown that the fabrication tolerance for the resonant coupler in this thesis can be improved by tapering the mode beating section at a certain angle.

- It has been shown in simulation that resonant coupling in the asymmetric twin waveguide structure of this thesis enables a polarization filter mechanism.

Furthermore, simulation results have demonstrated a polarization splitting effect in the same asymmetric twin waveguide structure.

- The asymmetric twin waveguide based spot size converter design of this thesis was integrated with a PIN-photodiode. The refractive indices of the two different InGaAsP compositions were measured. The developed process steps were successfully applied in a fabrication test run to obtain a spot size converter integrated with a photodiode.

- Process steps were developed to fabricate an asymmetric twin waveguide without regrowth. An $Cl_2/CH_4/H_2$ based ICP etch was analyzed and optimized. The ICP chuck was kept at room temperature. Smooth and vertical sidewalls were achieved with a $Cl_2/CH_4/H_2$ = 10/18/12 sccm chemistry. The passivation effect of CH_4 has been experimentally shown. 1 μm wide taper end widths were fabricated with a repeatable process guideline, based on a combined SiO_2 and Ti etch mask.

- For the first time polarization filters based on resonant coupling in an asymmetric twin waveguide were fabricated and characterized. Although divergencies in the epitaxial material and in the width of the input waveguide occurred, a polarization filter effect for the TE- and TM-polarization was measured at 1610 nm. The TE/TM power extinction ratio was (1.8±0.2) dB and the TM/TE power extinction ratio (0.7±0.2) dB respectively. The filters were only several hundred microns long and can be easily repeated several times to increase the power extinction ratio.

10.3 Outlook

The work conducted in this thesis demonstrated spot size converters that are integrable with many InP-based photonic elements. The shown polarization filter mechanism in the asymmetric twin waveguide coupler offers several opportunities, such as short filters with a high power extinction ratio and low fiber coupling loss, the fabrication of a polarization splitter, and the implementation of the polariza-

tion state as another degree of freedom in photonic integrated circuits. On the way towards a deployable technology for photonic integrated circuits a number of challenges and questions remain however.

The quality of the epitaxial material is one of the most important criteria to obtain a working device as designed. Therefore, all quaternaries to be used in any spot size converter structure must be characterized relative to its refractive index. With this knowledge and a repeatable growth run spot size converters, filters, etc. can be designed according to these values.

A spot size converter PIN-photodiode structure was designed according to the previous approach. The test fabrication showed promising results. Therefore, only epitaxial material similar to the characterized InGaAsP compositions is required to fabricate an integrated spot size converter with a PIN-photodiode.

On the theoretical side, a model would be useful that approximates the resonance and cut-off widths in an asymmetric twin waveguide without solving the Maxwell's equation along the whole structure. For example, the propagation constants of all guided modes are given at the taper start and end widths. Following, a model could be applied to calculate the propagation constants along the taper without solving the Maxwell's equations.

The design of a polarization filter can be simplified, if it is possible to approximate the ratio of transferred power among the guided modes without the necessity of simulating the whole propagating optical field.

A similar theoretical aspect arises for the large spot size diluted waveguide. For a given waveguide width, a certain ratios of the InGaAsP/InP refractive indices and of the layer thicknesses are required to obtain a single mode waveguide with a large circular spot size. An algorithm for this design step would be helpful.

Finally, further research on the polarization filter relative to its birefringence, refractive index differences, resonance and cut-off widths, and waveguide dimensions should improve the performance of the filter. For example, a difference of up to 1 μm between the resonance widths of the TE- and TM-polarization most likely increases the power extinction ratios and the fabrication tolerance. Additionally, this research can lead to an optimized design and finally to a polarization splitter.

Appendix A

Publications

Journals

- A. Wieczorek, B. Roycroft, J. OŚCallaghan, K. Thomas, E. Pelucchi, F. H. Peters, and B. Corbett, Polarizers in an Asymmetric Twin Waveguide Based on Resonant Coupling, IEEE Photon. Technol. Lett., submitted, 2013

- A. Wieczorek, H. Yang, B. Roycroft, F.H. Peters, B. Corbett, PIN-Photodiode with a Large Spot Size Input Waveguide, Opt. Quantum Electronics, no. 45, p. 365, 2013

- A. Wieczorek, V. Djara, J. O'Callaghan, K. Thomas, F.H. Peters, B. Corbett, Inductively coupled plasma deep etching of InP/InGaAsP in $Cl_2/CH_4/H_2$ based chemistries with the electrode at 20 °C, J. Vac. Sci. Technol. B, no. 30, 051208, 2012

- A. Wieczorek, B. Roycroft, F.H. Peters, and B. Corbett, TE/TM-mode pass polarizers and splitter based on an asymmetric twin waveguide and resonant coupling, Opt. Quantum Electronics, no. 44, p. 175, 2012

- A. Wieczorek, B. Roycroft, F.H. Peters, and B. Corbett, Loss analysis and increasing of the fabrication tolerance of resonant coupling by tapering the mode beating section, Opt. Quantum Electronics, no. 42, p. 521, 2011

Conferences and Workshops

- A. Wieczorek, H. Yang, B. Roycroft, F. H. Peters, and B. Corbett, Large, integrated spot size converter for an InGaAs PIN-photodiode, International Workshop on Optical Waveguide Theory and Numerical Modeling, 2012

- A. Wieczorek, B. Roycroft, F.H. Peters, and B. Corbett , TE/TM-mode pass polarizers and splitter based on an asymmetric twin waveguide and resonant coupling, International Conference on Numerical Simulation of Optoelectronic Devices, 2011

- A. Wieczorek, B. Roycroft, F.H. Peters, and B. Corbett, Analysis of mode coupling in an asymmetric twin waveguide, Photonics Ireland Conference, 2011

- Ko-Hsin Lee, B. Roycroft, J. O'Callaghan, Hua Yang, A. Wieczorek, P. H. Peters, and B. Corbett, Integration of low-pass filter with optical receiver using quantum well intermixing, Photonics Global Conference (PGC), 2010

- A. Wieczorek, B. Roycroft, F.H. Peters, and B. Corbett, Comparison of resonant coupling and adiabatic mode transfer for integrated mode adapters, International Workshop on Optical Waveguide Theory and Numerical Modeling, 2010

- A. Wieczorek, B. Roycroft, F.H. Peters, and B. Corbett, Mode converters using modal interference, Photonics Ireland Conference, 2009

Appendix B

Numerical Methods

B.1 Maxwell's Equations

The electric field $\vec{E}$ (V/m), the magnetic field $\vec{H}$ (A/m), the electric flux density $\vec{D}$ (C/m^2), and the magnetic flux density $\vec{B}$ (A/m^2) are related through the equations [19]:

$$\vec{D} = \epsilon \vec{E} \tag{B.1.1}$$

$$\vec{B} = \mu \vec{B} \tag{B.1.2}$$

where the permittivity ϵ and permeability μ are defined as

$$\epsilon = \epsilon_0 \epsilon_r \tag{B.1.3}$$

$$\mu = \mu_0 \mu_r \tag{B.1.4}$$

ϵ_0 and μ_0 are the permittivity and permeability of a vacuum, and ϵ_r and μ_r are the relative permittivity and permeability of the material. The electromagnetic field satisfy the following well-known Maxwell equations [19]:

$$\nabla \cdot \vec{D} = \rho \tag{B.1.5}$$

$$\nabla \cdot \vec{B} = 0 \tag{B.1.6}$$

$$\nabla \times \vec{E} = -\frac{\partial \vec{B}}{\partial t} \tag{B.1.7}$$

$$\nabla \times \vec{H} = \frac{\partial \vec{D}}{\partial t} + \vec{J} \tag{B.1.8}$$

where ρ is the charge density. The current density $\vec{J}$ is defined by Ohm's Law $\vec{J} = \sigma\vec{E}$, with the conductivity σ. The current density $\vec{J}$ is related to the charge density ρ as follows:

$$\nabla \cdot \vec{J} = -\frac{\partial \rho}{\partial t} \tag{B.1.9}$$

Non magnetic and non conductive material is assumed, therefore $\mu_r = 1$ and $\rho = 0$.

B.2 Finite Element Method

The scalar (SC) finite element method (FEM) is show here. There are two ways to solve optical waveguide problems: the variational method and weighted residual method, of which the Galerkin method is representative. Both methods are briefly described here.

B.2.1 Variational Method

In the variational method, the wave equation is not directly solved. Instead, the analysis region is divided into many segments and the variational principle is applied to the sum of the discretized functionals for all segments. Fig. B.1 shows an analysis region Ω surrounded by a boundary Γ. A variational method to calculate n_{eff} is discussed for the scalar wave equation [19]

$$\frac{\partial^2 \Phi}{\partial x^2} + \frac{\partial^2 \Phi}{\partial y^2} + k_0^2(\epsilon_r - n_{eff}^2)\Phi = 0 \tag{B.2.1}$$

where $n_{eff} = \beta k_0$. Multiplying this equation by variation $\delta\Phi$ of the function Φ and integrating the product over the whole analysis region Ω, we get

$$\iint_\Omega \delta\Phi(\frac{\partial^2 \Phi}{\partial x^2} + \frac{\partial^2 \Phi}{\partial y^2})dxdy + \iint_\Omega \delta\Phi k_0^2(\epsilon_r - n_{eff}^2)\Phi dxdy = 0 \tag{B.2.2}$$

After partial integration and substitutions the following equation is obtained

$$\begin{aligned} &\delta\left[\int_\Gamma \frac{\partial \Phi}{\partial x}dy + \int_\Gamma \frac{\partial \Phi}{\partial y}dx\right] \\ -\delta\frac{1}{2}&\left[\iint_\Omega \left\{\left(\frac{\partial \Phi}{\partial x}\right)^2 + \left(\frac{\partial \Phi}{\partial y}\right)^2 - k_0^2(\epsilon_r - n_{eff}^2)\right\}dxdy\right] = 0 \end{aligned} \tag{B.2.3}$$

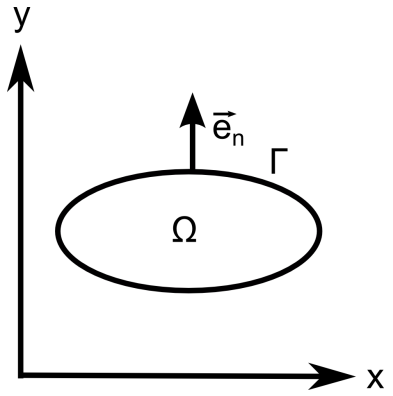


Figure B.1: *Analysis region.*

Here the following functional I is introduced:

$$\begin{aligned} I =& \frac{1}{2}\left[\iint_{\Omega}\left\{\left(\frac{\partial\Phi}{\partial x}\right)^2+\left(\frac{\partial\Phi}{\partial y}\right)^2-k_0^2(\epsilon_r-n_{eff}^2)\Omega^2\right\}dxdy\right] \\ &-\left[\int_{\Gamma}\frac{\partial\Phi}{\partial x}dy+\int_{\Gamma}\frac{\partial\Phi}{\partial y}dx\right] \end{aligned} \tag{B.2.4}$$

The functional can be rewritten as:

$$I = \frac{1}{2}\left[\iint_{\Omega}\left\{\left(\frac{\partial\Phi}{\partial x}\right)^2+\left(\frac{\partial\Phi}{\partial y}\right)^2-k_0^2(\epsilon_r-n_{eff}^2)\Phi^2\right\}dxdy\right] \tag{B.2.5}$$

$$-\left[\int_{\Gamma}\Phi\frac{\partial\Phi}{\partial\overrightarrow{e_n}}d\Gamma\right] \tag{B.2.6}$$

where $\partial/\partial\overrightarrow{e_n}$ is the derivative with respect to the normal vector $\overrightarrow{e_n}$

Using the functional I, Eq. B.2.3 can be rewritten as:

$$\delta I = 0 \tag{B.2.7}$$

which means that the stationary condition is imposed on the functional I. The calculation procedure for the application of the variational method to the FEMs is summarized as follows: The analysis region is first divided into segments, which are called elements, and the functional I_e is calculated for each element e. The total functional is the sum of all I_e.

B.2.2 Galerkin Method

The Galerkin Method is a weighted residual method. Because Φ is a true solution of Eq. B.2.1 the right-hand term is definitely zero. However, Φ cannot actually

be known. Only an approximated wave function $\overline{\Phi}$ can be obtained. With this approximation Eq. B.2.1 does not become zero, but generates an error R

$$\frac{\partial^2\overline{\Phi}}{\partial x^2} + \frac{\partial^2\overline{\Phi}}{\partial y^2} + k_0^2(\epsilon_r - n_{eff}^2)\overline{\Phi} = R \tag{B.2.8}$$

R is called the error residual. The difference between $\overline{\Phi}$ and Φ can be decreased by averagely setting the error residual R equal to zero in the whole analysis region. Some weighted function Ψ must be used when setting R to 0 to account for the unevenly concentrated electromagnetic field:

$$\iint \Psi R dx dy = 0 \tag{B.2.9}$$

After some further mathematics the variational and the Galerkin method lead to the same solvable eigenvalue matrix equation.

Appendix C

MOVPE Growth A0887

The layer structure starting from the top is as follows:

- 1000 nm InP
- 150 nm InGaAsP ($\lambda_g = 1350$ nm)
- 1000 nm InP
- 50 nm InGaAsP ($\lambda_g = 1170$ nm)
- 700 nm InP
- 50 nm InGaAsP ($\lambda_g = 1170$ nm)
- 700 nm InP
- 50 nm InGaAsP ($\lambda_g = 1170$ nm)
- 700 nm InP
- 50 nm InGaAsP ($\lambda_g = 1170$ nm)
- 700 nm InP
- 50 nm InGaAsP ($\lambda_g = 1170$ nm)
- InP substrate

Appendix D

Photodiode-Spot Size Converter MOVPE Growth

The layer structure starting from the top is as follows:

- 90 nm InGaAs, p-doped $4 * 10^{19} 1/cm^3$, similar to run A1023

- 600 nm InP, p-doped $1.5 * 10^{18} 1/cm^3$, similar to run A0434

- 100 nm InP, p-doped $1.5 * 10^{18} 1/cm^3$, similar to run A0434

- 500 nm $In_{0.53}GaAs$, undoped, similar to run A0434

- 100 nm InP, n-doped $1.6 * 10^{18} 1/cm^3$, similar to run A0434

- 200 nm InGaAsP, n-doped $2.0 * 10^{18} 1/cm^3$, similar to run A1034

- 600 nm InP n-doped $2.0 * 10^{18} 1/cm^3$, similar to run A0434

- 400 nm InGaAsP, undoped, similar to run A0983

- 1000 nm InP, undoped, similar to run A0983

- 55 nm InGaAsP, undoped, similar to run A0983

- 700 nm InP, undoped

- 55 nm InGaAsP, undoped, similar to run A0983

- 700 nm InP, undoped

- 55 nm InGaAsP, undoped, similar to run A0983

- 700 nm InP, undoped

- 55 nm InGaAsP, undoped, similar to run A0983

- 700 nm InP, undoped

- 55 nm InGaAsP, undoped, similar to run A0983

- InP substrate

Appendix E

Process Guideline

E.0.3 SiOSiNx Process

1. PECVD: 250 nm Si_3N_4		
2. Lithography UV26 (resist at room temperature)		
Primer	4000 rpm	50 s
UV26 (dynamic)	1000 rpm	20 s
	3000 rpm	10 s
	4000 rpm	20 s
Edge bead removal		
Hotplate: 130 °C 60 s		
Mask aligner MA6: vacuum contact, exposure: 11.2 s		
Post exposure bake: 110 °C 60 s		
Developer: MF-CD-26 20 s		
3. ICP etch: HFSiO recipe		
4. Resist removal		
Asher: 150 W 8 min		
1165 at 100 °C 10 min		
5. Sputtering of 400 nm of SiO_2		

6. Lithography UV26 (resist at room temperature)		
Primer	4000 rpm	50 s
UV26 (dynamic)	1000 rpm	20 s
	3000 rpm	10 s
	4000 rpm	20 s
Edge bead removal		
Hotplate: 130 °C 60 s		
Mask aligner MA6: vacuum contact, exposure: 12.2 s		
Post exposure bake: 110 °C 60 s		
Developer: MF-CD-26 20 s		
7. ICP etch: HFSiO recipe		
8. Resist removal		
Asher: 150 W 8 min		
9. ICP etch: 4 μm deep etch of InP/InGaAsP		
10. Removal of SiO_2 by diluted BoE		
11. ICP etch: 1 μm deep etch of InP/InGaAsP		
12. Etch mask removal: BoE 3 min		

E.0.4 TiSiO process

1. Sputtering of 250 nm SiO_2		
2. Lithography Lift-off (resist at room temperature)		
Primer	4000 rpm	50 s
LOR10A	4000 rpm	60 s
Hotplate: 150 °C 180 s		
Edge bead removal		
Primer	4000 rpm	50 s
UV26 (dynamic)	1000 rpm	20 s
	3000 rpm	10 s
	4000 rpm	20 s
Edge bead removal		
Hotplate: 130 °C 60 s		
Mask aligner MA6: vacuum contact, exposure: 11.2 s		
Post exposure bake: 110 °C 60 s		
Developer: MF-CD-26 30 s		
Developer: MF-319 90 s		
2. Temescal: 200 nm Ti-evaporation		
3. Resist removal and Ti-lift-off		
1165 at 100 °C 30 min		
Asher: 150 W 3 min		
4. Sputtering of 400 nm of SiO_2		

5. Lithography AZ5214		
Primer	4500 rpm	30 s
AZ5214	4500 rpm	50 s
Hotplate: 130 °C 60 s		
Edge bead removal		
Mask aligner MA1006: vacuum contact, exposure: 7.5 s		
Developer: AZ400K:DI = 1:4 25 s		
6. ICP etch: HFSiO recipe		
7. Resist removal		
Asher: 150 W 5 min		
1165 at 100 °C 30 min		
Asher: 150 W 5 min		
8. ICP etch: 4 μm deep etch of InP/InGaAsP with Cl2/CH4/H2 = 10/18/12 sccm		
9. ICP etch: HFSiO recipe		
10. ICP etch: 1 μm deep etch of InP/InGaAsP with Cl2/CH4/H2 = 10/18/12 sccm		
11. Etch mask removal: BoE 5 min		

E.0.5 Spot Size Converter and Photodiode

1. P-metal lift off		
Image reversal lithography		
Primer	4000 rpm	50 s
AZ5214	4000 rpm	50 s
Hotplate: 100 °C 50 s		
Mask aligner MA1006: vacuum contact, exposure: 1.6 s		
Reverse bake: 115 °C 105 s		
Mask aligner MA1006: flood exposure: 30 s		
Developer: MF-CD-26 22 s		
BOE Dip 10 s		
Temescal: 15 nm Cr 200 nm Au-evaporation		
Resist removal and metal-lift-off		
1165 at 100 °C 30 min		
Asher: 150 W 3 min		
2. Oxide deposition 340 nm with PECVD: HFSiO recipe		
3. Lithography with MA6 for etching SiO2 mask		
Primer	4000 rpm	50 s
UV26 (dynamic)	1000 rpm	20 s
	3000 rpm	10 s
	4000 rpm	20 s
Edge bead removal		
Hotplate: 130 °C 60 s		
Mask aligner MA6: vacuum contact, exposure: 11.2 s		
Post exposure bake: 110 °C 60 s		
Developer: MF-CD-26 30 s		

6. SiO2 etching with ICP STS: Oxidetch recipe		
7. Resist removal		
Asher: 150 W 5 min		
1165 at 100 °C 30 min		
Asher: 150 W 5 min		
8. Waveguide Etching with Oxford ICP: 2 μm deep etch with Cl2/CH4/H2 = 10/8/4 sccm		
9. N-metal lift off		
Image reversal lithography		
Primer	4000 rpm	50 s
AZ5214	4000 rpm	50 s
Hotplate: 100 °C 50 s		
Mask aligner MA1006: vacuum contact, exposure: 2.0 s		
Reverse bake: 115 °C 105 s		
Mask aligner MA1006: flood exposure: 30 s		
Developer: MF-CD-26 22 s		
Angled Temescal: Au:Ge:Au:Ni:Au		
Resist removal and metal-lift-off		
1165 at 100 °C 30 min		
Asher: 150 W 3 min		
10. Anneal N metal 380degree, 5mins, N2/H2		
11. Sputtering of 200 nm of SiO_2		
12. Lithography Lift-off (resist at room temperature)		
Primer	4000 rpm	50 s
LOR10A	4000 rpm	60 s
Hotplate: 150 °C 180 s		
Edge bead removal		

Primer	4000 rpm	50 s
UV26 (dynamic)	1000 rpm	20 s
	3000 rpm	10 s
	4000 rpm	20 s
Edge bead removal		
Hotplate: 130 °C 60 s		
Mask aligner MA6: vacuum contact, exposure: 12.5 s		
Post exposure bake: 110 °C 60 s		
Developer: MF-CD-26 30 s		
Developer: MF-319 90 s		
13. Oven 90degress 30 min		
14. Angled Temescal: 200 nm Ti-evaporation		
15. Resist removal and Ti-lift-off		
1165 at 100 °C 30 min		
Asher: 150 W 3 min		
16. Oxide deposition 400 nm with PECVD: HFSiO recipe		
17. Lithography AZ5214		
Primer	4500 rpm	30 s
AZ5214	4500 rpm	50 s
Hotplate: 130 °C 60 s		
Edge bead removal		
Mask aligner MA1006: vacuum contact, exposure: 7.5 s		
Developer: AZ400K:DI = 1:4 25 s		
18. STS ICP etch: Oxidetch recipe		
19. Resist removal		
Asher: 150 W 5 min		
1165 at 100 °C 30 min		
Asher: 150 W 5 min		

20. ICP etch: 4 μm deep etch of InP/InGaAsP with Cl2/CH4/H2 = 10/18/12 sccm		
21. ICP etch: Oxidetch recipe		
22. ICP etch: 1 μm deep etch of InP/InGaAsP with Cl2/CH4/H2 = 10/18/12 sccm		
23. Lithography for SI InP deep etching mask		
Primer	4000 rpm	50 s
S1813	4500 rpm	50 s
Hotplate: 115 °C 180 s		
Edge bead removal		
Mask aligner MA1006: vacuum contact, exposure: 7.0 s		
Developer: MF319 25 s		
Hardbake: oven 90degrees 30 min		
24. Deep Etching of Semi-Insulating InP substrate HCl:H3PO4=1:4 Dip in 5mins etching rate around 700-800nm/Min		
21. Remove SiO2 ICP etch: Oxidetch recipe		

Bibliography

[1] Datasheet of the UVIII photoresit, Rohm and Haas Company electronic materials subsidiary of The Dow Chemical Company, Midland, Michigan, USA.

[2] Datasheet of the UV26 photoresit, Rohm and Haas Company electronic materials subsidiary of The Dow Chemical Company, Midland, Michigan, USA.

[3] Cisco Systems, Inc. Cisco Visual Networking Index: Forecast and Methodology, 2011–2016, *White Paper*, 2012.

[4] C. Cole, B. Huebner, and J. E. Johnson, "Design and fabrication of monolithic optical spot size transformers (MOST's) for highly efficient fiber-chip coupling," *IEEE Commun. Mag.*, vol. 47, pp. S16–S22, 2009.

[5] B. Sartorius, C. Bornholdt, J. Slovak, M. Schlak, C. Schmidth, A. Marculescu, P. Vorreau, S. Tsadka, W. Freude, and J. Leuthold. All-optical DPSK wavelength converter based on MZI with integrated SOAs and phase shifters, *Optical Fiber Communication Conference, 2006 and the 2006 National Fiber Optic Engineers Conference*, 2006.

[6] D. Taillaert, R. Baets, P. Dumon, W. Bogaerts, D. Van Thourhout, B. L. adn V. Wiaus, S. Beckx, and J. Wouters. "Silicon-on-insulator platform for integrated wavelength-selective components", in *Proc. IEEE/Leos Workshop on Fibers and Optical Passive Components, 2005*, pp. 115-120.

[7] F. Van Laere, M. Ayre, D. Taillaert, D. V. Thourhout, T. F. Krauss, and R. Baets, "Compact and efficient fibre-to-waveguide grating couplers in InP-membrane," *Electron. Lett.*, vol. 42, pp. 343–345, 2006.

[8] I. Moerman, P. P. Van Daele, and P. M. Demeester, "A review on farication technologies for the monolithic integration of tapers with iii-v semiconductor devices," *Journal Sel. Topic in Quantum Electro.*, vol. 3, pp. 1308–1320, 1997.

[9] Y. Suematsu, M. Ymada, and K. Hayashi, "Integrated twin-guide algaas laser with multiheterostructure," *IEEE J. Quantum Electron*, vol. QE-11, pp. 457–460, 1975.

[10] L. Xu, M. R. Gokhale, P. Studenkov, J. C. Dries, C.-P. Chao, D. Garbuzov, and S. R. Forrest, "Monolithic integration of an InGaAsP-InP MQW laser/waveguide using a twin-guide structure with a mode selection layer," *IEEE Photon. Technol. Lett.*, vol. 9, pp. 569–571, 1997.

[11] F. Xia, J. Wei, V. Menon, and S. R. Forrest, "Monolithic integration of a semiconductor optical amplifier and a high bandwidth p-i-n photodiode using asymmetric twin-wavegudie technology," *IEEE Photon. Technol. Lett.*, vol. 14, pp. 452–454, 2003.

[12] T. Koch, E. G. Burkhardt, F. G. Storz, T. J. Bridges, and T. Sizer, "Vertically grating-coupled ARROW structures for iii-v integrated optics," *IEEE J. Quantum Electron.*, vol. 23, pp. 889–897, 1987.

[13] M. Glarza, K. De Mesel, S. Verstufyft, C. Aramburu, I. Moermann, P. Van Daele, R. Baets, and M. Lopez-Amo, "1.55 μm InP-InGaAsP Fabry-Pèrot lasers with integrated spot size converters using antiresonant reflecting optical waveguides," *IEEE Photon Technol. Lett.*, vol. 14, pp. 1043–1045, 2002.

[14] B.-H. V. Borges and P. R. Herczfeld, "Coupling from a single mode fiber to a iii-v thin-film waveguide via monolithic integration of a polymeric optical waveguide," *J. Franklin Inst.*, vol. 335B, pp. 89–96, 1997.

[15] S. S. Saini, V. Vusirikala, R. Whaley, F. G. Johnson, D. Stone, and M. Dagenais, "Compact mode expanded lasers using resonant coupling between a 1.55 μm InGaAsP tapered active region and an underlying coupling waveguide," *IEEE Photon. Technol. Lett.*, vol. 10, pp. 1232–1234, 1998.

[16] C. L. M. Daunt, H. Yang, W. Han, K. Thomas, E. Pelucchi, B. Corbett, and F. H. Peters, "Dielectric-free fabrication of compact 30-GHz photodetectors using the isolated pedestal contact configuration," *IEEE Photon. Technol. Lett.*, vol. 24, pp. 1082–1084, 2012.

[17] N. Kalonji and J. Semi, "High efficiency, long working distance laser diode to single mode fiber coupling," *Electron. Lett.*, vol. 30, pp. 892–894, 1994.

[18] H. M. Presby and C. A. Edwards, "Near 100 percent efficient fiber microlenses," *Electron. Lett.*, vol. 28, pp. 582–584, 1992.

[19] K. Kawano and T. Kitoh, *Introduction to optical waveguide analysis*. Reading, Massachusetts: Wiley, 2001.

[20] D. Marcuse, *Theory of dielectric optical waveguides*. Reading, Massachusetts: Academic Press, Inc., 1991.

[21] K. Okamoto, *Fundamentals of optical waveguides*. Reading, Massachusetts: Wiley, 2006.

[22] B. E. Saleh and M. C. Teich, *Fundamentals of photonics*. Hoboken, New Jersey: Wiley, 2007.

[23] E. A. Marcatili, "Dielectric rectangular waveguide and directional coupler for integrated optics," *Bell Sys. Tech. J.*, vol. 48, pp. 2071–2102, 1969.

[24] A. Kumar, K. Thyagarajan, and A. K. Ghatak, "Analysis of rectangular-core dielectric waveguides–An accurate perturbation approach," *Opt. Lett.*, vol. 8, pp. 63–65, 1983.

[25] O. C. Zienkiewitz, *The finite element method*. New York: McGraw-Hill, 1973.

[26] M. Koshiba, *Optical waveguide theory by the finite element method*. Dordrecht, Holland: KTK Scientific Publisher and Kluwer Academic Publisher, 1992.

[27] Y. Chung and N. Dalig, "Assessment of finite difference beam propagation," *IEEE J. Quantum Electron.*, vol. 26, pp. 1335–1339, 1990.

[28] Photon Design, Ltd., www.photond.com.

[29] A. Sudbo, "Film mode matching: a versatile numerical method for vector mode field calculations in dielectric waveguides," *Pure Appl. Opt.*, vol. 2, pp. 211–233, 1993.

[30] H. Kogelnik and C. V. Shank, "Coupled-wave theory of distributed feedback lasers," *J. Appl. Phys.*, vol. 43, pp. 2327–2335, 1972.

[31] K. H. Ylä-Jarkko and A. B. Grudinin, "Performance limitations of high-power DFB lasers," *IEEE Photon. Technol. Lett.*, vol. 15, pp. 191–193, 2003.

[32] K. Sato, "Chirp characteristics of 40-Gb/s directly modulated distributed-feedback laser diodes," *IEEE J. Lightwave Technol.*, vol. 23, pp. 3790–3797, 2005.

[33] A. Schülzgen, L. Li, D. Nguyen, C. Spiegelberg, R. Matei Rogojan, A. Laronche, J. Albert, and N. Peyghambarian, "Distributed feedback fiber laser pumped by multimode laser diodes," *Opt. Lett.*, vol. 33, pp. 614–616, 2008.

[34] R. D. Dupuis and E. P. Dapkus, "Room-temperature operation of distributed-Bragg-confinement $Ga_{1-x}Al_xAs$-GaAs lasers grown by metalorganic chemical vapor deposition," *Appl. Phys. Lett.*, vol. 33, pp. 68–69, 1978.

[35] R. Todt, T. Jacke, R. Meyer, J. Adler, R. Laroy, G. Morthier, and M.-C. Amann, "Sample grating tunable twin-guide laser diodes with over 40-nm electronic tuning range," *IEEE Photon. Technol. Lett.*, vol. 17, pp. 2514–2516, 2005.

[36] J. Fricke, F. Bugge, A. Ginolas, W. John, A. Klehr, M. Matalla, P. Ressel, H. Wenzel, and G. Erbert, "High-power 980-nm broad-area lasers spectrally stabilized by surface Bragg gratings," *IEEE Photon. Technol. Lett.*, vol. 22, pp. 284–286, 2010.

[37] T. W. Ang, G. T. Reed, A. Vonsovici, A. G. R. Evans, P. R. Routley, and M. R. Josey, "Effects of grating heights on highly efficient unibond soi waveguide grating couplers," *Opt. Express*, vol. 19, pp. 3592–3598, 2011.

[38] D. Taillaert, P. Bienstman, and R. Baets, "Compact efficient broadband grating coupler for silicon-on-insulator waveguides," *Opt. Lett.*, vol. 29, pp. 2749–2751, 2004.

[39] S. K. Selvaraja, D. Vermeulen, M. Schaekers, E. Sleecks, W. Bogaerts, G. Roelkens, P. Dumon, D. Van Thourhout, and R. Baets. Highly efficient grating coupler between optical fiber and silicon photonic circuit, Conference on Lasers and Electro-Optics, 2009 and Conference on Quantum electronics and Laser Science, pp. 1–2, 2009.

[40] M.Antelius, K. B. Gylfason, and H. Sohlstroem, "An apodized soi waveguide-to-fiber surface grating coupler for single lthography silicon photonics," *IEEE Photon Technol. Lett.*, vol. 12, pp. 59–61, 2000.

[41] Y. Tang, Z. Wang, L. Wosinski, U. Westergren, and S. He, "Highly efficient nonuniform grating coupler for silicon-on-insulator nanophotonic circuits," *Opt. Lett.*, vol. 35, pp. 1290–1292, 2010.

[42] P. Zory, "Laser oscillation in leaky corrugated optical waveguides," *Appl. Phys. Lett.*, vol. 22, pp. 125–128, 1973.

[43] Z. I. Alferov, V. M. Andreyev, S. A. Gurevich, R. F. Kazarinov, V. R. Lariono, M. N. Mizerov, and E. L. Portnoy, "Semiconductor lasers with the light output through the diffraction grating on the surface of the waveguide layer," *IEEE J. Quantum Electron*, vol. QE-11, pp. 449–451, 1975.

[44] P. Zory and L. D. Comerford, "Grating-coupled double heterostructure AlGaAs diode lasers," *IEEE J. Quantum Electron.*, vol. QE-11, pp. 451–457, 1975.

[45] R. D. Burnharn, D. R. Scifres, and W. Streifer, "Single-heterostructure algaas diode laser," *IEEE J. Quantum Electron*, vol. 11, pp. 439–449, 1975.

[46] F. K. Reinhart, R. A. Logan, and C. V. Shank, "GaAs-$Al_xGa_{1-x}As$ injection lasers with distributed bragg reflectors," *Appl. Phys. Lett.*, vol. 27, pp. 45–48, 1975.

[47] G. A. Evans, N. W. Carlson, J. M. Hammer, and J. K. Butler, *Surface emitting semiconductor lasers and arrays.* San Diego, California: Academic Press, Inc., 1993.

[48] C. Wu, M. Svilans, M. Fallahi, T. Makino, J. Glinsaki, C. Maritan, and C. Blaauw, "Optically pumped surface-emitting DFB GaInAsP/InP lasers with circular grating," *Electron. Lett.*, vol. 27, pp. 1819–1820, 1991.

[49] F. S. Choa, M. H. Shih, F. Y. Fan, G. J. Simonis, P. L. Liu, T. Tanbunek, R. A. Logan, W. T. Tsang, and A. M. Sergent, "Very-low threshold 1.55 μm grating-coupled surface-emitting lasers for optical signal-processing and interconnect," *Appl. Phys. Lett.*, vol. 67, pp. 2777–2779, 1995.

[50] K. Kasaya, Y. Kondo, M. Okamoto, O. Mitomi, and M. Naganuma, "Monolithically integrated DBR lasers with simple tapered waveguide for low-loss fibre coupling," *Electron. Lett.*, vol. 29, pp. 2067–2068, 1993.

[51] P. Doussiere, P. Garabedian, C. Graver, E. Derouin, E. Gaumont-Gaorin, G. Michaud, and R. Meilleur, "Tapered active stripe for 1.5μm InGaAsP/InP strained multiple quantum well lasers with reduced beam divergence," *Appl. Phys. Lett.*, vol. 64, pp. 539–541, 1994.

[52] J. N. Walpole, Z. L. Liau, L. J. Missaggia, and D. Yap, "Diode lasers with cylindrical mirror facets and reduced beam divergence," *Appl. Phys. Lett.*, vol. 50, pp. 1219–1221, 1987.

[53] J. N. Walpole, "Semiconductor amplifiers and lasers with tapered gain regions," *Optical and Quantum Electron.*, vol. 28, pp. 623–645, 1996.

[54] I. F. Lealman, L. J. Rivers, M. J. Harlow, and S. D. Perrin, "1.56 μm InGaAsP/InP tapered active layer multiquantum well laser with improved coupling to cleaved single mode fiber," *Electron. Lett.*, vol. 30, pp. 857–859, 1994.

[55] I. F. Lealman, L. J. Rivers, M. J. Harlow, and S. D. Perrin, "InGaAsP/lnP tapered active layer multiquantum well laser with 1.8 db coupling loss to cleaved singlemode fiber," *Electron. Lett.*, vol. 30, pp. 1685–1687, 1994.

[56] R. Zengerle, O. Leminger, W. Weiershausen, K. Faltin, and B. Huebner, "Laterally tapered InP-InGaAsP waveguides for low-loss chip-to-fiber butt coupling: a comparison of different configurations," *IEEE Photon. Technol. Lett.*, vol. 7, pp. 532–534, 1995.

[57] R. Zengerle, B. Huebner, C. Greus, H. Burkhard, H. Janning, and E. Kuphal, "Monolithic integration of DFB laser with spot-size transformer for highly efficient laser fibre coupling," *Electron. Lett.*, vol. 32, pp. 1142–1143, 1995.

[58] A. Kasukawa, N. Iwai, N. Yamanaka, and N. Yokouchi, "Output beam characteristics of 1.3 μm GaInAsP-InP SL-QW lasers with narrow and circular output beam," *Electron. Lett.*, vol. 31, pp. 559–560, 1995.

[59] M. Wada, M. Kohtoku, K. Kawano, H. Okamoto, Y. Kadota, Y. Kondo, K. Kishi, S. Kondo, Y. Sakai, I. Kotaka, Y. Noguchi, and Y. Itaya, "High-coupling-efficiency laser diodes integrated with spot-size converters fabricated on 2 inch InP substrate," *Electron. Lett.*, vol. 31, pp. 2102–2103, 1995.

[60] R. Y. Fang, D. Bertoni, M. Meliga, I. Montrosset, G. Olivetti, and R. Paoletti, "Low-cost 1.55 μm ingaasp-inp spot size converted (ssc) laser with conventional active layers," *IEEE Photon. Technol. Lett.*, vol. 9, pp. 1084–1086, 1997.

[61] K. Kawano, M. Kohtoku, N. Yoshimoto, S. Sekine, and Y. Noguchi, "2 x 2 ingaalas/inalas multiquantum well (mqw) directional coupler waveguide switch modules integrated with spot size convertors," *Electron. Lett.*, vol. 30, pp. 353–354, 1994.

[62] N. Yoshimoto, K. Kawano, Y. Hasumi, H. Takeuchi, S. Kondo, and Y. Noguchi, "InGaAlAs/InAlAs multiple quantum well phase modulator integrated with spot size conversion structure," *IEEE Photon. Technol. Lett.*, vol. 6, pp. 208–210, 1994.

[63] M. Wada, M. Kohtoku, K. Kawano, S. Kondo, Y. Tohmori, K. Kishi, Y. Sakai, I. Kotaka, Y. Noguchi, and Y. Itaya, "Laser diodes monolithically integrated with spot-size converters fabricated on 2 inch InP substrate," *Electron. Lett.*, vol. 31, pp. 1252–1254, 1995.

[64] T. Schwander, S. Fischer, A. Kraemer, M. Laich, K. Luksic, G. Spatschek, and M. Warth, "Simple and low-loss fibre-to-chip coupling by integrated field-matching waveguide in InP," *Electron. Lett.*, vol. 29, pp. 326–328, 1993.

[65] G. A. Vawter, R. E. Smith, H. Hou, and J. R. Wendt, "Semiconductor laser with tapered-rib adiabatic-following fiber coupler for expanded output-mode diameter," *IEEE Photon. Technol. Lett.*, vol. 9, pp. 425–427, 1993.

[66] J. G. Bauer, M. Schier, and G. Ebbinghaus. "High responsivity integrated tapered waveguide PIN photodiode", in *Proc. 19th Eur. Conf. Optical Communication (ECOC'93)*, Switzerland, pp. 277-280.

[67] I. Moerman, M. D'Hondt, W. Vanderbauwhede, P. P. Van Daele, P. M. Demeester, and W. Hunziker, "InGaAsP/InP strained MQW laser with integrated modesize converter using the shadow masked growth technique," *Electron. Lett.*, vol. 31, pp. 452–454, 1995.

[68] Y. Tohmori, Y. Suzaki, H. Oohashi, Y. Sakai, Y. Kondo, H. Okamoto, Y. Kadota, O. Mitomi, Y. Itaya, and T. Sugie, "High temperature operation with low-loss coupling to fiber for narrow-beam 1.3 μm lasers with butt-jointed selective grown spot-size converters," *Electron. Lett.*, vol. 31, pp. 1838–1839, 1995.

[69] Y. Sakai, Y. Tohmori, Y. Suzaki, Y. Kondo, and O. Mitomi, "Improved FFP of 1.3 μm spot-size converted laser for highly efficient coupling to optical fibre," *Electron. Lett.*, vol. 15, pp. 1372–1374, 1996.

[70] T. Brenner and H. Melchior, "Integrated optical modeshape adapters in InGaAsP/InP for efficient fiber-to-waveguide coupling," *IEEE Photon. Technol. Lett.*, vol. 50, pp. 452–454, 1993.

[71] T. Murakami, K. Ohtaki, H. Matsubara, T. Yamawaki, H. Saito, K. Isshiki, Y. Kokubo, A. Shima, H. Kumabe, and W. Susaki, "A very narrow-beam AlGaAs laser with a thin tapered thickness active layer (T^3-laser)," *IEEE J. Quantum Electron.*, vol. QE-23, pp. 712–719, 1987.

[72] A. Shahar, W. J. Thomlinson, A. Yi-Yan, M. Seto, and R. J. Deri, "Dynamic etch mask technique for fabricating tapered semiconductor optical waveguides and other structures," *Appl. Phys. Lett.*, vol. 56, pp. 1098–1100, 1990.

[73] K. Kawano, M. Kohtoku, H. Okamoto, Y. Itaya, and M. Naganuma, "Comparison of coupling characteristics for several spot-size-converter-integrated laser diodes in the 1.3 μm wavelength region," *IEEE Photon. Technol. Lett.*, vol. 9, pp. 428–430, 1997.

[74] G. Coudenys, I. Moerman, Z. Q. Yu, F. Vermaerke, and P. Van Daele, "Atmospheric pressure and low pressure shadow masked MOVPE growth of InGaAs(P)/InP and (In)GaAs/(Al)GaAs heterostructures and quantum wells.," *J. Electron. Mater.*, vol. 23, pp. 227–234, 1994.

[75] T. Brenner, W. Hunziker, M. Smit, M. Bachmann, G. Guekos, and H. Melchior, "Vertical InP/InGaAsP tapers for low-loss optical fiber-waveguide coupling," *Electron. Lett.*, vol. 28, pp. 2040–2041, 1992.

[76] G. Müller, B. Stegmüller, H. Westermeier, and G. Wenger, "Tapered In/InGaAsP waveguide structure for efficient fiber-chip coupling," *Electron. Lett.*, vol. 27, pp. 1836–1838, 1991.

[77] F. Ghirardi, B. Mersali, J. Brandon, G. Herve-Gruyer, and A. Carenco, "Quasi planar spot-size transformer for efficient coupling betwen a cleaved fibre and an InP/InGaAsP rib waveguide," *IEEE Photon Technol. Lett.*, vol. 6, pp. 522–524, 1994.

[78] A. Beling, H.-G. Bach, G. G. Mekonnen, R. Kunkel, and D. Schmidt, "Miniaturized waveguide-integrated p-i-n photodetector with 120-GHz bandwidth

and high responsivity," *IEEE Photon Technol. Lett.*, vol. 17, pp. 2152–2154, 2005.

[79] A. Umbach, D. Trommer, R. Steingrueber, S. Seeger, W. Ebert, and G. Unterboersch. Ultrafast, high-power 1.55 μm side-illuminated photodetector with integrated spot size converter, in *Tech. Dig. Optical Fiber Communication Conf.* (OFC 2000), pp. 117-119.

[80] R. J. Deri, C. Caneau, E. Colas, L. M. Schiavone, and N. C. Andreadakis, "Integrated optic mode-size tapers by selective organometallic chemical vapor deposition of InGaAsP/InP," *Appl. Phys. Lett.*, vol. 61, pp. 952–954, 1992.

[81] N. Yoshimoto, K. Kawano, H. Takeuchi, S. Kondo, and Y. Noguchi, "Spot size convertors using InP/InAlAs multi quantum well waveguides," *Electron. Lett.*, vol. 28, pp. 1610–1611, 1992.

[82] G. Wenger, L. Stoll, B. Weiss, M. Schienle, R. Müller-Nawrath, S. Eichinger, J. Müller, B. Acklin, and G. Müller, "Design and fabrication of monolithic optical spot size transformers (MOST's for highly efficient fiber-chip coupling," *J. Lightwave Technol.*, vol. 12, pp. 1782–1790, 1994.

[83] H. Ribot, P. Sansonetti, and A. Carenco, "Improved design for the monolithic integration of a laser and an optical waveguide coupled by an evanescent field," *IEEE J. Quantum Electron*, vol. 26, pp. 1930–1941, 1990.

[84] P. V. Studenkov, M. R. Gokhale, J. C. Dries, and S. R. Forrest, "Monolithic integration of a quantum-well laser and an optical amplifier using an asymmetric twin-waveguide structure," *IEEE Photon. Technol. Lett.*, vol. 10, pp. 1088–1090, 1998.

[85] P. V. Studenkov, M. R. Gokhale, and S. R. Forrest, "Efficient coupling in integrated twin-waveguide lasers using waveguide tapers," *IEEE Photon. Technol. Lett.*, vol. 11, pp. 1096–1098, 1999.

[86] P. V. Studenkov, F. Xia, M. R. Gokhale, and S. R. Forrest, "Asymmetric twin-waveguide 1.55 μm wavelength laser with a distributed bragg reflector," *IEEE Photon. Technol. Lett.*, vol. 12, pp. 468–470, 2000.

[87] F. Xia, J. K. Thomson, M. R. Gokhale, P. V. Studenkov, J. Wei, W. Lin, and S. R. Forrest, "An asymmetric twin-waveguide high-bandwidth photodiode using a lateral taper coupler," *IEEE Photon. Technol. Lett.*, vol. 13, pp. 845–847, 2001.

[88] M. A. Duguay, Y. Kokubun, and T. L. Koch, "Antiresonant reflecting optical waveguides in SiO_2-Si multilayer structures," *Appl. Phys. Lett.*, vol. 49, pp. 13–15, 1986.

[89] T. Baba, Y. Kokubun, T. Sakaki, and K. Iga, "Loss reduction of an arrow waveguide in shorter wavelength and its stack configuration," *IEEE J. Lightwave Technol.*, vol. 6, pp. 1440–1445, 1988.

[90] T. Baba and Y. Kokubun, "New polarization-insensitive antiresonant reflecting optical waveguide (ARROW-B)," *IEEE Photon Technol. Lett.*, vol. 1, pp. 232–234, 1989.

[91] T. Koch, W. Sang, and P. Corvini, "Spectral dependence of propagation loss in InP/InGaAsP antiresonant reflecting optical waveguides grown by chemical beam epitaxy," *Appl. Phys. Lett.*, vol. 50, pp. 307–309, 1986.

[92] M. Glarza, K. De Mesel, R. Baets, A. Martinez, C. Aramburu, and M. Lopez-Amo, "Compact spot-size converters with fiber-matched antiresonant reflecting optical waveguides," *Appl. Opt.*, vol. 42, pp. 4841–4846, 2003.

[93] T. Koch, U. Coren, G. Boyd, P. Corvini, and M. Duguay, "Antiresonant refecting optical waveguides for III-V integrated optics," *Electron. Lett.*, vol. 23, pp. 204–205, 1987.

[94] L. J. Mawst, D. Botez, C. Zmudzinski, and C. Tu, "Antiresonant reflecting optical waveguide-type, single-mode diode lasers," *Appl. Phys. Lett.*, vol. 61, pp. 503–505, 1992.

[95] M. Galarza, K. D. Mesel, R. Baets, and M. López-Amo. Design of InGaAsP-InP Tapered Ridge Mode Transformer Using an Underlying ARROW Coupling Waveguide, Proceedings Symposium IEEE/LEOS Benelux chapter, 2000.

[96] M. Glarza, K. D. Mesel, T. V. Caenegem, S. Verstuyft, C. Aramburu, I. Moermann, P. V. Daele, R. Baets, and M. Lopez-Amo, "InGaAsP-InP 1.55 μm lasers with integrated mode expanders using fiber matched leaky waveguides.," *Appl. Phys. B*, vol. 73, pp. 585–588, 2001.

[97] M. Glarza, K. De Mesel, S. Verstufyft, C. Aramburu, I. Moermann, P. Van Daele, R. Baets, and M. Lopez-Amo, "A new spot-size converter concept using fiber-matched antiresonant reflecting optical waveguides," *J. Lightwave Technol.*, vol. 21, pp. 269–274, 2003.

[98] R. Inaba, M. Kato, M. Sagawa, and H. Akahoshi, "Two-dimensional mode size transformation by δn-controlled polymer waveguides," *J. Lighwave Technol.*, vol. 16, pp. 620–624, 1998.

[99] N. Bouadma, J. Liang, . L. R, S. Grosmaire, P. Boulet, and S. Sainson, "Integration of a laser diode with a polymer-based waveguide for photonic integrated circuits," *IEEE Photon. Technol. Lett.*, vol. 6, pp. 1188–1190, 1994.

[100] R. S. Fans and R. B. Hooker, "Tapered polymer single-mode waveguides for mode transformation," *J. Lightwave Technol.*, vol. 17, pp. 466–474, 1999.

[101] J. gang Liu and M. Ueda, "High refractive index polymers: fundamental research and practical applications," *J. Mater. Chem.*, vol. 19, pp. 8907–8919, 2009.

[102] Y. Shani, C. H. Henry, R. C. Kistler, K. J. Orlowsky, and A. Ackerman, "Efficient coupling of a semiconductor laser to an optical fiber by means of a tapered waveguide on silicon," *Appl. Phys. Lett.*, vol. 55, pp. 2389–2391, 1989.

[103] R. M. de Ridder, R. A. Wijbrans, H. Albers, J. S. Aukema, P. V. Lambeck, H. J. W. M. Hoekstra, and A. Diessen. A spot-size transformer for fiber-chip

coupling in sensor applications at 633 nm in silicon oxynitride, 8th Annual Meeting Conference of the Lasers and Electro-Optics Society, LEOS, 1995.

[104] C. K. Wong, H. Wong, M. Chan, Y. T. Chow, and H. P. Chan, "Silicon oxynitride integrated waveguide for on-chip optical interconnects applications," *Microelectron Reliab.*, vol. 48, pp. 212–218, 2008.

[105] M. Fadel and E. Vogs. 207th Meeting of The Electrochemical Society, Quebec City, Canada, 2007.

[106] M. Fadel, M. Buelters, M. Niemand, E. Voges, and P. M. Krummrich, "Low-loss and low-birefringence high-contrast silicon-oxynitride waveguides for optical communications," *J. Lightwave Technol.*, vol. 27, pp. 698–705, 2009.

[107] M. Hoffmann, P. Kopka, and E. Voges, "Low-loss fiber-matched low-temperature PECVD waveguides with small-core dimensions for optical communication systems," *IEEE Photon. Technol. Lett.*, vol. 9, pp. 1238–1240, 1997.

[108] R. M. de Ridder, K. Woerhoff, A. Driessen, P. V. Lambeck, and H. Albers, "Silicon oxynitride planar waveguiding structures for application in optical communication," *Journal Sel. Topic in Quantum Electro.*, vol. 4, pp. 930–937, 1997.

[109] K. Woerhoff, C. G. H. Roeloffzen, R. M. de Ridder, A. Driessen, and P. V. Lambeck, "Design and application of compact and highly tolerant polarization-independent waveguides," *J. Lightwave Technol.*, vol. 25, pp. 1276–1283, 2007.

[110] M.-H. Shih, F.-S. Choa, R. M. Kapre, W. T. Tsang, R. A. Logan, and S. N. G. Chu, "Alignment-relaxed 1.55 μm multiquantum well laser fabricated using standard buried heterostructure laser processes," *Electron. Lett.*, vol. 31, pp. 1058–1060, 1995.

[111] H. Kogelnik. Coupling and conversion coefficients for optical modes in quasi-optics, *Microwave Research Institute Symposia Series*, 14, New York: Polytechnic Press, pp.333–347, 1964.

[112] J. Love, W. Henry, W. Stewart, R. Black, S. Lacroix, and F. Gonthier, "Tapered single-mode fibers and devices, Part 1: Adiabaticity criteria," *IEE Proceedings-J*, vol. 138, pp. 343–354, 1991.

[113] F. Xia, V. M. Menon, and S. R. Forrest, "Photonic integration using asymmetric twin-waveguide (ATG) technology: part I-concepts and theory," *IEEE J. Sel. Topics Quantum Electron.*, vol. 11, pp. 17–29, 2005.

[114] R. G. Hunsperger, *Integrated optics*. Berlin Heidelberg, Germany: Springer-Verlag, 2002.

[115] J. C. Campbell, F. A. Blum, D. W. Shaw, and K. I. Lawley, "GaAs electrooptic directionalcoupler switch," *Appl. Optics*, vol. 27, pp. 202–205, 1975.

[116] V. Vusirikala, S. S. Saini, R. E. Bartolo, S. Agarwala, R. D. Whaley, F. G. Johnson, D. R. Stone, and M. Dagenais, "1.55 μm InGaAsP-InP laser arrys with integrated-mode expanders fabricated using a single epitaxial growth," *IEEE J. Sel. Topics. Quantum Electron.*, vol. 3, pp. 1332–1343, 1997.

[117] A. Wieczorek, B. Roycroft, F. H. Peters, and B. Corbett, "Loss analysis and increasing of the fabrication tolerance of resonant coupling by tapering the mode beating section," *Opt. Quant. Electron.*, vol. 42, pp. 521–529, 2011.

[118] S. Benedetto and P. Poggiolini, "Theory of polarization shift keying modulation," *IEEE Trans. Commun.*, vol. 40, pp. 708–721, 1992.

[119] F. Heismann, P. B. Hansen, S. K. Korotky, G. Raybon, J. J. Veselka, and M. S. Whalen, "Automatic polarisation demultiplexer for polarisation-multiplexed transmission systems," *Electron. Lett.*, vol. 29, pp. 1965–1966, 1993.

[120] U. Hempelmann, H. Herrmann, G. Mrozynski, V. Reimann, and W. Sohler, "Integrated optical proton exchange TM-pass polarizers in $LiNbO_3$: modelling and experimental performance," *J. Lightwave Technol.*, vol. 13, pp. 1750–1759, 1995.

[121] M.-C. Oh, M.-H. Lee, and H.-J. Lee, "TE-pass and TM-pass waveguide polarisers with buried birefringent polymer," *Electron. Lett.*, vol. 35, pp. 471–472, 1999.

[122] L. B. Soldano, A. H. de Vreede, M. K. Smit, B. H. Verbeek, E. G. Metaal, and F. H. Groen, "Mach-Zehnder interferometer polarization splitter in InGaAsP/InP," *IEEE Photon. Technol. Lett.*, vol. 28, pp. 402–405, 1994.

[123] B. W. Hakki and T. L. Paoli, "Gain spectra in GaAs double-heterostructure injection lasers," *J. Appl. Phys.*, vol. 44, pp. 4113–4119, 1973.

[124] J. E. Bowers and C. A. Burrus, "High-speed zero-bias waveguide photodetectors," *Electron. Lett.*, vol. 42, pp. 905–906, 1986.

[125] A. Beling and J. C. Campbell, "InP-based high-speed photodetectors," *J. Lightw. Technol.*, vol. 27, pp. 343–355, 2009.

[126] R. J. Deri and O. Wada, "Impedance matching for enhanced waveguide/photodetector integration," *Appl. Phys. Lett.*, vol. 55, pp. 2712–2714, 1989.

[127] R. J. Deri, M. Makiuchi, O. Wada, A. Kuramata, H. Hamaguchi, and R. J. Hawkins, "Integrated waveguide/photodiodes using vertical impedance matching," *Appl. Phys. Lett.*, vol. 56, pp. 1737–1739, 1990.

[128] J. Buus, M.-C. Amann, and D. J. Blumenthal, *Tunable laser diodes and related optical sources.* Hoboken, New Jersey: John Wiley & Sons Inc., 2005.

[129] B. Broberg and S. Lindgren, "Refractive index of $In_{1-x}Ga_xAs_yP_{1-y}$," *J. Appl. Phys.*, vol. 55, pp. 3376–3381, 1984.

[130] K. Utaka, Y. Suematsu, Y. Kobayashi, and H. Kawanishi, "GaInAsP/InP integrated twin-guide lasers with first-order distributed bragg reflectors at 1.3 μm wavelength," *Jpn. J. Appl. Phys.*, vol. 19, pp. L137–L140, 1980.

[131] R. E. Nahory, M. A. Pollack, W. D. Johnston, and R. L. Barns, "Band gap versus composition and demonstration of vegard's law for $In_{1-x}Ga_xAs_yP_{1-y}$ lattice matched to inp," *Appl. Phys. Lett.*, vol. 33, pp. 659–661, 1978.

[132] R. L. Moon, G. A. Antypas, and L. W. James, "Bandgap and lattice constant of GaInAsP as function of alloy composition," *IEEE Photon Technol. Lett.*, vol. 4, pp. 627–630, 1992.

[133] P. Chandra, L. A. Coldren, and K. E. Strege, "Refractive index data from $Ga_xIn_{1-x}As_yP_{1-y}$ films," *Electron. Lett.*, vol. 17, pp. 6–7, 1981.

[134] M. J. Mondry, D. I. Babic, J. E. Bowers, and L. A. Coldren, "Refractive indexes of (Al, Ga, In)As epilayers on InP for optoelectronic applications," *J. Electron. Mater.*, vol. 3, pp. 635–643, 1974.

[135] S. Nojima and H. Asahi, "Refractive index of InGaAs/InAlAs multiquantum-well layers grown by molecular-beam epitaxy," *J. Appl. Phys.*, vol. 63, pp. 479–483, 1988.

[136] C. Grass, G. Boehm, M. Mueller, T. Gruendl, R. Meyer, and M.-C. Amann, "Empirical modeling of the refractive index for (AlGaIn)As lattice matched to InP," *Semicond. Sci. Technol.*, vol. 25, pp. 1–4, 2010.

[137] G. D. Pettit and W. J. Turner, "Refractive index of InP," *J. Appl. Phys.*, vol. 36, p. 2081, 1965.

[138] B. R. Bennett, R. A. Soref, and J. A. D. Alamo, "Carrier-induced change in refractive index of InP, GaAs, and InGaAsP," *IEEE J. Quantum Electron.*, vol. 26, pp. 113–122, 1990.

[139] P. F. Fewster, *X-Ray scattering from semiconductor*. London: Imperial College Press, 2000.

[140] D. H. Zhang, W. Shi, H. Q. Zheng, S. F. Yoon, C. H. Kam, and X. Z. Wang, "Physical properties of InGaAsP/InP grown by molecular beam epitaxy with valve phosphorous cracker cell," *J. Crystal Growth*, vol. 211, pp. 384–388, 2000.

[141] S. J. Moss and A. Ledwith, *The chemistry of the semiconductor industry*. New York, NY, USA: Springer, 1989.

[142] S. Wolf and R. N. Taubner, *Silicon Processing for the VLSI Era, Volume 1*. Sunset Beach, California, USA: Lattice Press, 1990.

[143] T. Soma, J. Satoh, and H. Matsuo, "Thermal expansion coefficient of GaAs and InP," *Solid State Commun.*, vol. 42, pp. 889–892, 1981.

[144] Y. Okada and Y. Tokumaru, "Precise determination of lattice parameter and thermal expansion coefficient of silicon between 300 and 1500 K," *J. Appl. Phys.*, vol. 56, pp. 314–320, 1984.

[145] R. Dylewicz, R. M. De La Rue, R. Wasielewski, P. Mazur, G. Mezösi, and A. C. Bryce, "Fabrication of submicron-sized features in InP/InGaAsP/AlGaInAs quantum well heterostructures by optimized inductively coupled plasma etching with $Cl_2/Ar/N_2$ chemistry," *J. Vac. Sci. Technol. B*, vol. 28, pp. 882–890, 2010.

[146] P. Strasser, R. Wüest, F. Robin, K. Rausche, B. Wild, D. Erni, and H. Jöckel. An ICP-RIE etching process for InP-based photonic crystals using $Cl_2/Ar/N_2$ chemistry, International conference on Indium Phosphide and related materials (2005).

[147] S. L. Rommel, J.-H. Jang, W. Lu, G. Cueva, L. Zhou, and I. Adesida, "Effect of H_2 on the etch profile of InP/InGaAsP alloys in $Cl_2/Ar/H_2$inductively coupled plasma reactive ion etching chemistries for photonic device fabrication," *J. Vac. Sci. Technol. B*, vol. 20, pp. 1327–1330, 2002.

[148] C.-Z. Sun, J.-B. Zhou, B. Xiong, J. Wang, and Y. Luo, "Vertical and smooth, etching of InP by $Cl_2/CH_4/Ar$ inductively coupled plasma at room temperature," *Chin. Phys. Lett.*, vol. 20, pp. 1312–1314, 2003.

[149] S. Guilet, S. Bouchoule, C. Jany, C. S. Corr, and P. Chabert, "Optimization of a Cl_2–H_2 inductively coupled plasma etching process adapted to nonther-

malized InP wafers for the realization of deep ridge heterostructures," *J. Vac. Sci. Technol. B*, vol. 24, pp. 2381–2387, 2006.

[150] S. Park, S.-S. Kim, L. Wang, and S.-T. Ho, "InGaAsPŰInP nanoscale waveguide-coupled microring lasers with submilliampere threshold current using Cl_2–N_2-based high-density plasma etching," *IEEE J. Quantum. Elect.*, vol. 41, pp. 351–356, 2005.

[151] J. Lin, A. Leven, N. G. Weimann, Y. Yang, R. F. Kopf, R. Reyes, Y. K. Chen, and F. s. Choa, "Smooth and vertical-sidewall InP etching using Cl_2/N_2 inductively coupled plasma," *J. Vac. Sci. Technol. B*, vol. 22, pp. 510–512, 2004.

[152] S. Dupont, A. Beaurain, P. Miska, M. Zegaoui, J.-P. Vilcot, H. W. Li, M. Constant, D. Decoster, and J. Chazelas, "Low-loss InGaAsP/InP submicron optical waveguides fabricated by icp etching," *Electron. Lett.*, vol. 40, pp. 865–866, 2004.

[153] C. Lee, D. Nie, T. Mei, and M. K. Chin, "Study and optimization of room temperature inductively coupled plasma etching of InP using $Cl_2/CH_4/H_2$ and CH_4/H_2," *J. Cryst. Growth*, vol. 288, pp. 213–216, 2006.

[154] F. Karouta, E. J. Geluk, R. W. van der Heijden, A. Yu. Silov, T. Eijkemans, J. G. M. van der Tol, M. K. Smit, and H. W. M. Salemink. Proceedings of the 16th Indium Phosphide and Related Materials Conference Kagoshima Japan (2004).

[155] J. W. Lee, J. Hong, and S. J. Pearton, "Etching of InP at >1 mm/min in Cl_2/Ar plasma chemistries," *Appl. Phys. Lett.*, vol. 68, pp. 847–849, 1995.

[156] C. S. Whelan, T. E. Kazior, and K. Y. Hur, "High rate CH_4:H_2 plasma etch processes for InP," *J. Vac. Sci. Technol. B*, vol. 15, pp. 1728–1732, 1997.

[157] C.-W. Lee and M.-K. Chin, "Room-temperature inductively coupled plasma etching of InP using Cl_2/N_2 and $Cl_2/CH_4/H_2$," *Chin. Phys. Lett.*, vol. 23, pp. 903–906, 2005.

[158] D. C. Montgomery, *Design and analysis of experiments*. John Wiley & Sons, Inc, 2005.

[159] J. C. Antony, *Design of experiments for engineers and scientists*. Elsevier Science & Technology Books, 2003.

[160] C. Sun, J.Wang, B. Xion, and Y. Luo. State-of-the-art program on compound semiconductor 46 (SOTAPOCS 46) and processes at the semiconductor/solution interface 2, proceedings (2007).

[161] S. Bouchoule, L. Vallier, G. Patriarche, T. Chevolleau, and C. Cardinaud, "Effect of Cl_2 - and HBr-based inductively coupled plasma etching on InP surface composition analyzed using in situ x-ray photoelectron spectroscopy," *J. Vac. Sci. Technol. A*, vol. 30, p. 031301, 2012.